UNIVERSITÀ DEGLI STUDI DI TRIESTE

UNIVERSITÀ DEGLI STUDI DI TRIESTE

XXXIV CICLO DEL DOTTORATO DI RICERCA IN

Scienze della Terra e Meccanica dei Fludi

Paleo and present oceanic modelling of the Ross Sea (Antarctica): evolution of water masses and ice shelf – ocean interactions during the last glacial cycle (21-0 ka)

Settore scientifico-disciplinare: **GEO/12**

DOTTORANDO / A
Enrico Pochini

COORDINATORE
PROF. Stefano Maset

SUPERVISORE DI TESI
PROF. Emanuele Forte

CO-SUPERVISORE DI TESI
DR. Florence Colleoni

ANNO ACCADEMICO 2020/2021

Contents

Abstract

The Antarctic ice sheet is expected to contribute a large amount to projected sea level change, in the context of present and future climate change scenarios. The accelerated melting is caused by the warming ocean that melts most of the ice shelves buttressing the Antarctic ice sheet inland flow. Observations of ice shelves basal melting by satellite are indirect and thus present large uncertainties. Direct observations of the sub-ice shelf environments are spatially and temporally limited. This lack of observations hampers a proper representation of ice shelves basal melting in state-of-the-art ice sheet models employed for the projections of sea level changes. The only way so far to fill the observational gap is to simulate ocean circulation beneath ice shelves and estimate basal melting by a physical model of the ocean – ice shelf thermodynamic interaction. In the Ross Sea, where a large ice shelf, i.e. the Ross Ice Shelf (RIS), is present, different water masses are causing melting. Even though the Ross ice shelf is not currently experiencing thinning compared to other sectors, there is evidence, from the geological record, that in this sector the Antarctic ice sheet underwent fast retreats during past glacial-interglacial cycles. Geological records indicate that at the peak of the Last Glacial Maximum (21 kyears BP), the ice sheet was grounded up to the continental shelf break, and during deglaciation it retreated in a few millennia, reaching its present-day configuration, hundreds of kilometres inland.

In this work, we want to investigate the influences of water masses on the basal melting under the RIS at present and in the past. In particular, the research aimed at understanding the influences of Ross Sea water masses variability on the RIS basal melting both at present and in the past. A regional adaptation of the Massachusetts Institute of Technology general circulation model (MITgcm) was implemented on the Ross Sea to simulate ocean circulation on the continental shelf and under the RIS. A present-day transient run, forced by ocean (GLORYS12V1) and atmospheric (ERA5) reanalysis over the period 1993-2018, shows that: [1] simulated water masses present different timescales of variability in their properties: Circumpolar Deep Water and Antarctic Surface Waters show a strong seasonal cycle, modulated by strong interannual variability. High Salinity Shelf Water (HSSW) and Low Salinity Shelf Water (LSSW), on the other hand, show a weaker seasonal cycle and a decadal oscillation in their salinity. Variability of Circumpolar Deep Water (CDW) and Antarctic Surface Water (AASW) is probably related to wind variability associated

with the Southern Annular Mode, the Amundsen Sea Low, and El-Niño Southern Oscillation, mediated by sea ice. Variability of HSSW and LSSW is probably related to variability of the sea ice and meltwater input, and katabatic wind strength, in turn associated with the Polar Cell. The same variability is observed for the water masses beneath the RIS. [2] Basal melting presents a distinct pattern, related to the current at draft level, and variability related to the changing water masses properties. A new method based on mixing of water masses was developed to disentangle the effect of mixing, and highlight the melting variability associated to each water mass. Results show basal melting of ∼78 Gt/yr, in line with the observations, and presenting variability at the seasonal, interannual and decadal scale indicative of changing water masses properties or volume expansion inside the cavity. Then, we run 21 snapshots at intervals of 1000 years, over the Last Deglaciation (∼21-0 kyears BP): each snapshot was 26 years long and branched on a separate 120 years-long spinup. Simulations are forced by the outputs from an existent transient global paleoclimate experiment TraCE-21ka. The purpose of the paleo experiment was: 1) to analyse the evolution of the water masses with varying deglacial climatic conditions, and 2) how circulation resumed on the continental shelf, starting from a condition restricted by a grounded ice sheet at LGM (∼21 ka), and retreating during the deglaciation. Results show that: [1] initially, circulation was limited to three sub-ice shelf cavities in the Western Ross Sea. In Pennel trough warm CDW water reached the cavity, whereas in the Drygaslki and Joides troughs, HSSW filled the bottom level. [2] During the millenium following the Meltwater Pulse 1A (14.6-14.3 ka), deep ocean warming and sub-surface ocean freshening caused a weakening of the Antarctic Slope Front, fostered CDW flow in Pennel and the Whales Deep cavity, which experienced high rates of basal melting. HSSW production in the Drygaslki and Joides stopped during this event. [3] In the Early Holocene (∼11.8 ka) grounding line retreat uncovered growingly portions of the continental shelf, allowing stronger atmospheric cooling and resumption of HSSW production. At ∼ 10 ka the RIS cavity began to form, and was melted on the Westward side by HSSW, and on the Eastward side by advected mCDW; therefore, the stronger melting role shifted to the HSSW at that time.

Chapter 1

Introduction

1.1 Scientific rationale

This PhD work is part of the Italian National Programme for Antarctic Research (PNRA), ANTIPODE research project (PI Florence Colleoni, OGS), which aims at investigating the interactions between the Antarctic Ice Sheet (AIS), the bedrock, and the ocean during the Middle Miocene (∼17-15 Ma) and the Last Deglaciation (∼21 ka to present) in the Ross Sea sector of Antarctica (Figure 1.1a,c). The AIS is trimmed at its margins by floating ice shelves that are under threat of collapsing due to ocean warming. The Ross Ice Shelf (RIS) is one of largest Antarctic ice shelves: buttressing land ice discharge from both the West Antarctic Ice sheet (WAIS) and the East Antarctic Ice Sheet (EAIS), it holds a volume of ∼11.6 m of water equivalent sea level in its catchment basin (Tinto et al., 2019). Geological records from the ANDRILL sediment cores (Figure 1.1) suggest that it has undergone partial or full collapses in past warm periods (Naish et al., 2009). Modelling work highlighted a mechanism of fast ice shelf disintegration and grounding line retreat in the marine-based sectors of the AIS known as Marine Ice Sheet Instability (MISI, Schoof, 2007; Joughin and Alley, 2011), which may be triggered where the ice sheet is grounded below sea level (Figure 1.1b, regions of negative bathymetry elevation). MISI is triggered when excessive ice shelf thinning caused by warming ocean induces acceleration of ice discharge at the grounding line on a retrograde sloping bed, eventually yielding to the disintegration of the ice shelf and subsequent loss of buttressing, finally leading to runaway acceleration of land-ice discharge into the oceans (Figure 1.2). Since MISI has not been observed yet, studying the interaction between the AIS, the ocean and the morphology of the bedrock during past periods of climate warming or, with climatic conditions warmer than today, is a key point to understanding how this mechanism evolved during geological time and how it may occur in the future. During the Middle Miocene Climatic Optimum (17-15

Ma, see Chapter 1.7), reconstruction of atmospheric CO_2 suggested concentrations higher than ∼500 ppm, similarly to what is expected for IPCC SSP concentration pathway scenario 8.5 by the end of the 21th century. The stratigraphic record of the Antarctic continental margin revealed that during that period, increased sediment erosion and deposition by the AIS led to the expansion and deepening of the continental shelf. This expanded the marine-based portion of the AIS, which was mostly terrestrial at that time, thus increasing its sensitivity to ocean warming (Colleoni et al., 2018b; Paxman et al., 2020). Investigating the past evolution of the AIS is crucial to understanding the tipping point of its marine-based sectors to past warming events, and to assess their future stability in a context of ocean warming (Colleoni et al., 2018a). Investigating the deep past ocean by numerical modelling involves high uncertainties, for the physics implemented in models it is constrained with present-day observations, and may not be suitable for strongly different climate conditions. Therefore it is necessary first to run an experiment for a past period of ocean warming that is relatively well known, and where the ocean played a significant role in the AIS retreat like the Last Deglaciation (21 kyears BP to present).

To achieve the objectives of ANTIPODE, my PhD focuses on three/four main scientific questions:

1. What are the characteristics of the main water masses in the Ross Sea and how do their variability relate to teleconnections?

2. How does each water mass impact on the basal melting of the RIS?

3. How did paleo-water masses evolve in the Ross Sea sector during the last deglaciation?

4. Which water mass was more determinant to drive AIS retreat in the Ross Sea?

To answer those questions, I have employed a numerical ocean circulation model, the MITgcm (Marshall et al., 1997a,b), which I implemented for the Ross Sea on a 5-km resolution cartesian regular grid. The model simulates circulation in the open ocean, on the Ross Sea continental shelf and inside the Ross Ice Shelf (RIS) cavity. Chapter 1 is dedicated to introducing the field of study from the glaciological, oceanographic and climatic point of view. Chapter 2 answers scientific questions 1 and investigates the present-day variability of the Ross Sea oceanic water masses by simulating ocean circulation over 1991-2018, and its link with local climatic fluctuations and remote teleconnections. Chapter 3 investigates scientific question 2 and shows how the Ross Sea water masses variability impacts on the RIS basal melting variability, proposing a new method to characterise the various modes of ice

melt. Chapter 4 answers the scientific question 3 and focuses on the evolution of the Ross Sea oceanic circulation and its consequences on the ice shelves basal melting over the Last Deglaciation, while the grounding line was retreating from the continental shelf edge to its current position. This has never been studied and quantified so far, by means of regional numerical ocean models. A similar work was planned over a deglaciation of the Miocene. This objective is still on-going and is the object of a follow-up post-doc research activity. The first step of this deep past objective is the reconstruction of the Ross Sea Middle Miocene ($\sim$14 Ma) paleo-bathymetry by means of the backstripping method applied to seismic stratigraphic records of the Ross Sea. This activity is reported in the Annex of this thesis.

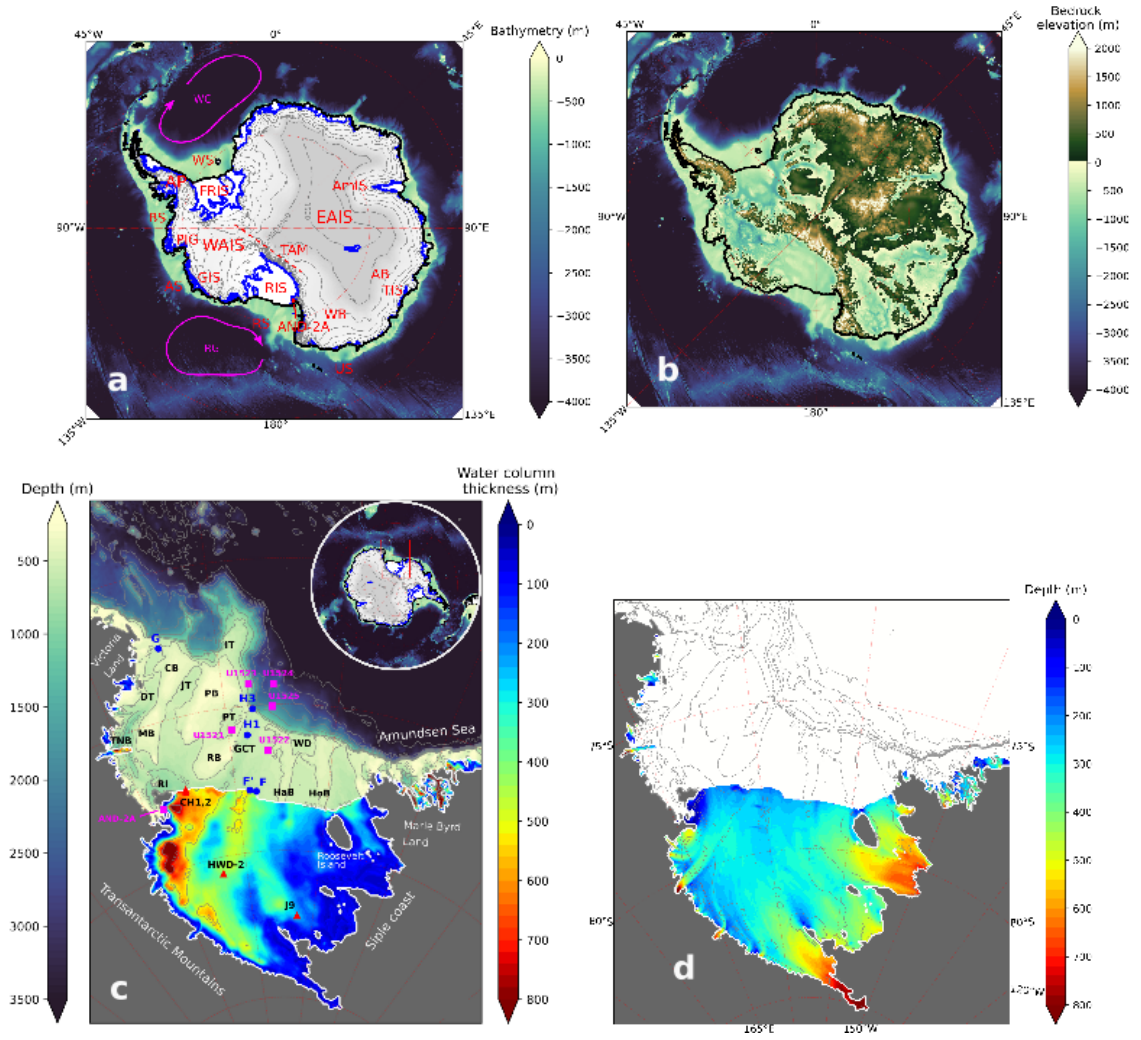

Figure 1.1: (a) Antarctic ice sheet elevation (Bedmap2, Fretwell et al., 2013), continental margin and Southern Ocean bathymetry (IBCSO, Arndt et al. 2013). Blue line indicates the Antarctic ice sheet grounding line (and Vostok sub-glacial lake) while the black line indicates the coastline, i.e the margin of the Antarctic ice sheet; AB = Aurora Basin, AmIS = Amery Ice Shelf, AND-2A=ANDRILL-2A, AP = Antarctic Peninsula, AS = Amundsen Sea, BW = Bellinghausen Sea, EAIS = East Antarctic Ice Sheet, FRIS=Filchner-Ronne Ice Shelf, GIS=Getz Ice Shelf, PIG = Pine Island Glacie, RG = Ross Gyre, RIS = Ross Ice Shelf, RS=Ross Sea, TAM = Trans-Antarctic Mountains, TIS = Totten Ice Shelf, US = D'Urville Sea, WAIS = West Antarctic Ice Sheet, WB = Wilkes Basin, WG = Weddell Gyre, WS = Weddell Sea. (b) Antarctic ice sheet bedrock elevation, and ocean bathymetry (m). Sectors with negative bathymetry are marine-based sectors where the ice sheet grounds below sea level. Black thick line corresponds to the coastline. (c) Bathymetry of the Ross Sea (in m depth). Colours correspond to the thickness of the water column within the Ross Sea sub-ice-shelves cavities, as implemented within the MITgcm numerical model. The white thick line corresponds to the ice sheet grounding line. (d) Depth of the ice shelves draft (m). The thick white line corresponds to the ice sheet grounding line. Names in (c): CB = Crary Bank, DT = Drygalski Trough, GCT = Glomar Challenger Trough, HaB = Hayes Bank, HoB = Houtz Bank, IB = Iselin Bank, JT = Joides Trough, MB = Mawson Bank, PB = Pennel Bank, PT = Pennel Trough, RB = Ross Bank, TNB = Terra Nova Bay, WD = Whales Deep (basin).

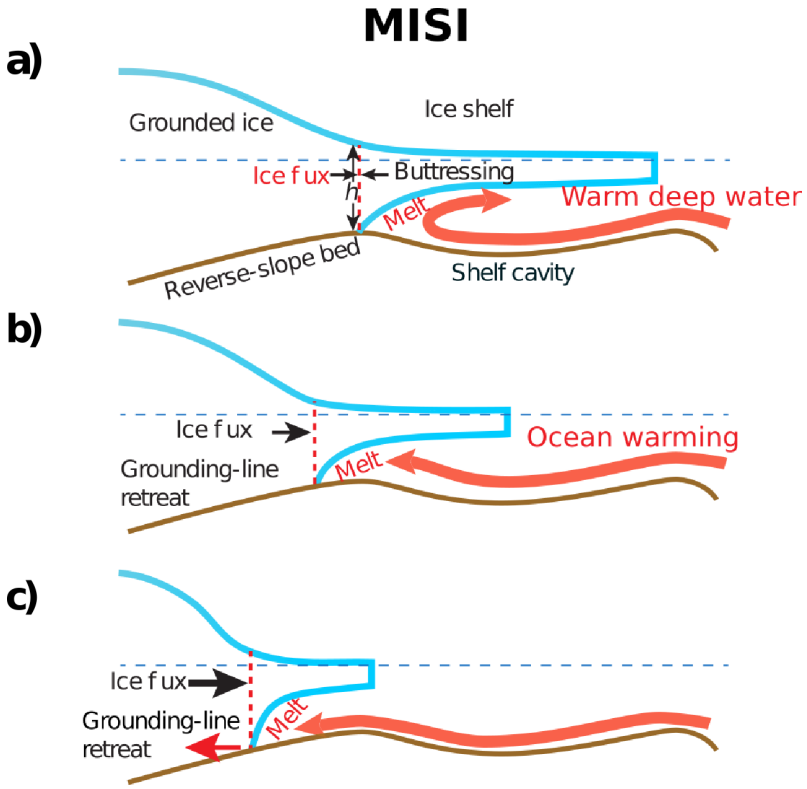

Figure 1.2: Marine Ice-Sheet Instability (MISI) adapted from DeConto and Pollard (2016). a) in equilibrium conditions, the ice shelf receives the ice flux at the grounding line, proportional to ice speed and grounding line thickness "h", which is partially lost to melting and calving (not shown). b) ocean warming can force the grounding line to retreat over retrograde sloping bedrock (deeper upstream of ice flow) once the ice shelf has thinned too much to be sustained by the ice fluxes from the grounding line. Disintegration of the ice shelf front occurs (not shown). c) the disintegration of the ice shelf causes the fast retreat of the grounding line. The system shifts to an unstable state: the ice flow at the grounding line, increases, draining the upstream ice into the ocean; the grounding line retreats to a new stable position (prograde slope) or is stabilised by pinning on the bed.

1.2 Glaciology of the Antarctic ice sheet

The Antarctic continent hosts one of the largest existing ice sheets since the Eocene-Oligocene transition ∼34 Ma (Escutia et al., 2019). The AIS is geographically divided into the East Antarctic Ice Sheet (EAIS) and West Antarctic Ice Sheet (WAIS) and the Northernmost sector, the Antarctic Peninsula. Estimates of the ice volume stored in the AIS is about 58 m of Equivalent Sea Level (m SLE), divided in 52.2 m SLE in the EAIS and ∼ 5.3 m SLE in the WAIS (Morlighem et al., 2020). There is greater concern about the WAIS stability in a context of future

ocean and atmospheric warming than about the EAIS stability. The WAIS is mostly marine-based, i.e. the ice sheet is grounded on a bedrock located below the sea level (Figure 1.1b), whereas the EAIS is mostly terrestrial, except for marginal basins, which are also marine-based such as the Wilkes Basin and the Aurora Basin (Figure 1.1). All the marine-based sectors of the AIS are sensitive to oceanic warming and therefore prone to experience MISI in the future (DeConto and Pollard, 2016).

In general, ice flows like a non-linear highly viscous medium, however its behaviour is different between inland sectors and marginal sectors, due to different stress regimes. In inner regions, the ice sheet is characterised by a cold base, which means that the ice is frozen onto the bedrock, and the ice flow deforms vertically driven by longitudinal shear stress (∼1-10 m/y, Mouginot et al., 2017, 2019). By contrast, where a sediment layer saturated with meltwater is present at the ice sheet base, the ice flows both by sliding and by internal deformation, achieving larger velocities (>1 km/yr, Mouginot et al., 2017, 2019). Those areas are called "ice streams" and present little vertical deformation, and greater lateral shear stress exerted by lateral confinement (ridges and mountains to the ice stream sides) or by friction caused by pinning points on the bed (MacAyeal, 1989). Ice streams flow toward the ocean, progressively thinning and start to float (ice density is lower than seawater density) and spread over the ocean, forming ice shelves.

There has been much interest in the glaciological community in studying ice shelves along the Antarctic coast, as they provide backstress "buttressing" the inland AIS (Reese et al., 2018), critically slowing ice discharge towards the ocean and stabilising the grounding line. Observations from satellite altimetry reveal that ice shelves have been thinning during past decades, with a large spatial heterogeneity (Pritchard et al., 2012; Rignot et al., 2013). Most of this thinning, observed along the WAIS coasts, results from the melting at the base of the floating ice shelves caused by warm ocean waters (Pritchard et al., 2012; Rignot et al., 2013; Schmidtko et al., 2014; Paolo et al., 2015; Rintoul et al., 2016). In particular, thinning has been accelerating in the regions largely exposed to warm water intrusions, which may be partially driven by tropical teleconnections (Paolo et al., 2015, see Chapter 1.4). Calculations of ice shelves mass balance, taking into account grounding line fluxes, iceberg calving and surface mass balance revealed that ice shelves are on a net negative balance, and there is scientific consensus that it is ascribable to the ocean (Depoorter et al., 2013; Liu et al., 2015), either because its warming (Schmidtko et al., 2014) or because of shifting currents due to changing winds or changing sea ice regime (Spence et al., 2014; Darelius et al., 2016; Dinniman et al., 2012, 2018).

Some of the ice shelves, whose grounding line rests on a retrograde sloping bed are particularly unstable (Gudmundsson et al., 2019), but are stabilised at their base by contact with pinning points (e.g. sills or tectonic highs), exerting friction on the ice column, or confined at the sides by mountain valleys. Thinning by oceanic basal melting may detach the ice shelf from pinning points, in turn decreasing buttressing of upstream ice flow, yielding increasingly fast ice discharge. Antarctic Ice Sheet mass balance calculations show that accelerated ice discharges at the margins affect the inner regions, in particular most of the WAIS, and the marine-based sectors of the EAIS (Rignot et al., 2019). Such acceleration of ice discharge related to the loss of buttressing has been modelled with a process-based approach forced by observations of ice shelf thickness (Gudmundsson et al., 2019) and also observed indirectly, by tracking grounding line retreat (Konrad et al., 2018): the retreating locations were found coincident with the presence of warm water masses, in particular the Circumpolar Deep Water (CDW, Jacobs et al., 2011; Jenkins et al., 2016).

The greatest acceleration rates are found for the glaciers and ice shelves fringing the Amundsen and Bellinghausen Seas (sectors of the WAIS, Rignot et al. 2013), such as the Pine Island glacier (101 Gt/yr), the Thwaites glacier (97 Gt/yr), the Getz glacier (144 Gt/yr) and for the Totten glacier (63.2 $\pm$ 4 Gt/yr, Rignot et al., 2013 to 80 $\pm$ 5, Liu et al., 2015) in the D'Urville Sea (EAIS) (Figure 1.1a), which are particularly sensitive to on-going ocean warming (Rignot et al., 2013; Silvano et al., 2016; Rintoul et al., 2016; Jenkins et al., 2018). Pine Island Glacier, in particular, is highly sensitive to on-going climate change (Dutrieux et al., 2014; Nakayama et al., 2018, 2019; Paolo et al., 2015, 2018; Jenkins et al., 2018), more specifically, changes induced by Pacific tropical teleconnections and SAM positive trend (see Chapter 1.3). By contrast the biggest sub-ice shelf cavities, i.e. the Ross Ice Shelf, the Filchner-Ronne ice shelves and the Amery Ice Shelf, filled predominantly with near-freezing water (Jacobs et al., 1979) have, until now, not shown any significant thinning trend (Paolo et al., 2015). In those cases, ice discharge to the ocean occurs by both basal melting and detachment of large tabular icebergs ("calving"), calving being the dominant ice discharge mode (Rignot et al., 2013). For the Ross Ice Shelf (RIS) basal melting is, at present, very little ($\sim$48 Gt/yr) and its buttressing potential is about 14.7% (Fürst et al., 2016). The Filchner-Ronne ice shelves basal melting amounts to 155 $\pm$ 36 Gt/yr.

The atmospheric CO_2 concentration threshold for the AIS to cross its tipping point and yield a multi-meters global mean sea level rise remains uncertain (Levermann et al., 2020; Siegert et al., 2020; Garbe et al., 2020). This is due to uncertainties in physical processes, as they are currently implemented in state-of-the-art climate

models and ice sheet models, and specifically in the parameterizations of the ice shelves basal melting in the afore-mentioned models (Asay-Davis et al., 2017). Although ocean-induced thinning can explain the accelerated discharge of the WAIS by reduced buttressing (Rignot et al., 2019; Sun et al., 2020), others have pointed out MISI being triggered already in some sectors (Favier et al., 2014). The vulnerability of all the marine-based sectors of the AIS, especially those at risk of MISI, is projected to increase in response to projected ocean warming (DeConto and Pollard, 2016). The Antarctic ice sheet (AIS) contribution to global mean sea level in the future decades and centuries is expected to be up to several metres (Golledge et al. 2015, 2019; SROCC Pörtner et al., 2019; Pattyn and Morlighem 2020; DeConto et al. 2021; Edwards et al. 2021; IPCC Masson-Delmotte et al., 2021). The ocean is also going to be affected by global warming. For instance, Hellmer et al. (2012, 2017) and Naughten et al. (2021) show that in Eastern Weddell Sea, the presently cold Filchner ice shelf cavity would become increasingly accessible to warm waters from the open ocean and experience a dramatic change in its basal melting regime. Therefore, even cold-water cavities such as the Filchner-Ronne Ice shelves and the Ross Ice Shelf, are also at threat in the future, and have possibly undergone such changes in the geological past. Geological evidences of past WAIS retreats during warmer periods (interglacials) over the last 5 Million years Naish et al. (2009) together with numerical models Pollard and DeConto (2009); DeConto and Pollard (2016) suggest that the Ross Ice Shelf underwent complete collapse, together with most of the WAIS.

1.3 Climate of Antarctica and teleconnections

Antarctic climatology

Antarctica is located around the South Pole; it extends northward about 60°S in the Antarctica Peninsula (Figure 1.1). As such, the climate of Antarctica varies substantially amongst the continental margins, the Antarctic Peninsula and the Antarctic plateau (Zhu et al., 2021). The presence of a 3-km thick continental sized ice sheet reaching an elevation of ∼4 km on the plateau, combined with the high albedo of the ice surface ($\alpha > 0.8$) decrease near surface air temperature down to -30 °C during austral summer (e.g. January in Figure 1.3a) and -60 °C in austral winter (e.g. August in Figure 1.3b). On the Antarctic margins, near-surface air temperature remains below, but close to 0 °C, on average during austral summer, and is about -30 °C during austral winter (Figure 1.3a,b). The Antarctic Peninsula is the northernmost sector of Antarctica and consequently, the warmest region, with temperatures ranging between -2.1 °C and -11 °C between austral summer and austral winter on average Turner et al. (2020). The Polar Cell, located at latitudes lower

than 60°S , associated with large-scale rising and descending air motions brings cold and dry air from the upper troposphere towards the surface layer at the descending branch, on the Antarctic plateau, whereas northward, at the Polar Front (∼60°S), the rising of warm moist air takes place. Moisture from the open ocean is brought to the continental margin in the Antarctic Peninsula, in the Pacific sector of the Southern Ocean, namely the Amundsen and Bellinghausen Seas (Ellsworth and Marie Byrd Land) and in the Indian sector of the Southern Ocean (George V Land, Adélie Land, Wilkes Land), where precipitation reaches ∼1 m/yr in winter (Figure 1.3d). On the contrary, the descending branch of the cell, on the plateau, is associated with dry conditions, and little precipitation (<0.1 m/yr, Figure 1.3c and 1.3d), constant throughout the year. On the plateau we find a stationary system of high mean sea-level pressure, whereas at the Polar Front (∼60°S) there is a stationary low mean sea-level pressure (Figure 1.3e and 1.33f). The meridional pressure gradient drives strong zonal winds: surface Easterly winds flow along the coast (Figure 1.3e,f). Off-shore, North of the Polar Front, high pressure drives Westerly winds that drive the Antarctic Circumpolar Current (45–55°S).

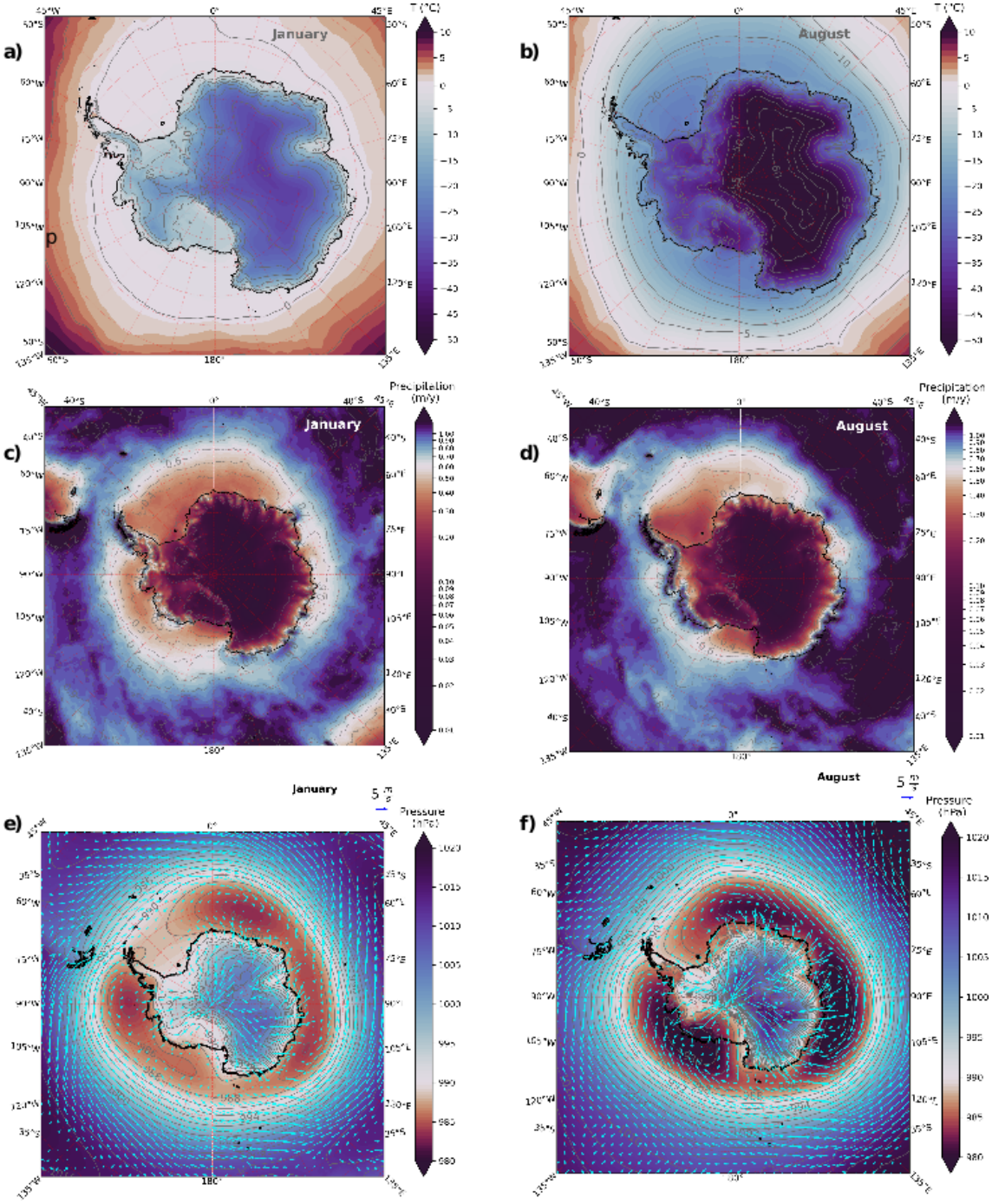

Figure 1.3: Peak austral summer (January, left column) and peak austral winter (August right column) climate fields: (a,b) 2-metres air temperature (°C), (c,d) total precipitation (m/yr), (e,f) mean sea-level pressure (hPa) and 10-metres wind (m/s). (data from ERA5 monthly climatology, 1990-2019).

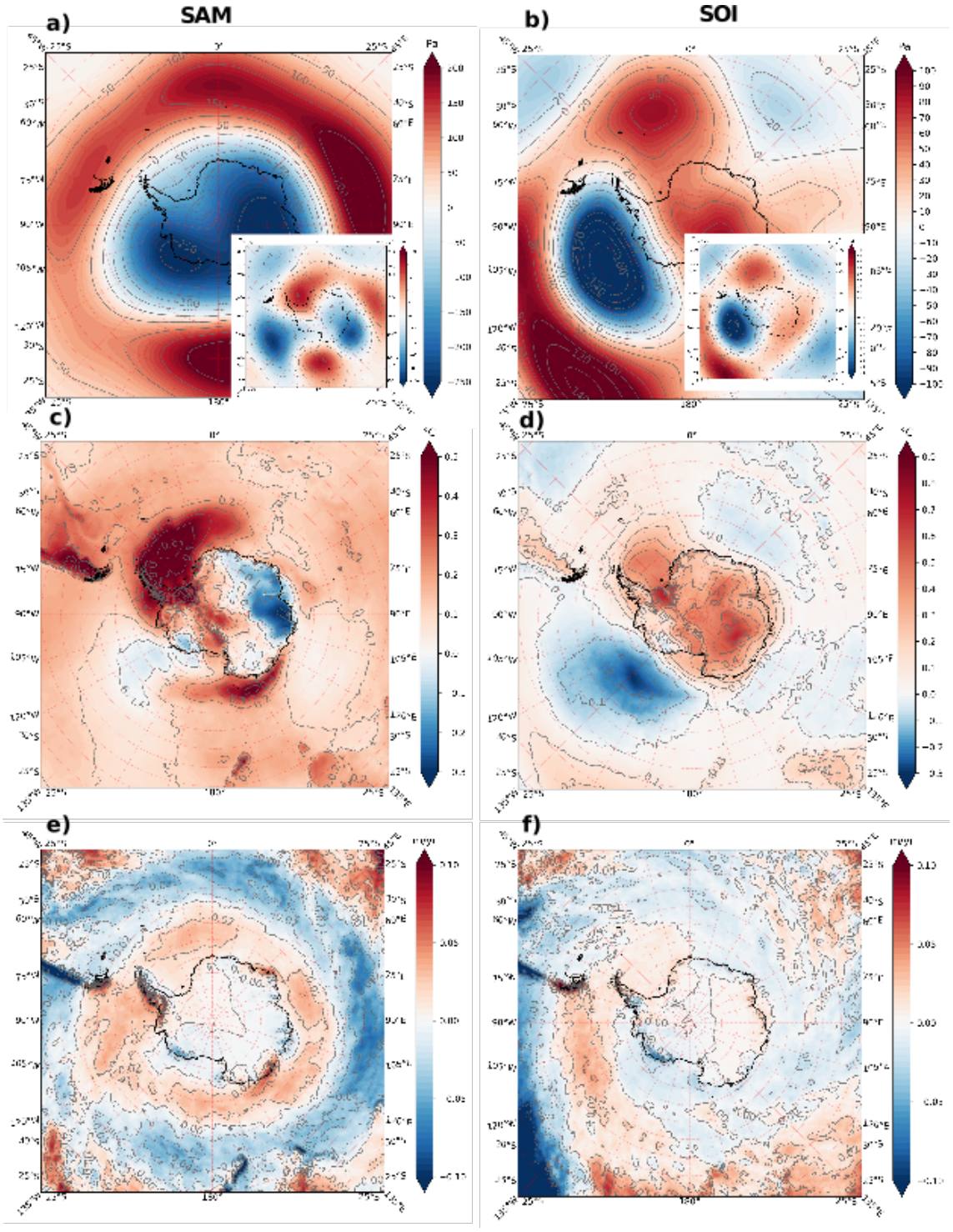

Figure 1.4: linear regression of Southern Annular Mode (SAM, left) and Southern Ocean Index (SOI, right) on mean annual (a,b) 500 hPa geopotential (inset, 500 hPa z*). The Amundsen Sea Low (ASL) correspond to the negative geopotential anomaly centred over the Amundsen Sea; the SOI is a teleconnection driven by ENSO: when the SOI is negative it corresponds to a positive state of ENSO, and a weakening of the ASL; (c,d) 2-metres air temperatures; (e,f) total precipitation. (data from ERA5 monthly climatology, 1990-2019).

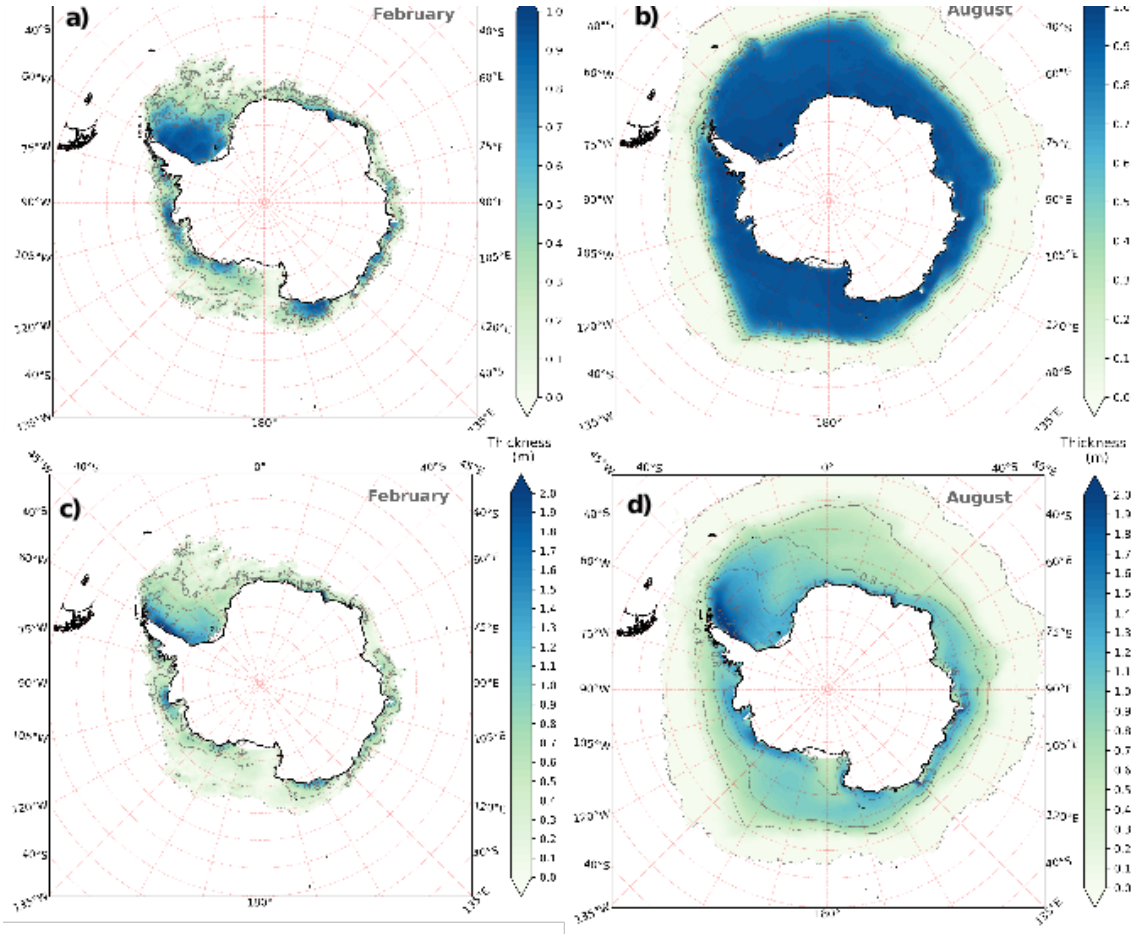

Figure 1.5: Sea ice (a) minimum and (b) maximum concentration (unitless). Sea ice peak austral summer (c) and peak austral winter thickness (d). (data from GLORYS12V1, monthly climatology average over 1993-2018).

A strong meridional atmospheric circulation is also present, where extremely cold and dry near-surface air from the plateau, – and therefore dense – subsides and generates strong winds that flow towards the coast, where they accelerate along the slopes of the AIS margins: they are the so-called "katabatic" winds. Katabatic winds are episodic and intense Bromwich and Kurtz (1984); Petrelli et al. (2008), and come into play in sea ice production in coastal polynyas Sansiviero and Maqueda; Thompson et al. (2020). As katabatic winds bring cold and dry air from the continent, they keep the surface of the ice shelves below the freezing point during austral summer ($\sim$ -5 °C), but as a matter of fact, their intensity prevents large snow accumulation (e.g. $<$ 0.2 m/y for the Ross Ice Shelf). Offshore, they coalesce with the Easterlies upon reaching the coast (Figure 1.3 e,f). Easterlies and Westerlies are in quasi-geostrophic equilibrium, however they spiral towards the stationary low-pressure systems. During austral winter, low-pressure systems are further depressed, atmospheric circulation

intensifies, and wind belts shift equatorward.

Precipitations are concentrated along the margins, in particular in the Antarctic peninsula, along the Amundsen Sea and the Bellinghausen Sea coasts (Marie Byrd Land) and the Indian sector coast (Adélie Land, Wilkes Land), where off-shore winds and Southerly winds converge, yielding precipitation, mostly during the austral fall and austral winter (e.g. Figure 1.3d). By contrast, in the Ross Sea and Weddell Sea sectors, and along the EAIS margins, except in the Indian Ocean sector, stronger Southerly circulation from inland brings dry air over the margins, and prevents strong precipitation over the year.

1.3.1 Antarctic climatic variability

Antarctic atmospheric variability is related to the changing strength of the Polar cell, the strength of the low pressure systems and the Westerlies. The first mode of climate variability is the Southern Annular Mode (SAM, Thompson and Wallace, 2000), Figure 1.4a, a bipolar zonal anomalies pressure pattern centred on Antarctica, associated with the strength of the meridional pressure gradient between the AIS and the open ocean. It is also indicative of the variability of the Westerlies and of the air pressure in the troposphere over Antarctica. In its positive phase, related surface air temperatures (total precipitation) are warmer (wetter) over the Antarctic Peninsula and colder (dryer) over the rest of Antarctica (Figure 1.4c,e), and vice versa during the negative phase. Observations show that the SAM has undergone a positive trend over the last 50 years, due to the opening of the ozone hole, tropical ocean warming, and the increased meridional temperature gradient Thompson et al. (2000).

The second mode of climate variability is the Amundsen Sea Low (Figure 1.4b). It corresponds to a stationary low-pressure system located off-shore the Amundsen Sea (120–150°W, 60–65°S), which shifts towards the Ross Sea sector during the austral winter. On the Atlantic sector a stationary a high-pressure system is present. The combination of the Amundsen Sea Low and this high-pressure system yields the so-called Antarctic Dipole, which drives surface winds of opposite direction, impacting on the sea ice advection and on the advection of warm moist versus dry air Yuan (2004). These modes of variability are influenced by the pressure fields that propagate from the tropical ocean to the polar latitudes as stationary trains of atmospheric Rossby waves in the high troposphere (<500 hPa, Li et al. 2021). These Rossby waves are produced by the strong heat fluxes associated with El-Niño events and evidenced by the El-Niño Southern Oscillation index (ENSO) in the tropical Pacific, and by similar, albeit smaller events in the tropical Indian and

Atlantic. The stronger influence of ENSO in the Southern Ocean is through the strengthening or weakening of the ASL and the Antarctic Dipole: during the positive ENSO ("El-Niño" event in the tropical Pacific), a weakening of the ASL occurs; during the negative ENSO ("La-Niña" event), a strengthening (deepening) of the ASL occurs. An opposite response occurs to the East of the Antarctic Peninsula, being the other side of the Antarctic Dipole.

1.4 Oceanography of the Southern Ocean

Antarctica is surrounded by the Southern Ocean, defined conventionally as the world ocean Southward of 60°S (International Hydrographic Organisation, 2002). It connects the Atlantic, the Indian and the Pacific Oceans at that latitude and is therefore a key component of the global ocean general circulation. It contributes to the thermohaline circulation with the Antarctic Bottom Water (AABW), the densest water mass that fills the bottom layer of most oceanic basins Figures 1.5 and 1.6. Due to currents divergence South of the Polar Frontal Zone (Orsi and Whitworth, 2005; Rintoul et al., 2001) in the ACC, it produces upwelling of North Atlantic Deep Water (NADW), sourced in the Labrador and Greenland Sea, and travelling in the lower branch of the AMOC. When reaching the Southern Ocean, the densest NADW, upwells (Anderson et al., 2009) and enters the circum-Antarctic circulation in the Antarctic Circumpolar Current (ACC) as the Circumpolar Deep Water (CDW, Marshall and Speer, 2012), at depth ∼200-2000 m (Figure 1.6). CDW is the warmest water mass observed at sub-surface depth, with core temperature ∼2 °C and salinity of ∼34.73 g/kg. Moreover, it is the densest water mass that can cross the Drake passage. The AABW is cooler (∼0 °C) but less saline, (<34.7 psu) than CDW flows at greater depths than CDW (the bottom layer). The surface layer, thin up to ∼100m, referred as Antarctic Surface Water (AASW), undergoes a strong seasonal cycle, freezing in winter and warming up to a few °C above 0 °C in austral summer, and it is much fresher than CDW (Figure 1.7a,b), due to the melting of the sea ice during austral summer and icebergs. Sea ice in the Southern Ocean has a strong seasonality (Figure 1.5a,b). The minimum summer extent reaches about 65°S, except in the Weddell Sea, where most of the sea ice is perennial. In winter it expands up to ∼60–55°S. Where sea ice persists during austral summer, thickness reaches ∼2m, whereas newly formed sea ice is less than 1 m thick.

In the Ross Sea and in the Weddell Sea, two cyclonic gyres are observed (Figure 1.1a). Both gyres result from the interactions between the eastward flowing ACC (∼50–60°S), driven by the Westerlies, and the westward flowing Antarctic Coastal

Current (AACC), driven by the Easterlies. The northernmost branch of those gyres is located in the ACC while the Southernmost branch is located in the AACC. The gyres are associated with cooler deep water temperatures (Figure 1.7, cfr longitude of the Ross Sea and Amundsen Sea, and Schmidtko et al. 2014).

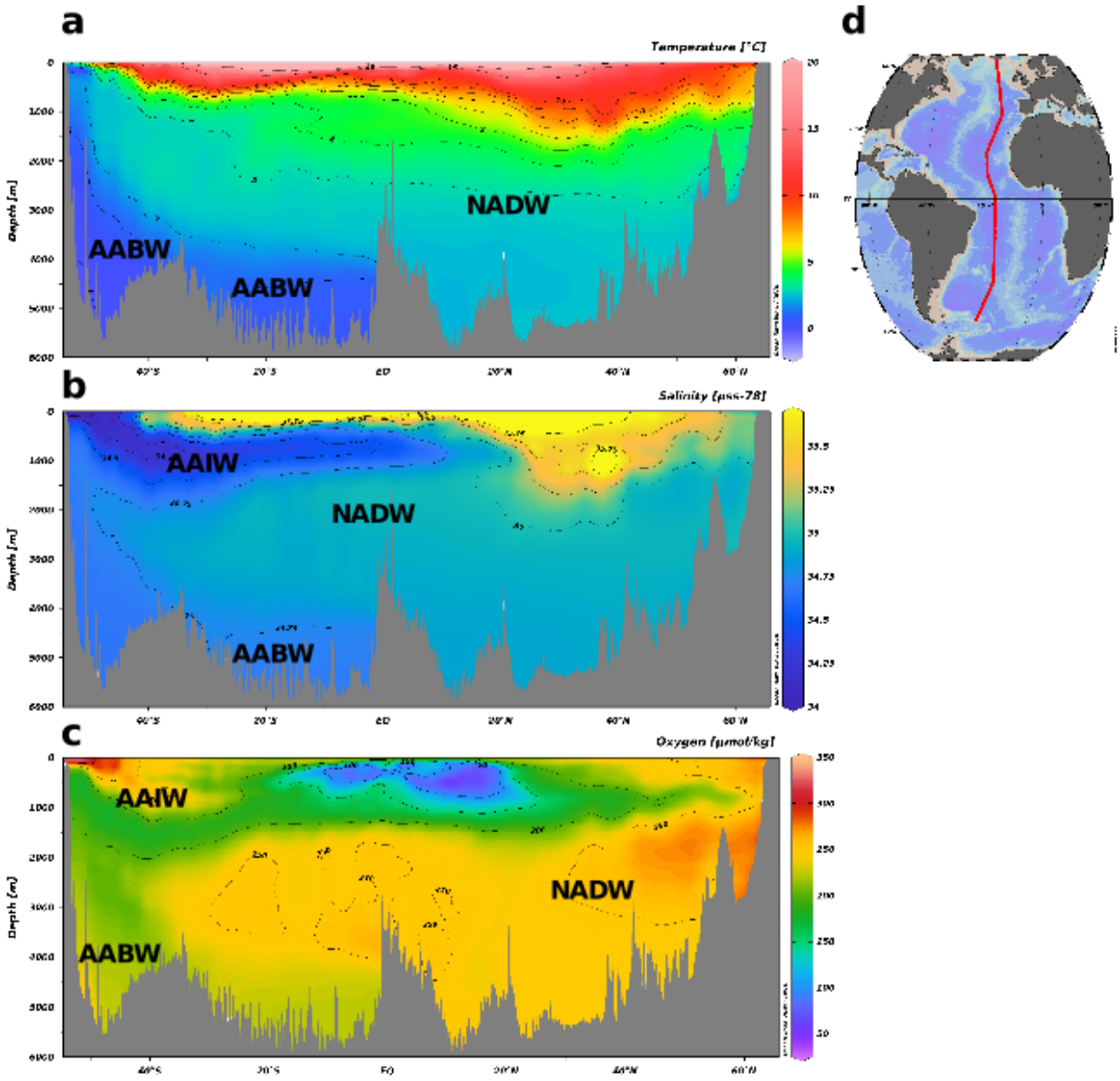

Figure 1.6: Meridional transect along the Atlantic Ocean showing the Atlantic Meridional Overturning Circulation (AMOC). a) Potential temperature (°C); b) Salinity (g/kg); c) Oxygen concentration ($\mu mol/kg$). The water masses flowing towards Antarctica (Lower Circumpolar Deep Water LCDW) and from Antarctica (Antarctic Bottom Water, AABW; Upper Circumpolar Deep Water, UCDW) are indicated on the transects. Data are from the World Ocean Circulation Experiment (WOCE) Atlas, section A16.

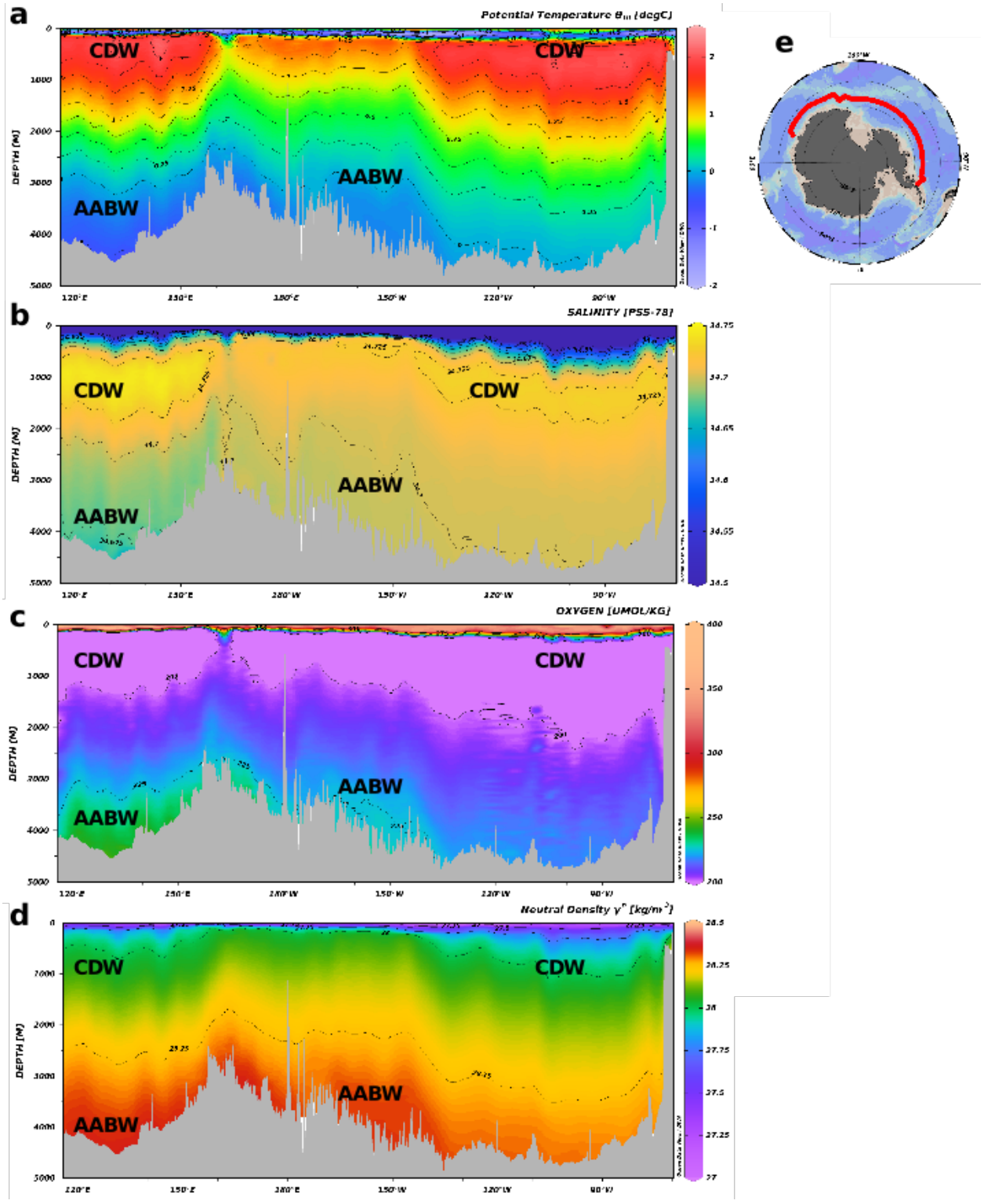

Figure 1.7: Vertical section across the Pacific and Western Indian sectors of the Southern Ocean at ~67°S (Data from the World Ocean Circulation Experiment (WOCE) Atlas, section S04P, S04I, cfr. With the same sections from GLORYS12V1, Lellouche et al. 2021, in chapter 2) (Pacific section from 22/2/1992 to 29/3/1992, Indian section 21/12/1994 to 16/1/1995). a) temperature, b) salinity, c) oxygen, d) neutral density.

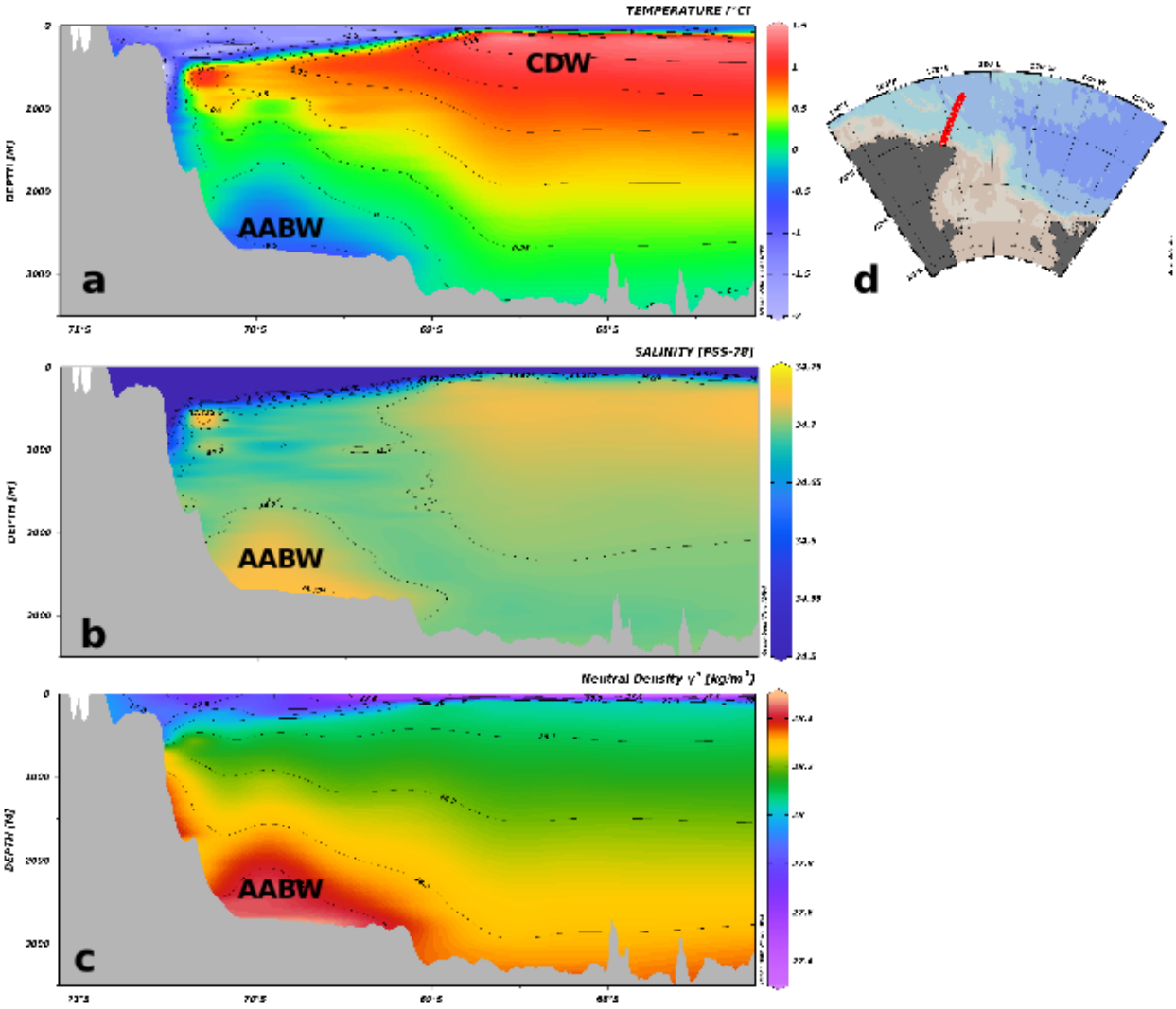

Figure 1.8: Section across continental slope in the Adelie land coast, captures cascading of AABW produced from overflow of RSBW across the continental shelf in the Ross Sea (Data from the World Ocean Circulation Experiment (WOCE) Atlas, Southernmost part of section S04P).

Types of continental shelves

Thompson et al. (2018) classified the continental shelves by the properties of the water masses present there, in turn depending on processes occurring on the continental slope and the shelf, e.g. prevailing winds, sea ice production, CDW intrusions, advection of AASW, strength of the Along Slope Front. They grouped the various Antarctic sectors according three main types of continental shelf:

1. Fresh continental shelves (Figure 1.9a): strong Easterlies drive strong Ekman transport of surface waters, which freshens considerably the continental shelf

waters. Another driver of the freshening is the import of meltwater from glaciers and ice shelves of other sectors (e.g. as in the Eastern Ross Sea and the Eastern Weddell Sea). In the Eastern Ross Sea, for instance, continental shelf waters are considerably fresher than in the Western Ross Sea, due to advection of ice shelves meltwater from the Amundsen Sea coast Nakayama et al. (2020).

2. Dense continental shelves (Figure 1.9b) are characterised by particularly cold and salty water masses (Shelf Waters, SW). Strong atmospheric cooling and katabatic winds cool the water column down to the freezing point, and sea ice formation releases salt ("brine") throughout the water column. Examples of cold continental shelves are the Ross Ice shelf, the Filchner-Ronne Ice Shelves, the Mertz glacier, the Amery Ice shelf. In "polynyas", i.e. regions of sea ice-free ocean, sea ice formation is kept active by katabatic winds blowing across a topographic barrier (e.g. an ice shelf front), creating new sea ice and moving it mechanically away from the barrier. High Salinity Shelf Water (HSSW) is formed in polynyas during winter, due to its high density, occupies the bottom layer; it can flow below ice shelves, and due to its high density, reaches and melt near the grounding line. HSSW is also called generically Dense Shelf Water (DSW); DSWs are precursors to AABW. Near the shelf break, to distinguish between AABW originating from different basins, they can be labelled geographically e.g. Ross Sea Bottom Water (RSBW). Overflowing RSBW on the continental slope is partly geostrophically adjusted, and redirected along the AACC, and partly undergoes cascading (Figure 1.8) and mixing with CDW, forming AABW (Figures 1.6 and 1.7). The newly formed AABW is characterised by high oxygen content and high density. The strong density contrast at the continental shelf break produces the Antarctic Slope Front (ASF), oceanic analogue of a thermal wind. The baroclinicity associated with the tilting of the isopycnals in the ASF produces a vertically sheared jet-like current, the Along-Slope Current (ASC), which is particularly strong in "dense" continental shelves and contributes to shielding it from warmer CDW intrusions. On the contrary, in "warm" shelves, the ASC is particularly weak or even developes as an undercurrent.

3. Warm continental shelves (Figure 1.9c): The ACC is a largely barotropic current, which meanders pinning to bathymetric features. Over the longitude of the Amundsen Sea and Bellinghausen Sea and along the Antarctic Peninsula, the ACC is forced to flow near the Antarctic coast, bringing the "warm" CDW near the continental shelf. Weakened Easterlies (by vicinity of Westerlies), and reduced sea ice conditions Spence et al. (2014); Darelius et al. (2016), eddies, astronomical tides, may foster the intrusion of CDW on the continental shelf

at particular locations where the morphology of the bathymetry is favourable, such astroughs or banks. On this kind of continental shelf, CDW has relatively direct access to the grounding line of the AIS (Jacobs et al., 2011; Dinniman et al., 2011; Dutrieux et al., 2014; St-Laurent et al., 2013; Nakayama et al., 2014, 2017, 2018, 2019). This type of shelf is found mainly in the Amundsen Sea and the Bellinghausen Sea as well as in specific locations of the Indian sector of the Antarctic margins, specifically Totten Ice Shelf (Rintoul et al., 2016; Gwyther et al., 2018).

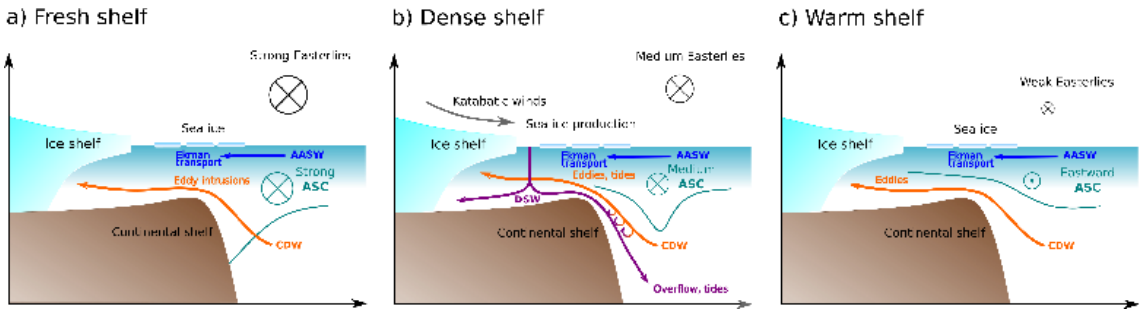

Figure 1.9: Classification of continental shelf types and processes found along the coasts of Antarctica. Adapted from Thompson et al. (2018). The green line shows the isopycnal tilt associated with the Antarctic Slope Front, and the Along Slope Current.

1.4.1 Drivers of ocean variability

Ocean has been pointed to as a key driver of changes in the marine-based sectors of the AIS. Depending on the oceanographic and atmospheric circulation and bathymetric settings, the different water masses impact differently on the ice-shelves basal melting. The Amundsen and Bellinghausen Seas are particularly sensitive to local winds: wind-induced upwelling along the coast caused by off-shore Westerlies and divergence induced by Easterlies (Schmidtko et al., 2014; Jenkins et al., 2016) brings CDW at shallower depth on the continental shelf, and changing winds can enhance the intrusion of CDW on the continental shelf (Dinniman et al., 2012). Synoptic circulation in the Southern Ocean is influenced by tropical teleconnections: atmospheric Rossby wave trains generated by strong tropical Pacific sea surface temperatures variations associated with ENSO, interact with the Amundsen Sea Low (ASL) causing long-term decadal variability in surface winds which impact on the upwelling of CDW and on sea ice formation (Turner, 2004; Yuan, 2004; Schmidtko et al., 2014; Jenkins et al., 2016; Jones et al., 2016; Turner et al., 2017; Paolo et al., 2018; Li et al., 2021). The intrusions of CDW within ice shelves cavities may be up to 3-4 °C warmer than the seawater freezing point, which results in strong ice

shelf basal melting, yet warming of the CDW and the increase in advected volume across the continental shelf is thought to be the main driver of fast thinning and ice discharge acceleration (Jacobs et al., 2011; Schmidtko et al., 2014). Owing to the presence of teleconnections, the Amundsen and Bellinghausen Seas water masses and ice shelves basal melting show a clear decadal variability. It is thus complicated to understand which part of the signal results from natural variability rather than from on-going climatic changes (Jenkins et al., 2016; Dinniman et al., 2016; Jenkins and Jacobs, 2008). The recent atmospheric warming observed over West Antarctica has been linked to persistent sea surface temperature changes in the tropical Pacific over the past 30 years that increased the advection of warm air to the Antarctic continent (Ding et al., 2011). The upwelling and advection of CDW to the continental shelf are also enhanced by the Southern Annular Mode (SAM, Thompson and Wallace, 2000), representative of the strength of the Westerlies. Since the 50s, the SAM has presented a positive trend that has been linked, in the Amundsen Sea and in the Bellinghausen Sea, to oceanic sub-surface warming, induced by weakened Ekman pumping, weakened coastal currents and Easterly winds shifted inland (Spence et al., 2014).

The across-slope transport and mixing of CDW with continental shelf waters is regulated by the Antarctic Slope Front (ASF, Gill, 1973; Jacobs, 1991; Whitworth and Orsi, 2006; Thompson et al., 2018). Different water masses can produce different ASFs, visible in steep isopycnals tilting (Figure 1.9). In cases where it intersects the continental slope (e.g. on "fresh" shelf, Figure 1.9), it partially shields the continental shelf from CDW intrusions. In cases where Dense Shelf Water (DSW) is present on the continental shelf, it forms a characteristic "V" shape; in this case it strongly regulates both DSW outflows and CDW inflows. In areas where the dominant bottom water mass is formed by CDW, this "V" shape is less pronounced or even absent (Thompson et al., 2018).

1.5 Ice shelf-ocean interactions

The global ocean has been warming over the last decades (Roemmich et al., 2015), with heat increase reaching also the deep layers (down to about 2000m). Most of this warming has been attributed to on-going climate change (Desbruyères et al., 2016). In the Southern Ocean, however, establishing a causal relation is more problematic due to regional differences and long-term natural variability. Consequently, the identification of a clear trend in subsurface ocean warming is highly uncertain (Jenkins et al., 2016; Jones et al., 2016).

A marine-terminating ice sheet flows by deformation driven by gravity, or slides driven by upstream stresses from the continent toward the ocean. Different situations arise for the Greenland Ice Sheet and the Antarctic Ice Sheet. In the case of the Greenland Ice Sheet, fast flowing ice streams and extensive summer surface melting yield highly crevassed marine termini in the proximity of the grounding line, with frequent icebergs calving events (e.g. Vieli, 2021). In the case of the Antarctic Ice Sheet, ice streams that become floating ice shelves undergo little surface melting; on the other hand their larger size allows for the ocean to circulate beneath it and cause extensive melting at their base. By melting, the ocean below an ice shelf exchanges heat and freshwater, which progressively thins the ice and subsequently weakens the structural integrity of the ice shelf. Then, some crevasses open due to the strong lateral stresses associated with ice stream flow (Kulessa et al., 2014) and in the case of Antarctica, calving occurs as detachment of large, tabular icebergs.

Generally, three water masses are identified to produce melting (Figure 1.10ab, Jacobs et al., 1992; Dinniman et al., 2016; Silvano et al., 2016):

1. Mode 1: associated with HSSW, a low-temperature and high-salinity water mass. Due to its high density, HSSW flows on the bottom and yields melting near the grounding line. Mode 1 is the dominant mode of ice shelf basal melting in cold cavities.

2. Mode 2: associated with CDW, a high-temperature and intermediate-density water mass. Because of its buoyancy, basal melting occurs at intermediate depth along the ice shelf draft, unless it occupies also the bottom layer (as in Amundsen-Bellinghausen Seas); in this case it produces melting also at the grounding line. When CDW intrudes on a dense continental shelf, by contrast, it mixes with the ambient Shelf Water, becoming colder and saltier, ultimately transforming into a "modified" CDW (mCDW), which retains its relative temperature maximum with respect to the other shelf waters.

3. Mode 3: associated with the AASW, a high-temperature and low-density water mass. This surface water warms up to a few degrees above 0 °C during summer in polynyas located at the ice shelf front, and is advected beneath (Stewart et al., 2019). Due to its high buoyancy, it can only reach a few kilometres inside the cavity and associated basal melting occurs at or close to the ice shelf front. Each of these water masses are affected by a different climatic driver, showing seasonality, and variability, in addition to internal ocean variability. Several water masses are advected beneath the ice shelves at different times,

depths and locations, especially in the largest sub-ice shelf cavities (e.g. Tinto et al., 2019).

Circulation beneath ice shelf cavities is usually described by means of ice pump mechanisms (Robin, 1979; Lewis and Perkin, 1986). The incoming water masses in contact with the ice shelf melt the draft and mix with the resulting freshwater. This mixing decreases their density and hence their salinity. Once their buoyancy is higher than the ambient waters at the same depth, they start overturning. As they flow out of the cavity, they find themselves cooled and freshened with respect to their initial properties. In particular, since they have been cooled at depths and pressures where the seawater freezing point is higher than at surface, they may have become, *supercooled*, .i.e., colder than the surface freezing point. Part of the glacial meltwater does not undergo intensive mixing, and exits the cavity as a plume of *supercooled* and fresh water, the Ice Shelf Water (ISW). In the largest cavities, this overturning circulation, driven by buoyancy fluxes, is superimposed on a larger geostrophic ("horizontal") circulation, which depends on the bathymetry, on the depth of the ice shelf draft, and on the horizontal pressure gradients associated with lateral density gradients (Jendersie et al., 2018).

Implementation of basal melting in ice-sheet and ocean numerical models

Such an important driver as the ocean, is still poorly represented in state-of-the-art stand-alone ice-sheet ice-shelf models: in fact, these rely on parameterizations that even though were complexified over the recent years to better represent observations, still do not capture the phenomenology of ocean dynamics in the sub-ice shelves cavities (e.g. Martin et al., 2011; Holland et al., 2008; Pollard and DeConto, 2012; Favier et al., 2019; Jourdain et al., 2020). Early implementations have a linear dependence on the water temperature outside the cavity (e.g. Martin et al., 2011), which does not capture the higher melting near the grounding line due to overturning and meltwater plume dynamics, resulting in underestimation of basal melting rates. Later, Holland et al. (2008) evidenced, by means of ocean circulation modelling, that a quadratic dependence of melting on far-field ocean temperature better matched with the few available observations within the cavities. Based on their finding, the simplified set of the equations they found was implemented in a few numerical ice-sheet models. However, it was clear that such a parameterisation could not universally compute the range of basal melting observed around Antarctica because of the highly variable regional oceanic settings. Pollard and DeConto (2012) introduced some regional variations by introducing a coefficient in the equations, that would implicitly account for the level of influence of the CDW on the grounding line, i.e., to take into account

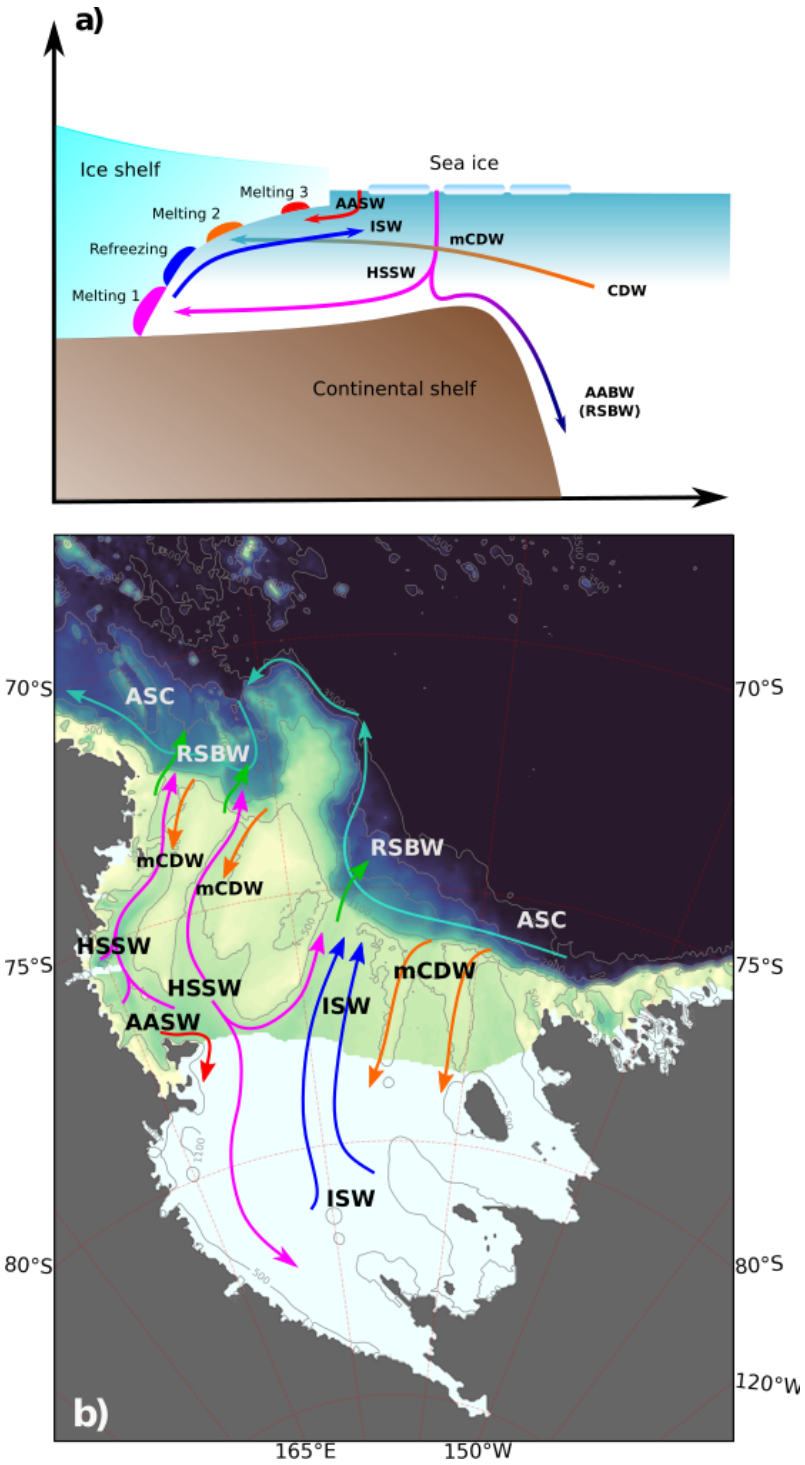

Figure 1.10: (a) classification of ice shelves basal melting modes after Jacobs (1991) and related water masses found in the Ross Sea. (b) pathways of the main continental shelf water masses.

the different types of continental shelves (e.g. Figure 1.9, Thompson et al., 2018). However, Pollard and DeConto's (2012) quadratic parameterisation was still far from reproducing the observed basal melting. To account for local oceanic settings, Favier et al. (2019) Jourdain et al. (2020), developed a local (point-wise) and non-local (whole ice-shelf wide) quadratic formulation of basal melting, which was adopted in the Ice Sheet Model Intercomparison Project phase 6 (ISMIP6). A statistical calibration procedure for tuning the parameters is attempted at pan-Antarctic level, for consistency. However, the local effects of turbulence associated with ocean currents are highly variable on a regional basis, depending on the current speed and location, and therefore, cannot be constrained by statistics alone. Attempting to fill the gap, so-called "oceanic box models" were implemented, e.g. PICO (Reese et al., 2018), to partially introduce some ocean dynamics into ice-shelves basal melting calculations. Such an ocean box model extrapolates continental shelf water masses observations beneath the sub-ice shelf cavities and only simulates buoyancy driven overturning. This approach does not take into account the dynamics and depth of the different water masses beneath the cavities. This is problematic in the case of large cavities, where the circulation has a larger geostrophic component (i.e. mostly horizontal flow), with little overturning.

By contrast, formulations adopted in ocean models are consistent with ocean dynamics and physics, and model the interaction with ice shelves in terms of heat and freshwater fluxes, only parameterising the smaller scale shear turbulence effect on such fluxes. The most widespread approach is the three-equation formulation (Hellmer and Olbers, 1989; Holland and Jenkins, 1999; Jenkins et al., 2001) which was implemented in several ocean models (MITgcm: Losch, 2008; ROMS: Dinniman et al. 2007; Galton-Fenzi et al. 2012; FESOM: Timmermann et al., 2012; COCO: Kusahara and Hasumi, 2013; MPAS-O: Ringler et al., 2013; NEMO Mathiot et al., 2017). This formulation relies on the relationship between *in-situ* freezing point, water masses temperature and salinity. In addition, the parameterizations of shear turbulence induced by currents to calculate heat and salinity fluxes results in spatially variable transfer coefficients that modulate the melting rates in space and time. This approach is more realistic, in particular in larger cavities where the Coriolis force deviates the horizontal flow and induces a spatial asymmetry in the distribution of basal melt rates (Holland et al., 2008), such as, for instance, the Ronne-Filchner Ice Shelf (Weddell Sea, Naughten et al. 2019), the Amery Ice Shelf (Prydz Bay, Wen et al. 2010), and the Ross Ice Shelf (Ross Sea, Dinniman et al., 2018).

1.5.1 Direct observations of sub-ice shelf cavities

Very few direct observations exist of the sub-ice shelf environment. Ice shelf cavities are highly difficult to reach from the logistical point of view, because the Antarctic environment is challenging in terms of weather and requires large research infrastructures and expensive instrumentations. Measurements were made initially by hot-water drilling through the ice shelf at few locations: they give very local observations of limited duration. Very few borehole have been achieved yet Dowdeswell et al. (2008). On the Ross Ice Shelf, the first bore-hole drilling was made at the J9 site (Zotikov, 1979; Clough and Hansen, 1979) in Siple Coast (82°22.5'S, 168°37.5'W) and reached 597 m below sea level; they estimated a water column thickness of 237m, but no hydrographic data was collected. Foster (1978) reported the first temperature and salinity measurements profiles carried out below the ice shelf, noticing a stratification of two water masses: warmer HSSW at the bottom and cold ISW on top. Jacobs et al. (1979) and Gilmour (1979) made more extensive oceanographic measurements at the J9 site. By now only 4 hot-water drillings were made on the RIS: [1] HWD-2: investigation of oceanographic properties below RIS (Stevens et al., 2020); [2] J9: two mixed layers, at the bottom and at the top, and a stratified layer in between; mixing was hypothesised to be due to tidal stirring of the water column (Jacobs et al., 1979; Foster, 1978); [3] (Coulman High) CH1,2: near Ross Island, used to measure directly near-frontal basal melting (Arzeno et al., 2014); [4] Whillans Ice Stream Subglacial Access Research Drilling (WISSARD): Observed low melting rate close to the grounding line, over a 7-days period at three observation sites (Begeman et al., 2018). Tidal mixing was not sufficient to homogenise the weak stratification between the upper layer and middle layer and bring warm bottom water in contact with the ice shelf.

More recently, Remotely Operated Vehicles (ROVs) for sub-ice shelf exploration were introduced, tethered to a mother ship by an umbilical power and control cable. Some have been deployed to investigate tidewater-glacier and ice-shelf margins, but their range is restricted to hundreds or, at most, a few thousands of metres (Dowdeswell et al., 2008), which make it feasible only on the smaller cavities. Free-flying Autonomous Underwater Vehicles (AUVs) have started to be employed, with an autonomy of tens to hundreds of kilometres they are more suitable for large cavities exporation (Dowdeswell et al., 2008). Cavity measurements using AUVs are still challenging due to inherent technical limitations: the long travel time needed to explore large cavities, combined with the issues of battery autonomy, navigation and tracking without GPS positioning, the development of collision-avoidance mechanisms and fast-changing sea ice conditions at the recovery site makes it still problematic to use McPhail et al. (2009, 2019).

According to Gwyther et al. (2020b), prior to 2019, AUVs have been used to investigate ocean properties within only two ice shelf cavities: the Fimbul Ice Shelf (East Antarctica, Nicholls et al. 2006, 2008) and the Pine Island Glacier (Jenkins et al., 2010). Interesting results from direct observations show that ice shelves draft is far from being uniformly smooth: AUV reveal regions with high roughness, incisions, and depressions, interleaved by regions of smooth surfaces as seen in Fimbul ice shelf (Nicholls et al., 2006) where oceanographic data were also collected. Deployments under the Pine Island Glacier and the Filchner-Ronne Ice Shelf were carried out with the purpose of testing the engineering aspects of the missions, but no scientific result was gathered (McPhail et al., 2009, 2019). Direct estimates of basal melt rates were made under the Sørsdal Ice shelf (EAIS) by Gwyther et al. (2020b) in combination with numerical modelling, finding a cold cavity environment, with low basal melting and low seasonal variability.

The few obtained direct observations do not allow, yet, to have a pan-Antarctic view of basal melt rates. The existing pan-Antarctic melting values, are retrieved indirectly from ice sheet mass balance estimates inferred from observed surface ice velocities (Moholdt et al., 2014; Rignot et al., 2013; Adusumilli et al., 2020; Das et al., 2020) and calving flux (Depoorter et al., 2013). As such, those basal melt rate distributions are subject to large uncertainties (e.g. due to lack of knowledge about ice shelf draft and ice sheet bed morphology). In addition, such estimates are highly influenced by the pattern of observed surface velocities, regardless of the method employed. At last, those estimates are only valid for a few decades of the 20th and 21st century. This calls for ocean-ice shelves coupled models to fill the gaps, to improve indirect estimates and provide values for melting in periods when observations were unavailable.

1.6 The Ross Sea and Ross Ice Shelf

1.6.1 Oceanography of the Ross Sea

The Ross Sea falls in the category of the "dense shelves": it is one of the few places in the world oceans where the densest waters are formed Jacobs et al. (1970). Several water masses are present in the Ross Sea, characterised in terms of temperature and salinity (Jacobs et al., 1970, 1985; Orsi et al., 1999; Whitworth et al., 1998; Orsi and Wiederwohl, 2009) and reported in Table 1.1. The lightest water mass is the Antarctic Surface Water (AASW), which occupies the surface layer. It is characterised by a large seasonal variability, with its temperature at freezing point

in winter and up to ∼2 °C in summer (Russo et al., 2011). The Circumpolar Deep Water (CDW) is denser than the AASW. It is advected by the Southern branch of the Ross Gyre, upwells along the bathymetry, and starts flowing in the Along Slope Current (ASC). The CDW is relatively warm and salty, and mixes with water masses residing on the shelf across the continental shelf and slope. On the continental shelf, Shelf Waters (SW) are considerably colder and saltier than the CDW, and the strong density gradient at the slope produces a "V-shaped" feature, the Antarctic Slope Front (ASF), that regulates the exchanges across the continental edge (Figure 1.9b). On the continental shelf, at the locations of troughs and banks, intrusions of CDW do occur (Dinniman and Klinck, 2004; Dinniman et al., 2011; Klinck and Dinniman, 2010; Russo et al., 2011; Castagno et al., 2017). Processes that drive the CDW transport are predominantly: eddies (Stewart and Thompson, 2013, 2015, 2016; Stewart et al., 2018), tides (Padman et al., 2009, 2018; Wang et al., 2013), and inertial overshooting (Klinck and Dinniman, 2010) where the bathymetry curves sharply and accelerates the flow of the ASC, breaking the potential vorticity locally; those mechanisms are summarised in (Dinniman et al., 2011). On the continental shelf, the CDW, that mixes with other water masses, is found in its "modified" (cooled) form (mCDW).

In the Western Ross Sea (160°E to 180°E, Figure 2.1a), three main "polynyas" are active (Gordon et al., 2009): the Terra Nova Bay polynya, the Ross Island polynya (McMurdo Bay) and, in the Central Ross Sea, the frontal Ross Ice Shelf polynya. In such regions sea ice is produced at a high rate and then pushed away by the wind, which allows new sea ice to form (see Figure 2.3 in Chapter 2). The brine rejected by the newly formed sea ice sinks into the water column, yielding the High Salinity Shelf Water (HSSW), that fills most of the Western Ross Sea continental shelf (Jacobs and Giulivi, 1999). The densest HSSW fills the bottom layer of the Western and neighbouring parts of the Eastern Ross Sea. The water masses of the Eastern Ross Sea (180°E to ∼150°W), on the contrary, are affected by ice shelves meltwater (freshwater) and sea ice advected from the Amundsen Sea (Figure 1.1a,c), transported downstream by the Antarctic Coastal Current (AACC). By mixing with the local SW, this yields the Low Salinity Shelf Water (LSSW) in the Eastern Ross Sea continental shelf. SW are generally close to the surface freezing point (∼ -1.8 °C), and according to their salinity are classified as LSSW or HSSW. The RSBW then is exported across the continental shelf break in energetic outflows (cascading) which feed the Antarctic Bottom Water (AABW) (Bergamasco et al., 2002, 2004; Gordon et al., 2009; Budillon et al., 2002, 2011); this outflow is enhanced by strong tidal fluctuations observed in Northwestern Ross Sea (Whitworth and Orsi, 2006; Padman et al., 2009).

Water mass	Potential temperature (°C)	Salinity (P.S.U.)
AASW[1]	< -1.5	< 34.3
AASW[2]	$0 < \Theta < 2$	< 34.5
CDW[2]	< 1.5	~ 34.7
mCDW[2]	$-1.5 < \Theta < 1$	$34.5 < S < 34.6$
mSW[1]	> -1.85	
SW[1]	< -1.85	
LSSW[1]	< -1.85	< 34.62
LSSW[2]	< -1.8	$34.4 < S < 34.6$
HSSW[1]	< -1.85	> 34.62
HSSW[2]	< -1.9	$S > 34.7$
ISW[1]	< -1.95	
ISW[2]	< -2.2	

Table 1.1: Different definitions of Ross Sea water masses after [1](Orsi and Wiederwohl, 2009); [2]Russo et al. (2011). Some water mass are not defined by both.

1.6.2 The Ross Ice Shelf

The Ross Ice Shelf (RIS) is the floating marine termination of the AIS in the Ross Sea sector. The RIS front thickness ranges from 150 to 400 m and is up to 800 m near the grounding line. It forms a barrier to geostrophic ocean circulation (Taylor-Proudman theorem). Nonetheless, driven along bathymetric furrows, winds, eddies, tides, continental shelf waters, namely the HSSW, the LSSW, the mCDW, the AASW, flow inside the cavity at different locations and times, depending on their different seasonality (Figure 1.10). In particular, the HSSW entering near the Ross Island, flows in an anticyclonic cell driven by the density gradient between Western and Eastern Ross Sea Shelf Waters (Assmann et al., 2003; Budillon et al., 2003; Jendersie et al., 2018);. In the central Ross Sea, mCDW reaching the front of the Ross ice Shelf was first detected by Jacobs et al. (1979) and during subsequent campaigns. When mCDWreach the ice shelf, they interact by melting the ice shelf draft (losing heat) and mixing with released meltwater (freshening) and or with ambient water (Figure 1.10). Even though the SWs are near the surface freezing point, the increasing pressure with depth in turn decreases the freezing point which allows them to melt the ice shelf draft. Pure meltwater is called Ice Shelf Water (ISW), which partially mixes with the water masses that cause the melting of the ice shelf draft. Two types of ISW, shallow and deep (Jacobs et al., 1985; MacAyeal, 1984b; Bergamasco et al., 2004), according to the depth at which melting occurs, exit the cavity in the Glomar Challenger Trough (Figure 1.1c). The ventilation

time of the Ross ice shelf cavity was estimated to be ∼6 years with radioactive geochemical tracer measurements at J9 (Michel et al., 1979); confirmed also by the first modelling attempt including the Ross Ice Shelf cavity (MacAyeal, 1984a,b, ∼5 years). Tides also play a role in regulating transport across the Ross Ice Shelf front and the circulation within the cavity. MacAyeal (1984a) identified the diurnal tidal wave K1 and O1 as the main tidal components that resonate with the characteristic length of the basin and the cavity shape, yielding topographic Rossby waves along the Ross Ice Shelf front.

Recent changes in the Ross Ice Shelf

The RIS underwent very small changes from the glaciological point of view in the last decades (Pritchard et al., 2012; Paolo et al., 2015). The Ross Sea oceanography, on the contrary, experienced important changes: the clearer corresponds to a freshening trend in continental shelf waters, notwithstanding the decadal natural variability: freshening of -0.03/decade was identified over the last 50 years, and 0.08/decade over the last 30 years in the Antarctic Coastal Current (Jacobs and Giulivi, 2010). This trend can be explained by increased glacial meltwater imported from the Amundsen Sea. Numerical simulations show that about a third of the meltwater from the Amundsen Sea, and from the Getz ice shelf in particular (Figure 1.1a), is imported in the Ross Sea (Nakayama et al., 2014). No significant warming of the ocean bottom layer was identified in the Ross Sea (Schmidtko et al., 2014). The freshening trend was also observed more recently in mooring stations on the continental shelf (Castagno et al., 2019), and was interrupted by a strengthening in sea ice production after 2014, followed by a rapid resalinification of the AABW. The causal link was found to be an unusual phasing of the SAM and the ENSO, which reduced sea ice import from the Amundsen Sea, subsequently increasing the activity of Ross Sea polynyas (Silvano et al., 2020).

1.7 Geological glacial history of Antarctica (34 Ma - present)

Sedimentary records collected so far provide an overview of the glaciation history of the AIS since its presumed formation at the Eocene-Oligocene Transition ∼34 Ma, during the Cenozoic (last 65 Myears) (Escutia et al., 2019). It is thought that the glaciation of Antarctica was driven by a drop in atmospheric CO_2 concentration below 1000 ppm (Figure 1.11a). The threshold for glacial inception Southern high latitudes remains however uncertain and is thought to be between 800-1200 ppm

(Ladant et al., 2014; Liakka et al., 2014). After the Eocene-Oligocene Transition, the AIS was mostly terrestrial, implying that most of the ice was grounded on a bed above sea level. As such, the AIS was particularly sensitive to the astronomical forcing and to variations in atmospheric CO_2 concentration (Galeotti et al., 2016; Levy et al., 2016). A second atmospheric CO_2 concentration drop below 400 ppm occurred in the late Oligocene, ~24 Ma (Levy et al., 2019). This caused a global climate cooling that further drove the expansion of the mostly terrestrial AIS onto the continental shelf, (e.g. Naish et al., 2022). The seismic stratigraphic records reveal, indeed, that the AIS advances reached the continental shelf break numerous times during the Oligocene and the Miocene in the Ross Sea (De Santis et al., 1995, 1999) and other sectors of Antarctica (e.g. Figure 1 in Colleoni et al. 2022. Recently, provenance analyses from the Ross Sea IODP exp. 374 showed that the West Antarctic Ice Sheet expanded significantly on the Ross Sea continental shelf before the Middle Miocene Climatic Optimum (MCO ~ 17-14.8 Ma), implying an AIS volume larger than estimated so far for this period of high atmospheric CO_2 concentration (Figure 1.12). Similarly, during the MCO, the AIS retreated from most of the Antarctic continental shelf due to high atmospheric CO_2 levels larger than 500 ppm (e.g. Paxman et al. 2020. After the MCO, a steady decline in deep ocean temperatures (Cramer et al., 2009; Miller et al., 2011), the stratigraphic record indicates a progressive re-expansion of the AIS towards the continental shelf break (Figure 1.12c, inset). Due to the ongoing basal erosion since about 34 Ma, which enlarged the AIS marine-based sectors, the AIS became increasingly sensitive to ocean warming (Colleoni et al., 2018a; Paxman et al., 2020). In terms of inferred ice volume (based on benthic $\delta^{18}O$ records, Figure 1.11b), when the AIS was largely terrestrial until about 20-15 Ma, it drove global sea level changes of up to 40 m amplitude (Figure 1.11c,d). Later, in colder periods between 14 and 3 Ma, a highly dynamic, marine-based AIS contributed up to 20 m of global sea level rise when atmospheric CO_2 level was higher than 400 ppm. The stronger AIS sensitivity to the ocean, may explain the higher amplitude of the glacial-interglacial cycles in benthic $\delta^{18}O$, (Figure 1.11b, inset) during the Pleistocene (Levy et al., 2019). A coupled atmospheric-ocean general circulation model, set-up for the Middle Miocene period (Knorr and Lohmann, 2014), highlights the changes that took place in atmospheric and ocean circulation and sea ice, and in the water masses at that time: the northward shift of the winds due to the growing ice sheet induced a northward shift of the major oceanic systems, including the main gyres around Antarctica, which lead to a local sea-surface temperature warming and deep water cooling. Therefore, understanding the complex feedback in the climate system in deep past periods remains a challenging topic, due to uncertainties in model physics and climatic proxies reconstructions (Escutia et al., 2019; Colleoni et al., 2022).

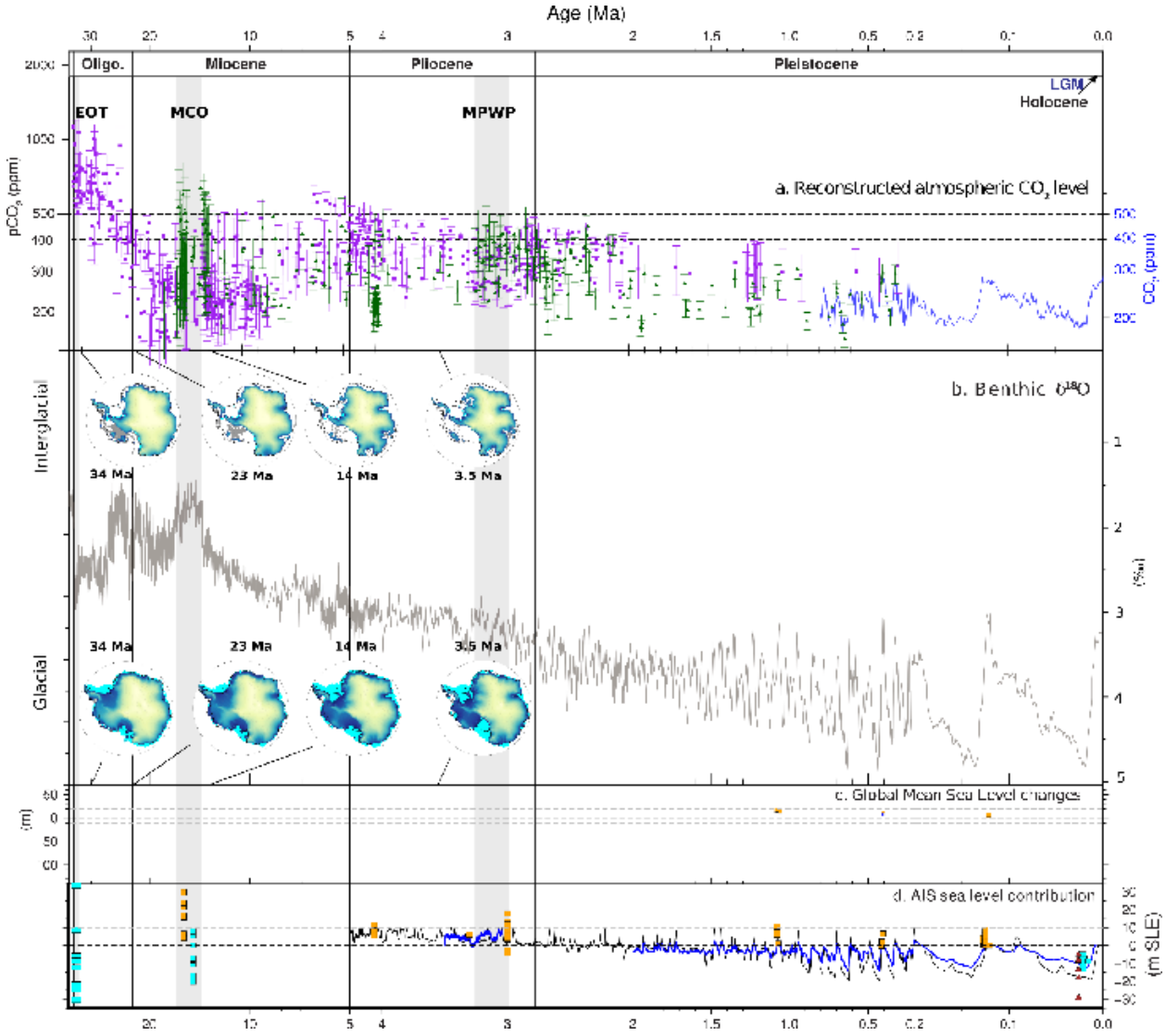

Figure 1.11: evolution since the Eocene-Oligocene Transition (∼34 Ma) of: (a) atmospheric CO_2 (1), (b) benthic $\delta^{18}O$ (2), (c) global-mean sea level change (3) (d) AIS volume contribution to sea level. Adapted from Figure 1 in Colleoni et al. (2022), in Antarctic Climate Evolution, Florindo et al., Elsevier, 2022). EOT: Eocene-Oligocene Transition; MCO: Miocene Climatic Optimum; MPWP: Mid-Pliocene Warm Period.

1.8 The Last Deglaciation (21 ka - present)

At the peak of the last glacial cycle, ∼21 ka, several ice sheets covered the polar regions of the Earth (Figure 1.12). In particular, the whole North American continent was covered by the Laurentide ice sheet; Northern Europe was covered by the Fennoscandian in actual Scandinavia, the Svalbard-Barents-Kara ice sheet and the British Islands ice sheet, which together formed the Eurasian Ice sheet Hughes et al.

(2016). Greenland was covered by an ice sheet slightly larger than the current one, and Antarctica was covered by the Antarctic Ice Sheet (AIS) that was also bigger than the actual one (e.g. the RAISED Consortium, Bentley et al., 2014b). Global mean annual temperature at LGM was on average 4-5 °C colder than present-day, and generally drier (Otto-Bliesner et al., 2006). Global-mean sea level, due to the large amount of water stored in the ice sheets, was lower by ∼125 m relatively to present (Figure 1.13) (Fairbanks, 1989; Bard et al., 1990; Peltier, 2004; Miller et al., 2011). Geomorphological and geological evidence have shown that during glaciations, the AIS grounding line advanced to the continental shelf edge almost everywhere in the Ross Sea, except in a few troughs (the RAISED Consortium, Bentley et al. 2014b; Halberstadt et al. 2016; Bart et al. 2018; Prothro et al. 2020. As a consequence, water masses could not flow on the continental shelves.

The astronomical forcing during the deglaciation favoured the retreat of most of the ice sheets on Earth. This led to a global mean sea level rise of about 120 metres (e.g. Rabineau et al. 2006, for the compilation of various sea level curves; and Figure 1.13). At the LGM, the astronomical forcing yielded high insolation during austral summer (Laskar et al., 2011; Figure 1.14a,b,c,i). Note that the LGM was defined based on the minimum global mean temperature and that this minimum was not reached at the same time in the various regions of the Earth (Clark et al., 2009). In addition, the insolation changes were mostly in opposite phases between the Northern and the Southern hemispheres, as a consequence of obliquity. Despite this opposed insolation, global mean temperature drop at LGM caused a cooling also in the Southern Hemisphere. At the LGM, proxy-based sea surface temperature reconstructions suggest a strengthening of the meridional temperature gradient Members (2009). This was likely caused by a strengthening of the mid-latitude wind belt system (Lamy et al., 2019) and by the expansion of the sea ice cover (e.g. Gersonde et al., 2005). The overall feedback loop induced a weakening of the Southerly winds (Lamy et al., 2019) and a strengthening and northward shift of the Easterly winds. Chavaillaz et al. (2013) analysed several climate models of the LGM, and obtained equatorward Westerlies shift in the NCAR model (employed in TraCE-21ka), with strong inter-model dependance.

During the deglaciation, the precession of seasons led to warm boreal summer and cool austral summers (Figure 1.14a,b,c,i), inducing the melting of most of the Northern hemisphere ice sheets before the peak of the Holocene, ∼10 ka (e.g. Hughes et al., 2016; Dyke, 2004). Nevertheless, near surface-air global mean temperature rose steadily (Figure 1.14g,l), as insolation increased and atmospheric CO_2 level started to rise from ∼180 ppm (LGM) to reach 280 ppm at pre-industrial times (Monnin

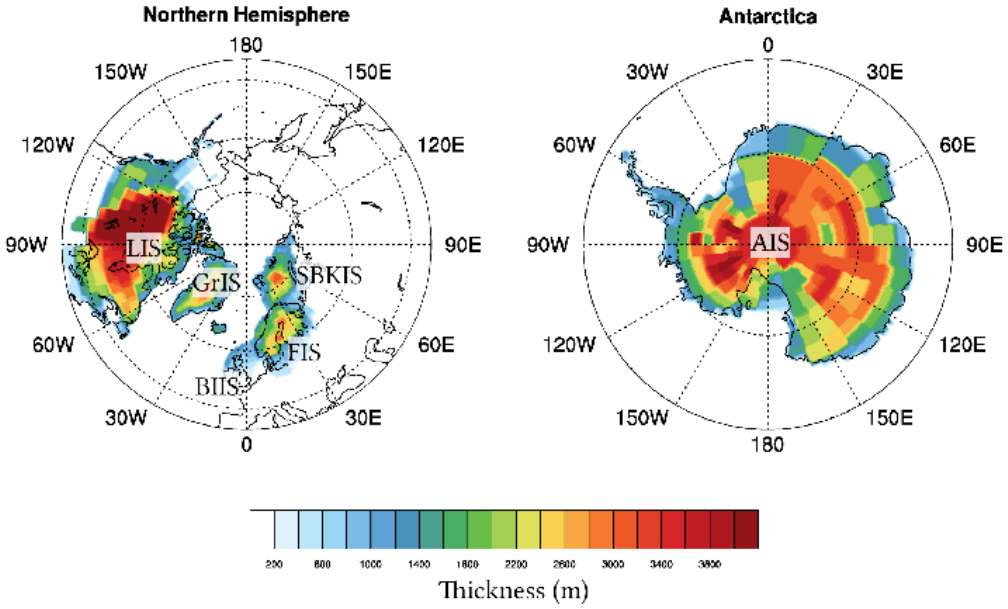

Figure 1.12: Ice sheets at the Last Glacial Maximum from ICE-5G chronology (Peltier, 2004): Laurentide Ice Sheet (LIS) Greenland Ice Sheet (GrIS), Svalbard-Barents-Kara Ice Sheet (SBKIS), Fennoscandian Ice Sheet (FIS), British Islands Ice Sheet (BIIS), Antarctic Ice Sheet (AIS). Note that the ICE-5G reconstruction accounts for the Northern ice sheets extent suggested by proxy reconstructions. On the contrary, the AIS is kept at present-day extension in all snapshots of the ICE-5G deglaciation chronology.

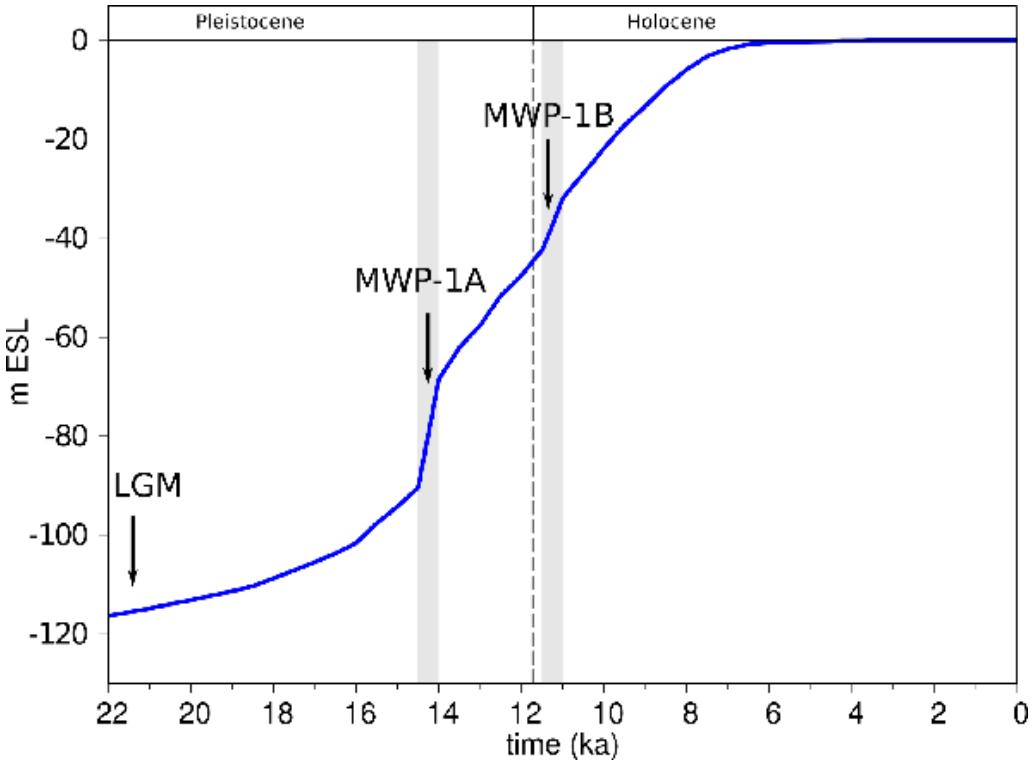

Figure 1.13: Post-LGM eustatic (global mean) sea level rise calculated with the sea-level equation solver SELEN (Spada et al., 2012) employing the ICE–6G (VM5a) ice sheet deglacial chronology (Peltier et al., 2015). LGM=Last Glacial Maximum, MWP-1A= Meltwater pulse 1A, MWP-1B= Meltwater Pulse 1B.

et al., 2004). As a consequence of global mean temperature rise, ice core δ^{18}O records suggest that more precipitation was able to reach the AIS (e.g. δ^{18}O EPICA, Monnin et al., 2004; and WAIS ice core, Members, 2013) and that near-surface moisture increased as well (Figure 1.14h,p,q). This led to an increase in Antarctic surface mass balance, which, combined with a decreased austral summer insolation, may have partially compensated for the global atmospheric and ocean warming trend (Weber et al., 2011).

The Northern hemisphere ice sheets retreat was, however, not linear and some dynamical instabilities related to oceanic warming and sub-glacial hydrology caused fast ice discharge (a few centuries) into the ocean, at formation locations of the NADW (Tarasov and Peltier, 2005). Such freshwater pulses induced a slowing down of the AMOC (Knutti et al., 2004). Such freshwater pulses have been associated with millennial-scale rapid events, the Dansgaard-Oeschger events (warm), followed by Heinrich (cold) events. Such millennial scale events were identified in the sediment cores of the North Atlantic and in the ice core records of Greenland first and Antarctica then (Members, 2015). The most prominent freshwater release event of the last deglaciation is the Meltwater Pulse 1A (∼14.6 ka). This pulse was presumably caused by the collapse of large portions of the Northern hemisphere ice sheets (Carlson and Clark, 2012; Peltier, 2004; Brendryen et al., 2020; Lucchi et al., 2015), that induced a sudden slowdown of the AMOC and a few centuries later (Liu et al., 2009). In the Ross Sea, as for other sectors of Antarctica, simulated ice sheet dynamics (Golledge et al., 2014) and Ice Rafted Debris, suggest that the ice sheet retreat was affected by such a warming event associated with feedbacks in the Southern Ocean. Comparison between the Greenland ice core records and the Antarctic ice core records revealed that the DO and Heinrich events were mainly out of phase. It suggested that when Northern hemisphere high latitudes were cooling, Southern hemisphere high latitudes were warming a few centuries after. Broecker (1998) and Stocker (2002) suggested a mechanism of inter-hemispheric heat transfer, linked with the freshwater release in the Northern Hemisphere high latitudes and the stratification of ocean waters, the so-called “bipolar seesaw”. One of the main consequences was to transfer most of the northern hemisphere oceanic heat to the southern hemisphere in the sub-surface and deep layers, (Knutti et al., 2004; Pedro et al., 2016). This process was also simulated at 14.6 ka (Meltwater pulse 1A) in the Ross Sea sector in the transient simulation TraCE-21ka (Liu et al., 2009), and accompanied by a second warming pulse at 13 ka (Figure 1.15a). This warming may in turn have been enhanced by the increased melting of the AIS margins. In fact, increased freshwater release to the surface layer at the AIS margin (Figure 1.154.1b), would have reduced mixing, increased stratification and further contributing to trapping ocean heat in the deep ocean by

favouring the upwelling of CDW on the Antarctic continental shelves (Bronselaer et al., 2018; Golledge et al., 2014, 2021; Silvano et al., 2019; Turney et al., 2020); a similar mechanism was observed recently in the Eastern Weddell Sea by (Ryan et al., 2020). The changing conditions in temperature, salinity and sea ice cover induced acceleration of the surface and sub-surface currents eastward and northward (Figure 1.15c,d) and an opposite flow anomaly at the bottom. Among the deglacial changes occurring in the ocean, the Southern ocean deep and bottom layers salinities are generally thought to be higher at the LGM (Adkins et al., 2002) and as such, +2 PSU were prescribed in TraCE-21ka (Figure 1.15b). In particular, Knorr et al. (2021) showed that high salinity is a prerequisite for deep ocean warming during deglaciation, although the question is still debated (Wunsch, 2016). Diatoms analysis suggests that sea ice extent was twice as large during the LGM in winter as during the pre-industrial, reaching ∼50°S in the Indian and Atlantic (Gersonde et al., 2005); scarce data for summer extent suggest strong seasonal fluctuations in limited sectors, however very little data exists for the Pacific sector of the Southern Ocean.

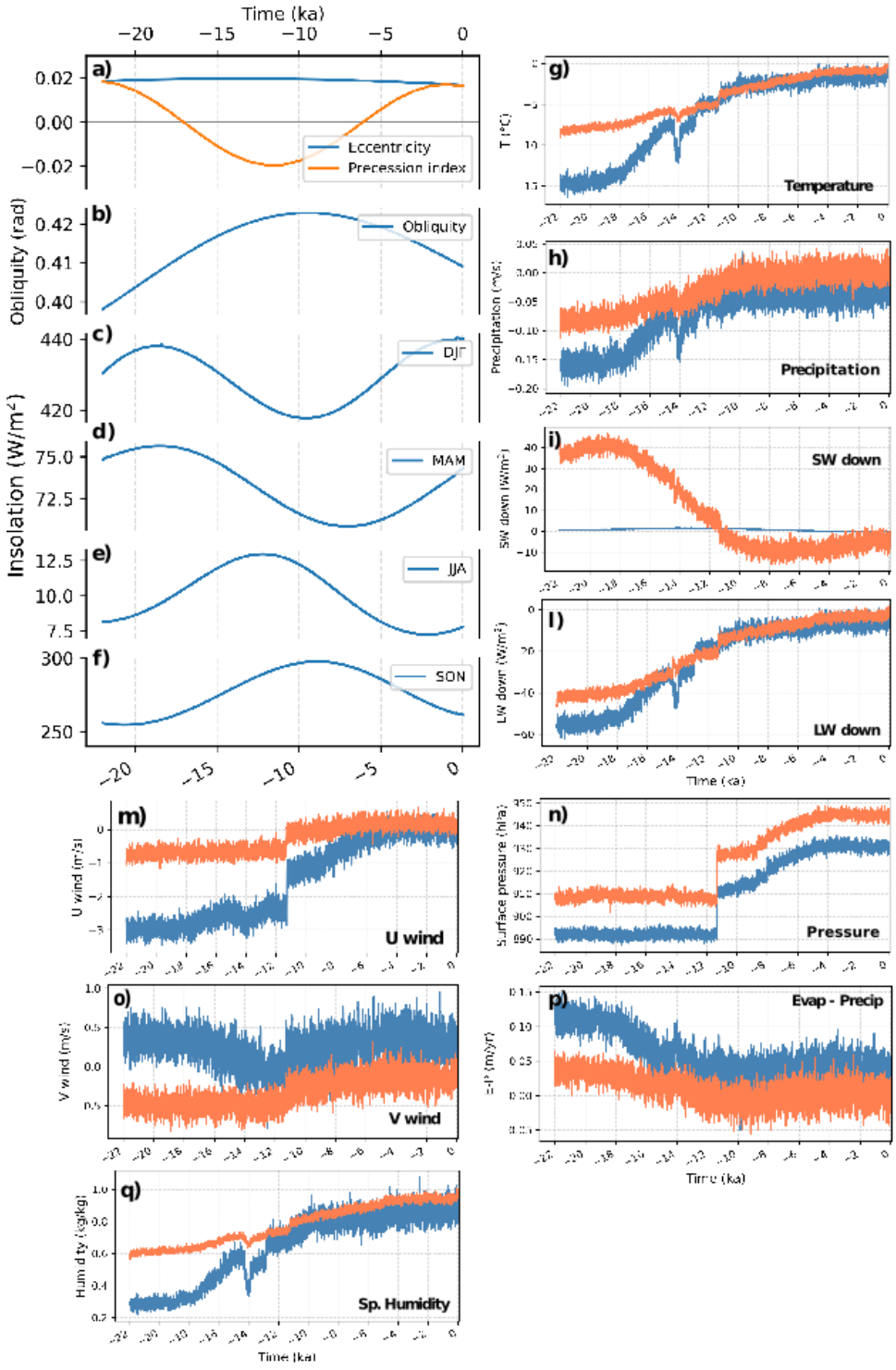

Figure 1.14: Astronomical forcings[1] shown from LGM to the present (∼22–0 ka): (a) eccentricity and precession index (b) obliquity (radians), (c-f) seasonal averages of insolation1 at TOA averaged zonally at 71°S: December-January-February (DJF), March-April-May (MAM), June-July-August (JJA), September-October-November (SON). (g-q) Summer (orange) and winter (blue) climate fields from TraCE-21ka[2] averaged over the Ross sector (156–220°E and 86–67°S) and smoothed with a moving average over a 10-years window)([1]Laskar et al., 2011; [2]Liu et al., 2009). Note the shift at 11 ka (g,m,n,o) associated with prescribed ice sheet topography changes in ICE-5G topography (Peltier 2004 as implemented in TraCE-21ka).

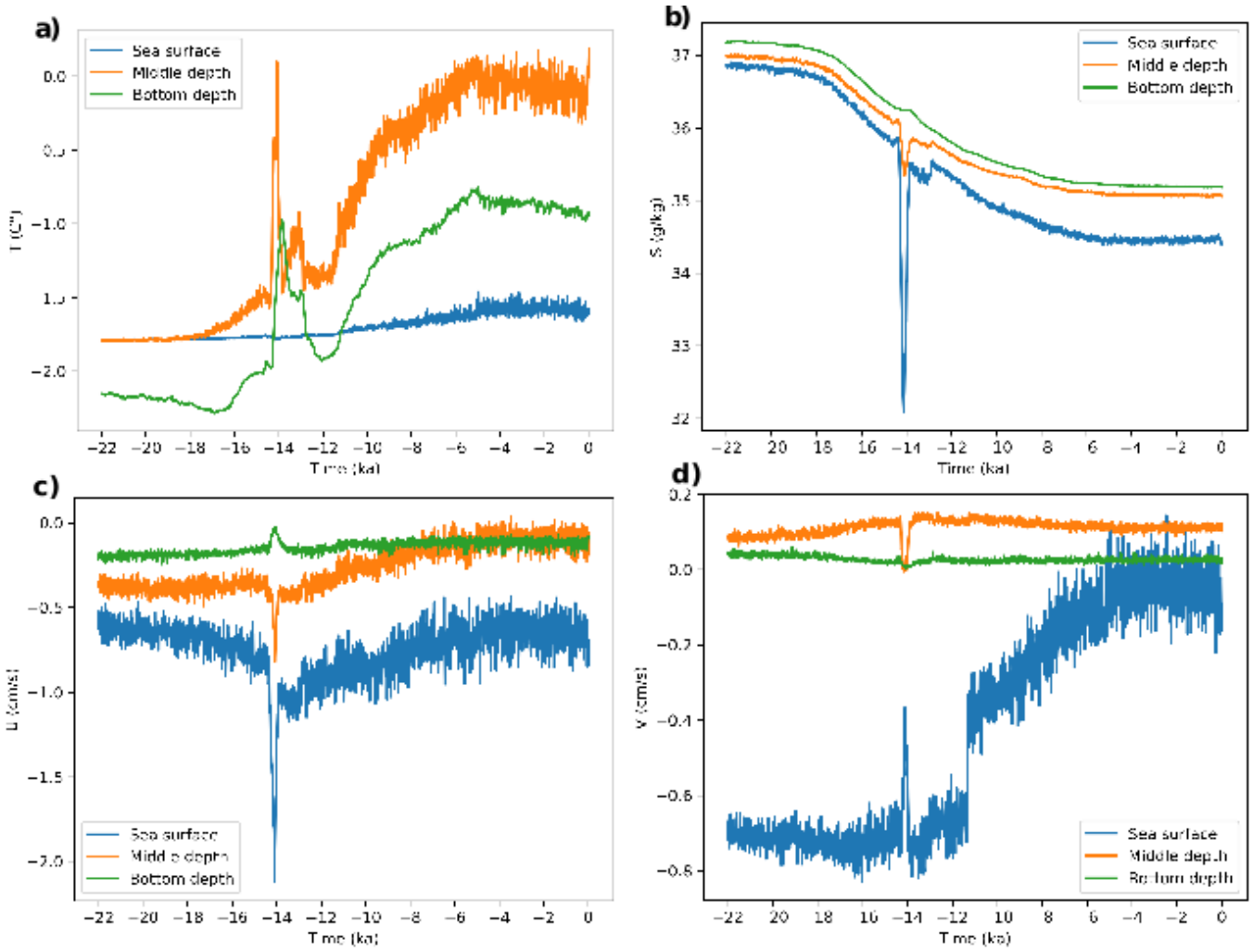

Figure 1.15: (a) TraCE-21ka Liu et al. (2009) simulated oceanic evolution in the Ross Sea during the last deglaciation at the surface, at middle depth (400m) and at the bottom: (a) temperature (°C); (b) salinity (g/kg); (c) zonal and (d) meridional velocities (cm/s) of the simulated along-slope current. Note that the fields displayed here are not bias-corrected and correspond to the original main TraCE-21ka transient simulation outputs (https://www.earthsystemgrid.org/project/trace.html).

Chapter 2

Spatio-temporal variability of Ross Sea water masses

2.1 Introduction

The global ocean has been warming in the last decades (Roemmich et al., 2015), with heat increase reaching also the deep layers (down to about 2000m). However, in the Southern Ocean, regional differences and long-term natural variability make the interpretation of observed changes more challenging, and the extraction of a warming trend in the subsurface ocean problematic (Jenkins et al., 2016; Jones et al., 2016). The recent (1979-2014) linear trends in surface air temperature measured by Antarctic stations and sea-ice extension and sea-surface temperature measured by satellites are superimposed on large interannual to decadal variability (Jones et al., 2016); most of these trends can be attributed to changes in atmospheric circulation and tropical teleconnections (Li et al., 2021).

The present study aims at improving the understanding of the current spatio-temporal variability of the Ross Sea continental shelf oceanic circulation and its interactions with open ocean circulation and regional to global teleconnections. We implement a regional configuration of the Massachussets Institute of Technology general circulation model (Marshall et al., 1997a,b) to simulate the transient Ross Sea ocean circulation over 1993-2018, including the circulation within the Ross Ice Shelf cavity and its thermodynamic interaction via the three-equation formulation (Losch, 2008, see Chapter 3). We analyse the relationship between the spatio-temporal evolution of the simulated water masses and basal melting. This analysis is further strengthened by comparing our simulated water masses circulation with existing time series from four Italian mooring stations of the MORSea observatory (e.g. Castagno

et al., 2019; Budillon et al., 2011; Russo et al., 2011; Bergamasco et al., 2002) and measurements taken along the RIS front during past PNRA cruises. Finally, the temporal variability of water masses is related to the main regional to global teleconnections influencing the Ross Sea sector. This overall analysis allows us to better understand the spatio-temporal variability of the Ross Ice Shelf basal melt rates, which will be analysed in detail in Chapter 3.

2.2 Methods

2.2.1 The MITgcm: Ross Sea regional implementation

The MITgcm has already been used in various studies focusing on the Southern Ocean and Antarctic. Losch (2008) implemented the three-equation formulation to calculate basal melting of ice shelves in the MITgcm and participated in the Ice Shelf-Ocean Model Intercomparison Project (ISOMIP; Holland et al., 2003), experiment to simulate the basal melting of the Filchner-Ronne Ice Shelf. The MITgcm was employed to study CDW intrusions in the Amundsen and Bellinghausen Seas at medium resolution (10 km, Nakayama et al. 2014, 2017), high resolution (2-3 km, Nakayama et al. 2018) and very high resolution (200 m, Nakayama et al. 2019), to study basal melting of Pine Island and Thwaites glaciers. They also simulated the impact of meltwater spreading from glaciers on Southern ocean hydrography (Nakayama et al., 2020). Stewart and Thompson (2015, 2016) used the MITgcm to investigate the Antarctic continental slope dynamics and water masses exchange at 1-km resolution, to resolve mesoscale eddy fields. Stewart and Thompson (2015) investigated the mesoscale eddy transport of the CDW in eddy resolving simulations of the MITgcm across idealised continental slope profiles, whereas Stewart et al. (2018) carried out the same investigation by employing a realistic slope bathymetry.

In the present study we implement a regional configuration of the Massachusetts Institute of Technology general circulation model (MITgcm, Marshall et al., 1997a,b) on the Ross Sea sector, Antarctica (Figure 2.1a). The domain includes the entire Ross Ice Shelf cavity, smaller glaciers fringing the Ross Sea and a part of the Amundsen Sea region in the North-Eastern sector (Figure 2.1), to allow for meltwater advection in the Ross Sea continental shelf. Our grid domain expands from 67°S to 86°S and from 156°E to 140°W (Figure 2.1a). The MITgcm employs a finite-volume discretization on an Arakawa C-grid and the vertical layers follow z-coordinate levels. The model bathymetry and ice shelves draft (Figure 2.1b) are set-up by interpolating the RTopo-2 dataset (Schaffer et al., 2014; based on the Bedmap2 dataset, Fretwell et al., 2013), on a cartesian regular 5-km grid (300x400 grid cells) with an oblique

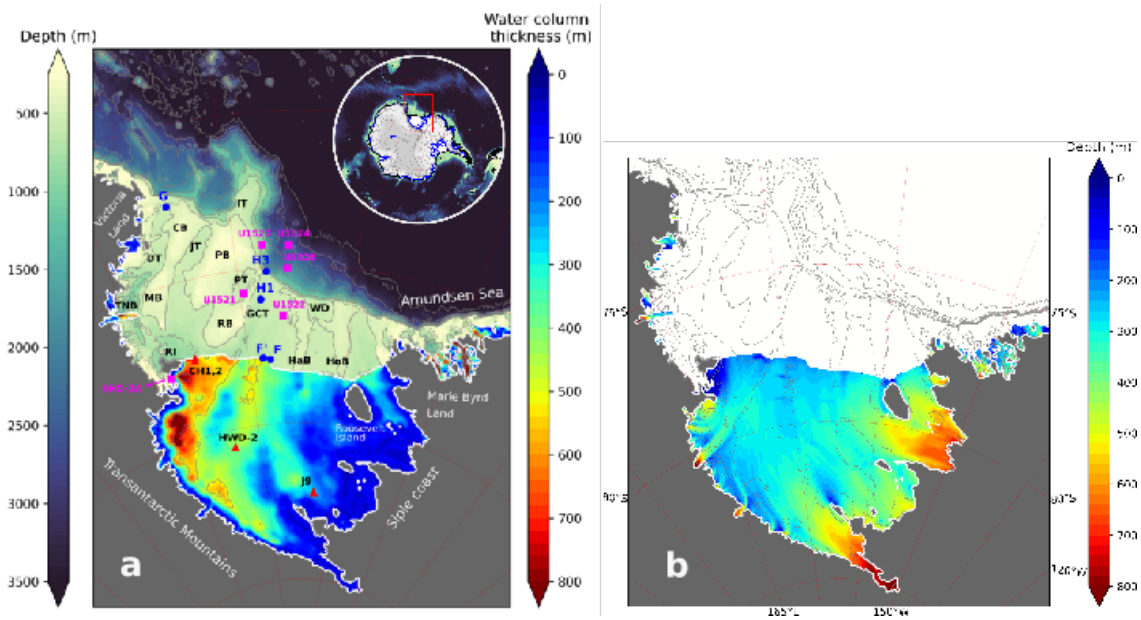

Figure 2.1: Ross Sea domain as implemented in the MITgcm. (a) Bedmap2 Ross Sea bathymetry (Fretwell et al. 2013 in the updated version: RTopo-2, Schaffer et al. 2014) and water column thickness below the cavity (m). The white lines delimit the grounding line and the ice shelf fronts; the gray area are above sea level (dry cells for the ocean)and correspond to the terrestrial part of the Antarctic ice sheet (dry cells for the ocean). The major seafloor basins, banks and troughs mentioned in this study are labeled. Blue dots indicate the location of the Italian moorings used in this study (F was moved to F' in summer 1997). (b) Depth (m) below sea level of the ice shelves draft. Names in (b): CB = Crary Bank, DT = Drygalski Trough, GCT = Glomar Challenger Trough, HaB = Hayes Bank, HoB = Houtz Bank, IB = Iselin Bank, JT = Joides Trough, MB = Mawson Bank, PB = Pennel Bank, PT = Pennel Trough, RB = Ross Bank, TNB = Terra Nova Bay, WD = Whales Deep (basin).

stereographic projection centred at (188°E, 78°S) using the OBLIMAP-2 mapping tool (Reerink et al., 2016). The grid has 50 vertical levels of variable thickness. The first 32 layers that are defined to obtain higher vertical resolution ($\lesssim$ 50 m) at the shallow and intermediate depths on the Ross Sea continental shelf and inside the cavity, down to 1000 metres depth. Below this depth, the vertical resolution on the Ross Sea continental slope is coarser, and the grid has 18 levels down to 4800 metres depth. The ice shelf draft falls in the depth range where layers are 40 - 50 metres thick. Compared to sigma-layer (terrain-following) models, such as ROMS (Shchepetkin and McWilliams, 2005) that adapt vertical levels according to water column thickness, models employing the "z-coordinate" vertical discretization are less suitable to simulate the oceanic circulation over a shallow continental shelf, and along the continental slope unless a high vertical resolution is defined at all depths. The former, however, needs to smooth the bathymetry to avoid the occurrence of spurious pressure terms. This can be an issue when resolving the steep geostrophic gradient at the ice shelf front. The MITgcm is able to resolve the sharp change in water column thickness across the ice shelf front without such smoothing. The MITgcm allows partially-filled cells to improve the vertical resolution of the draft and bathymetry (Adcroft et al., 1997; Losch, 2008). Inside the cavity, the seafloor bathymetry and the ice shelf draft were filtered in order to avoid the draft to intersect with the bathymetry and to remove ocean grid points isolated from the rest of the ocean domain. A commonly used technique called "digging", is applied. It consists in artificially deepening the bathymetry where the water column is too shallow, e.g. close to the ice sheet grounding line, to ensure that each tracer node has at least a top and a bottom velocity node to allow a minimal water circulation. Filtering of the bathymetry and draft was achieved by using this open-source python package (`https://github.com/knaughten/mitgcm_python`). A quadratic-law drag (drag $\propto u^2$) is applied to the stress in ocean-sea bed and ocean-ice shelf boundaries. A free-slip condition were set at the ice shelf-ocean boundary in stress calculation (tangential currents not constrained to be $\equiv 0$), whereas a no-slip condition was prescribed for stress formulation at the seabed. A stationary geothermal heat flux is provided after Shapiro and Ritzwoller (2004).

In the present study, we run the MITgcm in its semi-compressible hydrostatic form (however the model can be run in its fully non-hydrostatic mode). Atmospheric-ocean fluxes are calculated by bulk-scheme after Large and Pond (1981, 1982) from atmospheric mean states. Turbulent heat and evaporative fluxes are calculated internally, using bulk formulas. We use the non-linear equation of state (McDougall et al., 2003). The Gent-Mcwilliams-Redi Eddy parameterization (GMREDI, Gent and Mcwilliams, 1990; Gent et al., 1995; Redi, 1982) is employed for mixing and

advection of tracer properties along isopycnal surfaces. The vertical mixing in ocean-atmosphere boundary layer, and interior mixing, is calculated using the non-local K-Profile Parameterization (KPP) scheme (Large et al., 1994). Uniform vertical tracers diffusivity are also prescribed through the entire water column. Horizontal mixing is treated with eddy viscosity, together with horizontal harmonic and bi-harmonic Leith viscosities. Tides, which we acknowledge are an important factor in the Ross Sea, are not included in this implementation. The possible implications of lacking tides are discussed in detail in Chapter 2.4.1. The sea ice module is interactive and fully coupled to the ocean dynamics and climate (Losch et al., 2010). The dynamic sea-ice solver uses the Line Successive over Relaxation (LSR) method, with seven thickness classes. This configuration has shown to satisfactorily represent sea ice processes in high-resolution simulations (e.g., Losch et al., 2010; Heimbach et al., 2010). Basal melting of the ice shelf draft is calculated based on the three-formulation equation (Hellmer and Olbers, 1989; Holland and Jenkins, 1999; Jenkins et al., 2001). This formulation considers heat and salt exchange, accounting for horizontal oceanic velocities and turbulent coefficients, from an ocean mixed layer, through a boundary layer at the ice-shelf ocean interface (Figure 3.2). The MITgcm thus accounts for the effect of freshwater fluxes in terms of changes in temperature and a virtual salinity flux that impacts buoyancy, which however conserves mass. Model parameters are set and adjusted following a setup for a run in the Weddell Sea and the FRIS (`https://github.com/knaughten/UaMITgcm`) to set model parameters. The model wais run at the eddy-permitting horizontal resolution of 5 km, in hydrostatic mode.

2.2.2 Simulations design

We perform a transient simulation over 1993-2018 branched on a 6-years spin-up using perpetual 1993 climatic forcing, the 3-hourly atmospheric reanalysis ERA5 (Hersbach et al., 2020) and the monthly oceanic reanalysis GLORYS12V1 (Lellouche et al., 2021). The length of the spin-up was chosen on the basis of early model work by MacAyeal (1984b) and radioactive geochemical tracer measurements at J9 Michel et al. (1979) who found that the ventilation time for the RIS cavity circulation was around 5-6 years; 6 years is the spin-up time used in a Ross Sea model based on ROMS (Dinniman et al., 2007). We use the same atmospheric and oceanic reanalysis over the period 1993-2018 to force our transient simulation. This time interval was chosen for two reasons: the first one is the availability of oceanic reanalysis to force our simulations; the second one is because it coincides with the first satellite measurements of global mean sea level changes. A sponge layer of 40-km (8 grid cells) thickness is applied to 3D ocean values, whereas no sponge is applied to sea ice

conditions. Lateral open boundaries are treated with a double relaxation-timescale scheme at inner and outer sides of the sponge of one year and one week, respectively (only one week for sea ice).

2.2.3 Atmospheric forcing: ERA5

Atmospheric forcing from ERA5 is provided on a nominal 31-km horizontal grid. The fields used to force the MITgcm are: surface pressure, wind velocity, temperature and specific humidity at 2 metres height, surface precipitation flux, downwelling shortwave, and longwave radiations All the fields are downscaled onto the Ross Sea grid (see section 2.1) by means of the OBLIMAP-2 mapping tool (Reerink et al., 2016). A smoothing filter is applied to reduce the checkerboard effect due to the downscaling from ERA5 31-km grid to the higher-resolved 5-km grid of the Ross Sea. Near-surface specific humidity is obtained by calculating the saturation specific humidity for the dewpoint temperature. Calculations use near-surface temperature, and the surface pressure, after the method indicated in the the operational manual of the Integrated Forecasting System of the European Centre for Medium-Range Weather Forecasts (eqs 7.4 and 7.5 from Part IV, Physical processes section (Chapter 7, section 7.2.1b):

$$q_{sat} = \frac{\frac{R_{dry}}{R_{vap}} e_{sat}(T)}{p - (1 - \frac{R_{dry}}{R_{vap}} R_{vap} e_{sat}(T))}, \tag{2.1}$$

$$e_{sat} = a_1 exp\Big\{a_3 \frac{T - T_0}{T - a_4}\Big\}, \tag{2.2}$$

Where T $\rightarrow$ T_{dew} is substituted by the dewpoint temperature. Constants are: (a1 = 611.21 Pa, a3 = 17.502 and a4 = 32.19 K) for saturation over water.

10-metres wind zonal and meridional components need to be rotated to be aligned with the cartesian grid axes. This was done by applying at each point a rotation on the plane, of an angle equal to the difference in longitude between the longitude of the point and the centre of the grid.

2.2.4 Ocean initial and lateral boundary conditions: GLORYS12V1

To initialise the ocean state and to provide lateral open boundary conditions where the regional domain connects with the open ocean, we chose the reanalysis GLORYS12V1 (Lellouche et al., 2021). Its performance for the representation of several diagnostics, such as upper ocean heat and salt content (0-1500 m), seasonal cycle of

salinity, temperature, sea ice extension, mixed layer depth transport in the Antarctic Circumpolar Current, documented for the earlier version GLRYS2V4 in the Southern Ocean was among the highest (Uotila et al., 2019; Lellouche et al., 2021). GLORYS12 well reproduces the low-frequency variability (interannual and long-term variability) of the sea ice extent both in the Arctic and Antarctic Oceans, thanks to sea-ice data assimilation. Biases of GLORYS12V1 in temperature and salinity decrease after the start of the ARGO initiative, from 0.75 °C and 0.2 psu before to 0.45°C and 0.1 psu after, in the 0-2000 m layer. The reanalysis is provided on a high-resolution horizontal grid of 0.083°x 0.083°(1/12°x 1/12 with 75 vertical levels. This ocean reanalysis is a product of the Copernicus Marine Environment Monitoring Service (CMEMS) and is an open-access dataset. We interpolate monthly fields of 3D temperature, salinity, horizontal velocities, as well as sea-ice concentration, sea-ice thickness and sea-ice drift on the MITgcm Ross Sea grid. The vertical levels of the reanalysis are linearly interpolated on the MITgcm vertical levels. Since the reanalysis does not include any data within the Ross Ice Shelf cavity, and because of the paucity of oceanographic data in this region, the ocean fields are extrapolated to fill the sub-ice shelf cavity and the entire domain up to the coastlines.

2.3 Results

The simulated water masses and circulation are compared to available observations: moorings, CTDs and XBTs. The mooring instruments of the MORSea observatory (moorings F, H1, H3, G, Figure 2.1) provide timeseries of water masses properties and velocity at fixed locations and depths at fine time resolution (between 5 and 60 minutes): Seabird-CAT measure temperature and salinity (thermosalinographs); RCM currentometer measure currents velocities, but they also have a temperature sensor. We chose to consider for the analysis mostly bottom water masses as they more likely show variability associated with climatic conditions and less meteorological fluctuations. For mooring F, a middle depth of ∼400m was chosen, coincident with the typical depth at which we find warm inflows of mCDW/mSW and outflows of ISW. The time series of observations are complemented by two sections along the RIS front, made in 1995 during the CLIMA project cruise and in 2017 during the 33rd PNRA campaign OGS Explora. Sections of averaged simulated water properties were also reported in Figure 2.5 to illustrate the vertical structure along the major troughs (sections location in Figure 2.2f). Overview of mean water masses properties is shown in Figure 2.3). Typical sea ice conditions are highlighted in Figure 2.4, where thin ice in winter is indicative of katabatic winds, polynya activity, and new ice formation.

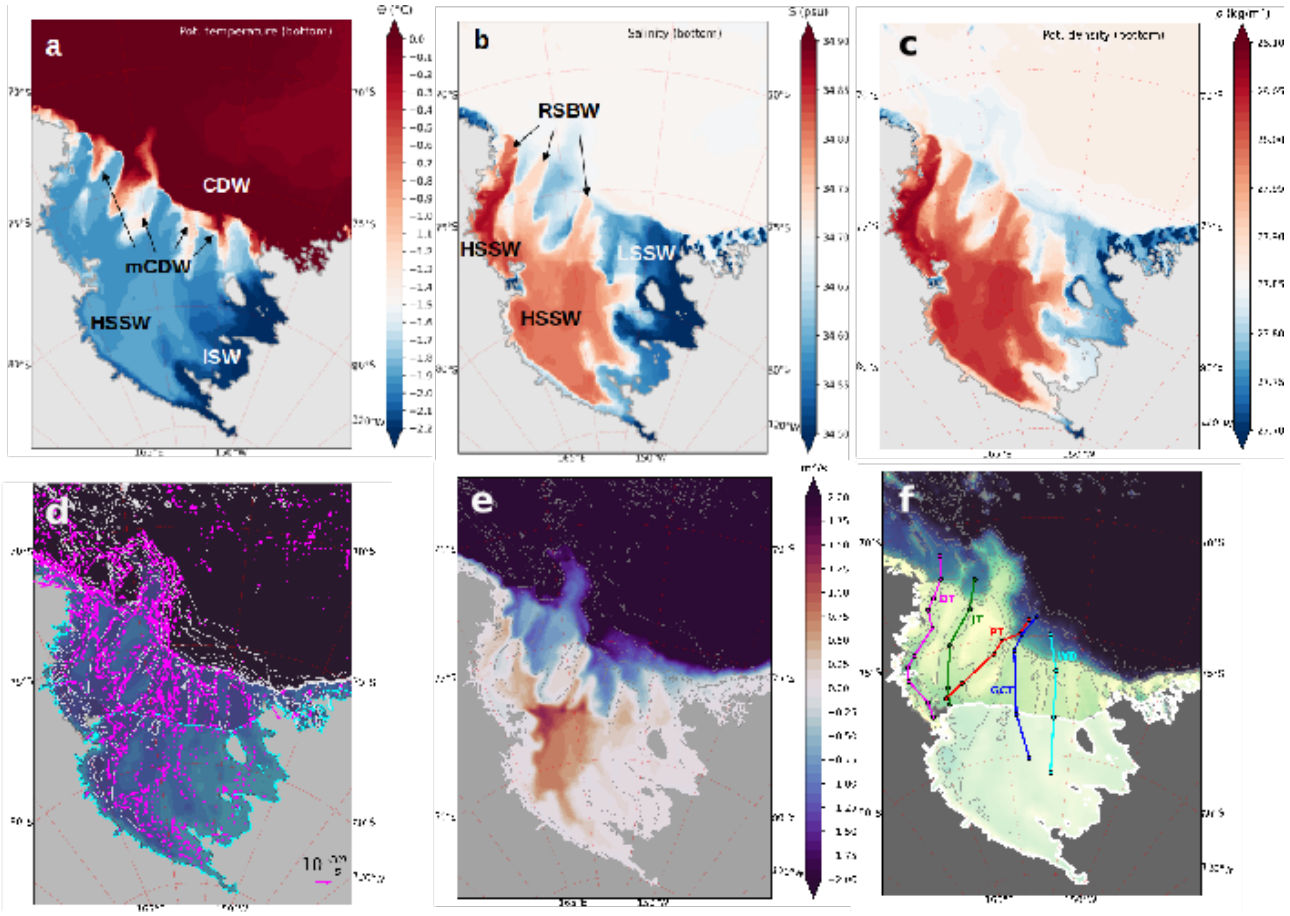

Figure 2.2: simulated bottom layer fields averaged over 1993-2018: (a) Potential temperature Θ (°C); (b) Salinity (psu); (c) Potential density (kg/m^3); (d) Bottom currents (>1 cm/s, cyan line indicates ice shelf margins); (e) barotropic stream function; (f) locations of transects for the vertical sections shown in Figures 2.5

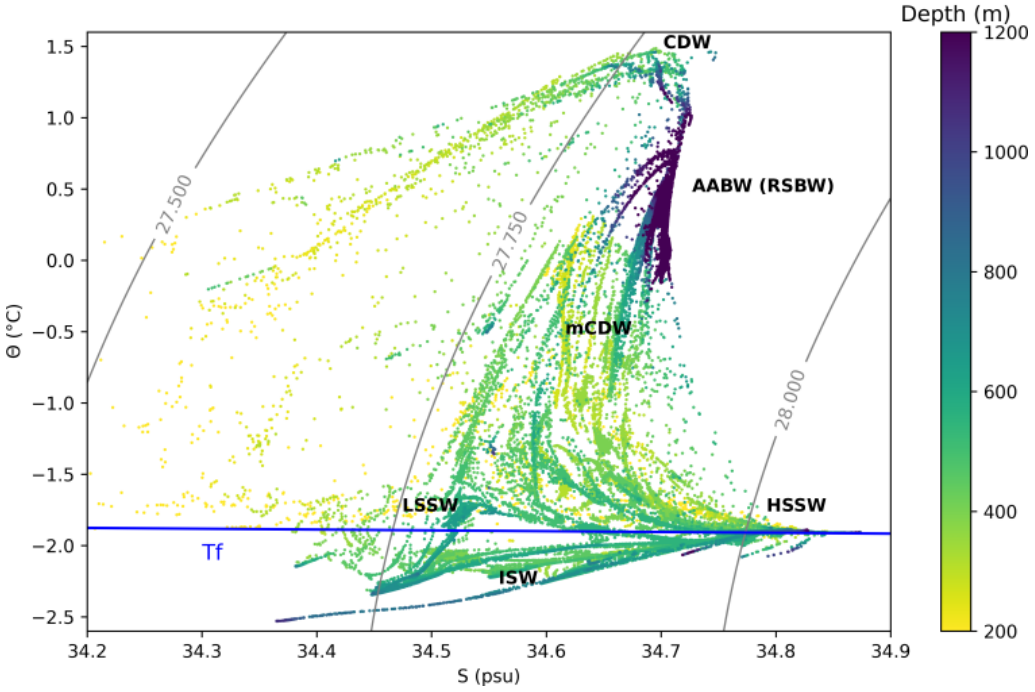

Figure 2.3: ΘS diagram of bottom water masses for the entire model domain. Main water masses are labelled: Circumpolar Deep Water (CDW), Antarctic Bottom Water (AABW), Low/High Salinity Shelf Water (LSSW,HSSW), Ice Shelf Water (ISW), Ross Sea Bottom Water (RSBW). Isopycnals of potential density are added as grey contours.

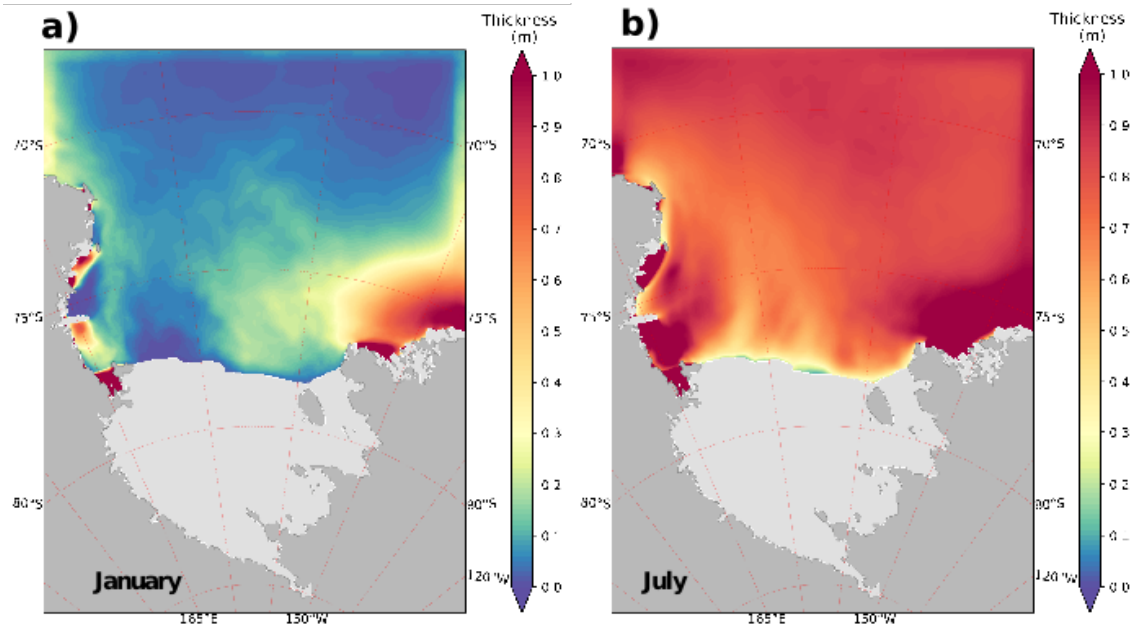

Figure 2.4: (a) summer and (b) winter simulated sea ice thickness (climatological mean 1993-2018). Patches of fast-ice remain during summer, but an ice-free corridor is present. In winter, regions of thin ice highlight the presence of polynyas and sea ice formation.

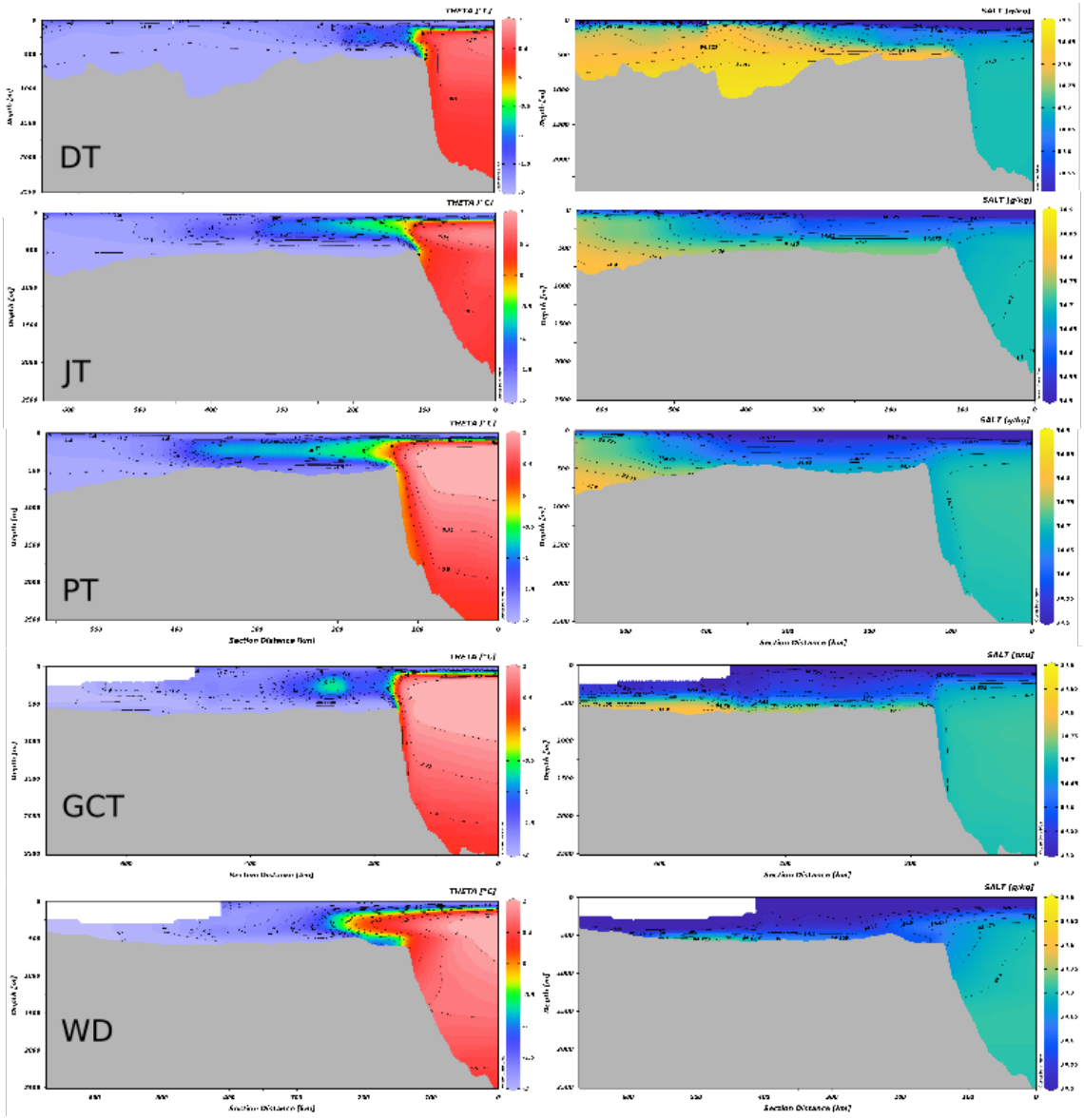

Figure 2.5: (left column) potential temperature and (right column) salinity section along the troughs defined in Figure 2.2f). Shown are yearly averages over the whole simulation period (1993-2018). Abbreviations are DT = Drygaslki Trough, JT = Joides Trough, PT = Pennel Trough, GCT = Glomar Challenger Trough, WD = Whales Deep (basin).

2.3.1 Continental slope

Bottom temperature, salinity and density (Figure 2.2a-c), show the locations of CDW intrusions along the continental shelf break over the prominent banks: Mawson, Pennel, Ross, Hayes and Houtz banks at and the eastern side of the troughs: Drygalski, Joides, Pennel and Glomar Challenger (Figure 2.1a). CDW is not present on the shelf in its undiluted form, but it modifies by mixing with SW and originating mCDW. Ross Sea Bottom Water (RSBW) is the name HSSW takes when it is near the shelf break and starts mixing with mCDW. It outflows at the Western side of major troughs, and is visible as streaks of high density water along the slope (Figure 2.2c). The exchanges at the shelf break are regulated by the ASF, which drives the ASC (jet-like current), visible also at bottom level (Figure 2.2d). Frontal features over banks and troughs are present, where waters of strong temperature and salinity contrast meet. These highly energetic outflows reach 0.4-0.55 m/s of monthly averaged velocities (Figure 2.2d) in the Drygalski and Glomar Challenger Troughs, respectively even though tidal forcing is not included in the model (cfr. Padman et al., 2009). Mooring H3 was placed on the continental slope, where the water column is 1200m deep, at the mouth of the Glomar Challenger Trough, one of the main pathways of exported RSBW, and intrusions of CDW (Bergamasco et al., 2002); it took measurements of temperature and current velocity between summer 2005 and summer 2008. Energetic outflows of RSBW and inflows of CDW are captured by the mooring in the daily bottom (∼1200m) temperature field, – minima and maxima respectively – and are also simulated by the model daily output at that location (Figure 2.6a); the two water masses cause a >1 °C fluctuation in the temperature from the Glomar Challenger Trough across the continental shelf break. Both the model and the mooring measures intense and highly variable currents, in particular the meridional components are between 20-80 cm/s (Figure 2.6b,c). Such fluctuations are indicative of strong eddying behaviour, and connected with variability of the ASC, that in part regulates these exchanges (Figure 1.9b). Mooring variability also includes the effect of tides, fostering slope currents at longer periods than tidal variability (Padman et al., 2009); tidal forcing was not included in the model. Inter monthly variability is visible in the timeseries, superimposed on stronger daily variability, Transects of averaged potential temperature and salinity (Figures 2.5) shows the cold and salty HSSW and RSBW and the warmer mCDW. They capture the stratification and the mixing process that occur at the shelf break, involving also lower salinity AASW (the first 50-150 metres in the water column). Notice that the “V-shaped” ASF, typical of the “cold” (and also “salty”) continental shelves, is visible in the Glomar Challenger Trough (GCT in Figure 2.5, and weakly visible in the Drygalski Trough, Joides Trough; the effect on the CDW intrusions is

to strongly mix them with SW. Notice also in the Whales Deep shelf break the ASF resembles more the "fresh" and "warm" continental shelf, and allows more CDW to arrive on the shelf.

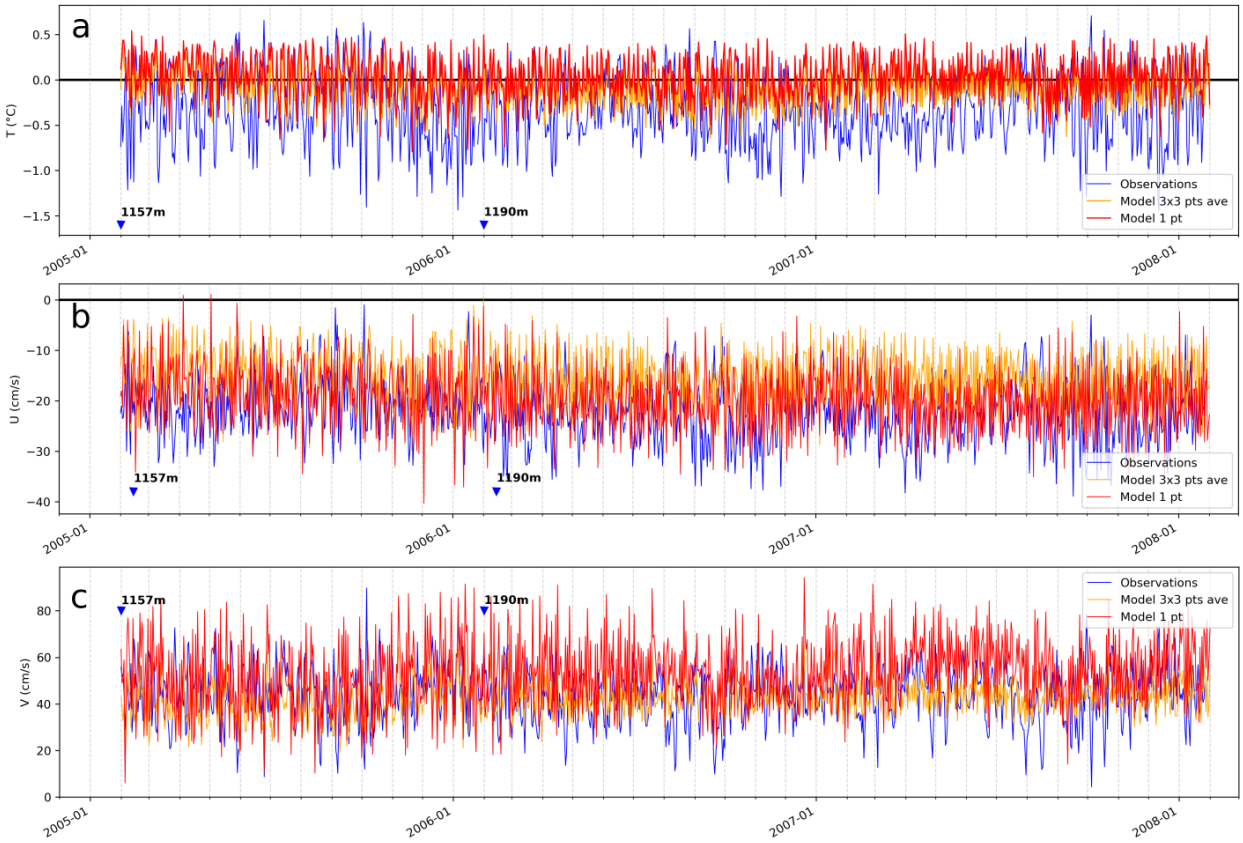

Figure 2.6: Data-model comparison at mooring H3, on the continental slope (see Figure 2.1a). Model (red, orange) vs observations (blue, 1157m depth, before 2006; 1190m depth, after 2006). (a) *In-situ* temperature, (b,c) zonal and meridional velocity. Velocities averaged over 3x3 grid points are masked over water depth equal or shallower than the instrument depth (∼1200m), to capture the shallower portion of the slope.

2.3.2 Continental shelf

The continental shelf of the Ross Sea is characterised by processes of sea ice formation in the West, of sea ice and meltater import in the East and exchanges water with the RIS cavity. In the Drygaslki Trough (Figure 2.1a) mooring G was deployed to measure outflowing HSSW (becoming RSBW) and inflowing mCDW from the slope. HSSW is produced in the Western Ross and in a polynya opening in front of the RIS, and is exported to most of the Western Ross Sea, Western half of the RIS cavity, and in the Glomar Challenger Trough, however the maximum presence is

in the Drygalski Basin and Trough (DT in Figure 2.5), as simulated by our model (Figure 2.2b). It took measurements of temperature between summer 2004–2014 (Figure 2.7b), with only a small 6 months gap in 2007; the measurements of salinity covered only three years, 2004-2007 (Figure 2 2.8b); velocity coverage was extremely patchy (Figure 2.8b,c). The mooring captured intrusions of warm mCDW at bottom, on a background of near-freezing temperature (Figure 2.8b). Warm temperature fluctuations had high amplitude until 2009, later became more subdued. The model is not able to capture these strong intradaily variability, which we can assert is because this region is strongly affected by tides (Bergamasco et al., 2004; Padman et al., 2009; Gordon et al., 2009), and only simulates the background -1.8 °C temperature with weak yearly variability. Measured salinity shows a distinct seasonal cycle, associated with sea ice production in the Drygaslki basin, during austral autumn and winter, and reaching mooring G with a lag (Figure 2.8c). Oscillations of 0.1 g/kg in salinity are observed. Model salinity reproduces partially this yearly cycle, but it shows a salty bias of ∼0.1 g/kg (Figure 2.8a,c). This bias may be inherited by GLORYS12V1, where it was documented after the implementation of the setup (Lellouche et al., 2021). Measured salinity lower than 34.7 indicates probably mixing with mCDW and AASW to form RSBW.

The Glomar Challenger Trough (Fig 2.1a) is the location where most of the water outflowing from the cavity is found. HSSW entering beneath the RIS from the West and mCDW/mSW and LSSW entering from the East are cooled and freshened. Two types of ISW are formed, a saltier form from HSSW, and a fresher form from mCDW/mSW outflowing at different depths (Jacobs et al., 1985; Bergamasco et al., 2002) into the Glomar Challenger Trough (Figure 2.2b,d; GCT in Figure 2.5). Mooring H1 was placed at this strategic location, and was active from 1995-2008. This mooring captured, at the bottom layer, the outflows of HSSW in the Glomar Challenger Trough, which is *supercooled* at about -1.9 °C, (0.1°C colder than in the Drygaslki trough, where it reaches the surface freezing point ∼-1.8°C), therefore could be classified as ISW; this water mass mixes with SW on the continental shelf slope (Figure 2.7; Figure 2.2a,b,d). This deep ISW is clearly seen in the vertical section, GCT in Figure 2.5 beneath the cavity at distance 600 km along the transect, and a second cold core, not *supercooled*, at the depth of the RIS draft, at ∼450 km along the transect. The yearly warming signal is probably caused by increased mCDW advection in summer, and by the generally weaker (more mixed) ISW produced by the model with respect to the observations. The ΘS plot show the bias in salinity as well as the warmer temperature of the bottom water (Figure 2.7a). Salinity matched well, except for a faster seasonal cycle in the model (Figure 2.7c). The mooring measured strong anomalies in salinity, and currents in autumn 2000; is likely the

result of a large tabular iceberg, B-15A, which detached from the RIS in summer 2000 and was advected oceanward over Glomar Challenger Trough (Arrigo et al., 2002). A second trunk, B-15B, was advected to the Western Ross Sea, but became stuck between Ross Island and a bank. Such features are difficult to model, and currently not implemented in the MITgcm.

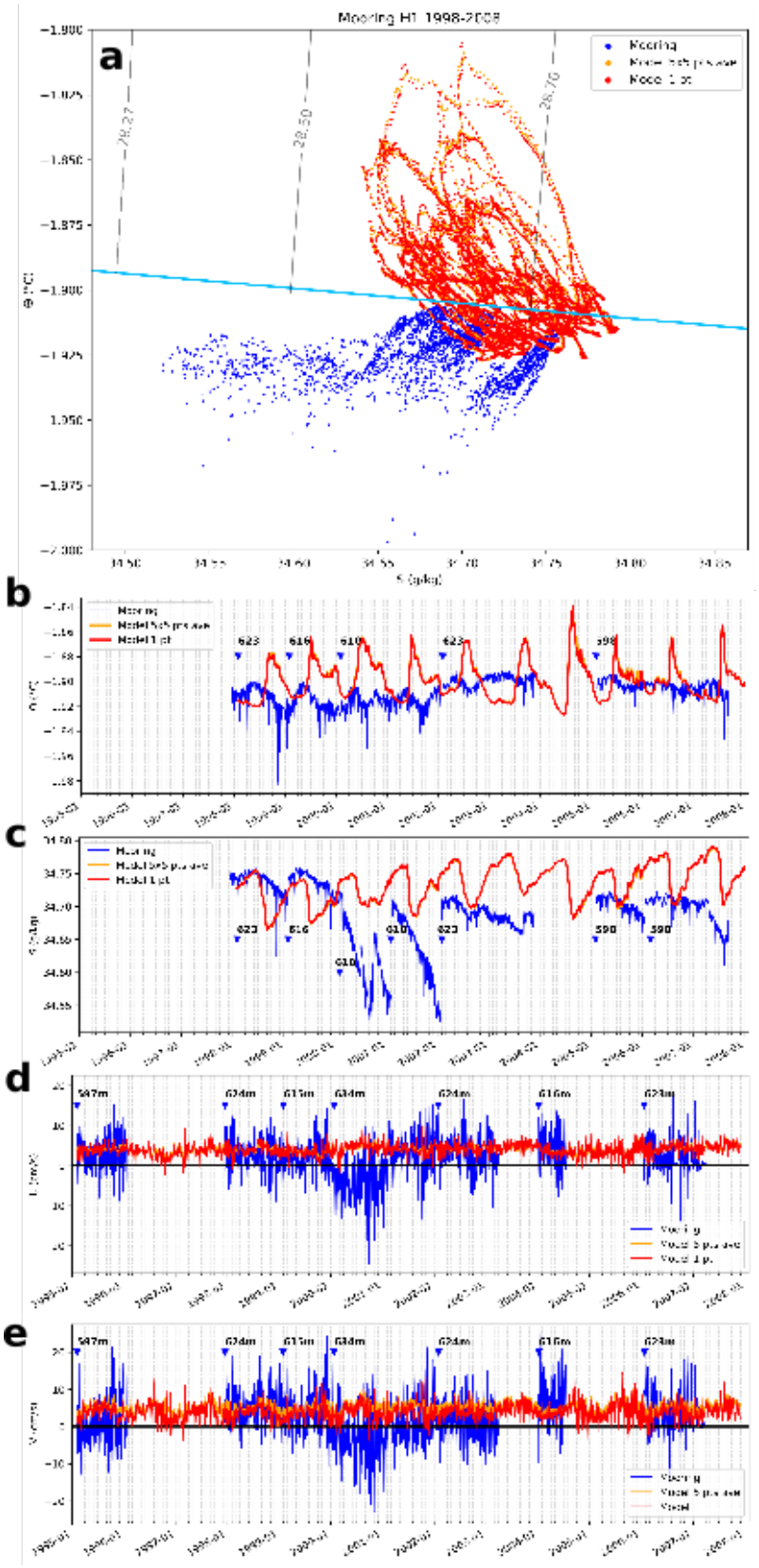

Figure 2.7: model (red) vs observations (blue) comparison at mooring H1 site in the Gomar Challenger Trough (Figure 2.1a). (a) ΘS plot, (b) potential temperature, (c) salinity, (d,e) zonal, meridional velocity.

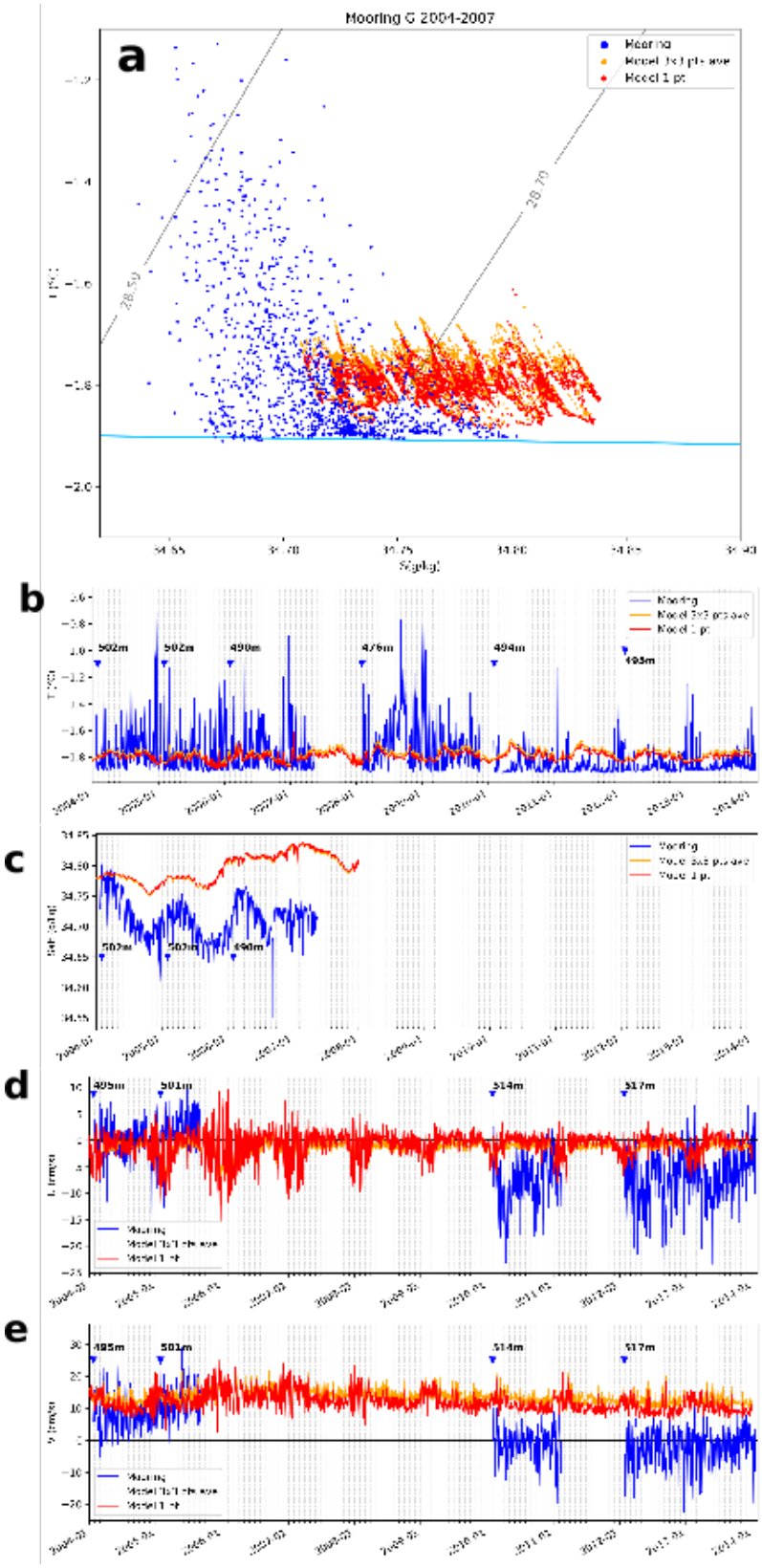

Figure 2.8: model (red) vs observations (blue, *in-situ* temperature SBE instrument) daily comparison at mooring G, in the Drygalski Trough (see Figure 2.1a). (a) TS plot, (b) temperature, (c) salinity, (d,e) zonal, meridional velocity.

2.3.3 The Ross Ice Shelf front and cavity

On the Western side of the RIS HSSW and AASW are advected beneath the RIS. Circulation flows in an anticyclonic cell in the West, driven by the lateral density gradient associated with the salinity gradient between HSSW and ambient ISW and LSSW, found in the Eastern side (cfr. Jendersie et al., 2018). ISW is *supercooled* water (T< T_f (p=p_{atm})), which means it has been cooled at depths (and pressures) greater than the surface, inside the cavity. ISW can also be found in plumes of very fresh and cold water (Figure 2.10a, 2.11c), if it does not undergo mixing (ISW plumes are not simulated by this model). HSSW may be also considered ISW, when colder than surface freezing point; however it is able to melt the ice shelf by the pressure dependence of the freezing point (cfr. Figure 3.3a,b,c). Water masses circulating beneath the RIS and causing melt acquire buoyancy as they are mixed with produced meltwater, and gradually shoal, returning to the open continental shelf. This vertical overturning is generally much weaker in "cold" cavities such as the RIS with respect to "warm" cavities, such as those in the Amundsen and Bellinghausen Seas.

In the Eastern continental shelf, CDW intrusions occur along ridges (Hayes Bank and Houtz Bank, Figure 2.1a, Figure 2.2a). CDW mixes with near-freezing SW on the continental shelf, becoming "modified" CDW (mCDW); on the other hand SW that mix with CDW or mCDW are warmer than original SW, and are named as well "modified" SW (mSW). mSW are warmer than SW (having T > -1.85 °C whereas SW have T < -1.85 °C, as defined in Orsi and Wiederwohl 2009) but still colder than mCDW ($-1.5 < T < 1.5$, Russo et al., 2011). This brings water even a few degrees warmer than the *in-situ* freezing point below the RIS (see Figure 3.3a-c). and melt the ice shelf in the first 150 km from the front.

Mooring F

This dynamics in the Eastern RIS front was observed by mooring F: this mooring was placed near the RIS central front (Figure 2.1a) to study the outflows of ISW, and was active in 1995-1998. It was moved in summer 1997 westward 25 km (to new location F') to better capture the ISW plumes. Seabed depth changed from 602m before 1997 to 698m after 1997. We compared output with measurements at depth ∼400m, chosen as depth of outflows and inflows of ISW and mSW respectively, the latter impacting basal melting near the RIS front. to better capture ISW outflows). The instruments were always set at a sampling frequency of 30 minutes.

Mooring F recorded data are shown in Figure 2.9: daily time series of potential temperature, salinity and current velocities and ΘS scatter plot, compared to the

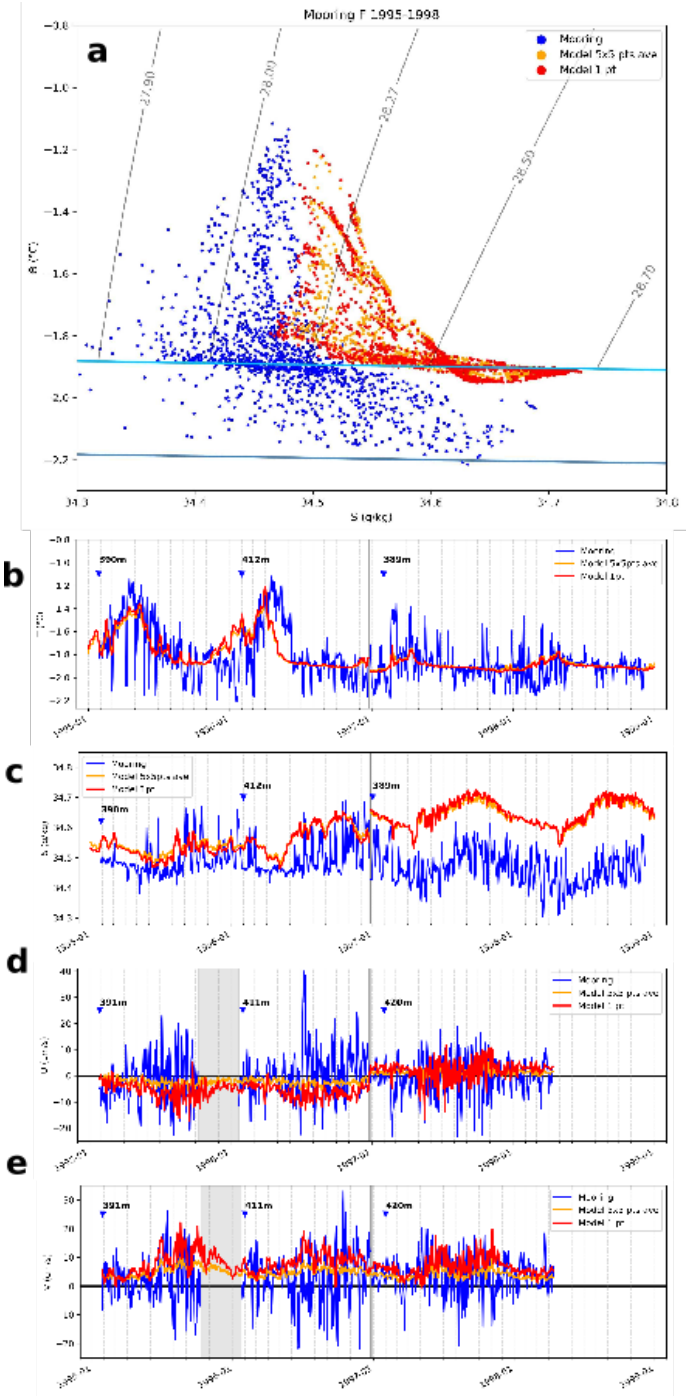

Figure 2.9: model (red) vs observations (blue) comparison at mooring F (390m depth in front of RIS). (a) ΘS plot, (b) potential temperature, (c) salinity, (d) zonal velocity, (e) meridional velocity. Pot. temperature was obtained by converting *in-situ* temperature by GSW (Gibbs Sea Water) routines. Notice the grey shaded region around summer 1996, where due to technical problems the currentometres stopped working, and the grey line in summer 1997, marking the displacement of the mooring to the new position F' (Figure 2.1a)

model daily output at the same location (which was updated with the mooring displacement in 1997). Model output was taken both at the exact grid point, corresponding to the mooring (red line) and averaged on a 5x5 grid points square (orange line). Model reproduces well the observations in temperature, without accounting for daily variability which are probably due to diurnal tides (not included in the numerical setup). In the pre-97 location mooring F measured inflows of mCDW/mSW with warm peaks of ∼1.2 °C, about 0.7°C higher than the surface freezing point, and ∼1°C higher than the *in-situ* freezing point. However the instrument also measures peaks of *supercooled* ISW, with strong daily variability, which are not well captured in the simulation: either they are not energetic enough and/or rapidly mixed with ambient water. Meridional velocity indicates constant outflow in the simulation whereas the instrument measures both energetic inflows and outflows. Zonal velocity is negative before 97 and positive afterwards reflecting the change of location and the relative change with respect to the RIS front. The simulated velocities are much smaller with respect to observations, partially due to missing diurnal tides which have been observed and modelled in the past to which produce strong jets along the RIS as topographically trapped vorticity waves, generated by the interaction of the basin-scale diurnal tidal Kelvin waves with steep bathymetry trapped to propagate along isolines of constant water column thickness, such as the continental slope and ice shelf front (MacAyeal, 1984b; Padman et al., 2003). The model may reproduce, howevere, partially trapped topographic Rossby waves, as already found in numerical models (MacAyeal, 1984a). Simulated salinity shows a salty bias of ∼0.1 g/kg, however the monthly variability is captured. The bias may be the result of generally slower simulated circulation on the continental shelf, as well as below the ice shelves, causing increased residence time of shelf waters, enabling in turn for increased salinity from winter-time brine rejection, but may also be inherited from the reanalysis GLORYS12V1, which has in the upper 2000 m a bias in temperature and salinity of +0.75 °C and ∼+0.2 g/kg. In the ARGO period (1999-2019) it is reduced to 0.45°C and 0.1 psu.

ΘS plot show the water masses properties at mooring F and F' in the period of activity. The salty bias is evident, as well as the missing simulated ISW plumes. The modelled water masses high salinity tail, reaches neutral density of $\gamma_n \simeq 28.70$ kg/m^3 and shows mixing with ISW (it is *supercooled*). Observed water masses have several measurements below surface freezing point (cyan line). A second darker-cyan line is the *in-situ* freezing point at 400m, showing the melting potential of nearly all water masses observed. Mixing with CDW is evident in the temperature maximum and the bell shape of the points in Figure 2.9a, lying in the range of $28.0 < \gamma_n < 28.27$ kg/m^3. Note that although there are inflows of mCDW/mSW along Hayes

Bank that are also captured in the temperature signal at the mooring location, at that location modelled velocities are always directed outward from the cavity, as intrusions occur farther East. Model overestimates mixing of ISW and does not capture the interdaily variability at the front. However the main water masses are found at the same locations where they have been observed at depth which are consistent as well. The agreement, considering the model limitation and the absence of tides, is good, since we are interested in calculating basal melting and not tracking the outflowing ISW.

Sections along RIS front

To further extend our comparison with direct observations at the front, model daily temperature, salinity and current velocities along the front were compared with direct observations from transects made during past cruises. Data from the 2017 33rd PNRA cruise and 1995 CLIMA project cruise were employed. In the former, XBTs were launched, which allowed the measurements of *in-situ* temperature; velocities were measured by vessel-mounted Acoustic Doppler Current Profilers (vmADCP). In 1995 CTD casts were made, which allowed the measurement of potential temperature and salinity.

Transect along RIS made in February 2017 (PNRA 2017 campaign OGS Explora) show *in-situ* temperature along the section measured by XBTs, compared with model daily output (Figure 2.10a,b), zonal and meridional velocity along the RIS measured by vmADCP, compared with daily output (Figure 2.12). Good match with location of mCDW/mSW intrusions and ISW outflows (mCDW/mSW at Central RIS observed in Jacobs et al. (1970, 1979); Jacobs and Giulivi (1999)). Simulated ISW outflows are less cold in model and less energetic. Velocities are underestimated in our model, probably because observed vmADCP take into account tidal components, strengthened along RIS; this indicates missing topographic Rossby waves generated by tides along RIS front (MacAyeal, 1984a). Temperature, Figure 2.10, are broadly consistent, however we highlight main differences: excessive temperature/volume of mCDW/mSW inflowing from Hayes Bank (obs. -1.6 °C vs model -1.2 °C. Some process connected with coarse model bathymetry, resolution and flow viscosity may be the cause of this modelled feature. Excessive warming is observed in the surface layer, and a sharp thermocline located at ∼130m, compared with observations with finer patterns of warmer and cooler waters, and a thermocline at ∼160m depth. Slow modelled flow at the front may induce weaker turbulence than reality and produce this warm surface layer. The model lacks a strong undiluted (T<-2.0 °C) ISW, however the locations of the outflows are consistent with observations.

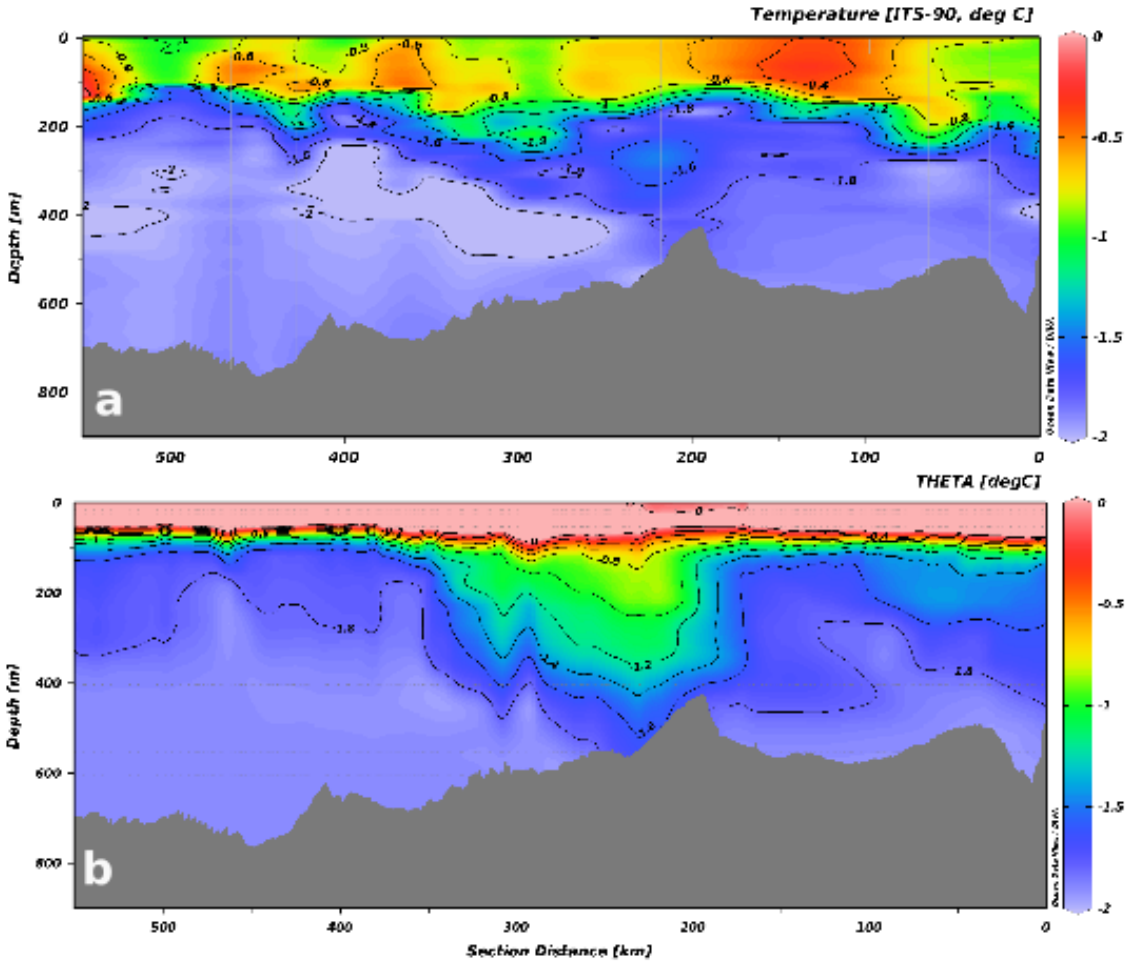

Figure 2.10: Temperature sections along the RIS front from XBTs measurements in summer 2017: (a) measurements by XBTs, (b) simulated. Note the sampling points visible as thin grey dotted lines: casts have high vertical resolution, coarse horizontal resolution; the opposite for simulated output.

Observations from the CLIMA project cruise (summer 1994 - 1995) (Figure 2.11) allowed comparison of salinity and calculation of potential temperature, however no velocity measurements were taken. agreement with salinity is very good, especially at intermediate depth and Western of Hayes Bank, where HSSW is predominant. Higher salinity is simulated in the bottom layer in the Eastern part of the section as well (first 100 km), which may represent expanded HSSW in the Eastern cavity in the model. Along Hayes Bank excessively warm MmW/mCDW is found (model -0.8 °C vs obs. -1.4 °C). Western of Hayes Bank the observed plume of ISW is found in the model with subdued temperature extremes. Surface layer temperature and salinity are similar, except for cooler temperature in the first 200 km of the transect.

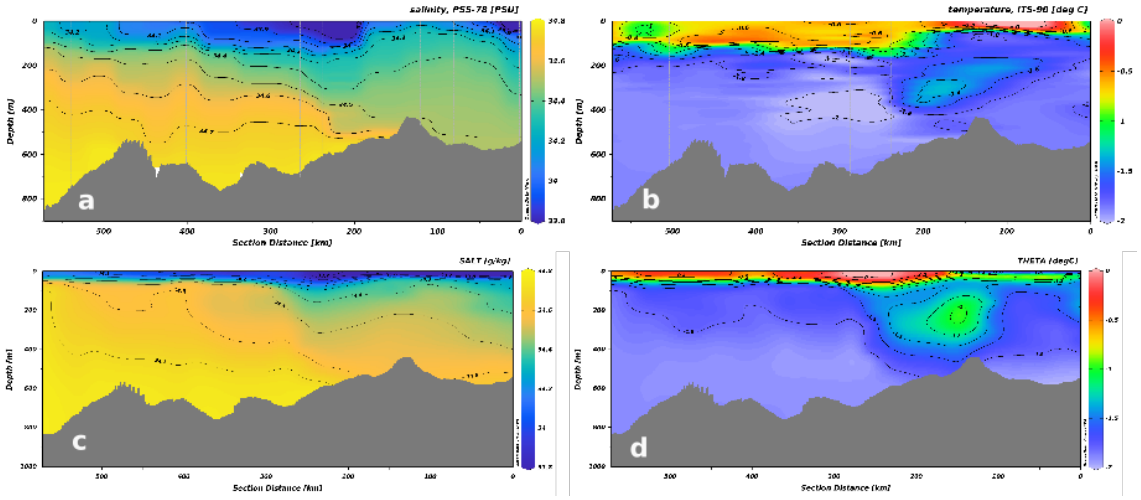

Figure 2.11: CTD measurements of salinity (a) and temperature (b) in a section along the RIS front (22/01/1995 to 25/01/1995). Same simulated quantities in (c) and (d) extracted from daily output of 23/01/1995.

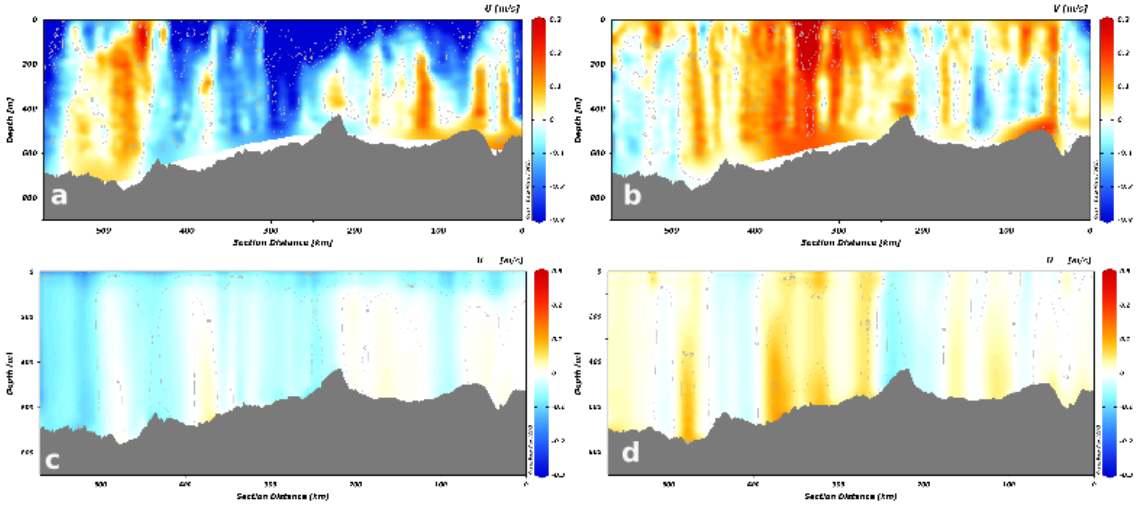

Figure 2.12: velocity measurements along RIS front (vessel mounted acoustic doppler current profiler vmADCP, 2017 PNRA expedition) Zonal (a) and meridional (b) measured velocity (m/s), and in (c,d) the same quantities simulated.

This may be related to more expanded sea ice in the model, advected by the AACC from the Amundsen Sea to the Eastern Ross Sea.

2.3.4 Impact of teleconnections on water masses variability

Extended time series of model output at mooring F,F' location (Figure 2.1) shows a long-term oscillation in salinity and strong interannual oscillation in temperature (Figure 2.13). Figure 2.14 shows bottom temperature, salinity, and velocities averaged in the WesternEastern continental shelf troughs and banks, and inside the RIS cavity. Strong interannual temperature variability is observed in all the continental shelf bottom waters, but the amplitude is higher in the Eastern continental shelf (Figure 2.14a). The salinity long-term oscillation in Figures 2.13b, 2.14b may be related to changing long-term sea ice conditions or long-term changes in katabatic wind, and are observed over all the continental shelf. In Eastern troughs, a seasonal signal may be related to the seasonal variability of the outflows out of the RIS cavity. Meridional currents averaged on the bottom layer follow the same oscillations as the temperature, and are also simulated inside the cavity (Figure 2.14c,d). Zonal velocity is instead more variable on the Eastern continental shelf. These may be related to teleconnections interfering with the ASL and the SAM, impacting intrusions of CDW on the shelf. We analysed indices of the SOI, relative to ENSO, the SAM, the ASL longitude and pressure anomaly (Figure 2.15) to highlight possible correlations. Moorings, whose recording time is patchy, although useful for model validation, are not particularly valuable to extract trend and long-term oscillations. We did not find a significant correlation with the said climatic index alone, suggesting that more modes can be impacting on different time scales at different places, therefore hidering analysis.

2.4 Discussion

2.4.1 Impact of tides

Tides are shown, in general, to greatly affect the cavity exchanges with the shelf, especially in the Weddel Sea (Richter et al., 2020). This depends on the particular amphidromic system's location with respect to the slope and shelf. In the Ross Sea, results from Whole Antarctic Ocean Model (WAOM, Richter et al., 2020) show that the difference is very small for the Western RIS (part of the EAIS), whereas it accounts for about 30% increase in the Eastern RIS (part of the WAIS), close to the grounding line. Modelling work by Arzeno et al. (2014) show a 30% increase as well, but confined to the frontal region (mode 2 and 3). From these two studies, it appears

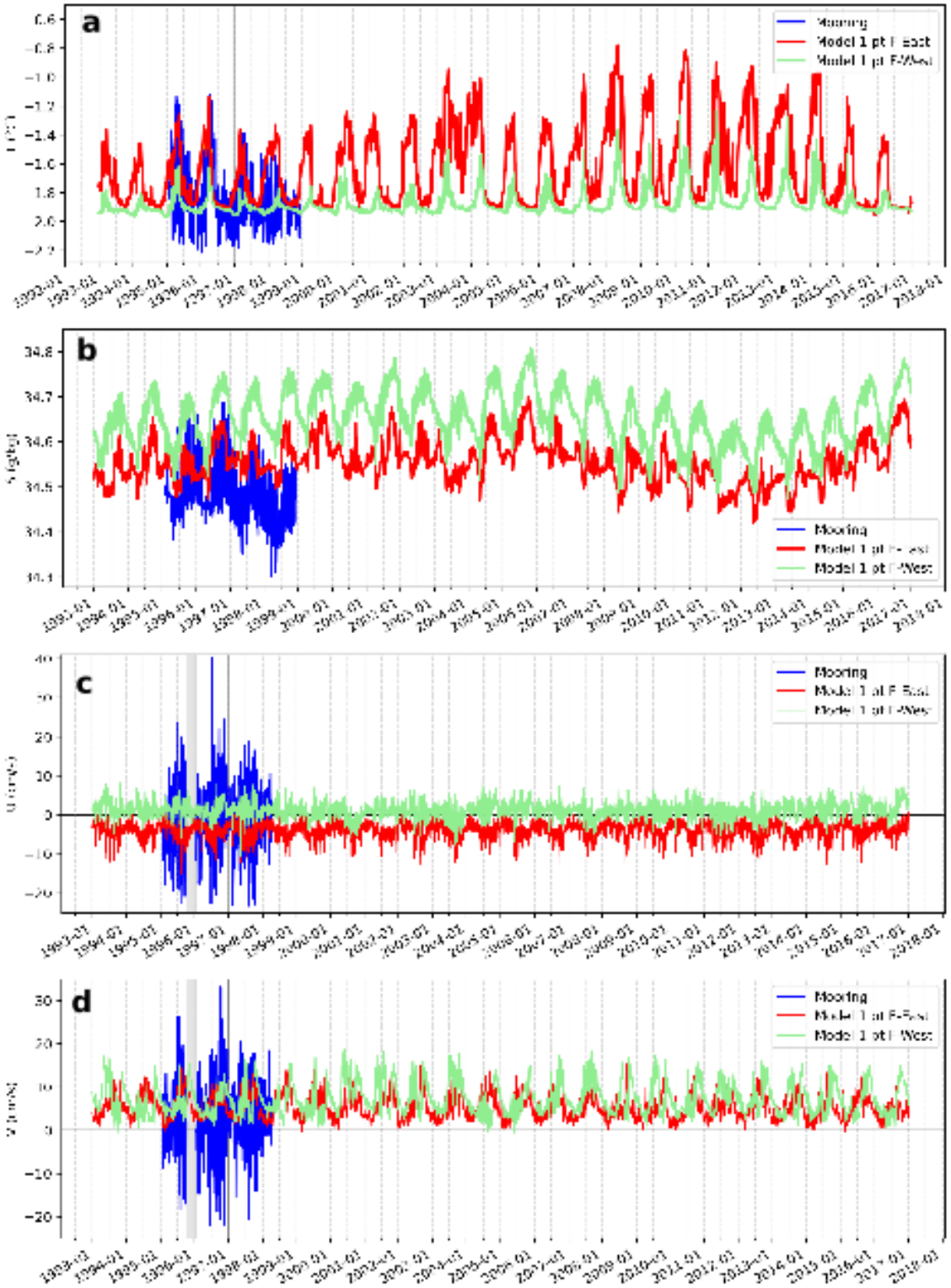

Figure 2.13: extended synthetic time series of model output extracted at mooring F (F-East) and F' (F-West). (a) temperature (°C), (b) salinity (g/kg), (c,d) zonal and meridional velocities (cm/s) showing a long-term oscillation in salinity, and a strong interannual variability of temperature. Velocities do not undergo strong variability, except for a strong seasonal cycle.

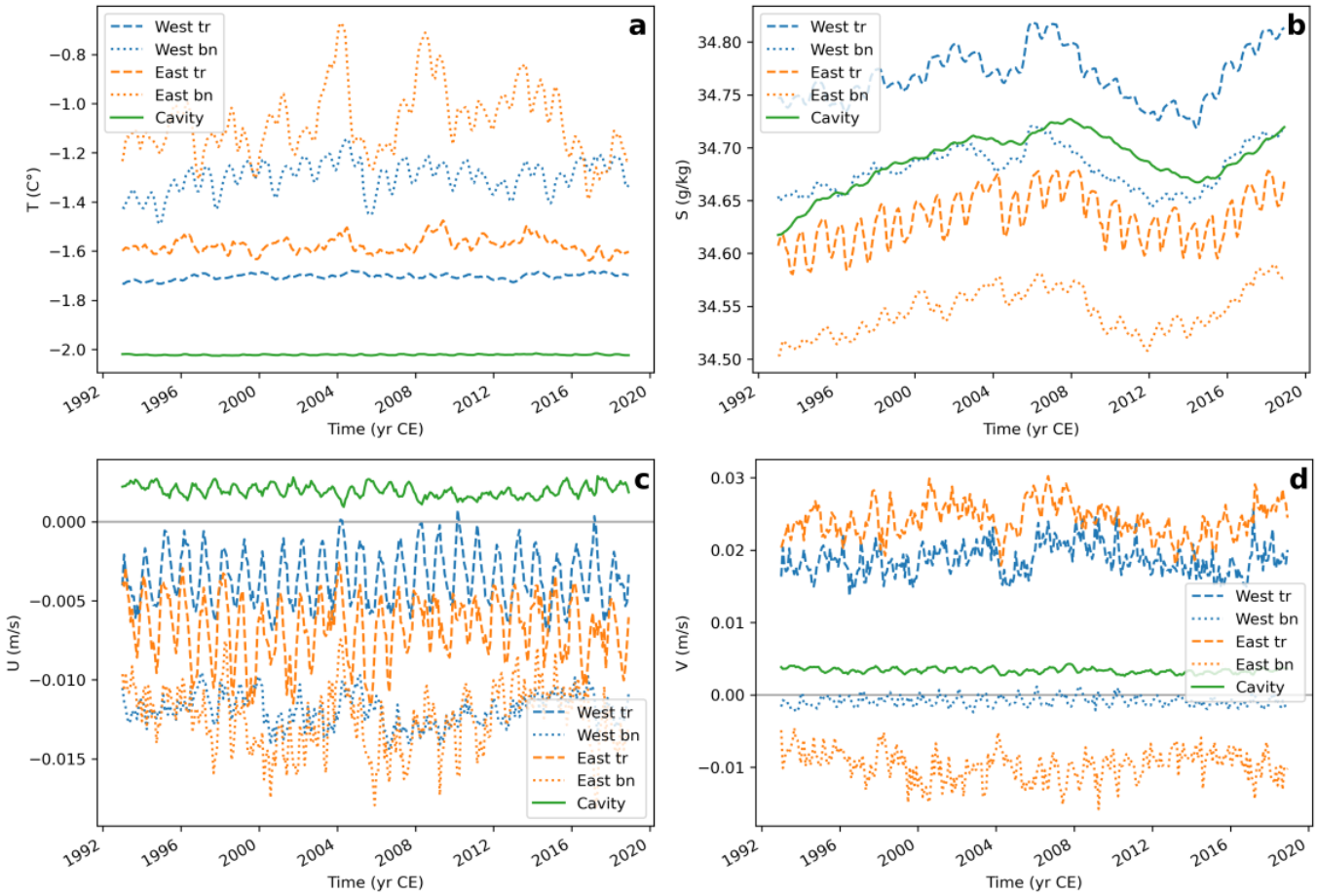

Figure 2.14: timeseries of averaged values of the bottom water in the Western/Eastern continental shelf (blue/orange) and beneath the RIS cavity (green). The dashed line indicates the troughs (depth >500 metres), whereas the dotted line indicates the banks (depth <500 metres). (a) Temperature; (b) salinity; (c,d) zonal and meridional velocity. Calculations are based on the masks defined in Figure 4.17

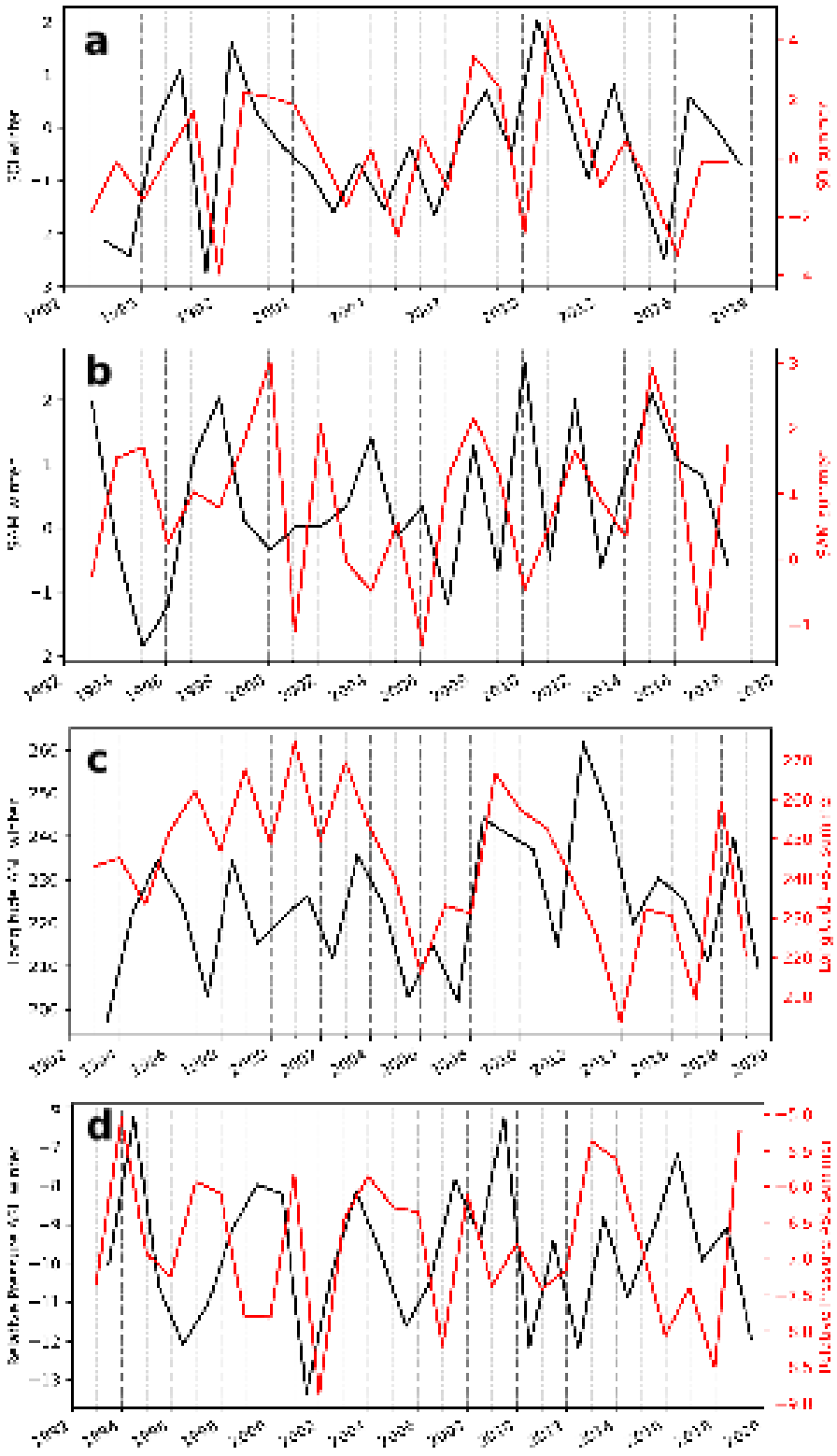

Figure 2.15: Indices of modes of climate variability extractred for austral winter, (JJA, black) and austral summer (DJF, red), between 1992 and 2019: (a) Southern Oscillation Index (SOI) related to the impact ENSO has on the atmospheric pressure; (b) Southern Annular Mode; (c) longitude of the ASL (°E); (d) relative pressure of the ASL (hPa).

that the impact of tides on basal melt is twofold: it can enhance the across-front exchange at RIS or increase mixing and energise the otherwise stagnant circulation in the inner Eastern RIS. Comparing this study melt rates with WAOM, the values for the RIS are quite similar: 78 vs 66.9 Gt/yr. Tidal forcing is a possible (missing) driver of AASW across the RIS front (Jacobs et al., 1992).

2.4.2 Impact of model resolution

The resolution of 5 km only allows for the largest eddies generated at the continental slope. Due to strong stratification and small Rossby deformation radius, it is particularly difficult to obtain a eddy-resolving simulation of the Antarctic Seas. The (baroclinic) Rossby radius of deformation (Ro) gives an order of magnitude of the eddies that arise by turbulence, and it depends on: water column stratification N; water column depth H; Coriolis parameter f (Equation 2.3).

$$Ro = \frac{c_n}{f}, \qquad c_n = (n \cdot \pi)^{-1} \int_0^H N dz, \tag{2.3}$$

Figure 2.16 shows the Rossby radius for typical summer and winter conditions: it is evident that 5km is not eddy-resolving even in summer, when stratification is higher, and $Ro = 3.5$ km. In winter, weak stratification makes it even more difficult to obtain high resolution, $Ro = 2$ km and smaller in regions of deep convection caused by sea ice production. Interestingly beneath the RIS cavity, and in particular near the grounding line in Siple Coast the Rossby radius is smaller than 500m. This poses limits to modelling studies, as it requires relatively large setup to cover the RIS with a grid more resolved than 500m. However numerical studies at 1 km in the Ross Sea with ROMS, (Mack et al., 2019) highlighted the insensitivity of basal melting to a twofold increase in eddy activity, which hints that not resolving eddies is not critical to simulate basal melting modes beneath the RIS.

2.4.3 Impact of atmospheric and oceanic forcing

ERA5 is a reasonable at reproducing Antarctic climate and its variability (Zhu et al., 2021). Atmospheric forcing captures the variability associated with winter-summer shift in the wind system and the ASL, and also captures some katabatic wind intensification across the TAM, although extremely short-lived events are damped. The wind forcing is particularly important in the Ross Sea as, together with the ice shelves geometry and coastline shape, determines the occurrence of polynyas, whose locations are well captured. GLORYS12V1 shows a salty and warm bias, documented after the implementation of the boundary conditions (Lellouche et al., 2021), that may partially impact the results of our simulations. The salty bias observed in the

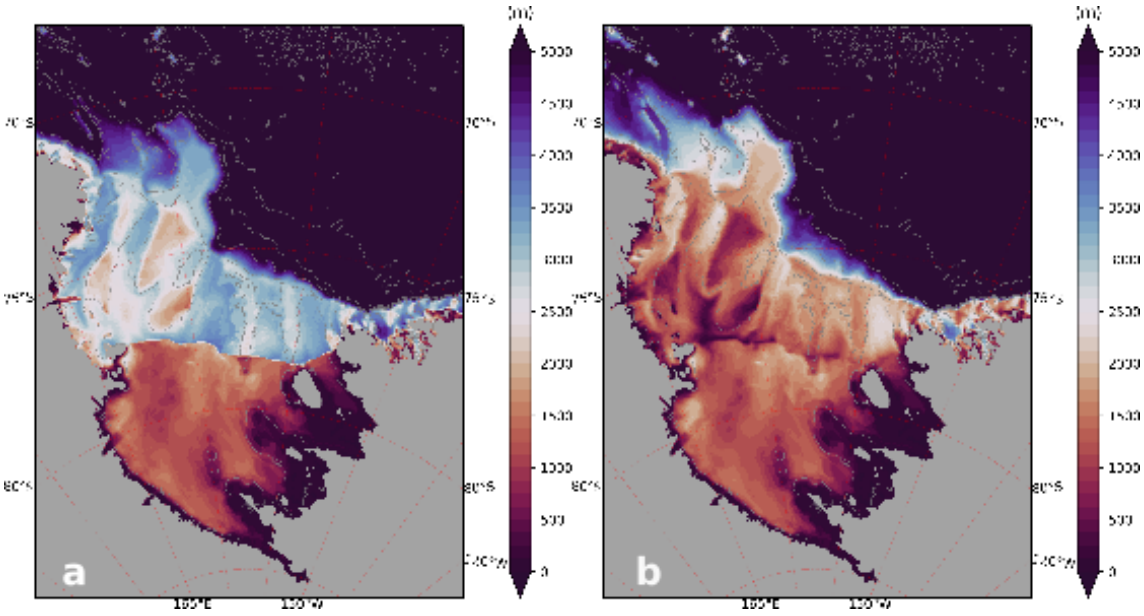

Figure 2.16: Rossby deformation radius (first baroclinic mode) in: (a) January, (b) August. Show are climatological mean based on the whole model simulation (1993-2018).

simulations may be related to the salty bias of GLORYS12V1, and the same can be said for the warmer than observed intrusions of mCDW along Eastern Ross Sea banks. The higher GLORYS12V1 open ocean salinity and warmer subsurface to deep layer can also cause changes in the ASF in the Eastern Ross Sea, making it less effective at regulating across slope exchanges (as "warm"-shelf ASF, Figure 1.9c). In addition to boundary conditions, random events such as iceberg calving and advection, which are not implemented in the MITgcm, could alter considerably the ocean properties, by deviating currents causing freshwater released at depth, and providing temporary barriers for unusual polynyas formation. This, in reality, may impact ocean circulation and sea ice, in turn affecting basal melting.

2.4.4 Direct observations below the cavity

Scarce and temporally limited direct observations exist for the sub-RIS environment, that do not allow for robust comparison with ocean model output. At site HWD-2 in the pathway of HSSW, Stevens et al. (2020) observed a stratification compatible with our modelled fields: ISW near the draft in a thin ice-ocean mixed boundary layer, a stratified layer underneath and a mixed layer of warmer and saltier HSSW at the bottom. The same was observed in early measurements at site J9, closer to the grounding line, still on the pathway of HSSW; mixing there was hypothesised to be due to tidal stirring of the water column (Jacobs et al., 1979; Foster, 1983). At sites CH1,2, borehole CTD casts highlighted the same water masses distribution (Arzeno

et al., 2014). Moorings were also deployed, covering the period 24 November 2010 to 22 January 2011 at the same sites, but recorded only small variations of water masses properties, <0.3 °C around the mean, near-freezing temperature and salinity fluctuations of 0.2 psu, suggesting freshening due to thicknening and advection of the AASW layer, that however was still cold.

2.4.5 Impact on basal melting

We showed main simulated water masses at key points for ocean circulation and compared them with available observations. Since we want to apply the model to study basal melting we consider how the model-observations comparison may impact on the accuracy. Excessive mSW/mCDW may cause overrepresentation of mode 2 melting, although mooring F indicates that warm mCDW frequently reached such location, therefore the mismatch with CTDs and XBTs may be the result of lack of synchronicity between the simulated and the observed intrusions. Excessive surface layer warming may impact mode 3, AASW intruding below the ice shelf; however given the thickness of the ice shelf (Figure 2.1b) greater almost everywhere than the thermocline depth, except in Ross Island its impact is probably limited. Circulation only advects AASW near Ross Island, where the cruise didn't reach. Salinity accordance suggests that mode 1 melting (HSSW), which is thought to be the most important contributor to melting, is well represented in the model. Weak ISW signal is a normal feature of the basal meltwater flux implementation in the MITgcm, meltwater is immediately mixed with ambient water of the uppermost wet cell in contact with the ice shelf.

2.5 Conclusions

We simulated the transient evolution of the Ross Sea water masses over 1993-2018 using a regional implementation of the MITgcm, that includes the RIS cavity and thermodynamical interaction with it. The model was able to reproduce main water masses characteristics and pathways, and a realistic seasonal cycle of sea ice. The simulated water masses at bottom show good agreement with mooring instrument measurements, over the years of activity of the mooring, and show reasonable agreement with CTDs and XBTs from along the RIS front. Stronger presence of mCDW/mSW than what is observed along the RIS may induce an overrepresentation of Mode 2 in basal melting. Weakened ISW signal is also a probable impact of model resolution and of the melting ice shelf implementation, which adds an already mixed freshwater flux to the mixed layer. The model is capable of simulating across slope transport of mCDW and export of RSBW, although it is not able to generate high

intensity cascading of AABW, probably due to coarse vertical resolution on the slope and due to weaker than real across-slope exchange due to missing tides. The missing tides are a likely cause of the subdued velocities observed along the RIS with respect to the instantaneous measurements, and the possible weak RSBW export. The stratification beneath the cavity is realistic and matches well with other model studies (Jendersie et al., 2018; Mack et al., 2019), and the scarce observations by hot-water drilling at J9, HWD-2 and CH1,2. Teleconnections impact on Ross Sea oceanography is difficult to find probably for their interconnected impact on water masses.

Results show that the model is a reasonable approximation of the processes we are interested in, and can be applied with confidence to study the RIS basal melting (Chapter 3). It can also be applied to study Ross Seas oceanography evolution during past periods, such as the Last Deglaciation (Chapter 4).

Chapter 3

Spatio-temporal variability of Ross Ice Shelf basal melting

3.1 Introduction

It has been shown, over the last decades, that ocean warming reaching the ice shelves on the margins of the Antarctic ice sheet is causing a decisive thinning and retreat at several locations (Pritchard et al., 2012). Many of those ice shelves are located in regions where the bedrock lies below sea level, and are therefore reported as "marine-based", and it has retrograde sloping, that is, becomes deeper towards the interior of the continent. These regions are subject to intrinsic Marine Ice-Sheet Instability (MISI, Schoof, 2007), a process that increases exponentially ice discharge if the buttressing effect of the ice shelves is removed. Such a process has been observed to be potentially on-going in the fast melting regions of Antarctica (Joughin et al., 2014) and there is confidence that occurred in past warm periods (Bart et al., 2018). Such processes, currently under specific analysis , are still not included in the most recent 2019 IPCC report, and are among the causes of uncertainties in sea level projections (Siegert et al., 2020).

Measurements of basal melting can be achieved by several methods. Indirect observations: involve modelling surface mass balance, measuring surface velocity and ice topography measurements from satellite and ice discharge across the grounding line; the result is a Pan-Antarctic map of averaged basal melting (Figure 3.1a, Rignot et al. 2013). Basal melting is calculated as a residual term in the equations, and has a high uncertainty, particularly where yearly averaged melting is low. In fact, unknown bedrock topography and the necessary inversion of observed surface velocities to infer ice column fluxes calculations hampers the accuracy of the estimate.

Other methods include oceanographic-based estimates: ocean properties are measured near an ice shelf front and either by numerical modelling (Jacobs et al., 2011) or by tracers measurements (Jenkins and Jacobs, 2008) basal melting is calculated. These measurements can be long; e.g. Foldvik et al. (2001) estimated one year of basal melting of the Ronne Ice Shelf, but are still relying on extrapolation of water masses and currents. Direct measurements of ice thinning are scarce: e.g. Arzeno et al. (2014) measured directly by hot-water drilling, ice column thinning at a frontal location of the RIS, where high melting occurs. This kind of method obviously yields great accuracy, but is extremely limited in time and space, therefore it is obviously not applicable to the whole Antarctic ice sheet.

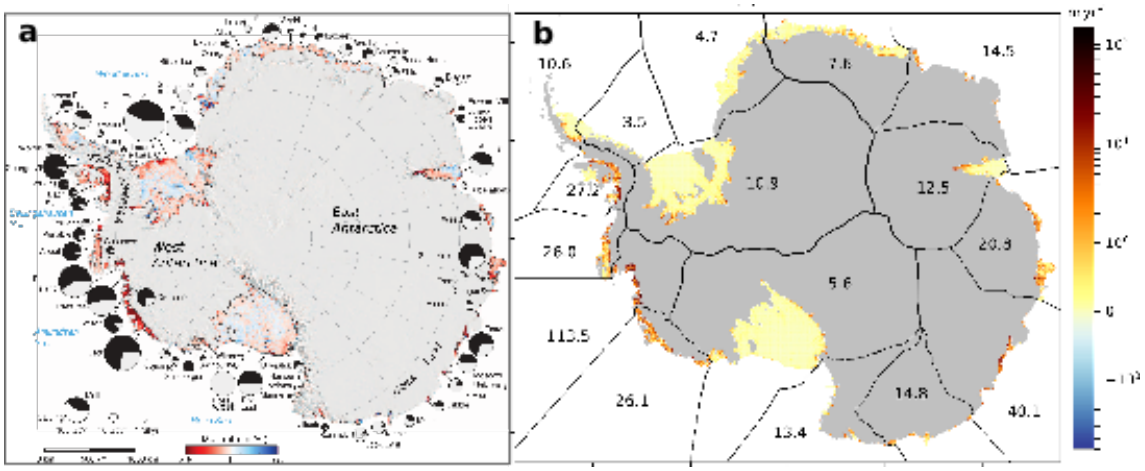

Figure 3.1: (a) observed basal melting rates from Rignot et al. (2013); simulated basal melting rates from ISMIP6 (Jourdain et al., 2020) with their non-local calibration based on observed mean Antarctic melting rates.

On the RIS several estimates of basal melting are available, obtained by indirect observations, direct observations and modelling, reportated in Table (3.1).

Basal melting can be simulated, alternatively, by employing parameterisations calibrated on other observations. The most theoretically sound calibration has been made in the ISMIP6 (Figure 3.1b, Favier et al., 2019; Jourdain et al., 2020), based on the observations by Rignot et al. (2013). In the calibration they made large use of statistical sampling of the observations, and extrapolation of ocean properties from the ocean to beneath the ice shelves. This clearly does not take into account the spatial variability of basal melting, strongly associated with ocean currents. In literature, three modes of melting are usually considered (Figure 1.10, see Chapter 1.5, and Jacobs et al., 1992; Dinniman et al., 2016): melting by HSSW, highly saline,

Study	Basal melt (Gt/yr)	Freshwater flux w_b (cm/yr)
This study	78.7 ± 13.3	18.3 ± 3
Richter et al. (2020)	69.1	15
Mack et al. (2019)	102.0	21.4 ± 0.9
Naughten et al. (2018) MetROMS	53.8	12
Naughten et al. (2018) FESOM HR	112	24
Dinniman et al. (2015)	66.7	14 ± 6
Arzeno et al. (2014)	138	25 (no tides) / 32 (tides)
Kusahara and Hasumi (2013)	110.7	N.a.
Timmermann et al. (2012)	260	N.a.
Dinniman et al. (2011)	72.9	15.3
Adusumilli et al. (2020)	80 ± 82	26 ± 27
Moholdt et al. (2014)	50	N.a
Depoorter et al. (2013)	34 ± 25	8 ± 6
Rignot et al. (2013)	48 ± 24	10 ± 7

Table 3.1: Values of integrated (Gt/yr) and averaged (cm/yr) basal melting found in literature: the first section are valued obtained with modelling, the second section are indirect observations.

therefore dense, and cold (Figure 1.10a); this is the melting near the grounding line of the "cold" cavities such as the RIS. Melting by CDW, usually found in the "warm" cavities, and in the "modified" form (mixed with SW), mCDW, in the Ross Sea. Finally AASW, usually associated with polynyas heating. In the Ross Sea, due to a complex oceanographic background, several water masses are advected beneath the RIS cavity, causing melting. Understanding how much melting is caused by each water mass can provide insight into what climatic processes cause melting.

3.2 Methods

3.2.1 Three-equation formulation of basal melting

This approach to calculate basal melting as described in Hellmer and Olbers (1989); Holland and Jenkins (1999) consists of (Figure 3.2):

1. an estimation of the *in-situ* freezing point of water at the ice-ocean interface;
2. a balance of the heat flux at the ice shelf-ocean boundary;
3. a balance of salinity flux (virtual meltwater flux) at the ice shelf-ocean boundary.

The ice-ocean interface is the uppermost partially-filled "wet" (ocean) cell, however in practice all the quantities are evaluated in an ocean mixed layer as for the ice shelf implementation in the MITgcm of Losch (2008). This mixed layer thickness, in this implementation, is equal to the full-cell vertical layer thickness at that depth. In reality, an ice-ocean boundary layer is present at the interface. The exchanges of heat and salinity fluxes occur in this layer as well (see Discussion, Section 3.4, and Gwyther et al., 2020a). The equations were modified by Jenkins et al. (2001) to take into account the volume conservation of meltwater.

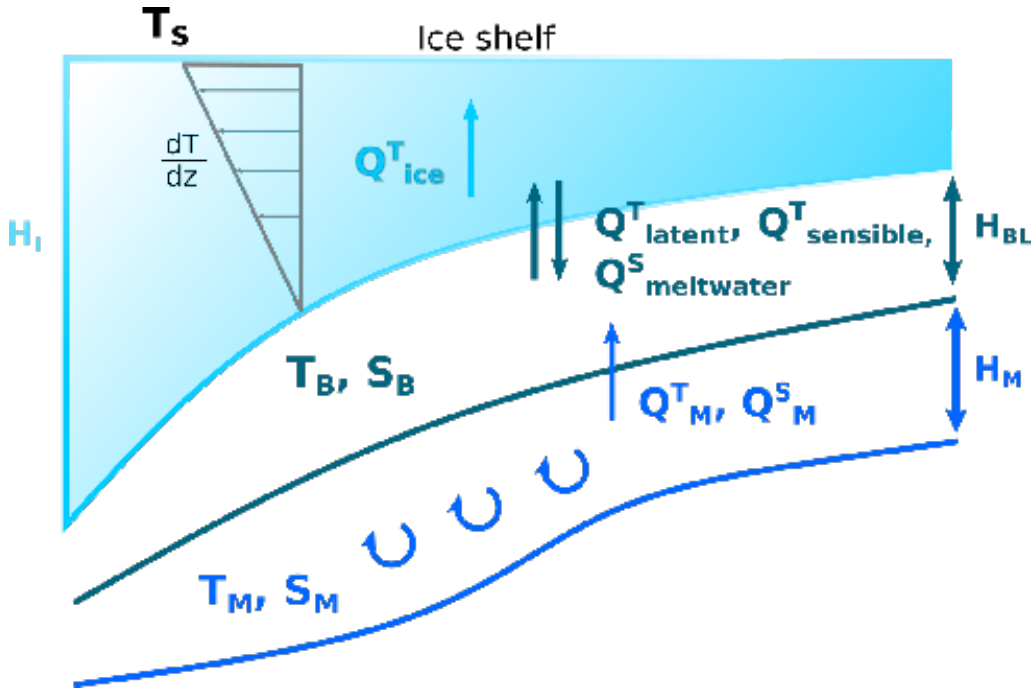

Figure 3.2: Schematic view of sub-ice shelf boundary layer fluxes, implemented in the three-equation formulation. Adaptation of Figure 1 in Holland and Jenkins (1999). The sub-ice shelf boundary layer exchanges heat and meltwater (Q^T_{latent}, $Q^T_{sensible}$, $Q^S_{meltwater}$) with the ice shelf (top boundary) through melting and mixing with the resulting meltwater; it also exchanges heat and salt (Q^T_M, Q^S_M) from the ocean mixed layer (bottom boundary). Inside the ice column, a vertical temperature gradient between the surface and the ice shelf draft, causes a conductive vertical heat flux (Q^T_{ice}).

Using a linear equation of state as also used in the MITgcm, the *in-situ* temperature T_f of freezing point is expressed as:

$$Tf(S,p)[°C] = aS + b + cp = (0.0901 - 0.0575\ S[psu]) - 7.61 \cdot 10^{-4}\, p[dbar] \quad (3.1)$$

$$Q^T_I - Q^T_M = Q^T_{latent} \qquad \text{(fluxes divergence)}, \quad (3.2)$$

where subscript "I": flux across the ice-ocean boundary layer (Figure 3.2); "M": flux across the ambient water to the boundary layer. The imbalance is given by the heat expended for melting. This equation constrains the ice-ocean interface to be at the *in-situ* freezing temperature. Heat fluxes balance at the ice shelf draft –ocean interface, in a mixed boundary layer, defined positive upwards (heat absorbed by ice column) are given by:

$$\begin{aligned} Q^T_{latent} &= -\rho_I L_I w_b, \\ Q^T_{diff} &= -\rho_I \, c_{pI} \, \kappa^T_I \, (T_S - T_B)/h. \end{aligned} \tag{3.3}$$

where ρ_I is ice density (917 kg/m^3), c_{pI} corresponds to ice specific heat at constant pressure (2 $\cdot$ 103 J/kg K), L_I ice latent heat of fusion (3.34 $\cdot$ 105 J/kg K), κ^T_I thermal diffusion coefficient (1.54 $\cdot$ 10^{-6} m^2/s). T_W is the temperature of ambient water at the uppermost layer in contact with the ice shelf draft and T_B is the temperature of the ice at ice shelf draft, which is assumed to be at the *in-situ* freezing temperature $T_B = T_f$ (S_B, p_B). w_b is the meltwater flux (<0 if melting, with Q^T_{latent} >0, or the reverse when $T_W < T_f$ and refreezing occurs). The diffusive heat flux is based on a linear temperature profile between a constant ice temperature at surface TS and the temperature at ice shelf draft T_B, where h is ice column thickness.

Finally, turbulent heat flux is given by mean of a bulk turbulent transfer formulation:

$$Q^T_{turb} = \rho_W \, c_{pW} \, \gamma^T \, (T_W - T_B) \qquad \text{(fluxes divergence)}, \tag{3.4}$$

where ρ_W is the seawater density (1028 kg/m^3), γ^T is the velocity-dependent thermal exchange velocity (m/s), computed from friction velocities estimated from ocean speed, turbulent and molecular transfer coefficients, following Holland and Jenkins (1999). $\gamma^{T,S}$ depend on friction velocities u, which represent turbulent kinetic energy near ice shelf base; thermal forcing accounts available heat for melting (Hellmer and Olbers, 1989; Holland and Jenkins, 1999). A common parameterization is a quadratic drag law u^2=C_D $|\mathbf{u}|^2$ with C_D the drag coefficient and u the velocity of the ambient water layer. We employed $C_D = 0.0015$, inside the range of reported values, that span 0.001 to 0.01. A similar set of equations is employed to provide the salinity balance due to exchanges between the ambient water masses and the ice shelf. As for the heat flux, the salinity flux divergence at the sub-ice shelf base(draft) is:

$$Q^S_I - Q^S_M = Q^S_{brine} \qquad \text{(fluxes divergence)}, \tag{3.5}$$

The melt and diffusive salinity fluxes are given by:

$$\begin{aligned} &Q^S_{turb} = Q^S_{brine} + Q^S_{diff}, \\ &Q^S_{diff} \equiv 0 \qquad\qquad \text{(no salinity diffusion inside the ice column)}. \end{aligned} \tag{3.6}$$

Meltwater from the melting ice is added as a (negative) virtual salinity flux:

$$\begin{aligned} Q^S_{brine} &= \rho_W w_b (S_I - S_B) \qquad \text{(virtual salt flux)}, \\ Q^S_{turb} &= \rho_W \gamma_S \ (S_W - S_B). \end{aligned} \tag{3.7}$$

Q^S_{turb} is the salinity flux by ambient water to maintain the ice-ocean interface at salinity SB in the presence of meltwater flux. Treatment is slightly different in Jenkins et al. (2001), where meltwater flux is not only treated as a turbulent diffusion of virtual salt flux, but an advective term concurs to the flux. Even though there is melting ($w_B \neq 0$) the ice-ocean interface is not allowed to evolve consistently by changing the shape to account for the ice lost. In this approach the ice-shelf is a sink of heat and salinity, and we neglect the ice-related feedback. The same set of equations was used by Holland et al. (2008), which demonstrated in an idealised cavity experiment (with full GCM), a linear dependence of both temperature difference ($T-T_B$) and the velocity in the mixed layer, on the warming of the ambient oceans, which in turn led to a quadratic dependence on the basal melting. The results were consistent for warm and cold cavities, however tidal forcing was neglected.

3.3 Results

Figure 3.3 report the averaged main fields at draft level, used for the subsequent analysis, and the pattern of basal melting; it is evident the West-East gradient in salinity, that induces a similar gradient in density. Figure 3.3c shows that most of the cavity is above the *in-situ* freezing point. Figure 3.4 shows the turbulent transfer coefficients, that enhance turbulent fluxes, resulting from the three-equation formulation. We employed different methods to characterise basal melting, i.e. to assign each grid point basal melting value at a specific water mass, at each time. The simplest is a characterisation based on temperature, with a threshold determined by the surface freezing point (Mack et al., 2019), that discriminate between "cold" melting modes (in the inner cavity) and "warm" melting modes (near the front). A more complex approach takes into account the water temperature at ice shelf draft and its salinity (or density) and based on classes of the two fields discriminate between water masses. However this method is strongly dependent on the subjective choice of the thresholds, although based on observed or simulated water masses properties. We decided to develop a new method that calculated the mixing of cavity water masses at draft, in terms of five endpoints, the five main water masses as they enter the cavity in their relatively unmixed condition. Based on mixing we can quantify the amount of a certain water mass at each point beneath the

RIS. The basal melting field was integrated in space over the region identified by the mixing method, which allowed univocal attribution of melting caused by a specific water mass. This highlighted basal melting variability driven by ocean variability.

Those modes are better defined in the cases of "warm" cavities, i.e., cavities exposed almost directly to inflow of CDW such as in the Amundsen Sea and Bellingshausen Sea (Thompson et al., 2018) or small "cold" cavities, where only HSSW is present. Large "cold" cavities, as for example the Ross Ice shelf, the Ronnie-Filchner Ice Shelf, or the Amery Ice Shelf, show more complex interactions with the continental shelf waters. Their grounding line is located far from the continental shelf break and as such, the continental shelf waters properties change, driven by changing atmospheric and tidal forcing, and by mixing. As a result, the variability of the basal melting can result both from open ocean dynamics and remote teleconnections, and from local climatic variability. We thus explore different ways to characterise melting modes, specifically:

3.3.1 Melting modes characterisation

By identifying the water masses in contact with the ice shelf it is possible to characterise the basal melting according to the three melting modes defined by Jacobs et al. (1992): Mode 1, which is mostly caused by HSSW; Mode 2, resulting from mCDW/mSW; Mode 3, triggered by the summer warming of the AASW.

Freezing point criterion

This method separates *supercooled* waters (i.e. with temperature lower than the surface freezing point) from the others inside the cavity (Figure 3.3). All *supercooled* water masses are classified as Mode 1, as they must have interacted with the inner cavity region and mixed with ISW. In this classification Mode 2 and 3 are grouped together and represent a "frontal melting mode".

Density-temperature criterion

This method is based on a classification using potential densities at the first sub-ice shelf ocean cell (ice shelf draft level), together with potential temperature (Table 3.2). The temperature criterion is necessary to avoid including ISW in basal melting mode 2, given its similar density anomaly (e.g. $\rho_{ISW} \sim 27.7\,kg/m^3$; $\rho_{mCDW} \sim 27.7\,kg/m^3$)
.

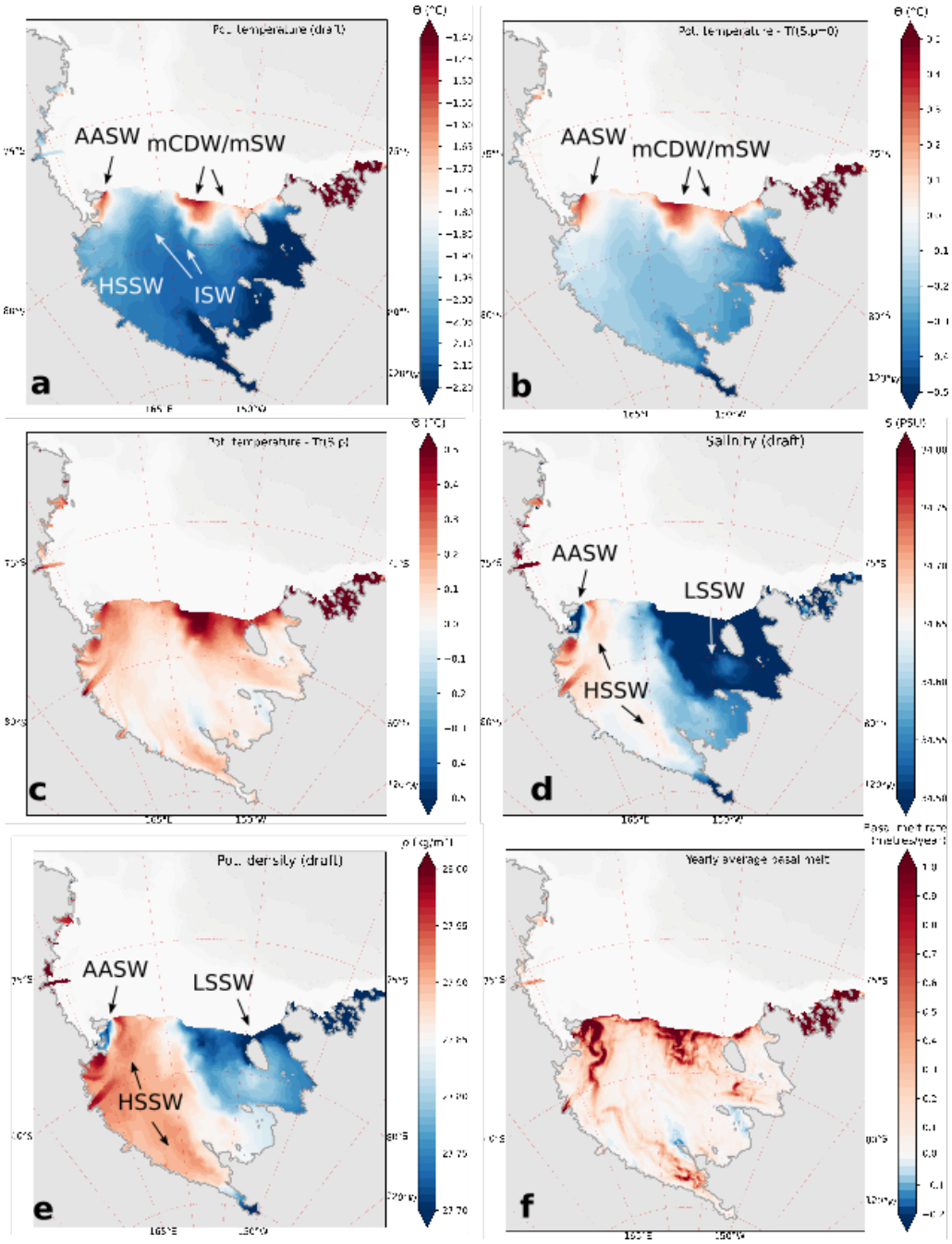

Figure 3.3: Mean annual simulated oceanic fields at the ice shelf draft, averaged over 1993-2018: (a) potential temperature Θ (°C); (b) potential temperature anomaly relative to surface freezing point (°C); (c) potential temperature anomaly relative to *in-situ* freezing point T_f (°C); (d) salinity (PSU); (e) potential density (kg/m^3); (f) mean basa melting rate (m/yr).

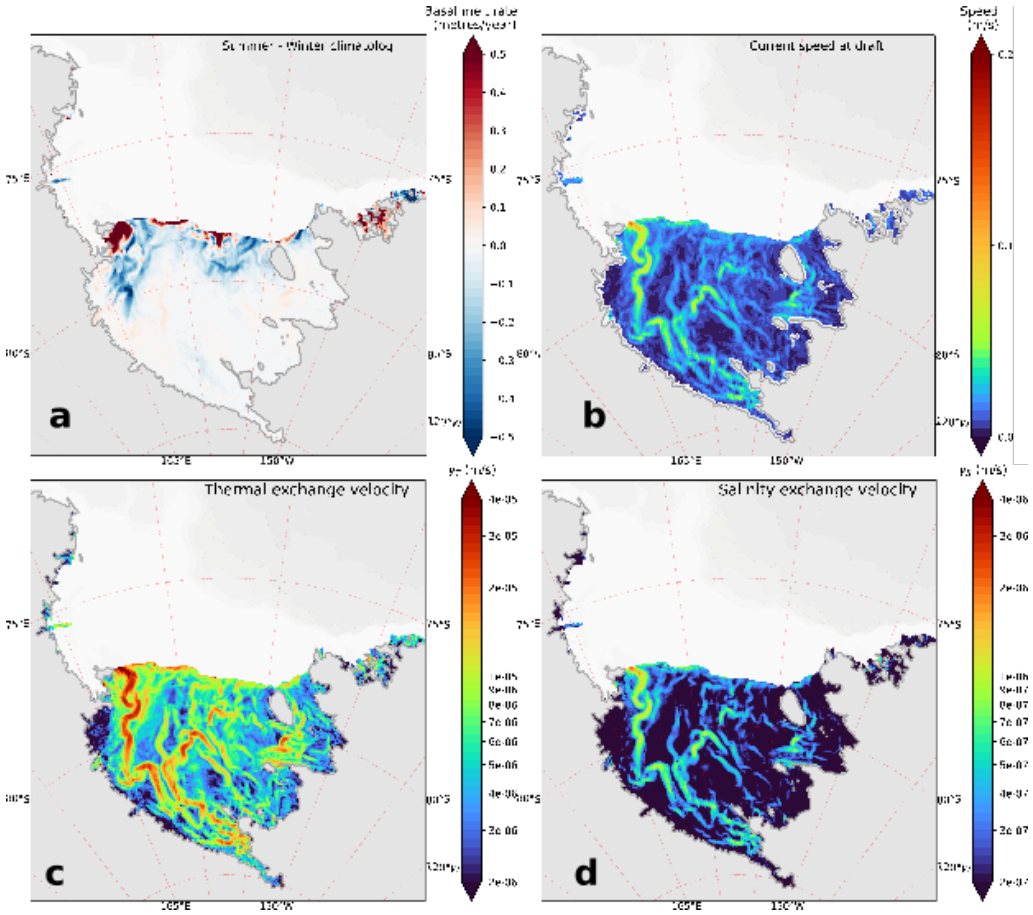

Figure 3.4: (a) Difference between austral summer and austral winter basal melt rates (m/yr); (b) velocities at ice shelf base (m/s); (c) thermal exchange velocity (γ_T) and (d) salinity exchange velocity (γ_S). Notice the scale for (d) 10 times smaller than for (c). All quantities are averaged over 1993-2018.

Water mass	$\rho\ draft(kg/m^3)$	$T\ draft$
AASW	$\rho < 27.6$	$T > T_f(p = p_{atm})$
mCDW/mSW	$27.6 < \rho < 27.8$	$T > T_f(p = p_{atm})$
HSSW	$\rho > 27.8$	$T < T_f(p = p_{atm})$

Table 3.2: The potential density and temperature criteria employed for the characterisation based on density-temperature classes at draft level. "Warm" modes are discriminated by temperature warmer than surface freezing point and by density. The "cold" mode (here only HSSW) is determined by *supercooling* and high density; *supercooling* is caused by mixing of initially near-freezing HSSW with ISW produced during melting at the depth of the ice shelf draft (Cfr. Figure 3.3).

5-way mixing ratios

This basal melting characterisation is based on the decomposition of a water mass in each grid point in contact with the ice shelf draft as mixing of endpoints water masses. The determination of the endpoints was made based on the climatological monthly mean of simulated water masses temperature and salinity at draft (Figure 3.5a,c), and was kept fixed in time. Five enpoints were identified: AASW, mSW, HSSW, LSSW, ISW. The calculation of the mixing ratios is a generalisation of the mixing triangle scheme (three water masses):

$$\begin{cases} m_1 T_1 + m_2 T_2 + m_3 T_3 = T \\ m_1 S_1 + m_2 S_2 + m_3 S_3 = S \\ m_1 + m_2 + m_3 = 1 \end{cases} \tag{3.8}$$

as implemented in python in (https://ocefpaf.github.io/python4oceanographers/blog/2014/03/24/watermass/) to five water masses. The resulting (non-invertible) system of linear equations is:

$$\begin{cases} m_1 T_1 + m_2 T_2 + m_3 T_3 + m_4 T_4 + m_5 T_5 = T \\ m_1 S_1 + m_2 S_2 + m_3 S_3 + m_4 S_4 + m_5 S_5 = S \\ m_1 + m_2 + m_3 + m_4 + m_5 = 1. \end{cases} \tag{3.9}$$

where endpoints are labelled 1 to 5 = AASW... ISW; T,S are the temperature and salinity at each grid point at draft. The system is solved approximately in terms of the mixing ratios $m_1 \ldots m_5$ at each grid point of the RIS, by applying a least square method. The mixing percentage was employed to determine which was the main water mass responsible for melting: a threshold of 50% was set for the "cold" modes: HSSW, ISW; a lower threshold of 30% was set for AASW and mCDW/mSW, since a lower percentage of warm water can still cause more melting than higher percentage of cold water. Finally we set a low threshold of 20% was set for LSSW, since salinity

variations in mixed waters are small and salinity is not weighted differently in the calculation of the mixing ratio.

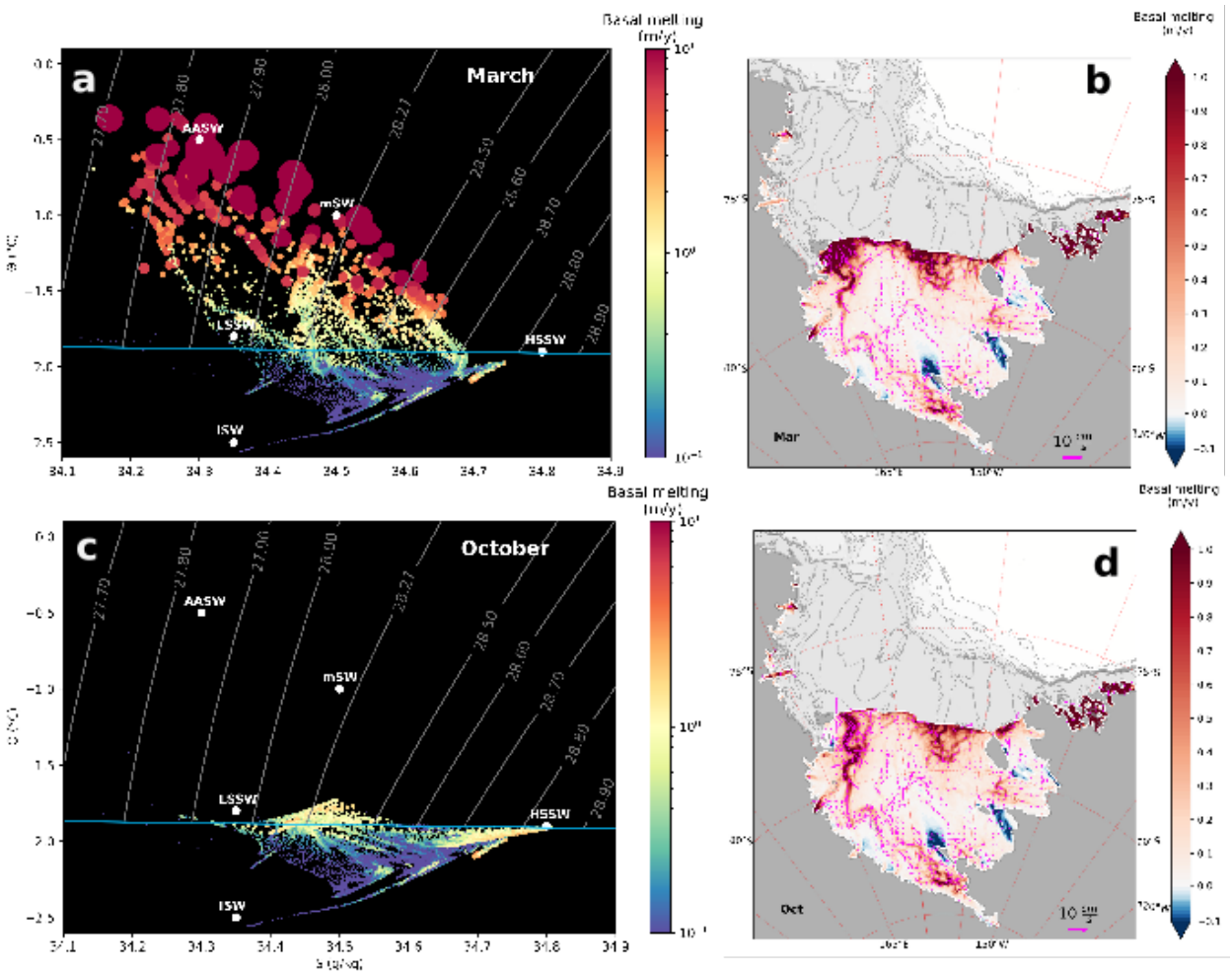

Figure 3.5: (a) simulated March temperature and salinity at the ice shelf draft and corresponding basal melt rates (m/yr) (value given by dots colors and sizes) at the respective grid point. Neutral density contours are overlaid, and the blue line indicates the surface freezing point. (b) corresponding map of basal melt rates (m/yr). Oceanic circulation pathway at the ice shelf draft is indicated by magenta arrows; (c) same as (a) but for October; (d) corresponding map of basal melt rates (m/yr) Climatology is averaged over 1993-2018.

As we are interested in understanding the basal melt rates variability associated with water masses variability, we did not use a depth criterion to define the melting modes in any of the methods described above, as in Jacobs et al. (1992). Depth criterion would encompass several water masses and thus a climatic analysis would be hampered.

Water mass	Potential temperature (°C)	Salinity (psu)
AASW[1]	< -1.5	< 34.3
AASW[2]	$0 < \Theta < 2$	< 34.5
CDW[2]	< 1.5	~ 34.7
mCDW[2]	$-1.5 < \Theta < 1$	$34.5 < S < 34.6$
mSW[1]	> -1.85	//
SW[1]	< -1.85	//
LSSW[1]	< -1.85	< 34.62
LSSW[2]	< -1.8	$34.4 < S < 34.6$
HSSW[1]	< -1.85	> 34.62
HSSW[2]	< -1.9	$S > 34.7$
ISW[1]	< -1.95	//
ISW[2]	< -2.2	//

Table 3.3: Different definitions of Ross Sea water masses after [1](Orsi and Wiederwohl, 2009); [2]Russo et al. (2011). Some water mass are not defined by both.

Method	Mode 1	Mode 2	Mode 3	LSSW	ISW	Not classified
freezing point	58.3 %	41.7 %	//	//	//	//
density classes	56.6 %	28.1%	2.9 %	//	//	//
5-ways mixing	45 %	15 %	7 %	12 %	3 %	20 %

Table 3.4: For each method, the fraction of the integrated basal melt attributed to each mode and the total is given. Some regions do not fall in any category and basal melt over those regions is not classified.

3.3.2 Basal melting variability

A map of the average basal melt rate for the whole period 1993-2018 is shown in Figure 3.3(f). Basal melt rate is calculated using the three-equation formulation after Hellmer and Olbers (1989); Holland and Jenkins (1999) in the volume-conserving form of Jenkins et al. (2001). In the current implementation of three-equation formulation in the MITgcm (Losch, 2008), the interaction between ocean and ice depends on the temperature, salinity and velocity of the uppermost "wet" cell below the ice base. The available heat provided by the cooling of the water ("melting potential" or "thermal forcing", Figure 3.3c) depends on ambient temperature with respect to the freezing point, which in turns depends on both salinity and pressure (depth). It is transferred across the sub-ice shelf boundary layer by turbulent fluxes that are parameterized by means of a velocity-dependent thermal and salinity exchange velocities γ_T and γ_S (Figure 3.4c,d). Thermal forcing and exchange velocities marks

the large and short space-scales of melting pattern.

The main water masses at the ice-ocean interface are represented in Figure 3.5(a,c) for the peak of the melting season (March) and the peak of the sea ice production season (October). We identified the water masses thermohaline characteristics in the ice-ocean interface and implemented a method to decompose each water mass by mixing of different endpoint water masses: HSSW, LSSW, AASW, mSW, ISW. The mixing was based on regional occurrence of the endpoint water masses simulated. The melting modes found are a generalisation of the three modes first presented in Jacobs et al. (1992). By these means, a connection between the water masses properties and basal melting is possible, and long-term and seasonal variability in basal melting is shown to represent changing volume or properties of the endpoint water masses.

Close to the front high temperature, AASW warmed in summer time is advected into the cavity Eastward of Ross Island. Being in the lightest density class ∼27.6, it can't intrude very deep in the cavity, and its melting is limited to the first 120 km beyond the ice shelf front. Stewart et al. (2019) measured at a mooring station positioned through the ice shelf the intrusions of AASW, and upward looking sonar measured melt rates of maximum 5 m/yr in summer and as low as 1 m/yr in Winter, with a strong seasonal cycle. Modelled results show similar amplitudes of summer melt rates at the same site, however in the model the site lies at the boundary of the AASW core (∼230 m depth). Inside the core, closer to Ross Island and shallower than 230 m, values of 20-25 m/yr are reached. A time series of area integrated basal melt rate over the region classified with the 5-way mixing method is given (Figure 3.6(a-d). Masks obtained by this method, of the water masses in a typical summer and winter are shown in Figure 3.6(e,f). Years of high melting are identified: 1996, 2004, 2007-2008, 2012-2014. This variability is probably related to the lower presence of sea ice and extended polynya area, that point to regional wind patterns, determined by Southern Annular Mode (SAM) and Amundsen Sea Low (ASL) variability and upstream processes in the Amundsen Sea (Silvano et al., 2019). The signal time series is unrelated to salinity and temperature time series of intruding AASW at frontal RIS at draft level. In the Central RIS melting is sustained throughout the year by SW warmed by mixing with mCDW that has intruded along Hayes Bank. This is similar to what was modelled by Jendersie et al. (2018). In the central RIS, mCDW is driven along Hayes Bank towards the cavity. Being characterised by low density Figure 3.3e, mCDW belong to intermediate potential density classes (∼27.75), and are able to melt only at middle depth, within 150 km of the RIS front. Variability of this water mass may be related to strength of the Ross Sea gyre, stability of the Antarctic Slope Front, which in turn modulates the across-shelf break access

of CDW to the shelf. The basal melt time series is covarying with the Eastern SW temperature (Figure 2.14a). The seasonal cycle has a maximum of melting in the summer months.

The deepening of the ice shelf draft towards the grounding line,makes it possible to be melted by relatively cool water, due to the pressure dependence of the freezing point (lowering with pressure/depth, eq. 1, Fig 3c). This effect makes HSSW, which reaches a higher potential density $\gtrsim$27.8 and therefore greater depths, to melt over the inner parts of the cavity, up to the grounding line, classified as mode 1. HSSW is formed in Northwestern Ross Sea, specifically in the Drygalski Basin where lies the Terra Nova Bay polynya, and Southwestern Ross Sea, in the polynya that opens near Ross Island, however only water from this latter site of formation is advected inside the cavity. Nonetheless, we may think that the processes that form HSSW are sensitive to the same drivers also in Northwestern Ross Sea and look at the variability recorded from moorings, far from the RIS.

This trend is also apparent in a time series of HSSW salinity at draft level at the Western frontal RIS, and a time series of salinity of bottom HSSW and SW at bottom (Figure 2.14b). The period 2008-2013 marks a decisive decline in mode 1 melting, with a sudden rebound in 2014. This is consistent with what was observed by Castagno et al. (2019), however the low peaks in salinity observed in 2000 are not seen in the modelled HSSW. The rebound is explained by changes in sea ice import regime from the Amundsen-Bellinghousen Sea driven by positive Southern Annular Mode and extreme El Niño conditions between 2015 and 2018 Silvano et al. (2020). Fit of integrated basal melt over 26 years with a shifted sine function resulted in a frequency of $\sim$ 31 years, and amplitude of 11 Gt/y. Two trends are visible in basal melt: one related to the temperature of mCDW/mSW and mode 2, the other in salinity of HSSW and mode 1. Mixed trend in the salinity of mCDW/mSW. Seasonal variability: mode 2 and 3 show a definite increase in summer months, due to increased stratification of the water column, that allows access to the cavity to surface and intermediate depth waters. In mode 1 the seasonal cycle is inverted with respect to the first two modes, with wintertime melting increasing with a defined spatial pattern (Figure 3.4a), where the difference between summer and winter climatology is shown (DJF-JJA). In figure, red marks the increased melt close to the front in summertime, while blue marks the increased melt in wintertime. Interestingly, some frontal regions show greater melting in winter time, due to the strong brine rejection in RIS frontal polynya. This departs from the classical view of the three modes associated strictly with increasing depth from the front to the grounding line, as HSSW is not constrained to the deepest levels in the Western RIS. Where RIS polynyas are present, strong brine rejection at the RIS front produces a frontal region

of high density water that isolates the cavity by outer less dense waters.

3.4 Discussion

Impact of teleconnections

Simulated basal melting, integrated over the RIS and averaged over 1993–2018, is within the range of the literature values given by other existing modelling work or remote sensing observations (Table 3.1). The areas of the RIS draft influenced by distinct water masses are shown in Figure 3.6(e,f) for a typical winter and late summer case, respectively, and shows the different presence of the water masses in summer and winter. Decadal variability of the basal melt rates is influenced by the variability of the HSSW and LSSW, which together produce two thirds of the total annual averaged basal melt (78.8 Gt/yr) over 1993-2018. The other one third is melted mostly by mCDW/mSW, and secondarily by AASW. The basal melting resulting from the intrusion of AASW and mSW within the cavity shows a strong seasonal cycle, being present only in late austral Summer, and a strong interannual variability.

We suggest that interannual variability of mCDW/mSW and AASW may be related to wind variability, associated with internal variability of the ASL and SAM, and forced variability from ENSO teleconnections. The Indian Ocean Dipole (IOD) as well may impact wind variability in the Western Ross Sea. A stronger ASL, typical of austral winter, would drive stronger Easterly winds, pushing more sea ice from the Amundsen sea into our domain. The ASL is also subject to longitudinal shifts of the centre of low pressure; typically the shift is Westward to the Ross Sea in austral winter, and drive Southerly wind flow anomaly, reducing import of sea ice and increasing the amount of sea ice produced on the Ross sea continental shelf (as in Silvano et al., 2020). Similarly, stronger SAM would weaken coastal easterlies and foster intrusions of CDW. Variability of the katabatic winds is currently not represented by an index, although we may consider defining an index representative of the Polar Cell strength. Overall we suggest that ASL, SAM, ENSO and katabatic winds combined, would have caused the simulated interannual and decadal variability. In particular the periodogram of integrated basal melting shows frequencies in the range between 2.5 - 6 years, which shows remarkable similarities with the ENSO index 3.4 periodogram (Figure 3.7). Studies of long-term variability of basal melting are scarce, only Adusumilli et al. (2020) measured interannual variability in the RIS, but only near the Ross Island sector and in Byrd glacier. Melting due to water masses that are undergoing strong mixing inside the cavity and are therefore

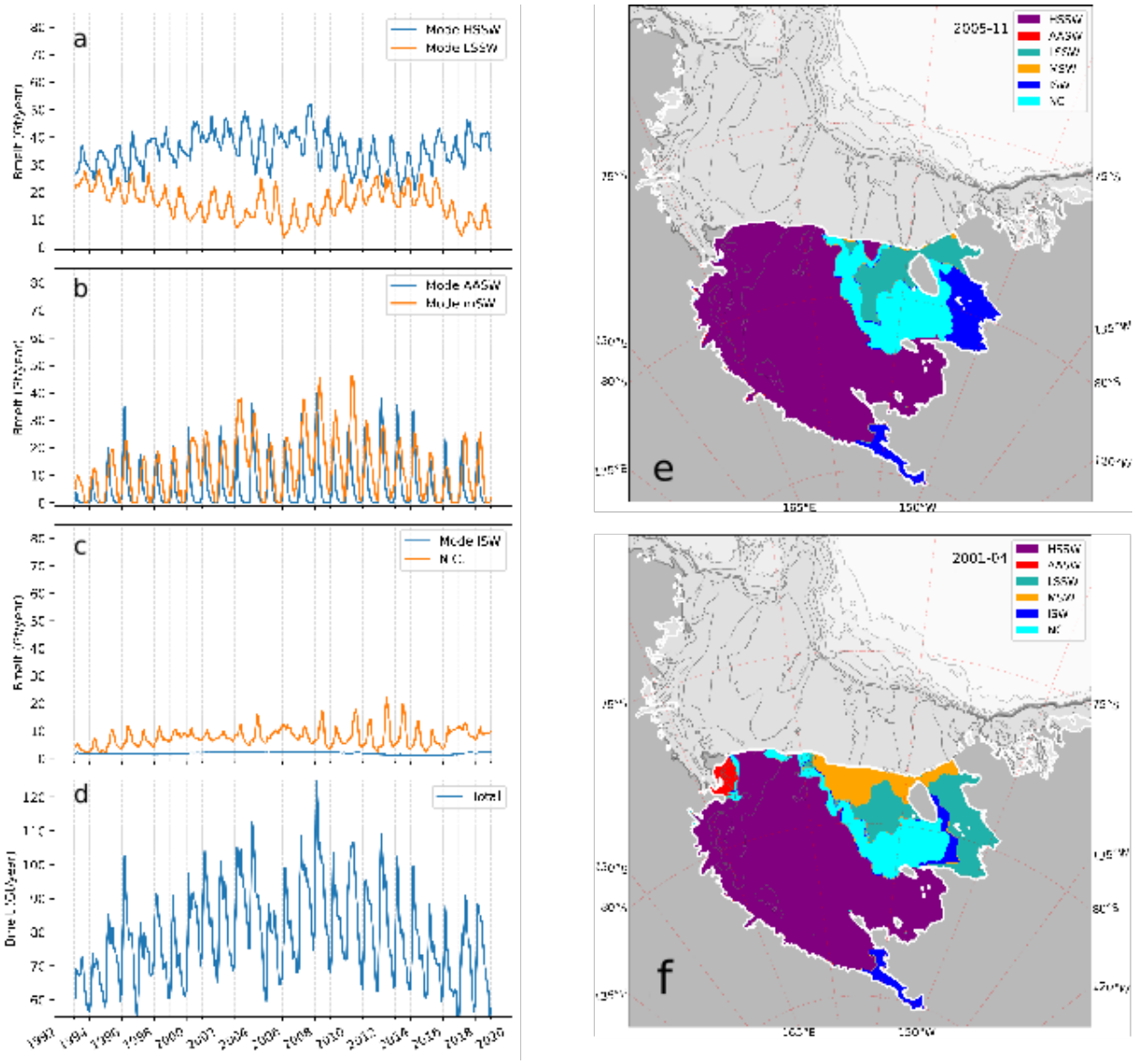

Figure 3.6: (a-d) basal melting timeseries (Gt/yr), integrated over the areas of influence of the various water masses entering into the RIS cavity, identified based on the mixing method, (e) water masses masks for the peak of a typical winter, (f) water masses masks for the peak of a typical melting season. Some water masses that undergo strong mixing are not attributed to any cathegory by the 5-way mixing method; these are referred to as Not Classified (N.C.) or "transforming" waters.

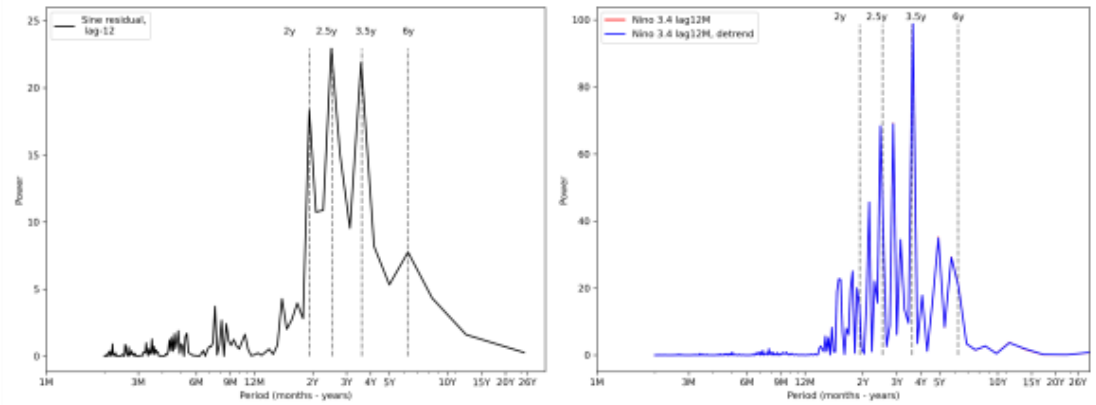

Figure 3.7: (a) power spectrum computed for the overall RIS basal melting. (b) power spectrum of the ENSO 3.4 index. To calculate the power spectrum (periodogram) a detrending and removal of the seasonal cycle was applied to the timeseries.

"transforming", is labelled N.C. (not classified).There is a clear difference between ocean model-derived basal melt rates and indirect observations (satellite altimeter, radar, flowline methods), the former being almost twofold higher (Table 3.1). All indirect models treat basal melt as a residual term in the mass budget equation, which also leads to great uncertainty in the estimates. Comparison with observations is also often limited by the time span of the observations, which may not be concurrent. Direct observations such as hot water drilled boreholes in ice shelves are punctual measurements and limited in time, and may be affected by lateral variations, or short timescale transients of the processes under investigation, and are not suitable for comparison with monthly rates (e.g., Arzeno et al., 2014; Stewart et al., 2019).

Mesoscale eddies

The Antarctic coastal oceans are troublesome to be modelled in "high resolution", i.e. eddy-resolving way, due to the weak stratification, large Coriolis parameter, and shallow water column depth over the continental shelf and inside sub-ice shelf cavity; this produces a relatively small baroclinic Rossby Radius of deformation ($Ro \lesssim 3$ km), which decreases dramatically in winter (Figure 2.16). Previous high-resolution studies with a eddy-resolving setup at 1.5-km resolution with ROMS (Mack et al., 2019) identified a more than two-fold increase in the number of eddies on the continental shelf with respect to a control case of 5-km grid spacing (as the setup shown here with the MITgcm). However, no statistical correlation was found between increased number of eddies and basal melting, so that the RIS is either insensitive to eddy-transport or that resolution was still not sufficient to be eddy-resolving inside the RIS cavity.

Impact of grid vertical discretization type

Modelled melt rates are usually determined by the three-equation formulation, however, depending on the model framework, important differences arise in the practical calculation of turbulent heat, salinity fluxes, and meltwater addition (Gwyther et al., 2020a). In the three-equation implementation in the MITgcm (Losch, 2008), and in the current Ross Sea implementation in particular, heat and salinity fluxes are calculated from ambient water of the lower ice-ocean mixed layer, neglecting the presence of a thin ice-ocean boundary layer. Ocean models that employ a terrain-following vertical discretization, e.g. ROMS, are better able at resolving the vertical structure of the water column in shallow parts, i.e. the cavity, since they are able to redistribute the same amount of vertical levels in each point. The MITgcm, having a fixed vertical discretization, makes it impossible to have vertical resolution high enough to represent the ice-ocean boundary layer in detail: the present implementation has ∼10 levels spanning the cavity average depth, with average full-cell thickness of about 40 - 50 metres. In the MITgcm, this layer is equivalent to the full cell (not fractioned) below the ice shelf draft (Losch, 2008). This is the same layer where the meltwater is injected and immediately mixed. The boundary layer that forms below the ice shelf, just 15-30 m thick (Stevens et al., 2020) is not simulated by the model, given its vertical discretization, while it may be simulated in ROMS, whose upper layers would be just a few metres thick. Higher resolution implies however that the correct value for vertical diffusivity of tracers and momentum must be well prescribed or tuned to achieve realistic fluxes in the three-equation formulation. This may be problematic due to the lack of observations inside ice shelf cavities, but a study carried out through hot-water borehole by Stevens et al. (2020) identified a strongly convective and unstable ice-ocean "mixed" layer, therefore suggesting a vertical kinematic viscosity of 10^{-3} m^2/s, higher than normally employed in ocean models (10^{-4} m^2/s is employed here). A coarse vertical representation of this layer would be more problematic for warm cavities, as their temperature and salinity would be strongly different with respect to ambient waters.

On the other hand, at 5-km resolution the bathymetry and ice shelf draft would be too rugged for ROMS, which needs smoothing of both, whereas the MITgcm is not impeded by this. z-levels models are better able at resolving the sharp water column jump at the RIS front, and may simulate more realistically intrusions of AASW along the front; compare, for instance, a 5-km run with ROMS Dinniman et al. (2018) where a high band of temperature representative of AASW is present all along the RIS. Excessive mixing can explain why the outflows of simulated ISW are subdued in temperature with respect to the more extreme properties of observed

ISW (by mooring F and XBTs from 2017 PNRA Cruise).

Frazil formation

Direct refreezing vs frazil crystals forming in the water column and floating upward (Robinson et al., 2017). Frazil formation leads to static instability in the water column, where ISW is continuously supplying *supercooled* water (Galton-Fenzi et al., 2012; Reese et al., 2018). Frazil formation releases a significant amount of brine and latent heat that warms the ambient water as observed from MacMurdo Bay(Robinson et al., 2014); it also modifies salinity of ISW (Holland and Feltham, 2006) and has stabilizing effect on ice shelves by sealing cracks (Kulessa et al., 2014).

Double diffusion

Hypothesis turbulent sheared boundary layer at ice-ocean boundary, but ice shelf melting generates the conditions for double-diffusion: a stable vertical salinity gradient by meltwater release and an unstable inverse temperature gradient through concurrent latent heat absorption (Begeman et al., 2018). Double diffusion may lead to diffusive convection: this can produce a stratification organised in well-mixed layers separated by interfaces with steep gradients in temperature and salinity, a structure called a double-diffusive staircase (Begeman et al., 2018). This was observed below an Antarctic ice shelf by Kimura et al. (2015). In Losch (2008) formulation, meltwater is added as salinity flux and flux term in advection. This smooths out the buoyancy meltwater input and the ice-pump feedback mechanism. Simulated ISW properties are less extreme than those observed. Ice-water drag Cd very uncertain and very variable below ice shelf ($u^2 = C_D\ |\mathbf{u}|^2$) (see e.g., direct draft observations). Also regions of upwelling ISW are subject to refreezing of frazil crystal: this impact on ice shelf draft roughness and on drag coefficient C_D (Robinson et al., 2017).

3.5 Conclusions

A new method based on mixing of water masses beneath an ice shelf has been applied to the simulated water masses beneath the Ross Ice Shelf, for the period 1993-2018. The results show that it is possible to determine the drivers of basal melting in terms of main water masses, and to relate melting variability to regional/global climatic drivers of the water masses variability by computing water masses mixing ratios. HSSW and LSSW form together two thirds of total melting, with HSSW having the biggest role. A decadal variability affects HSSW salinity and volume, and its increase displaces partially LSSW from the RIS cavity. Decadal variability is associated to

decadal variability of the SW of the whole Ross Sea and HSSW in particular. AASW and mCDW/mSW show a strong seasonal cycle, melting strongly in summer and near the ice shelf front, due to isopycnals in front of the RIS enabling easer exchanges across the front. Interannual variability is associated to varaibility of the temperature of SW, and in particular Eastern SW (see Conclusions of Chapter 2). We hypothesise that these conditions are affected by teleconnections, however it proved difficult to isolate a single climatic driver, as the situation is complicated by sea ice import and sea ice production. Uncertainties remain as to the impact of tides would have affected the results, in particular near the grounding line, where tides provide stirring of the otherwise stagnant water column. The vertical discretization may also impact on the three-equation formulation of basal melting. The successful application to a present day scenario allows us to apply the same method to a scenario with different climatic conditions in the past, for instance during the last deglaciation, which is the subject of Chapter 4, as well as in deep past, such as the Miocene, as it is planned, in future dedicated researches.

Chapter 4

Ross Sea paleo circulation and basal melting during last deglaciation (21-0 ka)

4.1 Introduction

At the LGM (∼21 ka) the AIS was predominantly grounded up to the continental shelf break (Bentley et al., 2014a; Whitehouse et al., 2019) and retreated to its present-day position during the deglaciation. However, little is known about how fast the retreat was and how it happened in the various sectors of the AIS (e.g. steady retreat or Marine Ice Sheet Instability). Ice core records have provided an overview of the AIS mass balance, indicating that the ice sheet thickened substantially during the LGM and then thinned to its present-day morphology. Though numerous marine geophysical campaigns have provided understanding of some of the sub-glacial processes and grounding line retreat mechanisms by revealing geomorphological features on the seafloors (e.g. Anderson et al., 2014; Prothro et al., 2018, 2020), the lack of knowledge about the deglaciation mainly results from the difficulty of dating those geomorphological features attributed to the AIS retreat during the last Deglaciation (e.g. Bart et al., 2018).

During the last deglaciation the Ross Sea sector underwent dramatic changes in oceanographic properties and in the extension of the AIS. The ice flow dynamics was of the type of ice stream flow, strongly sensitive to thinning by increased melting, which may have triggered MISI (DeConto and Pollard, 2016), and stabilised by the presence of bathymetric pinning points, and lateral confinement (Gudmundsson et al., 2019; Reese et al., 2018; Kingslake et al., 2018). To understand past AIS dynamics

in the Ross Sea sector, a large number of scientific drilling on Antarctic continental margin and several cruises aimed at collecting high resolution data were carried out, in order to reconstruct the WAIS and EAIS dynamics across the Late Cenozoic (Bart, 2003; Bart and DeSantis, 2012; Anderson et al., 2019; Kim et al., 2018) (Figure 4.1). IODP expedition 374 (De Santis et al., 2018; McKay et al., 2019) contributed to our understanding of the AIS and the paleo ocean dynamics in the Ross Sea sector by: [1] evaluating the contribution of West Antarctica to far-field ice volume and sea level estimates; [2] reconstructing ice-proximal oceanic and atmospheric temperatures to quantify past polar amplification; [3] assessing the role of oceanic forcing (e.g., temperature and sea level) on AIS variability; [4] identifying the sensitivity of the AIS to Earth's orbital configuration under a variety of climate boundary conditions; and finally [5] reconstructing Ross Sea paleobathymetry to examine relationships between seafloor geometry, ice sheet variability, and global climate. Recently, there has been growing interest in investigating paleoceanographic circulation and changes related to seabed morphology and AIS dynamics (Tinto et al., 2019; Ashley et al., 2021; Gales et al., 2021).

Marine geomorphology allows us to track the grounding line stable point and the step-wise retreat following deglaciation together with ice flow direction (Anderson et al., 2014). Analysis of marine geological formations associated with ice sheet presence and sub-glacial dynamics, such as Grounding Zone Wedges, (GZW), suggest where the grounding line was relatively stable and extensive sedimentation occurred. Mapping of megascale glacial lineations, deep furrows in the continental shelf bathymetry, produced by ice stream flows, and sub-glacial drainage systems, allowed allowed to reconstruct flow directions (Anderson et al., 2014), which enabled to understand the sources of the ice streams: the Eastern Ross Sea sector ice streams were sourced by WAIS only; the Western Ross Sea sector, from the Drygalski to the Pennel troughs, were sourced by the EAIS through the Transantarctic mountains; in the Eastern Ross Sea, namely in the Glomar Challenger Trough ice streams from the two sources coalesced.

One of the most detailed ice sheet retreat scenario reconstruction involved the investigation by sediment cores and sub-glacial landforms of the Whales Deep basin, Eastern Ross Sea (Figure 2.1a) and the sub-ice shelf environment (Bart et al., 2018). The grounding line was advanced up to the continental shelf at LGM, then $\sim$ 17 ka it retreated to a saddle point where it deposited extensive GZWs, and an ice shelf was present. At 12.5 ka, the ice shelf collapsed and the grounding line underwent a fast, 200 km long retreat, with a delay between 200 and 1400 years after its collapse (uncertainty associated to the radiocarbon dating), until a new stable position was

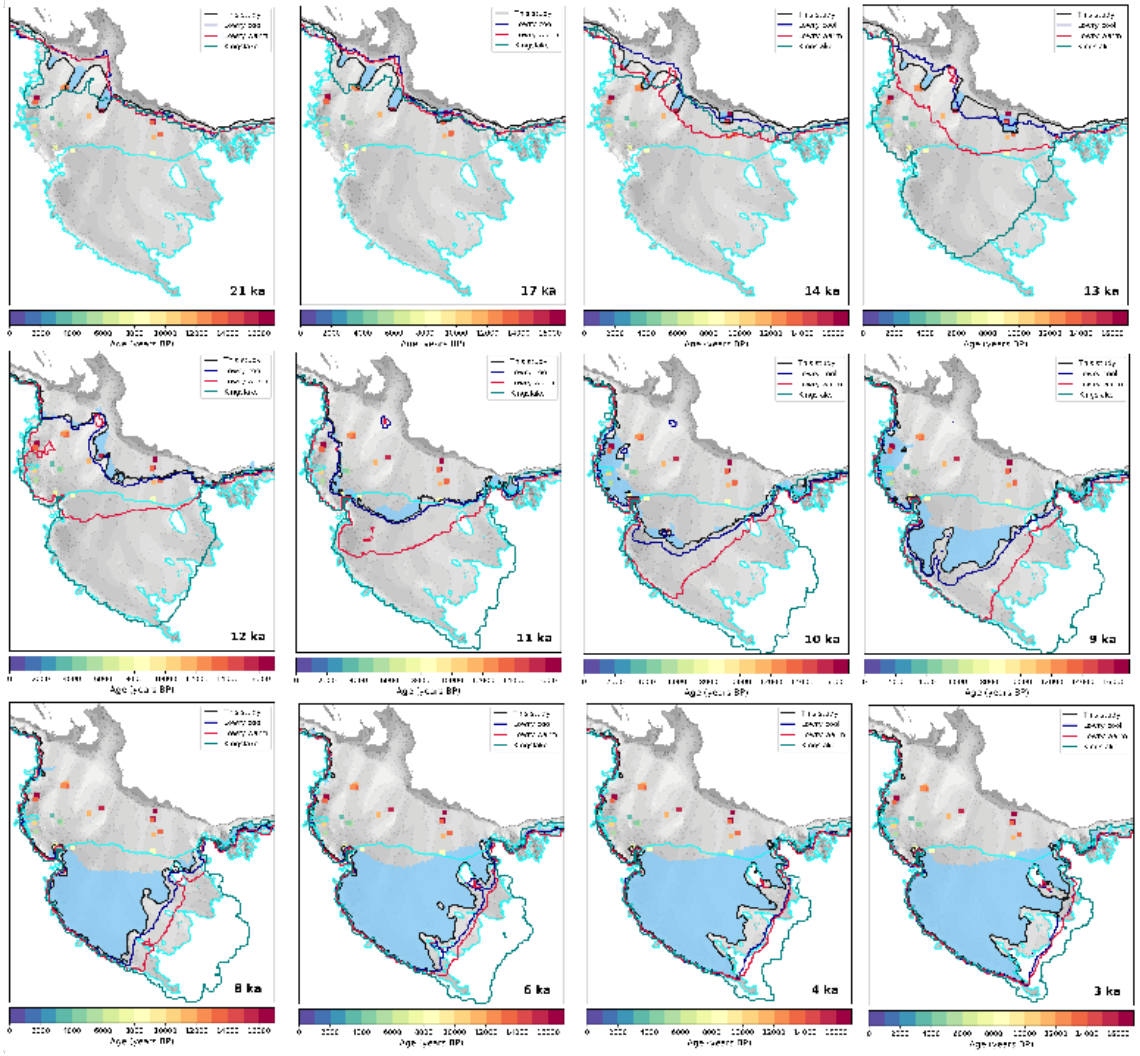

Figure 4.1: Last Deglaciation grounding line data-based or simulated reconstructions in the Ross Sea: blue/red lines are "cold"/"warm" simulated retreat scenarios from Lowry et al. (2019); green line is simulated from Kingslake et al. (2018). The grounding line retreat scenario used in our regional oceanic simulations is shown in black. It accounts for marine geomorphology observations (Halberstadt et al., 2016) and sedimentological evidence (solid squares indicate the time of open-marine conditions based on Bart et al., 2018; Prothro et al., 2020) from 21 ka to 13 ka. For snaptshots younger than 13 ka, the grounding line position is based on Lowry et al. (2019) "cold" scenario, (see Chapter 4.1). Blue areas correspond to the paleo ice shelves prescribed in our regional oceanic simulations. The cyan line indicate the present-day ice shelves front and Antarctic ice sheet grounding line (Bedmap2, Fretwell et al., 2013)

found near Roosevelt Island, at ∼11.5 ka (Bart et al., 2018). Despite the delay, this scenario confirms the theory of MISI. At this new stable position it started to reform an ice shelf, until a second episode of retreat occurred at 3.2 ka, with the grounding line retreating past Roosevelt island and reaching a stable position close to present day grounding line in Siple Coast. The formation of GZWs from sediment aggradation eroded by ice streams, had a strong stabilising potential which could halt temporarily MISI (McGlannan et al., 2017; Bart and Tulaczyk, 2020). Unfortunately scarce records exist for the Central Ross Sea to infer the retreat timing, due to missing pinning points to halt the retreat.

A similar methodology was used in the Western Ross Sea, where GZWs formed at the head and sides of the three major troughs: Drygalski, Joides and Pennel. Analysis of GZWs and other landforms morphology enabled the identification of the grounding line position at the LGM and at the stable positions where it temporarily stopped during deglaciation (Halberstadt et al., 2016; Simkins et al., 2017). Sediment cores radiocarbon dating allowed to constrain the age of the retreat and the environmental types (ice proximal, open-marine, sub-ice shelf environments, Prothro et al., 2020) although some inconsistencies remain in independent radiocarbon dating of open-marine conditions in Victoria Land (Baroni and Hall, 2004) and from cosmogenic nuclide surface exposure records (e.g. Anderson et al., 2017. During deglaciation, the ice streams extending from the EAIS through the Transantarctic mountains in Victoria Land into the Western Ross Sea, retreated past the Transantarctic mountains, leaving only a few ice tongues, such as the Drygalski ice tongue.

In the early to middle Holocene, ice streams sourced from the WAIS in Siple Coast and from the EAIS through the Transantarctic mountains, coalesced into a single ice ice stream giving birth to the newly formed Ross Ice Shelf and its sub-ice shelf cavity. There is evidence, obtained by modelling of radiocarbon decay in subglacial sediments from a subglacial lake, for the grounding line to have retreated past its present-day position and to have readvanced in late-Holocene (Neuhaus et al., 2021). Some ice sheet models show the same behaviour (Kingslake et al., 2018); in contrast, other more realistic reconstructions in terms of retreat timing, obtain this feature only by setting extremely low viscosity of the bedrock subsidence response (Lowry et al., 2019).

Past glaciological research highlighted the deglacial retreat of the WAIS and EAIS in the Ross Sea sector, through sedimentology, geomorphology, and ice sheet modelling, and provided constraints for the timing and pathways of the retreat. However the question remains, as to whether and how much did the ocean impact

on the AIS retreat. Earlier attempt at studying the past basal melting of the AIS with an ocean model was done by Obase et al. (2017), who developed a pancircum-Aantarctic numerical ocean model forced by LGM climate, but employing present day ice shelves configuration. Their results suggest that basal melting at the LGM was still considerably high, despite simulated sub-surface ocean temperature colder by -2.8 °C: this is because their simulated ocean temperature structure was not altered considerably with respect to the present, despite the colder climate. Their study highlights the need for more realistic boundary conditions to be used when modelling the past ocean circulation.

Here, employing a regional ocean model coupled to the ice shelves and forced with transient global paleoclimate simulation outputs (TraCE-21ka) we investigate water masses and circulation changes during the deglaciation in the Ross Sea, suggesting how the changing water masses may have responded to external forcing and feedbacks in the Southern Ocean and how their effect on the AIS may have driven its retreat, at different locations and time.

4.2 Methods

The simulations consist of 21 snapshots separated by 1'000 years. The snapshots are composed of a spinup, 120 years long, and a transient run 26 years long, in order to allow comparison with the present-day transient experiment (Chapters 2,3), which run over 26 model years. The forcing and boundary conditions are based on a bias-corrected fully-coupled transient climate deglaciation experiment that covered the entire last glacial cycle, TraCE-21ka (Liu et al., 2009), which includes Greenhouse gases forcing, time varying Earth orbitals, and which adopted the ICE-5G ice sheets chronology (Peltier, 2004) as topography and albedo varying conditions. The TraCE-21ka atmospheric and oceanic output were bias-corrected with present day reanalysis, to reduce model biases associated with low resolution of the paleoclimate grid setup (Yeager et al., 2006); the procedure is described below. The model boundary conditions were updated at each snapshot, alongside bathymetric, ice sheet geometry configuration and sea level.

4.2.1 Forcing and boundary conditions: TraCE-21ka

Paleo atmospheric and ocean boundary conditions were obtained by a fully-coupled transient climate deglaciation experiment that covered the entire last glacial cycle, TraCE-21ka (Liu et al., 2009), which includes Greenhouse gases forcing, time varying Earth orbitals, and which adopted the ICE-5G ice sheets chronology (Peltier, 2004)

as topography and albedo varying conditions. Consistently with the volume loss during deglaciation, meltwater fluxes were prescribed in TraCE-21ka. To force our Ross Sea model, a bias correction with respect to present-day reanalysis was applied to all the ocean and atmospheric fields of TraCE-21ka. For the atmosphere, available in TraCE-21ka at monthly frequency, we calculated the offset of the last 6 years of TraCE-21ka (1985-1990) as monthly climatology fields from a baseline monthly climatology of the years 1990-1995, from ERA5 (Hersbach et al., 2020), and subtracted it from all the fields. As for the ocean, fields in TraCE-21ka are available as decadal means, and the offset was removed between the last decade, 1980-1990 and a GLORYS12V1 (Lellouche et al., 2021) time average over 1993-1998 (the earliest years available in the reanalysis). Vertical smoothing of TraCE-21ka ocean components was done to reduce the surface mixed layer to the same depth as the renalysis. As for the ocean basin geometry, it needs to take into account the different sea level, different ice sheet geometry, and the loading effect that the ice sheet loading exerted on the bedrock. We modified the present day bathymetry already employed for the present-day setup (Bedmap2, Fretwell et al., 2013; Schaffer et al., 2014), at 5-km horizontal resolution and 50 vertical levels of varying thickness, and applied corrections to take into account the different conditions that affected the domain in the last deglaciation, specifically: 1) sea level was lower by ∼125 m on global average, at LGM and rising to present-day values during deglaciation (Peltier et al., 2015; Yokoyama et al., 2019); 2) expanded and thicker AIS, which evolved during deglaciation, exposing increasingly more continental shelf to the ocean, and forming ice shelves during stationary phases of the retreat and collapsed ice shelves during fast grounding line retreat. 3) ice-loading lithospheric subsidence has the effect of increasing water column depth near the ice sheet, and producing a fore-glacial bulge that reduced water column depth in the far field.

For 1) the paleo-sea level, the eustatic value (global-mean) was calculated by solving the Sea level equation with SELEN (Spada et al., 2012), with the ICE-6G ice chronology (Peltier et al., 2015); in this implementation, we left the sea surface at the reference present-day value (0 m) and applied a shift to the bathymetry opposite to the calculated paleo-sea level shift. For 2) and 3) the grounded ice and floating ice shelves from the numerical ice sheet/shelves model after (Lowry et al., 2019); this model was already run over last deglaciation with two atmospheric forcing: a colder one, forced with TraCE-21ka output, and a warmer one, forced with LOVECLIM (Menviel et al., 2011); the cold scenario was found to match well the retreat history reconstructed from geological records, especially in Eastern Ross Sea (Figure 4.1). In the Western Ross Sea, the grounding line in the "Lowry cold" scenario is missing the reentrances in the three major troughs (Halberstadt et al., 2016), possibly due to

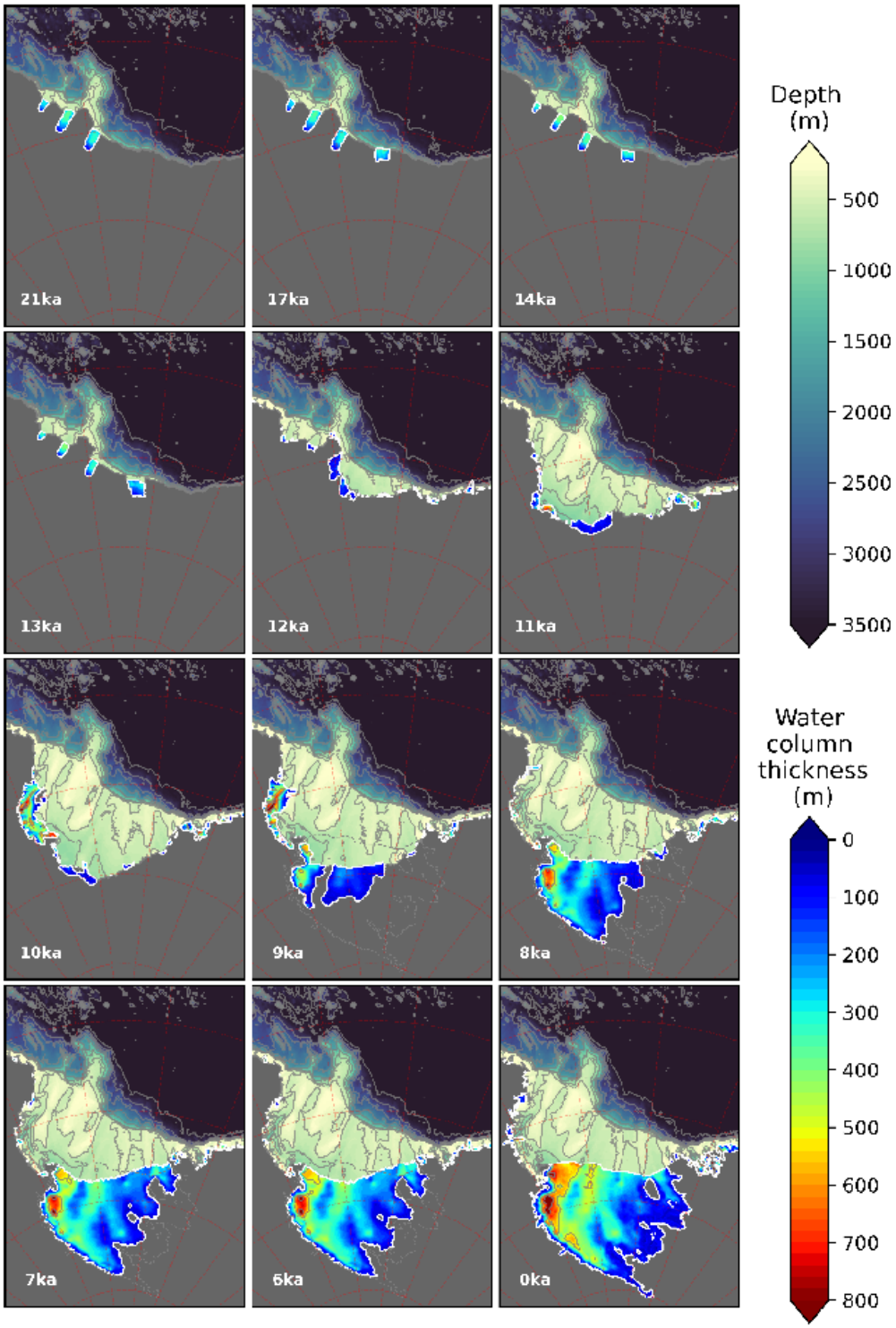

Figure 4.2: Paleobathymetry and water column thickness below ice shelves used in the paleo-oceanic simulations. The grey area corresponds to the grounded ice (and the position of the grounding line) while the white thick lines indicate the ice shelves area prescribed in our simulations. For snapshots 9-1 ka the boundary of present day RIS is added as dashed line.

the horizontal resolution of 10 km, not enough to capture the ice dynamics of these constrained ice streams. In these cases the grounding line position was produced by hand to match geomorphology reconstructions of Halberstadt et al. (2016). Ice shelves as well were added by prescribing a parabolic surface as ice shelf draft, starting near the grounding line and with a thickness at the front to match the present day RIS front; ice shelves extent was defined according to sedimentology analysis of paleo-environment (Prothro et al., 2020). The setup bathymetries for some snapshots are shown in Figure 4.2.

Model parameters are kept the same as the present-day run (see Chapter 2). That was a transient simulation forced by 3-hourly atmospheric reanalysis and monthly ocean reanalysis, for the period 1993-2018. It was validated qualitatively against Italian moorings, CTD and XBT casts of past cruises. Showing good overall agreement, and not having strong constraints on paleo-oceanography, the same set of parameters were employed for the paleo runs, with a few distinctions that were necessarily introduced to take into account the different atmospheric input frequency (monthly vs 3-hourly). An initial test was done by forcing the model with a monthly climatology based on ERA5 1990-1995, to see how the different frequency of atmospheric forcing impacted. The most dramatic change was an excessive warming of the surface layer in summer, related to the missing turbulent fluxes from wind fluctuations as documented in Wu et al. (2020). To decrease the amount of surface warming the incoming shortwave and longwave fluxes were reduced by 10%, which proved sufficient to reduce the gap in present-day run with monthly forcing with respect to the present-day 3-hourly forcing.

4.3 Results

Here we present the evolution of Ross Sea water masses and oceanic circulation, together with changes in ice shelves and grounding line. We focus on the continental slope, the continental shelf, and on the sub-ice shelf cavities that developed during the last deglaciation. The analysis has been done on the bottom water masses (Figures 4.3 to 4.5) and currents (Figure 4.6), on the water masses at ice shelf draft level (Figures 4.20 to 4.24), and on simulated basal melting (Figure 4.21). In general continental shelf water masses underwent gradual warming and desalinification starting from the LGM, (Figure 1.15 a,b). We analysed the vertical structure of the averaged SW in six vertical sections defined in Figure 4.11, coincident with the major Ross Sea troughs in Figures 4.12 to 4.16. Timeseries of average temperature and salinity at bottom and draft levels, and basal melting are calculated over the

Western and Eastern continental shelf and the RIS (masks shown in Figure 4.17), are shown in Figure 4.18. The overall evolution of the bottom and draft water masses is shown in Figure 4.8a,b. Basal melting evolution is reported in Figure 4.24.

4.3.1 Last Glacial Maximum (21 ka)

Simulated bottom water in the Southern Ocean, near to the continental slope are ∼-1.5 °C and high salinity of ∼36.75 g/kg (Figures 4.3 and 4.4). CDW on the slope was about 2.5 °C colder, at ∼-1.5 °C and 1.8 g/kg saltier, at 36.5 g/kg than in the present-day case. Vertical sections in Figures 4.12 to 4.15 and 4.16 show the evolution of the ASF, (compare with the present-day sections, Figure 2.5). Western of the Iselin Bank (Figure 4.2) a narrow area of continental shelf was available for circulation and brine rejection produced strong salinification and cooling down to the freezing point (Figure 4.3,4.4). This produced a strong V-shaped ASF and an intense ASC at the bottom level (Figure 4.6). Eastward of the Iselin Bank, by contrast, the bottom layer was warmer and fresher (Figure 4.3, 4.5), and the ASF there is much weaker. A persistent polynya was present in front of Whales Deep basin that produced deep convection, energising the bottom level ASC. The simulated bottom level ASC at the LGM was generally weaker than at present.

This difference in continental slope water masses is reflected in the water masses inside the sub-ice shelf cavities. The Drygalski trough, the westernmost (Figure 4.2), is the smallest and saltiest (Figures 4.3, 4.5 and 4.23). The whole water column is at near-freezing point (∼-2 °C), and has a salinity of ∼36.57 g/kg, with very weak stratification (Figure 4.12). This cold and salty water mass is produced in short lifetime polynyas opening in front of the ice shelves (not visible in winter sea ice concentration, (Figures 4.9, 4.10), and it is the LGM equivalent of present-day HSSW. The Joides trough, the centermost (Figure 4.2), has a vertical stratification of two water masses, caused by mixing of HSSW and meltwater (ISW): a water layer of salinity ∼36.52 near the ice shelf draft front, and a bottom layer of HSSW of salinity ∼36.57 g/kg, which reaches the grounding line (Figure 4.13). Finally the Pennel Trough, the easternmost (Figure 4.2), has two layers showing inverse temperature stratification: a top layer of fresh (34.45 g/kg) and cold (-2 °C) layer, overlaid onto a warmer (-1.8 °C) and saltier (36.5 g/kg) bottom layer (Figure 4.14).

The three different cases arise from different processes to the East and the Western of the Iselin Bank, and from the different ice sheet geometry that allowed for a HSSW reservoir in the Western continental shelf to be formed. The Pennel trough is frequently accessed by warm CDW (∼-1.5 °C), brought by geostrophic flow along the

AACC. Ocean circulation below the ice shelves is peculiar (Figure 4.7): in the Pennel Trough, a cyclonic gyre develops, and is active throughout the year. In the Joides Trough, an anticyclonic gyre develops during Autumn. In the Drygalski Trough only frontal currents develop in Autumn, probably due to its smaller size. Circulation in Joides and Drygalski is influenced by the input of negative buoyancy from brine-rejection and lateral density gradients between the cavities and the continental shelf waters. On average, the melting is much stronger in the Pennel trough ice shelf (Figure 4.21), and overall the three cavities of the Western Ross Sea (which includes the Pennel trough, even though it is Eastward of the Iselin Bank), produced a mean basal melting more than double than the present day value (Figure 4.26a). An overview of the water masses at draft level and their associated basal melting is reported in Figure 4.20. Monthly variability of bottom temperature and salinity are shown in Figures 4.18e,f.

4.3.2 The Meltwater Pulse 1A (14.6 - 14.3 ka)

The MWP-1A was the most intense episode of deglacial meltwater input to the ocean and of sudden sea level rise. Through feedbacks in the AMOC, it impacted the Southern Ocean oceanography a few centuries later, starting at 14.0 ka, and lasting until ∼13 ka. The AMOC response to the MWP-1A was captured in TraCE-21ka and therefore its impact is included in the regional model. At this period the ocean properties underwent strong changes: a sudden and intense warming of 1.5 °C of the sub-surface (400m depth) and up to 1 °C in the bottom layer, and a freshening of about 0.5 g/kg in the sub-surface and ∼4 g/kg in the surface layer, consistent with a large meltwater released from sea ice melting (Figures 1.15a-b, but notice when comparing with model output, that the fields in Figure 1.15 were not bias-corrected).

This impacted the bottom water properties on the slope, with warming of ∼0.5 °C. Western of the Iselin Bank (Figure 4.3, 4.12, 4.13) and 1 °C in the Pennel trough (Figure 4.14), with respect to glacial conditions. By contrast the Joides trough remains partially isolated by this event. The three cavities in Western Ross Sea had all the same bottom water salinity of 35.1 g/kg, consistently with a strong freshening of the surface layer, that inhibited sea ice formation and HSSW production. By 17 ka a new cavity had formed in the Whales Deep Basin (Figure 4.2), and at 14 ka it also underwent strong warming of the bottom level. The warmer CDW (∼-0.5 – 0 °C) reached the grounding line in the Pennel and Whales Deep troughs, and in the latter it filled the cavity up to the ice shelf front (4.16). The MWP-1A modified the properties of the ASF, by freshening and warming the subsurface layer, and where the core of CDW is found, causing sub-surface and deep isopycnals to flatten and

allowing inflows of CDW towards the continental shelf and the grounding line (as in the "warm shelf" depicted in Figure 1.9c). Overall the water masses at shelf draft had a markedly different response in temperature (Figure 4.22) and salinity (Figure 4.23). Interestingly, the greater depth of the Whales Deep continental shelf (∼600m) with respect to the Pennel (∼500m) allows more easily, and more saline (35.25 g/kg) CDW to access to the bottom layer and the ice shelf (Figure 4.16). The MWP-1A was therefore accompanied by a peak increase in basal melting, concentrated in the Pennel Trough and the Whales Deep Basin ice shelves. Figure 4.20 shows the importance of warm water masses for melting at 14 and 13 ka, and highlights the role of warm CDW and its mixing with meltwater (producing the slanted lines). Sea ice was affected as well: at 14 ka very few openings are produced and simulated sea ice cover persists during summer. At 13 ka summer polynyas start to open in the Western Ross Sea and on the Eastern side of the Iselin bank, allowing for more frequent cracks to develop, both in summer and winter.

4.3.3 Early holocene (∼11.8 ka - 9ka)

The Early holocene was characterised by low austral summer insolation (Figure 1.14c,i) warmer air temperature and higher longwave radiation fluxes, contributing to increased ice loss during summer and increased sea ice production in winter, in particular at 12 ka in the Western continental shelf (Figure 4.10). This increases HSSW production on the shelf, which increases the density gradient between the Western and the Eastern continental shelf at 12 ka Figure 4.5, and contributes to cooling the continental shelf waters (Figure 4.3). We begin to see outflows of RSBW across the slope in the Glomar Challenger Trough and strengthening of outflows from the Drygalski Trough. Ocean warming was on-going, with warm CDW (∼0 °C) impinging on the continental slope. Simulated intrusions of mCDW are present in all troughs, (Figures 4.12-4.16), penetrating by about 200 km in the direction along the troughs, in particular in those of the Western Ross Sea. However mCDW does not reach the ice shelves front, except for the Drygalski trough. At 12 ka, as the grounding line retreated, in Eastern Ross Sea an embayment had formed. Since the grounding line was in a retreat state, with scarce pinning points, especially on the Eastern continental shelf, only a few and small ice shelves formed, as highlighted in surface area extension over continental shelf, reaching ∼5% (Figure 4.19). Those two most prominent are formed: 1) in the inner Glomar Challenger Trough at 11 ka, when the grounding line reached Ross Island and 2) at 10 ka, in the Drygalski basin, sourced by ice streams from the EAIS crossing the Transantarctic mountains, and pinned to Mawson bank (Figure 4.21). At 11ka the grounding line had retreated enough to allow for the Eastern and Western continental shelf to become connected

by ocean circulation. Still at 10 ka the ice shelf in the Glomar Challenger was pinned to a submarine ridge that partially slowed the retreat, at least in our ice sheet geometry reconstruction. This Eastern cavity, which at 9 ka was split in two sub-cavities separated by the ridge, began to slowly enlarge and coalesce into a single cavity, forming the proto-Ross Ice Shelf cavity (Figure 4.21). Ice stream retreat allowed the ice thickness to decrease and water column thickness to increase, fostering circulation beneath it. The water masses responsible for this retreat are: 1) warm modified CDW intruding from the Eastern continental shelf along the Hayes and Houtz Banks, and melting beneath the Eastern sub-cavity (Figure 4.21-4.22) and 2) HSSW from the Western Ross Sea melting in the Western sub-cavity. The Drygalski cavity, instead, is not reached by strong currents, possibly shielded by a East-to-West current that flows along the Southernmost extremity of the Ross, Pennel and Crary Banks (Figure 4.6); basal melting there is quite low (Figure 4.21). It is noteworthy that in this period extended sea ice is found over most of the Southern Ross Sea continental shelf.

4.3.4 Middle and Late Holocene (6 - 2 ka)

Since 6 ka the climate in the Ross Sea sector shows little difference with the present day Figure 1.14g-q). Ocean fields as well have reached a vertical structure very similar to the present day. With respect to the Early Holocene, two features are strikingly different: 1) HSSW is broadly present with strong salinity characteristics, filling the bottom layer of the continental shelf (Figures 4.12-4.16); 2) the salinity of the open ocean deeper than 1000m, is now less than the HSSW continental shelf; in particular the AABW if now less salty than HSSW (cfr 6 ka with 9 ka, Figure 4.4). This has implications for the density gradient across the shelf break, which is markedly stronger. HSSW now fills most of the continental shelf. The ASF, which regulates across slope transport, is now well developed and strengthened by the baroclinicity of the tilted isopycnals at the continental shelf break. We now have strong outflows of RSBW across the slope in the Glomar Challenger Trough and Drygalski Trough and exchanges of RSBW and mCDW across the Joides, Pennel. The RIS cavity at 6 ka is well developed and similar to the present day extension, although the central frontal part has a concavity, due to the ice sheet model probably underestimating ice stream flux. Circulation across the cavity is similar to the present day (Figure 4.6), with HSSW entering near Ross Island and reaching far inside, near the grounding line. The Western side of the RIS cavity is this highly saline and near freezing (Figure 4.22,4.23). On the Eastern RIS, warm intrusions along Hayes Bank and Houtz Bank warm the frontal part of the cavity, which, with respect to the Western side, is also less saline (Figure 4.22-4.23). Dense HSSW outflowing from

the cavity into the Glomar Challenger Trough is now strong and continuous. Sea ice is now experiencing a seasonal cycle similar to the present-day one, with an ice free corridor opening in summer, driven by Southerly circulation. Interestingly the Drygalski trough remains covered by fast-ice.

4.4 Discussion

The results shown in the previous section highlight the main changes that took place during the last deglaciation in the Ross Sea. The observed changes during the simulations are broadly determined by:

1. external forcing, long term trends in ocean and climate and feedbacks contained in the TraCE-21ka simulations;
2. ocean dynamics at the continental slope (the ASF), determining the transport of water masses over the continental shelf break;
3. internal ocean dynamics and interplay of the continental shelf waters;
4. interactions with the sub-ice shelf environments.

At the LGM, different ocean salinity and temperature are simulated Westward and Eastward of Iselin Bank at the LGM, showing the strong impact that the Iselin Bank had on sea ice transport and the AACC. The Eastern Ross Sea shelf was already fresher than the Western, which already was a region of HSSW formation. Higher AABW salinity at LGM than HSSW may represent stronger open ocean sea ice formation, and weaker coastal polynyas formation; the latter is supported in the Weddell sea, by Nd and Pb isotope records, showing missing AABW sourced by the Weddell Sea at last two glacial maxima (Huang et al., 2020).

The difference in temperature and salinity between the two sides of Iselin Bank may have had an impact on the evolution of the water masses and on the AIS deglaciation. In general a fresh anomaly Eastern continental slope is more prone to allow warm intrusions and make them more persistent: this was observed with moored instruments in Eastern Weddell Sea in 2017 (Ryan et al., 2020). Simulated impact of the MWP-1A highlights that a similar mechanism may have occurred in the past, and would have likely triggered AIS initial retreat in the Ross Sea sector, around 14-13 ka. Following the strong input of freshwater in the North Atlantic and AMOC slowdown, by the "bipolar-seesaw" heat remains trapped in the deep levels of the Southern Ocean, and pushed towards the AIS margins. The high salinity

and high temperature of the deep Southern Ocean, which reached the depth of the continental margins, and the freshening of the continental slope surface and sub-surface, visible in all 14 ka snapshots (notice the slope of the 35.1 g/kg isohaline in the first ∼600 m depth, and the flatter 35.3 g/kg isohaline at ∼800-1000m depth, corresponding to the 0 °C isotherm, Figure 4.12-4.16) was probably a sufficient cause to tilt the "fresh"-type isopycnals (Figure 1.9a) of the Eastern ASF into a "warm"-type ("flat") state, which allowed free access of CDW to the grounding line in the Whales Deep Basin (Figure 4.16), at the longitude of the Glomar Challenger (4.16), and partially in the Pennel Trough (Figure 4.15). The meltwater feedback that further depressed the surface and sub-surface isopycnals provided a positive feedback for the process. Interestingly no ice shelf was detected in the Glomar Challenger Trough, as for the reconstruction of Halberstadt et al. (2016), which suggested that the ice sheet was grounded near the shelf break. Still between 14-13 ka, our simulations show high ocean temperature (∼0 °C) at the grounding line (4.15), coincident with the frontal wall. This would have caused high frontal melting, not implemented in the MITgcm that may have provided means of causing retreat by destabilising the ice column at the front, even in the case no ice shelf existed. Numerical ice sheet modelling by Golledge et al. (2014) shows AIS retreat following the MWP-1A starting in the Glomar Challenger Trough region at 13 ka, rather than in Whales Deep at 12.5 ka, hinting for a possible generilised retreat over all the Eastern Ross Sea, with the same machanism involving ASF perturbation to a "warm" state. It is interesting to note that the shelf in the Whales Deep Basin is about 100m deeper than the shelf break in the Pennel, which despite being accessed by warm CDW since the LGM did not experience a sudden collapse; a possible explanations is that lateral buttressing from the walls of the trough may have provided the necessary stability. The "cold" (or "salty") type ASF probably resisted in the Drygaslki and Joides, that faced a shallow shelf break, located (∼500m), and ∼100m shallower than the 0 °C isothermal and the 35.3 g/kg isohaline, whereas the Glomar Challenger and Whales Deep face a deeper shelf break (∼700m). This makes the background oceanic setting ("cold/salty" shelf vs "warm/fresh" shelf) a strong precursor for triggering AIS retreat. The impact of the shelf break depth, makes it important to correctly include GIA and flexural deformation (i.e. foreglacial bulge) processes also in paleo-oceanographic studies. The impact of wind-driven upwelling seems to be not significant to drive large volumes of CDW (Figure 4.25) although given the presence of sea ice cover an analysis on surface wind stress on the ocean would be more suitable.

Later in the Early Holocene (11.8 - 9 ka), although the Eastern continental shelf and the main troughs were still accessed by the warm mCDW, a large portion, mostly the West, increased interaction with the atmosphere, by heat fluxes and

sea ice production. HSSW reached the newly formed RIS on the Western side. In the final stages of deglaciation, thus, HSSW impacted more on the AIS retreat. Quantifying the amount of melt caused by each water mass, as done in Chapter 3, remains challenging here, since the water masses experienced large changes in their properties (Figure 4.8), and therefore this characterisation was not attempted in the course of this work. Interestingly the fast retreat of the AIS, occurred in an insolation regime that was unfavourable to the austral summer warm, and increased precipitations by global warming may have had a compensating effect on the AIS mass balance. Analysing the impact of varying teleconnections was not attempted here, although there are indications that ENSO became increasingly important over the deglaciation, possibly affecting coastal winds, and sea ice transport in the Amundsen Sea. Strengthening of the subpolar jet during deglaciation may also foster enhanced advection of CDW towards the continental margins (Lamy et al., 2019).

Uncertainties

There are several uncertainties that need to be considered in this work: 1) the external forcing and boundary conditions and the bias correction; 2) the simulated AIS geometry employed, and the parabolic ice shelves added accordingly to Prothro et al. (2020).

1) The paleoclimate Atmospheric Ocean General Circulation Model (AOGCM) that was employed in TraCE-21ka, the Community Climate System Model version 3 (CCSM3) was run on a coarse grid that badly represents surface near processes at the resolution employed here (5 km). The AIS topography also employed in TraCE-21ka is the poorly realistic ICE-5G over Antarctica, that in the Ross Sea did not feature an expanded ice sheet, therefore greatly impacting winds and coastal circulation. The ocean component of the AOGCM is even coarser: this causes a well-known cold bias (Yeager et al., 2006) and displaced currents and water masses (i.e. the Ross gyre is displaced Westward and Northward). As such the bias correction was necessary to reduce the offset with observation, based on high resolution reanalysis that assimilated a growing number of observations. The poorly realistic sea ice simulated here, is possibly a cause of the combined effects of the "cold bias", the low resolution and the possibly shrinked wind belt. Forcing with monthly frequency atmospheric fields highlighted several issues, reported here (Wu et al., 2020), in the surface layer. Moreover the missing high frequency variability of the winds, such as the katabatic winds did not cause the sea ice cover to break apart, unless considerably extensive summer polynyas already provided the conditions. Another set of uncertainties comes from the relatively unknown and uncertain physical properties of the Southern Ocean at the LGM.

2) The simulated ice sheet retreat scenario adopted here (Lowry et al. 2019, "cold scenario"), forced by TraCE-21ka inherited some of the issues described above, although it matched well the reconstructed retreat of Bart et al. (2018) in the Whales Deep Basin, it does not match well with the reconstructions of the Western Ross Sea, some of which suggest an early retreat in the Drygalski region (Figure 4.1). Reconstructions in the Western Ross Sea are uncertain also from the observation point of view, with some unexplained open marine onset at old ages (Prothro et al., 2020). This may have provided the wrong ice sheet geometry to our model. The Glomar Challenger Trough may have been a major location of AIS retreat, given the lack of pinning point and low GZWs left inland; reconstructions have not reached certainty on it being completely grounded at the LGM, however in our study we implemented it as grounded, and we were therefore not able to simulate basal melting beneath.

Comparison with observations

A broader difficulty of paleoceanographic studies is the comparison with observations. High resolution models proxy reconstructions of the results are associated with the forcing and boundary conditions, and with the physical implementation of processes in the ocean model. Sedimentary foraminiferal analysis of proximal glacial environment at LGM in the Joides and Pennel troughs by Majewski et al. (2020) points out at deposition at LGM in an environment of HSSW and moderate circulation, compatible with our simulations in the Joides Trough; the comparison differs for the Pennel, which in our simulation is much fresher at the bottom level than the other troughs. mCDW in foraminiferal assemblages was recorded during deglaciation, which confirms our results of mCDW intrusions at early stages of grounding line retreat in the Western Ross Sea. The widespread presence of HSSW in the reconstructed open-marine environment is also in line with our results. Interestingly, low production of HSSW in the LGM scenario, compatible with reduced available volume of the continental shelf reservoir, is paralleled by missing AABW production in the Weddell Sea at the LGM Huang et al. (2020). Kim et al. (2018) observes in two cores drilled in Northwestern Iselin Bank, that glacial periods are typically characterised by low surface water productivity and nutrient utilisation, with sea ice diatoms and planktonic foraminifera indicative of extensive sea ice cover. They hypothesise a strengthening of the ASC driven by stronger glacial winds, despite that more persistent and extended sea ice cover would have partially decoupled the ocean from the atmosphere. Marine radiocarbon dates from previous studies suggest that the Eastern Ross Sea deglaciated before the Western Ross Sea (Licht and Andrews, 2002; Mosola and Anderson, 2006), despite complications dating Antarctic glacimarine

sediments. Western Ross Sea banks supported an extensive ice shelf that buttressed WRS grounding lines and contributed to the long-lived presence of the EAIS in the WRS (Anderson et al., 2014; Yokoyama et al., 2016; Prothro et al., 2020).

4.5 Conclusions

We run a regional ocean model of the Ross Sea, for 21 snapshots at intervals of 1000 years, to simulate ocean circulation in the Ross Sea over the last deglaciation (21 - 0 ka). The main findings are:

1. LGM circulation limited to three sub-ice shelf cavities in the Western Ross Sea; of these, the Drygaslki and Joides were filled with HSSW, and the Pennel was instead frequently reached by CDW;

2. Following the Meltwater Pulse 1A (14.6 - 14.3 ka), deep ocean warming and sub-surface ocean induced a weakening of the Antarctic Slope Front, which fostered CDW flow in the Pennel and the Whales Deep cavities. Those experienced high rates of basal melting, whereas the Drygalski and Joides were not impacted considerably. HSSW production in the Drygaslki and Joides troughs stopped during this event;

3. In the Early Holocene (∼11.8 ka) grounding line retreat uncovered growingly portions of the continental shelf, allowing stronger atmospheric cooling and resumption of HSSW production. After RIS cavity formation (∼10 ka), a pathway for HSSW established to the Westward side by HSSW, whereas on the Eastward side, mCDW was advected along the Banks.

These results indicates a shift in the stronger melting role, from the CDW, that initially triggered retreat in the Eastern Ross Sea, to the HSSW formed on continental shelf polynyas. Tides, which are not included in these simulations, may contribute to weaken the ASF in the Western Ross Sea, where the shift to a "warm" state is not reached alone by deep ocean warming and surface ocean freshening; that would have the effect of enhancing CDW intrusions also at that locations. Tides may also increase melting by enhancing currents speed in Western Ross Sea cavities, filled with HSSW. However impact of tides on the ASF in Eastern Ross Sea is probably small, due to a baseline state already in a "warm" ASF state. Simulated water masses agree with the scarce geological observations of Majewski et al. (2020), that report HSSW at LGM in the Joides and Pennel, followed by mCDW during Early Holocene, and again HSSW formation Majewski et al. (2020) in the Late Holocene. It is uncertain

how the Glomar Challenger Trough would have responded to the ASF perturbation, for it is grounded in the reconstructions we employed; nonetheless warm water is able to reach its grounding line during the MWP-1A, and it would trigger a fast runaway retreat. This set of simulations points to deep ocean warming, intermediate ocean freshening, and bipolar "seesaw" feedbacks in the Southern Ocean as main drivers of past AIS retreat in the Ross Sea. It will be the subject of future work to compare these simulated results with the range of paleo observations that have been collected during the last IODP and PNRA missions, which are also integrated in the framework of ANTIPODE (Figure 4.26).

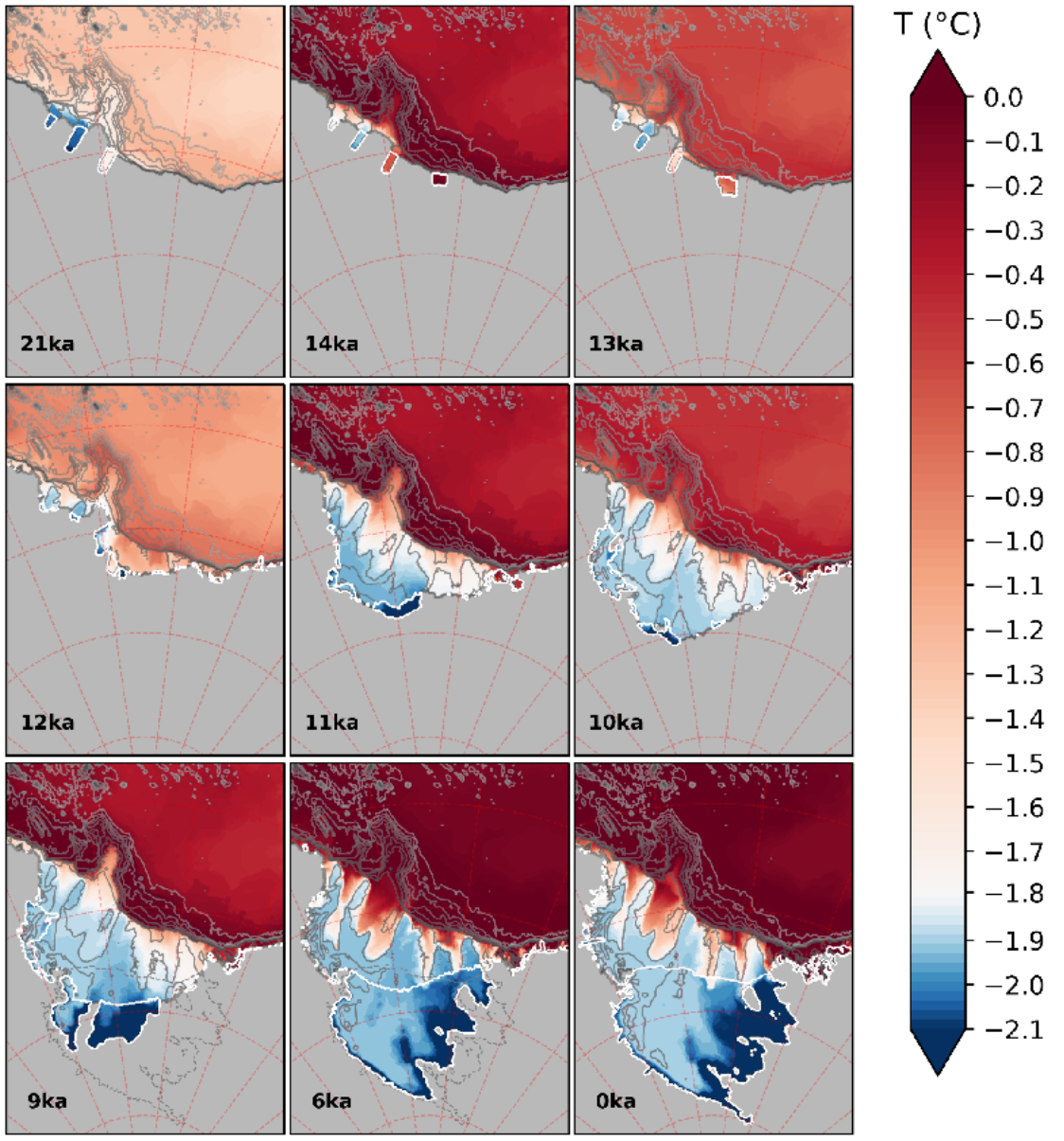

Figure 4.3: Simulated mean annual bottom temperature (°C) for some of the snapshots of the Last Deglaciation. Temperatures are averages over the 26 years long snapshots. Grounded ice is shown in gray and the thick white line represents the ice shelves areas. The dashed line shown in the 9 ka and the 6 ka snapshots shows the location of the present-day grounding line (Bedmap2, Fretwell et al. 2013). 0 ka is the present day control (see Chapter 2).

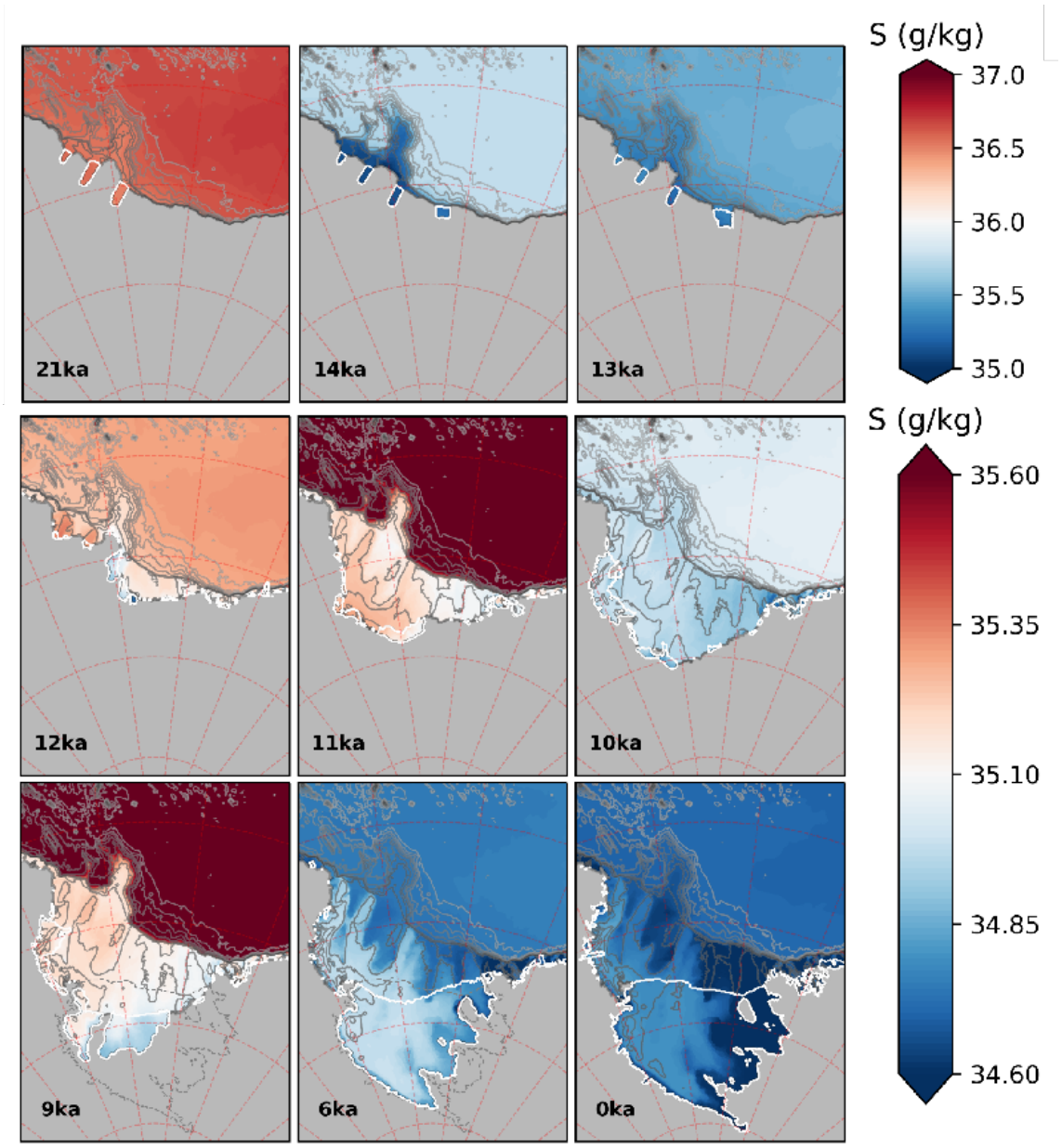

Figure 4.4: As for Figure 4.3, but for simulated mean annual bottom salinity (g/kg). Note that for the 21 ka, the 14 ka and the 13 ka, the colour scale differs from that of the other snapshots due to the large salinity variations.

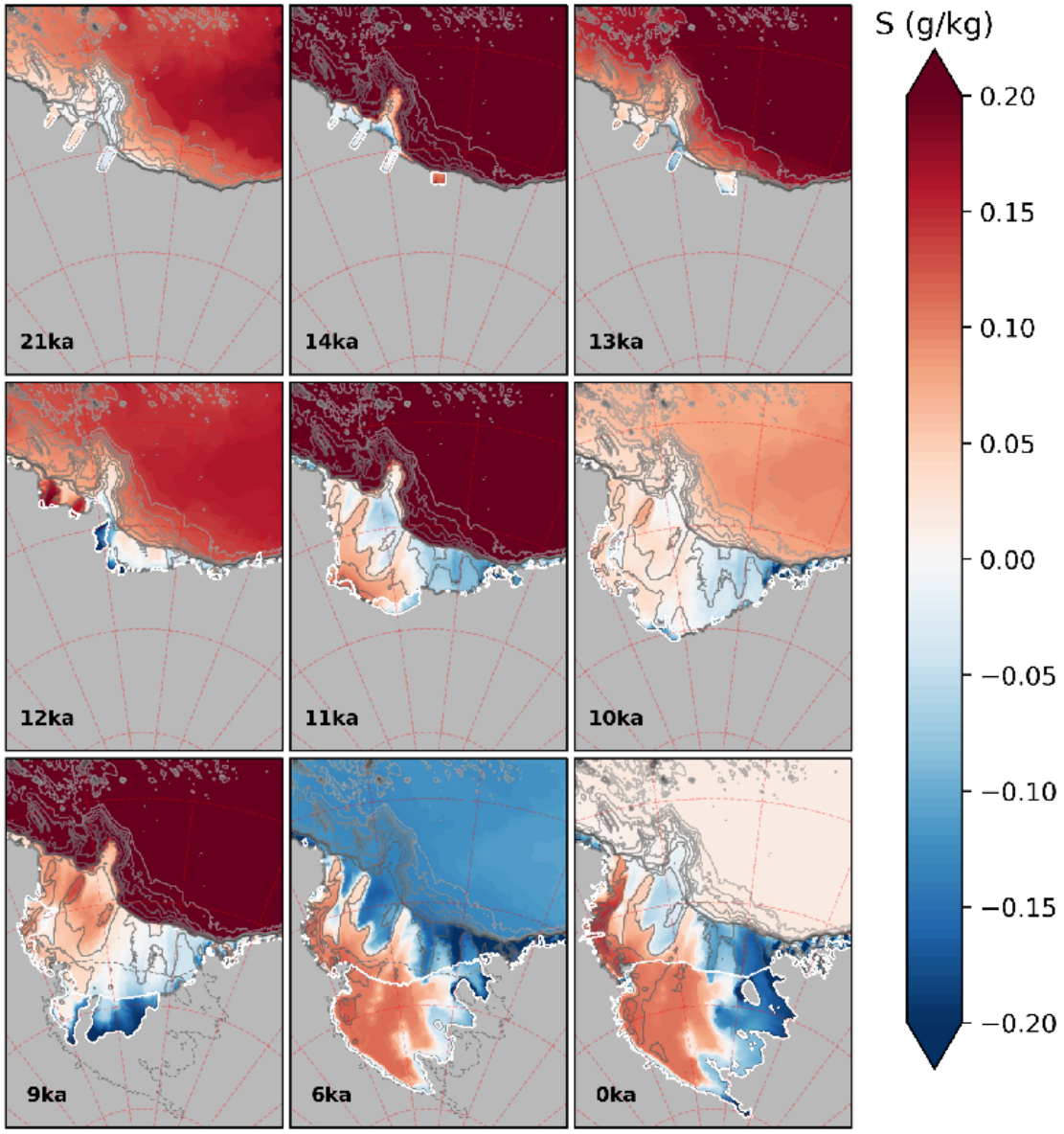

Figure 4.5: As for Figure 4.3, but for mean annual simulated bottom salinity **anomaly** (average over 26-years) with respect to spatial mean over the continental shelf region. The anomaly highlights the relative difference in salinity of Western and Eastern continental shelf.

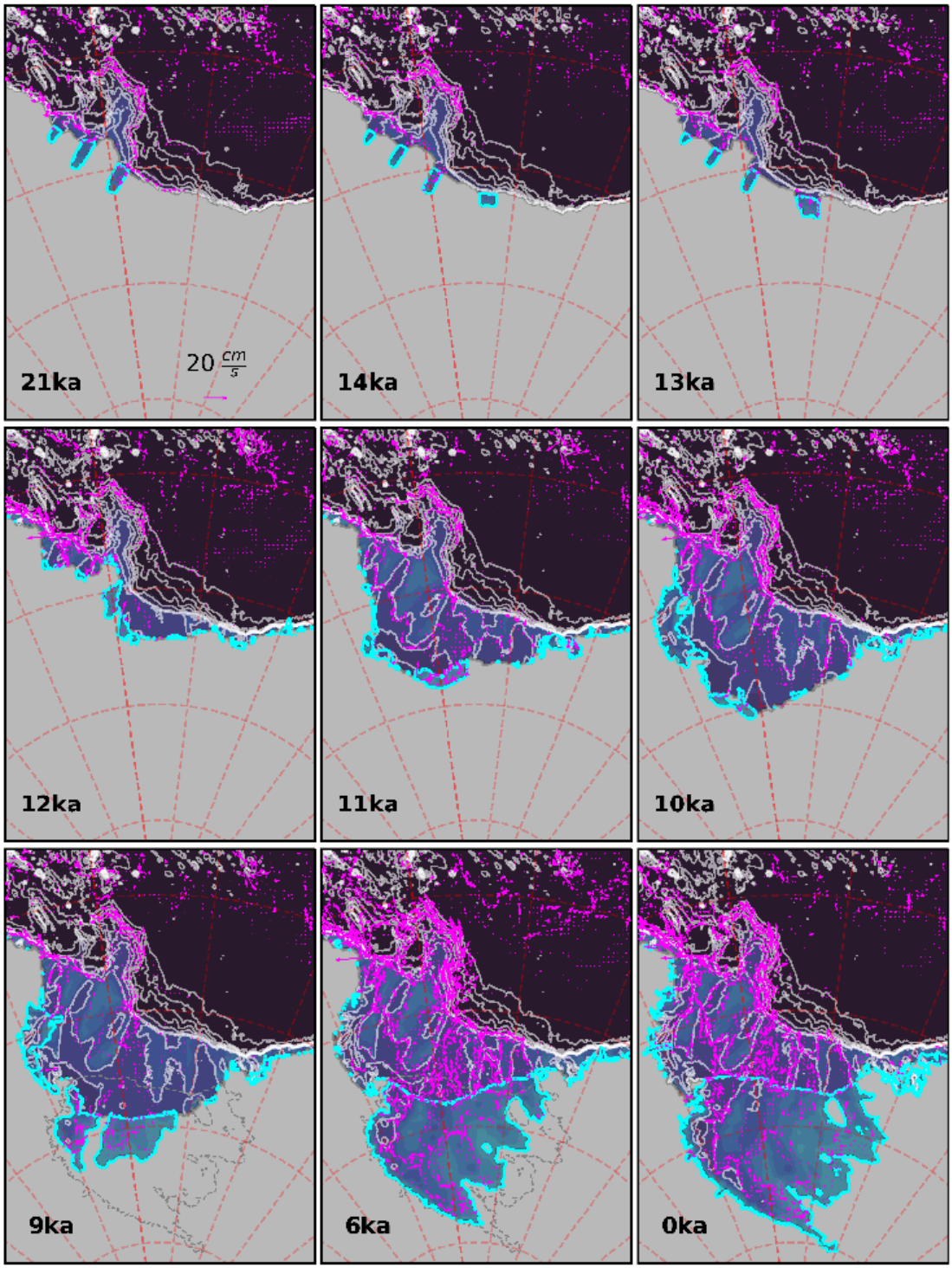

Figure 4.6: Bottom currents evolution during the last deglaciation averaged of the entire duration of the snapshots. Only currents stronger than 1 cm/s are shown, for readability. Grey area corresponds to the grounded ice, the thick cyan line represents the ice shelves area. The dashed line shown in the last row is the present-day grounding line (Bedmap2, Fretwell et al. 2013). Snapshot at 0 ka is the present day control, as of Chapters 2,3.

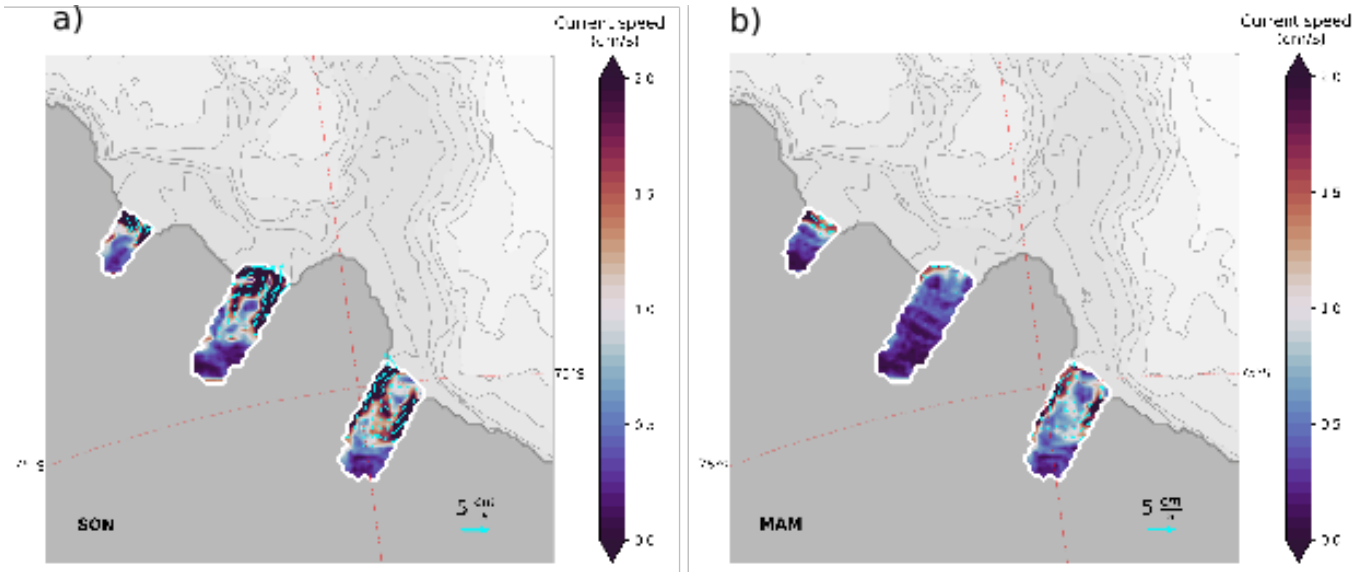

Figure 4.7: Simulated LGM (21 ka) mean annual currents speed at ice shelves draft for(a) austral spring and (b) austral autumn

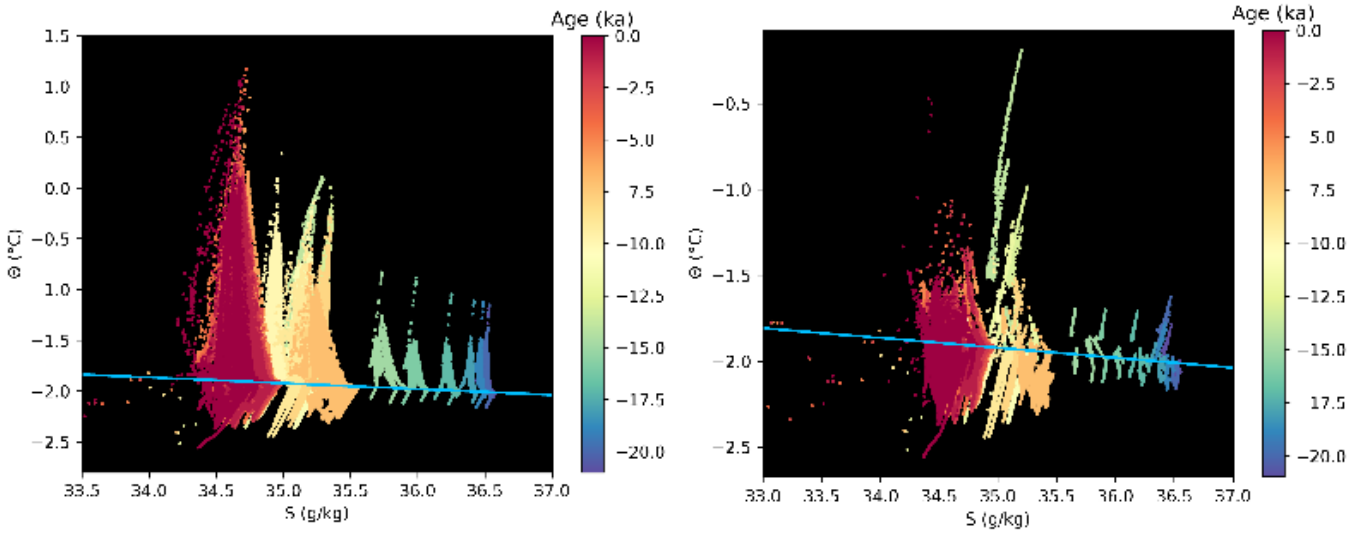

Figure 4.8: Scatter plot of the mean annual simulated temperature and salinity at bottom level (a) and at the ice shelf draft (b). Colours correspond to the time of the snapshots, from LGM (21 ka, blue) to present (0 ka, bordeaux).

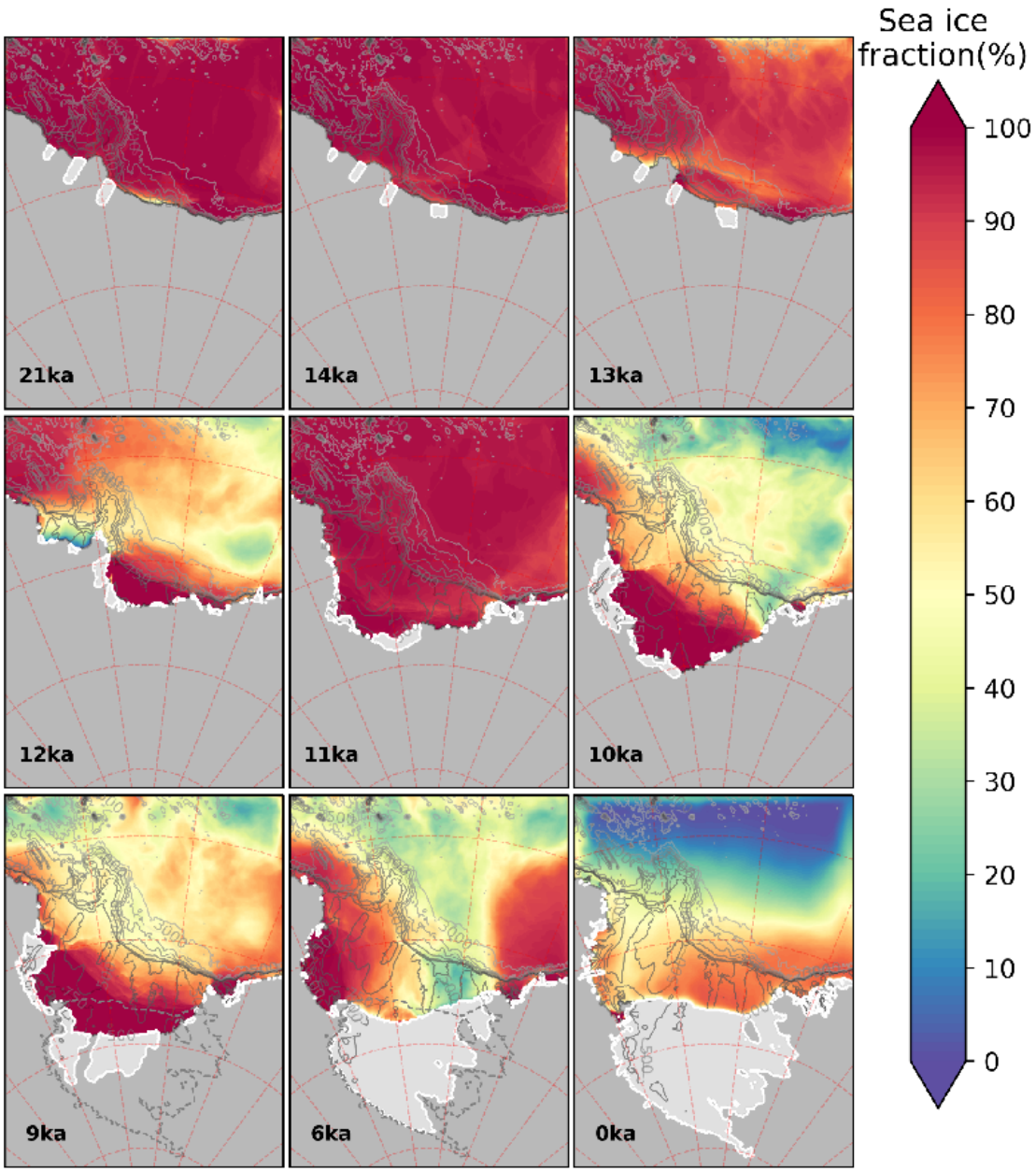

Figure 4.9: Simulated February sea ice concentration (%), highlighting austral summer sea ice extent (climatological mean over the duration for the snapshots). Multi-year ice areas in the snapshots correspond to the bordeaux colour.

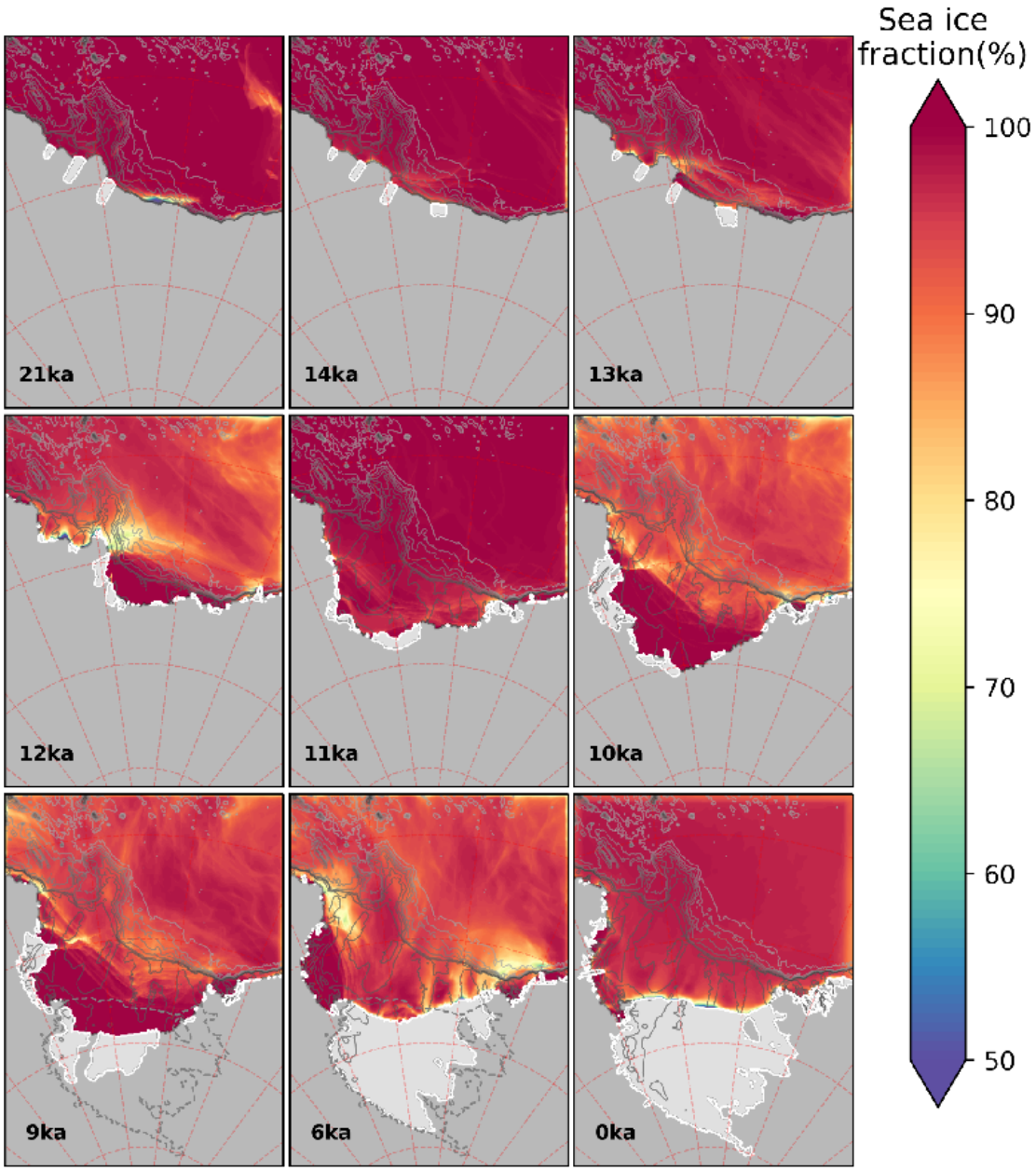

Figure 4.10: Simulated sea ice concentration (%) in the month of September (climatological mean), highlighting late winter sea ice extent. Note that our model simulates some opening of small polynyas as well as frequent cracks in the sea ice cover (green to yellow colours). Small but active polynyas that formed on a daily basis are not captured by this monthly climatology.

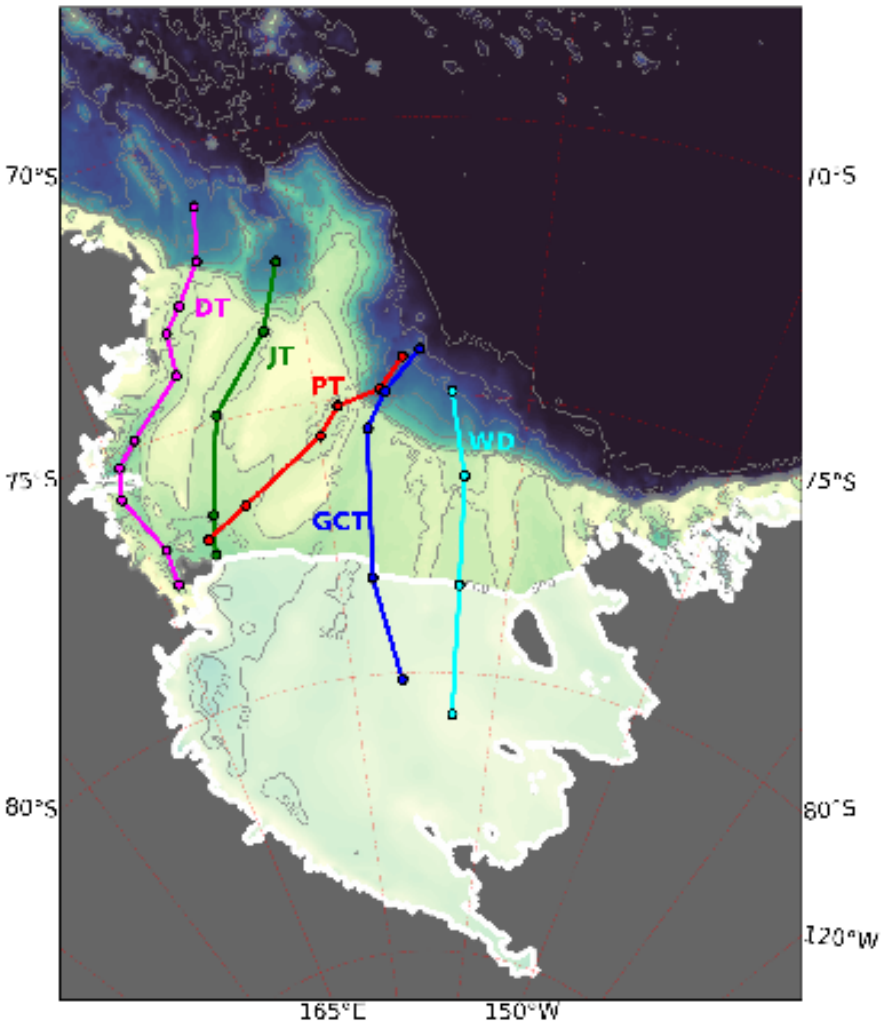

Figure 4.11: Transects along the major troughs discussed in the text, plotted over the present day bathymetry, where mean ocean temperature and salinity are extracted in Figures 4.12 to 4.16. Note that in 4.12 to 4.16 the bathymetry and ice shelf are those employed in the paleo experiment.

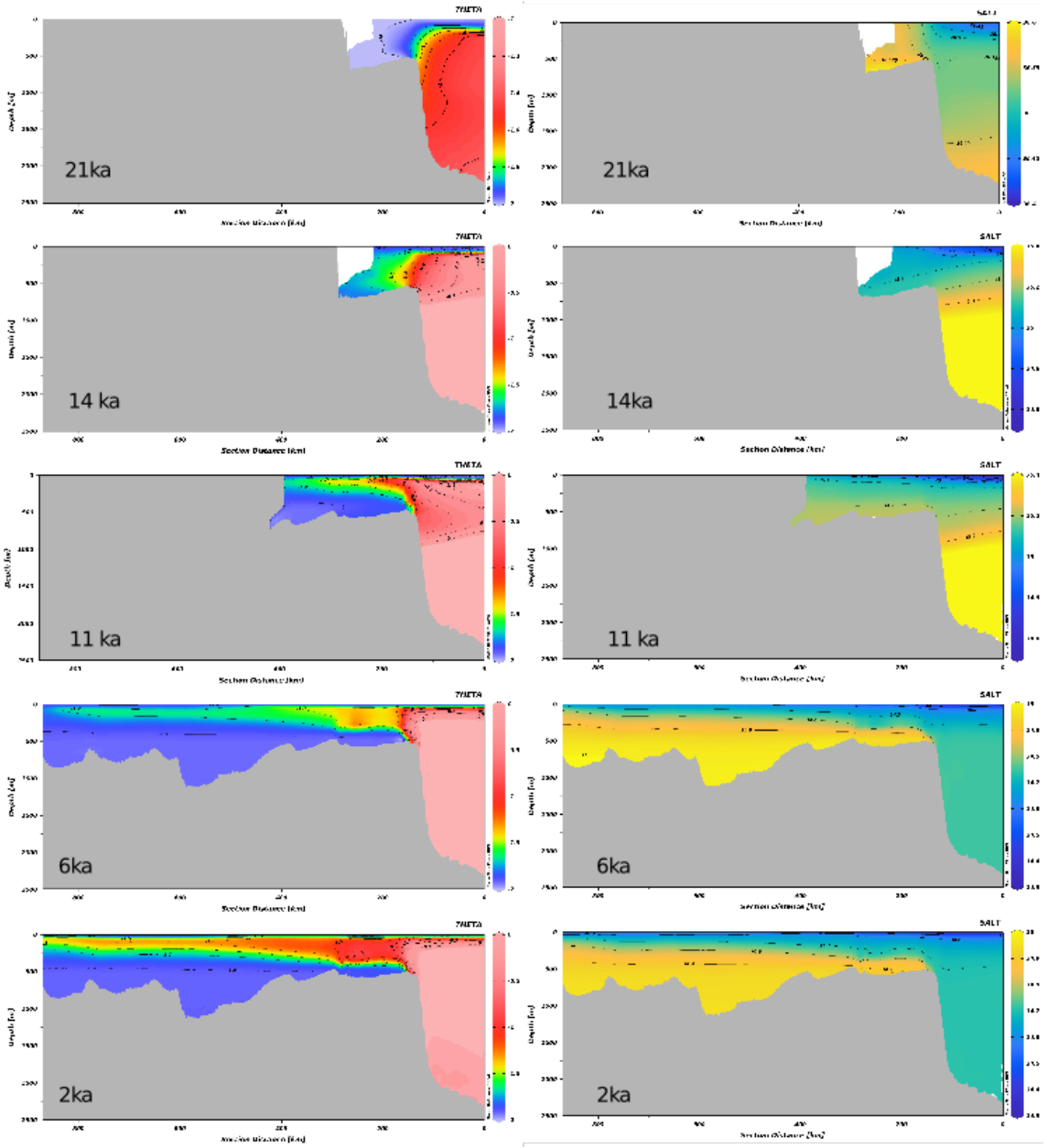

Figure 4.12: Vertical transect of mean annual simulated oceanic temperature (°C, left column) and salinity (g/kg, right column) over the last deglaciation in the **Drygalski Trough** (see Figure 4.11). Note the change of colour scale in temperature, between 21 ka and the other snapshots and the change of colour scale in salinity between 21 ka and 14 ka and between 11 ka and 6 ka. This was necessary for a better understanding of the processes.

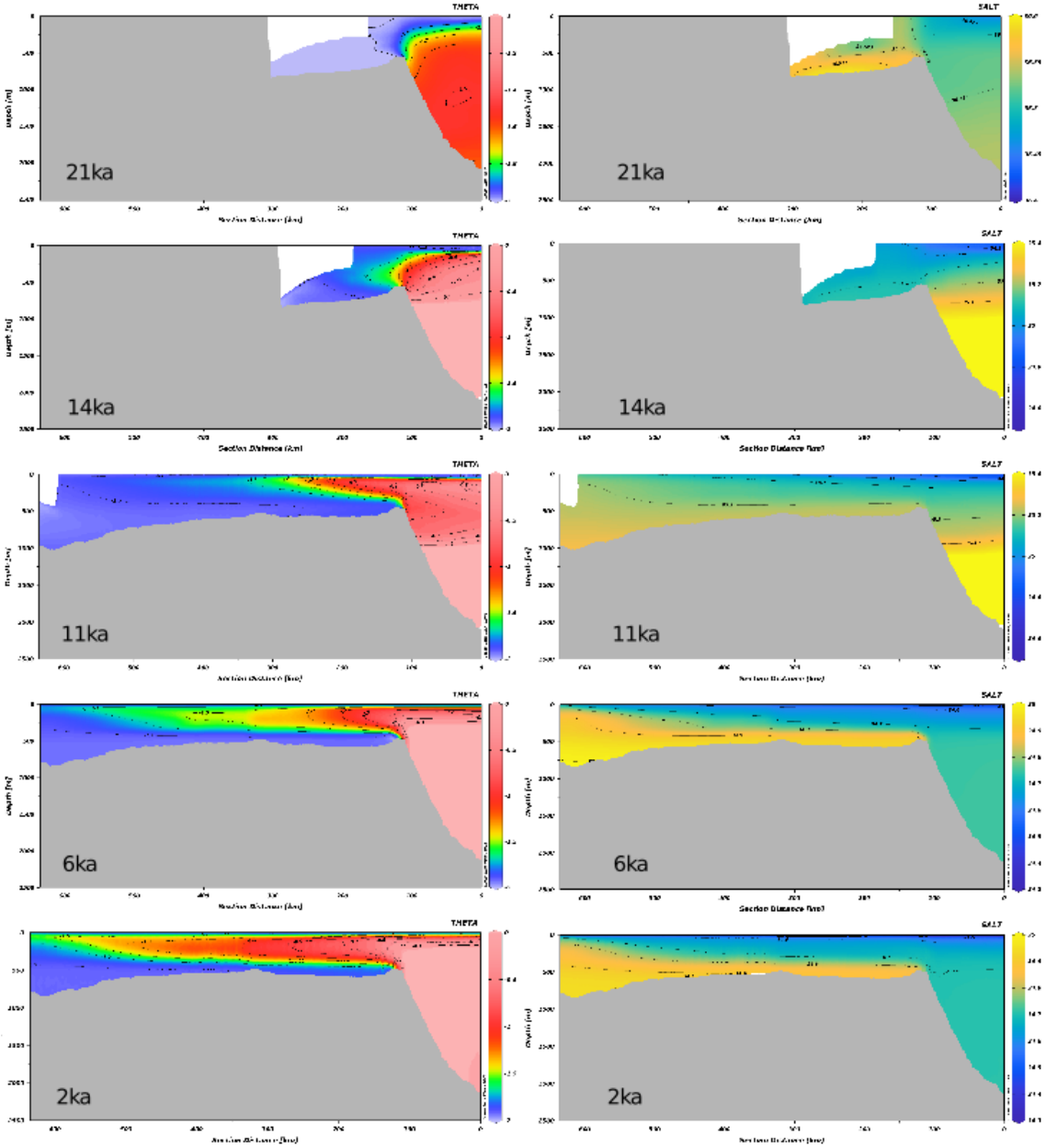

Figure 4.13: As for Figure 4.12 but for the **Joides Trough** (see Figure 4.11). Note the change of colour scale in temperature at 21 ka relative to the other snapshots and the change of colour scale in salinity between 21 ka and 14 ka and between 11 ka and 6 ka. This was necessary for a better understanding of the processes.

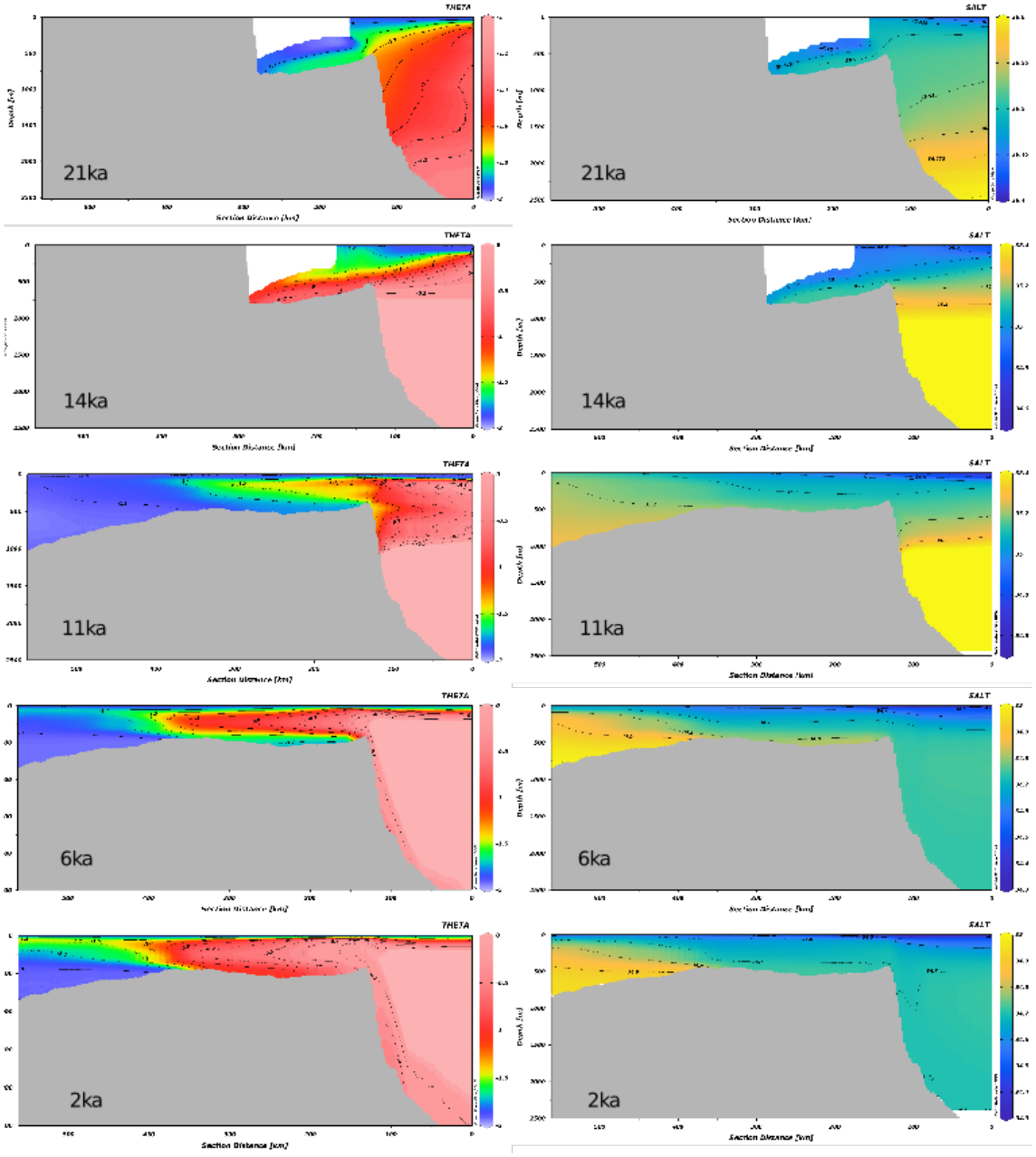

Figure 4.14: As for Figure 4.12 but for the **Pennel Trough** (see Figure 4.11). Note the change of colour scale in temperature at 21 ka relative to the other snapshots and the change of colour scale in salinity between 21 ka and 14 ka and between 11 ka and 6 ka. This was necessary for a better understanding of the processes.

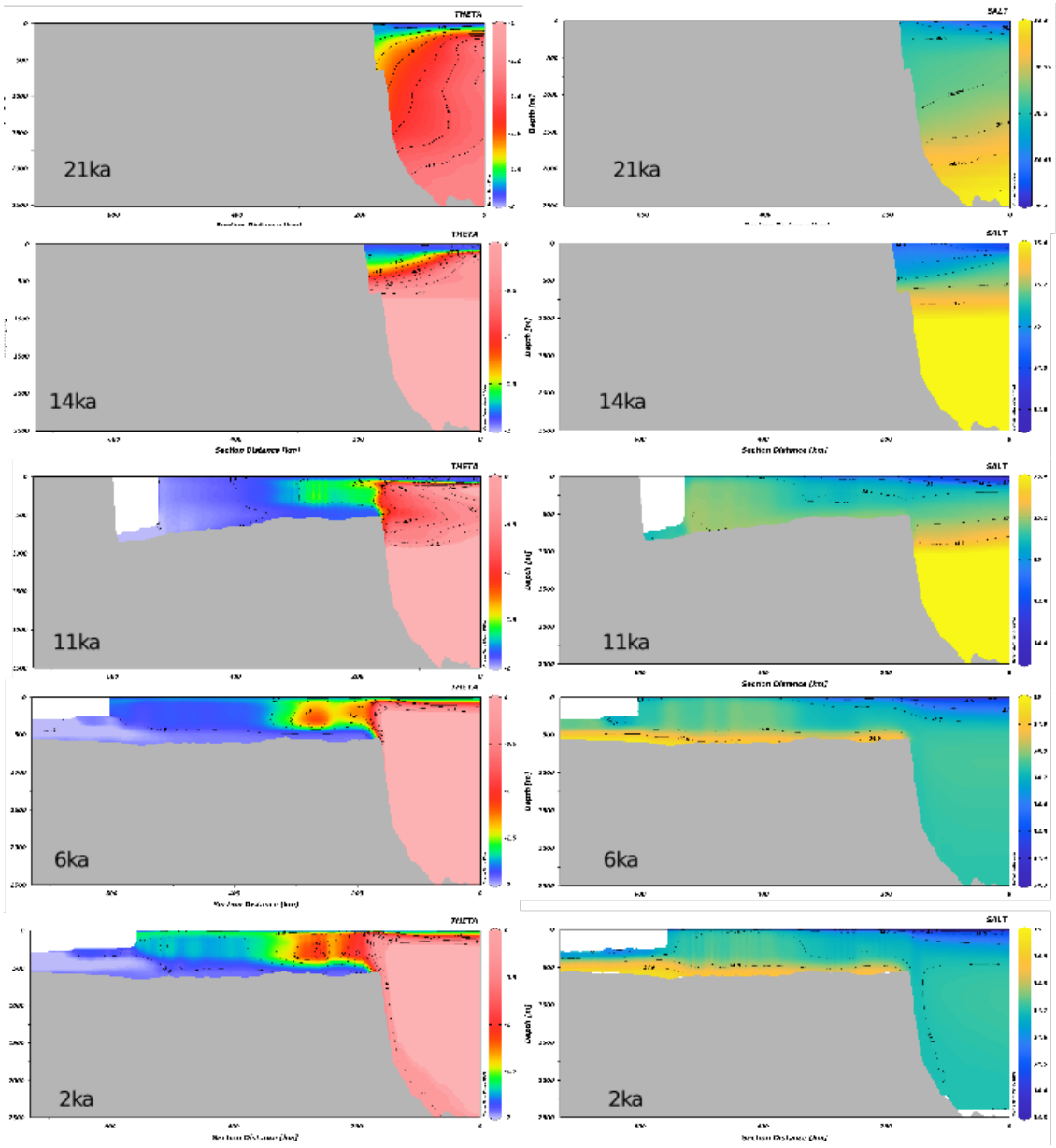

Figure 4.15: As for Figure 4.12 but for the **Glomar Challenger Trough** (see Figure 4.11). Note the change of colour scale in temperature at 21ka relative to the other snapshots and the change of colour scale in salinity between 21 ka and 14 ka and between 11 ka and 6 ka. This was necessary for a better understanding of the processes.

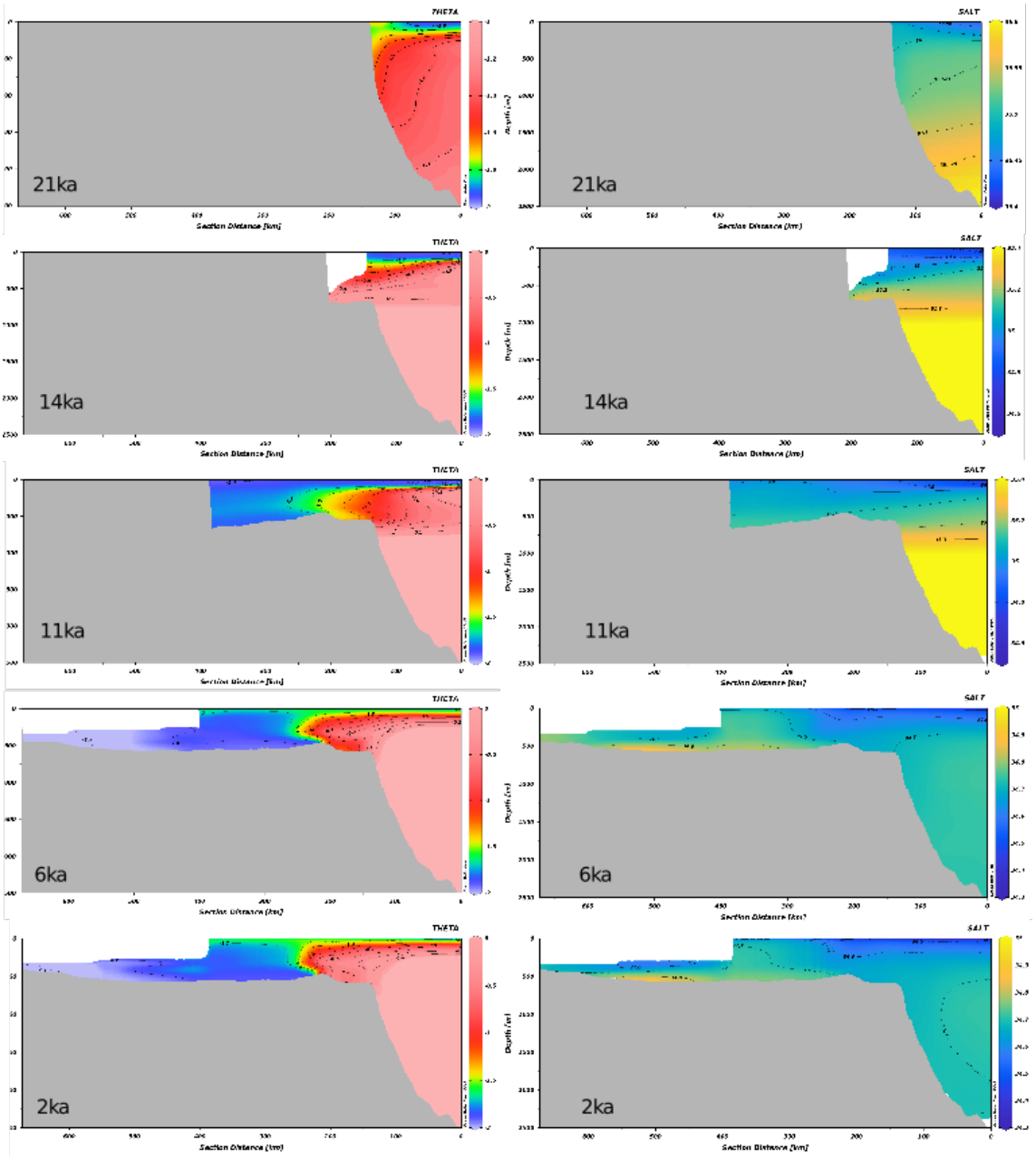

Figure 4.16: As for Figure 4.12 but for the **Whales Deep Basin** (see Figure 4.11). Note the change of colour scale in temperature at 21 ka relative to the other snapshots and the change of colour scale in salinity between 21 ka and 14 ka and between 11 ka and 6 ka. This was necessary for a better understanding of the processes.

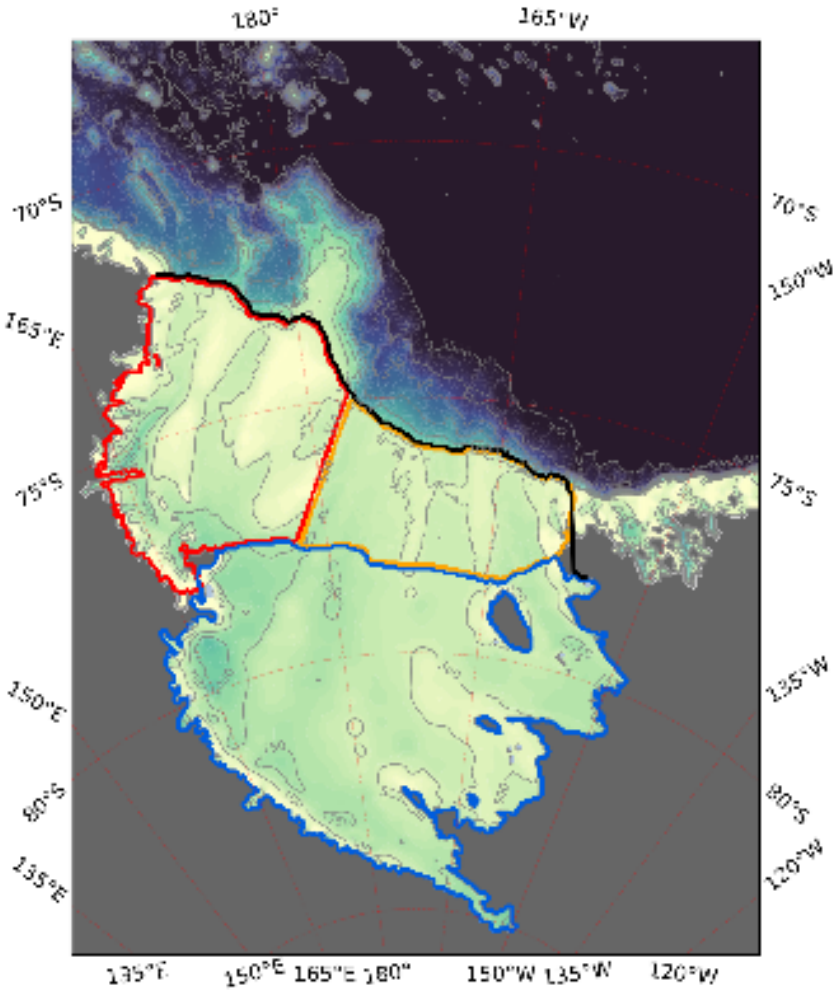

Figure 4.17: Areas used to compute oceanic averages for each snapshots. The Western Ross Sea continental shelf (red), the Eastern Ross Sea continental shelf (orange) and Ross Ice Shelf cavity (blue). Note that the Eastern Ross Sea, is located where longitudes are °W and vice-versa for the Western Ross Sea, where longitudes are °E, following the convention of the community (with South pole downward). The thick black line shows the continental shelf break at ∼700 m depth, which is the isobath used for fluxes computation.

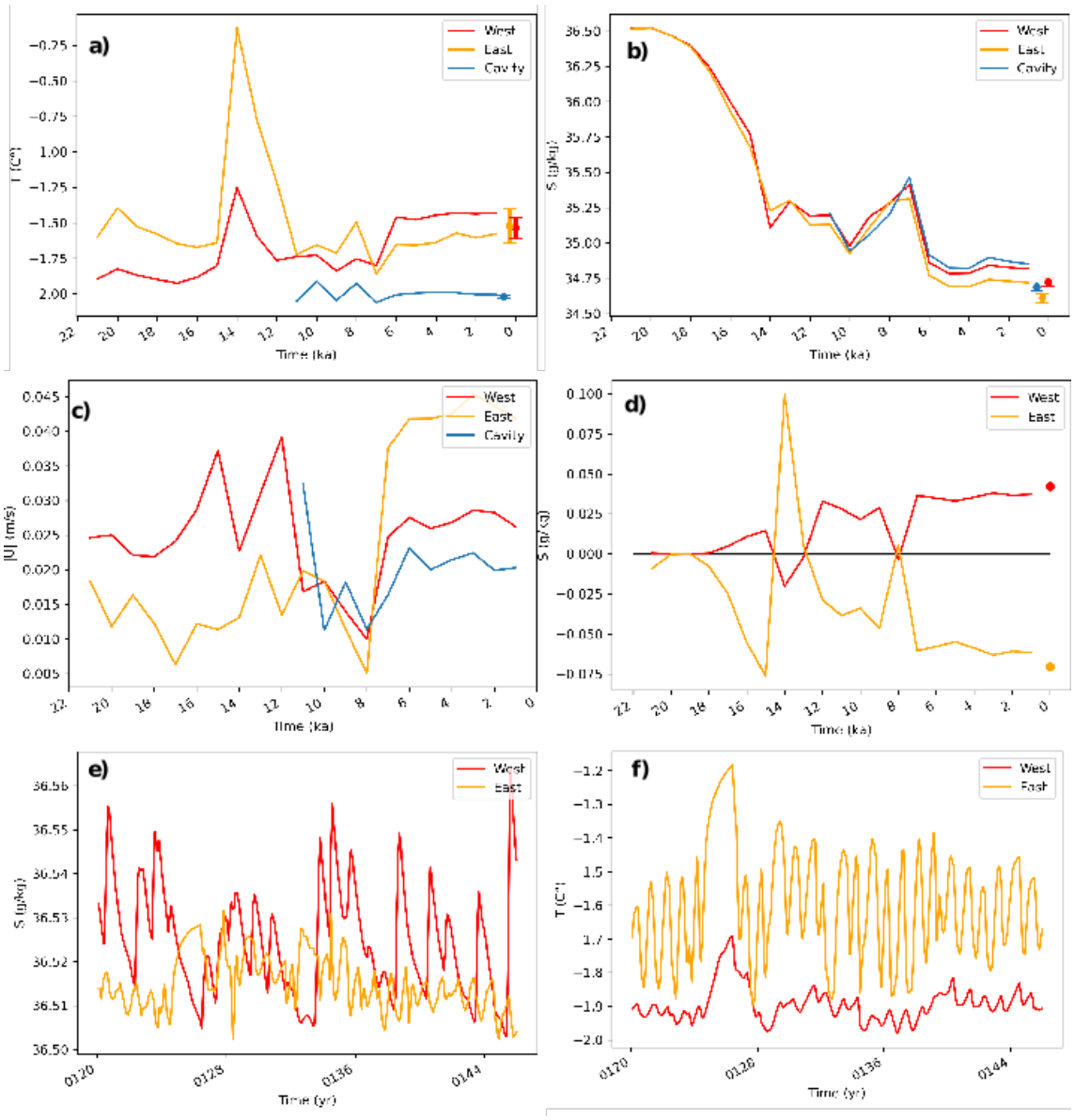

Figure 4.18: Time series over the Last Deglaciation for (a) bottom temperatures (°C), (b) the bottom salinity (g/kg), (c) bottom currents speed (m/s), (d) salinity anomaly (g/kg) with respect to the spatial mean calculated on the entire open continental shelf (red and orange in Figure 4.17). The present day values from the control simulation (Chapter 2) are added as dots with standard deviation.. Monthly variability of 21 ka bottom water masses: (e) averaged temperature, (f) averaged salinity. Time averages of bottom water temperature and salinity are calculated for each snapshots based on the regions defined in Figure 4.18

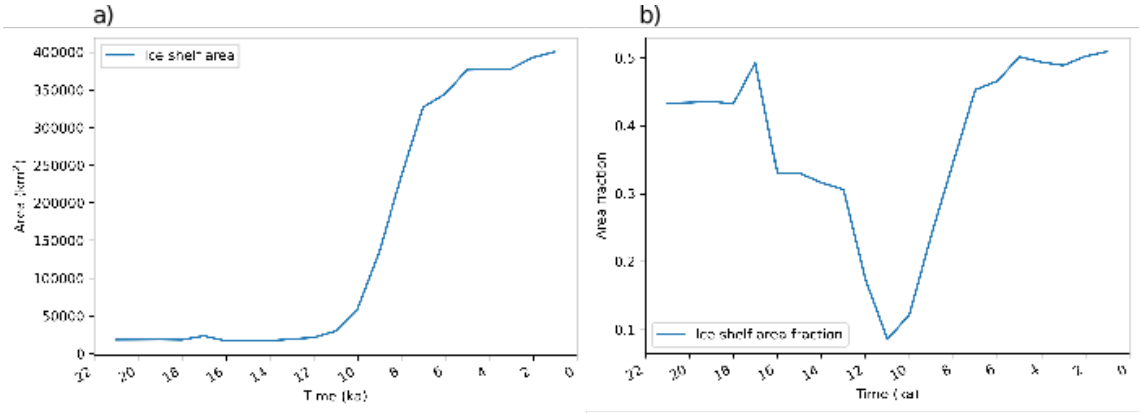

Figure 4.19: (a) Simulated evolution of Ross Sea ice shelf surface and (b) surface fraction with respect to the whole continental shelf, available for circulation.

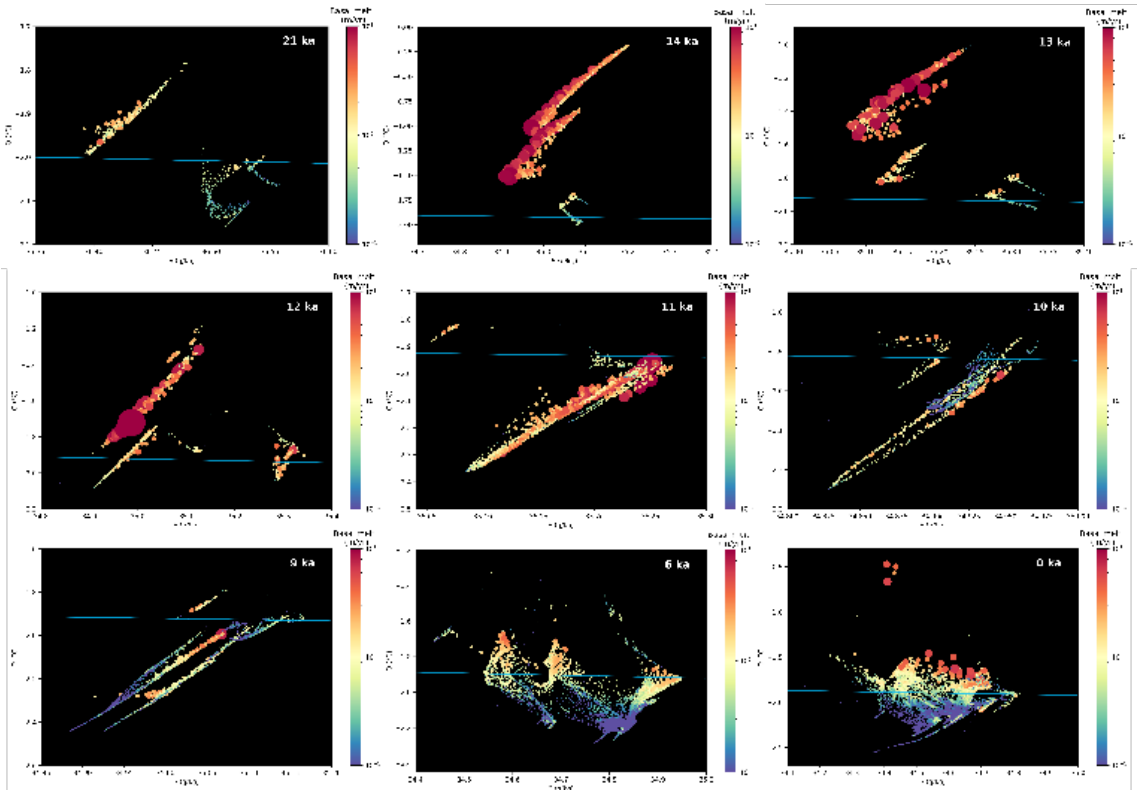

Figure 4.20: Scatter plot showing averaged mean annual simulated temperature and salinity of water masses in contact with the Ross Sea ice shelves draft. The dots are coloured and sized according to the averaged basal melting in the corresponding grid point (m/yr). Averages are calculated over the entire duration of each snapshot. The blue line represents the *in-situ* surface freezing point, and is a function of salinity. Note that our model domain contains ice shelves in the Amundsen Sea, which are not included in these plots.

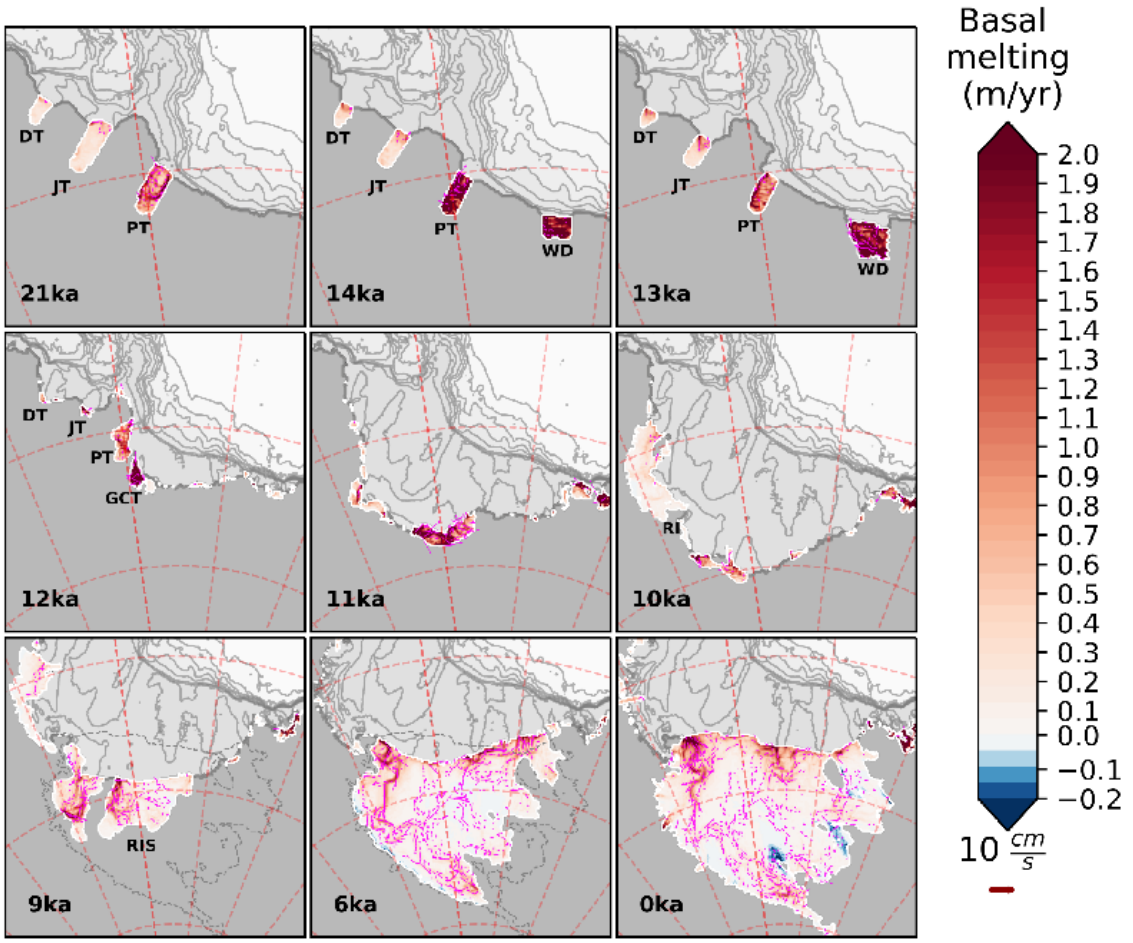

Figure 4.21: Simulated basal melting below ice shelves, in mean annual average over the entire 26-years snapshots duration. Overlayed arrows show current velocity at the ice shelves draft. Abbreviations: DT= Drygalski Trough; JT=Joides Trough; PT=Pennel Trough; WD=Whales Deep (basin); GCT=Glomar Challenger Trough; RI=Ross Island; RIS=Ross Ice Shelf.

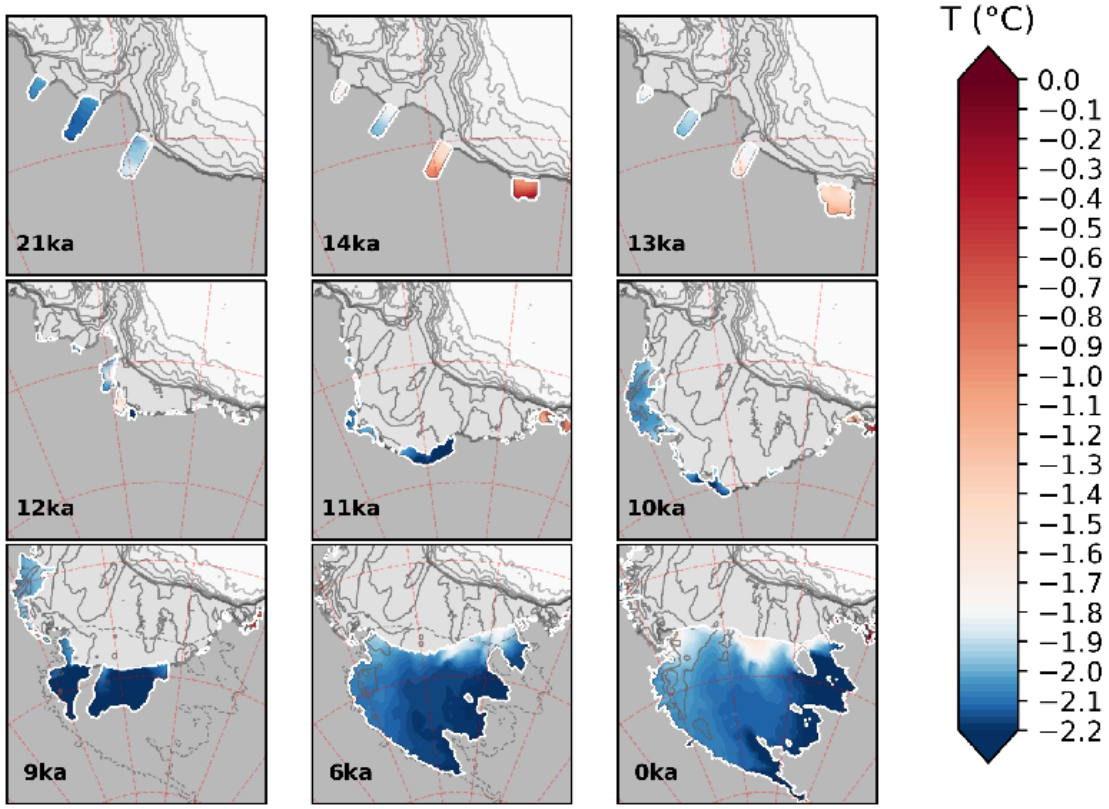

Figure 4.22: Simulated ocean temperature at ice shelves draft level (mean annual average over 26 years).

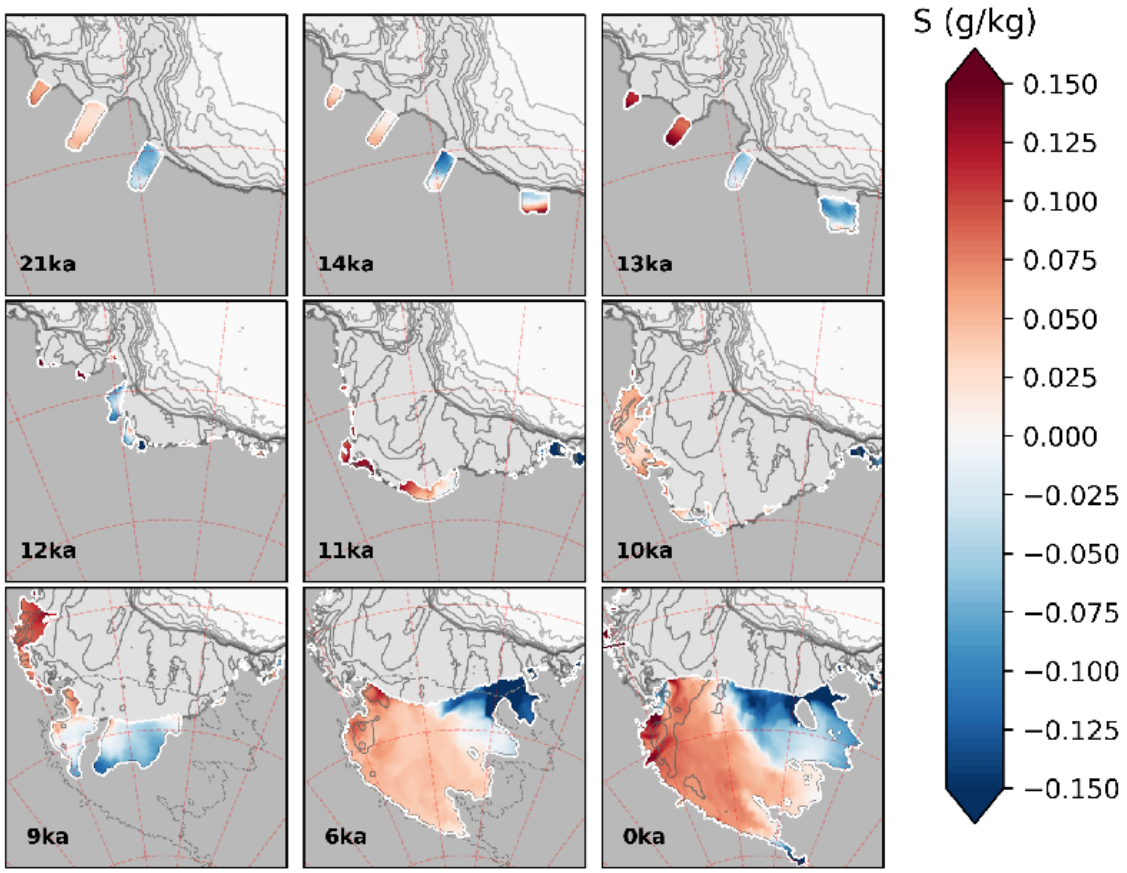

Figure 4.23: Same as Figure 4.22 but shown is ocean salinity anomaly with respect to spatial mean, calculated over all ice shelves.

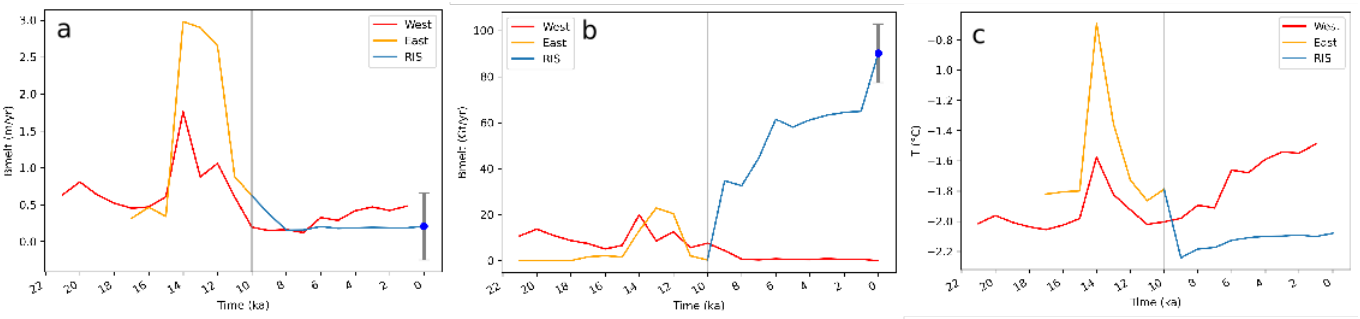

Figure 4.24: Simulated basal melting: (a) averaged (m/yr) and (b) integrated (Gt/yr), for all cavities of the Western/Eastern Ross Sea (red/orange) and for the RIS (blue) after its formation (grey vertical line at 10 ka; masks shown in Figure 4.17). (c) Timeseries of mean annual temperature averaged over the ice shelves draft. In (a,b) the dot at 0 ka corresponds to the average/integrated basal melt rates of the present-day contronl run (1993-2018, Chapter 3), with the vertical bar representing uncertainty associated with monthly variability (standard deviation). Notice that after the major retreat and the formation of the main RIS cavity, only a few ice shelves remain in the Western and Eastern Ross Sea coastal areas. Notice that the ice shelf that developed in the Eastern Ross Sea started to expand and coalesce in the Ross Ice Shelf (RIS) at ∼10 ka. After RIS formation, to take into account the different shape of the RIS front in the paleo experiment and the present-day, melting of the small Eastern Ross Sea ice shelves were added to the RIS.

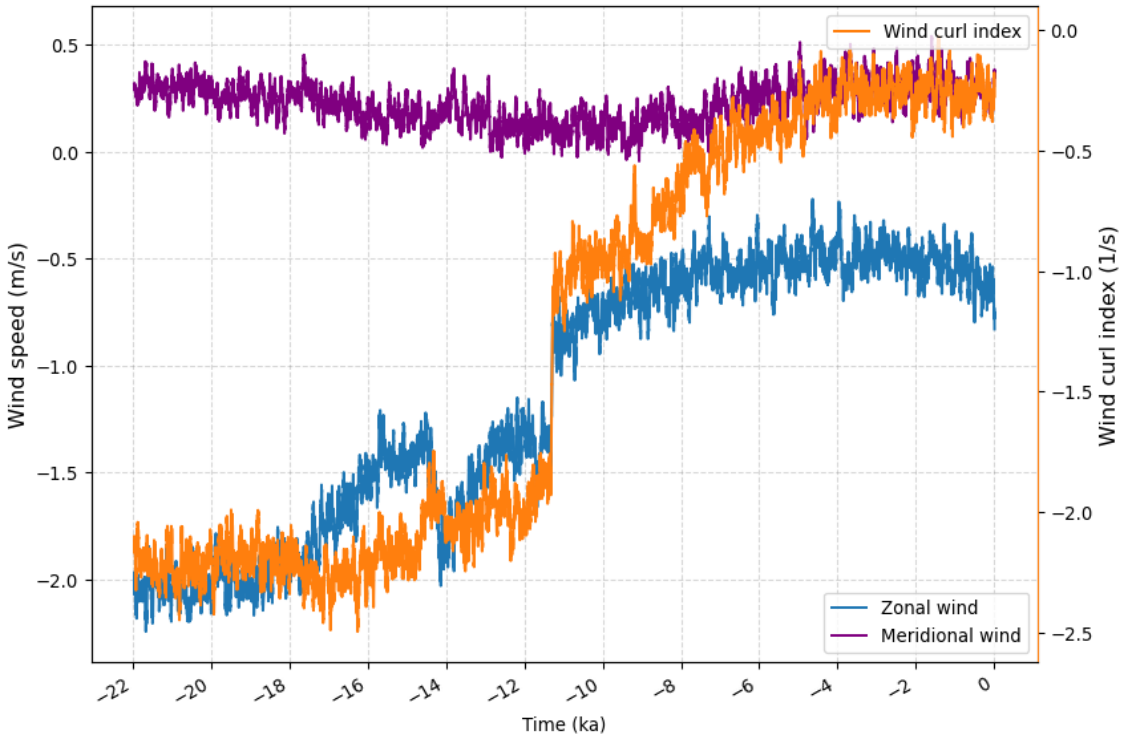

Figure 4.25: Yearly winds (m/s) averaged in the Eastern Ross Sea near the continental shelf break (183.8 - 217.5 °E, 72.36 - 68.65 °S, left y-axis), negative zonal wind (blue curve) imply easterly circulation, positive meridional wind (purple curve) imply southerly circulation. An index based on the simulated wind curl (1/s) is also shown (orange curve, right y-axis), where negative values are conditions associated with stronger upwelling.

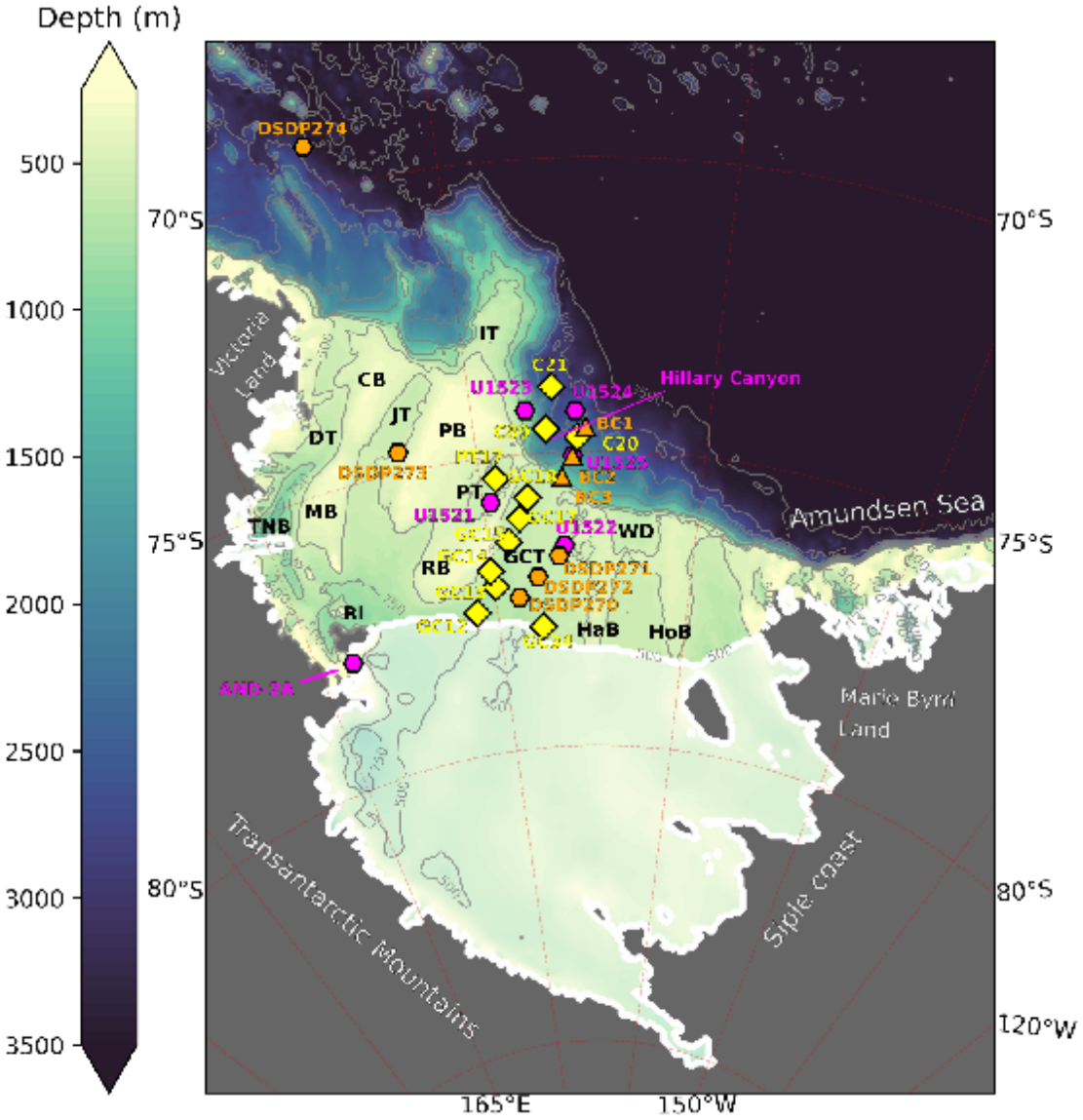

Figure 4.26: Sediment cores from International Ocean Discovery Program (IODP) 374 expedition, leg 28 Deep Sea Drilling Project (DSDP), and ANDRILL (AND-2A) drilling sites (hexagon); box cores (diamond) and gravity cores (triangle) from PNRA Italian expeditions, considered in the framework of the PNRA ANTIPODE project (see Chapter 1). Abbreviations: CB = Crary Bank, DT = Drygalski Trough, GCT = Glomar Challenger Trough, HaB = Hayes Bank, HoB = Houtz Bank, IB = Iselin Bank, JT = Joides Trough, MB = Mawson Bank, PB = Pennel Bank, PT = Pennel Trough, RB = Ross Bank, TNB = Terra Nova Bay, WD = Whales Deep (basin).

Chapter 5

Discussion and Conclusions

The initial scientific questions that motivated my PhD work were:

1. What are the characteristics of the main water masses in the Ross Sea and how do their variability relate to teleconnections?

2. How does each water mass impact on the basal melting of the Ross Ice Shelf?

3. How did paleo-water masses evolve in the Ross Sea sector during the last deglaciation?

4. Which water mass was determinant to drive Antarctic Ice Sheet retreat in the Ross Sea during the last deglaciation?

In my PhD work I attempted to answer based on numerical modelling results:

1. The MITgcm was implemented for a regional setup of the Ross Sea, which includes the sub-ice shelf cavities and was run for the period 1993-2018, forced by high resolution reanalysis data (ERA5 and GLORYS12V1). We investigated the simulated water masses variability and compared them with past mooring measurements available at specific sites and with observations collected along the RIS front from past cruises. Variability of the simulated water masses was reproduced in the simulations, although the teleconnection with the tropics proved to be difficult to extract, probably due to superposed effects and ocean – atmosphere variable coupling caused by variable sea ice cover. Overall the model shows good agreement with observations, which makes the results reliable for paleo applications and for the analysis of basal melting. This is the first modelling study that employ mooring in the Ross Sea systematically for validation. Secondly, given the limited domain, it was possible to simulate longer periods of time, to capture long term teleconnections.

2. Simulated basal melting from the present-day simulation was studied in connection with water masses. It was shown to be in line with other modelling work and remote sensing observations, within the reported uncertainty. A new method was developed to partition basal melting into the present water masses, based on mixing ratio thresholds, which helped understanding the impact of each water mass on melting and its variability in space and time. HSSW is the strongest contributor to melting on a yearly average; its variability shows decadal oscillations in salinity, difficult to relate to katabatic winds or sea ice formation alone. The second contributor is mCDW/mSW, which causes melting near the front with a strong seasonal cycle. Although probably overestimated, it shows that warm CDW intrusions, although subdued by mixing with colder warer, still affects the Ross Ice Shelf. The third contributor is the AASW which intrudes only near Ross Island and only in summer. Water masses variability do not match alone any climatic index that we analysed, namely the ENSO, the SAM, the ASL, the PDO; however the frequencies of ENSO appear in the periodogram of integrated basal melting, and show significant correlation, although the phasing if the signal need to be further analysed. This work shows that the RIS is not simply a "cold" cavity: given the large number of different water masses it is therefore difficult to represent in simplified parameterisations commonly employed in ice sheet models. It shows also that RIS oceanography and ice sheet - ocean interactions are sensitive to tropical and polar teleconnections, although this requires further and stronger statistical analysis.

3. We simulated ocean circulation and ice sheet interactions for several snapshots along the last deglaciation (21 - 0 ka), with evolving climatic conditions, bathymetry, sea level and ice sheet geometry, based on other numerical models and geological reconstructions. This is the first numerical study that analyses in a realistic setup, oceanographic changes in the Ross Sea during last deglaciation, and impact on ice shelves by basal melting. A general trend of desalinification and warming was simulated, with sudden deep ocean warming and intermediate ocean freshening related to feedbacks in the AMOC during the MWP-1A ($\sim$ 14.3-14.0 ka). Our findings suggest that the MWP-1A triggered the initial AIS destabilisation in the Eastern Ross Sea Sector, around 14-13 ka. The main driver of the retreat was CDW, largely accessing the continental shelf and reaching the grounding line in Eastern Ross Sea troghs. This was made possible by the perturbed state of the Along Slope Front, caused by the MWP-1A and feedbacks in the AMOC and Southern Ocean (deep warming/intermediate freshening), making the ASF similar to a "warm" state, as observed today in

high melting ice shelves, which allows strong and persistent CDW intrusions. As the continental shelf became more open to shelf circulation,and as the ASF returned to a non-perturbed state, ocean – atmosphere interactions became more important, with increased HSSW formation and flow beneath the newly formed Ross Ice Shelf; overall the continental shelf became more alike to the mostly "cold" shelf type, as we observe today. These results comfirm the hypothesis that the AIS retreat was triggered by the ocean, and highlights the conditions for it to occur, which involves the feedback in the AMOC driven by a release of meltwater in the North Atlantic during the MWP-1A. This is a regional improvement to the paleo oceanographic work done in the past, e.g. Obase et al. (2017), that may be employed by the geological and glaciological community working on the Ross Sea.

Uncertainties

In our methodology sources of uncertainty can be summarised, for both the present and past numerical experiments in:

1. Forcing and boundary conditions:

   - Basin and present-day ice shelves morphology: Bedmap2 (Fretwell et al., 2013);

   - Timing and pathways of ice sheet retreat (Lowry et al., 2019; Halberstadt et al., 2016; Prothro et al., 2020)

   - Present-day forcing: ERA5, GLORYS12V1;

   - Paleo forcing: TraCE-21ka (Liu et al., 2009);

2. Model physics limitations:

   - Missing processes: tides, frazil-formation;

   - Parametrisations: turbulence, eddies, representation of sub-ice shelf roughness;

3. Numerical setup:

   - Grid resolution

   - Resolution: vertical and horizontal;

   - Forcing frequency

Model-observations discrepancies may be related to several of the points stated above. At present, no high resolution map of the bathymetry beneath the RIS exist, as well as a detailed map of the RIS draft morphology, which are measured by remote sensing; Bedmap2 (Fretwell et al., 2013) therefore carries this limitation. As for the paleo bathymetry and ice sheet/ice shelves, the deglaciation simulation output that we employed does capture well the retreat in the Eastern Ross Sea, but on the contrary, the Western Ross Sea is not very well represented, due probably to the more complex bathymetry. Geological reconstructrions (Prothro et al., 2020) suggest an early retreat in the Drygalski basin, although that is not supported by numerical modelling.

Present-day forcing from ERA5 is based on loosely constrained observations in Antarctica, especially for the katabatic winds, which have high spatial and time variability and may not be represented adequately well for our purposes. As for the ocean reanalysis GLORYS12V1, it has small biases in temperature and salinity, that were not corrected since were not documented at the time of the setup preparation; however these biases were much decreased as more observations were introduced in the more recent years of the reanalysis. Notice that the paleoclimate forcing based on TraCE-21ka was based on another ice sheet chronology (ICE-5G, Peltier 2004), which has a very static AIS. In our study we employed the ice sheet model output from Lowry et al. (2019), with local adaptations from geological records for snapshots earlier than 16 ka, which however was forced by TraCE-21ka, so the results are not inconsistent. Other issues with TraCE-21ka are the very coarse grid, in particular for the ocean bathymetry, that produces shifts in the currents, gyres and in the AMOC, but also in the atmosphere, which may be responsible especially for unrealistic sea ice patterns of accumulation. Even though TraCE-21ka were bias corrected, the winds remain difficult to treat properly, in particular katabatic winds are not even fairly simulated in TraCE-21ka.

Water masses and basal melting may be impacted by missing processes such as frazil-ice formation, double diffusion processes, which have been documented but are not yet implemented in the three-equation formulation, in most ocean models up to date. Uncertainties in simulating sub-ice shelf cavities involve the badly resolved bathymetry, and even less resolved ice shelf draft roughness, which has been observed directly in some places to be highly variable. Tides have been shown to be important in determining across slope transport and in driving basal melting in shallow regions near the grounding line, and therefore are an important missing driver in this study. However the implementation of tides to a paleoclimate scenario would be problematic, for the different ocean basins volume and gateways, and also a different Earth orbital configuration, that would make it unreliable the application of existing barotropic tidal circulation models.

As for model setup regarding the chosen resolution, there is difficulty in obtaining eddy-resolving models of the Antarctic Seas, because of the smallness of the Rossby number, although recent study suggest that mesoscale eddies do not impact significantly on basal melting (Mack et al., 2019). We find 5-km horizontal resolution enough to capture the main processes on the shelf and slope, and CDW intrusions, while retaining good performance for the longer paleo runs. Simulated basal melting depends strongly on the type of vertical grid discretization (z-level, sigma-level, terrain following), that result in different vertical discretization of the water column, directly impacting the heat and salinity fluxes into the upper-most ocean cell in the three-equation formulation. A terrain-following model such as ROMS would be more suitable to study a cavity in a shallow ocean basin and the continental slope, but would require more resources, and higher resolution in order to avoid generation of spurious pressure gradients at the ice shelf front (Mack et al., 2019), making problematic to apply to a paleo scenario.

Despite model limitations, simulated 3D circulation and basal melting can still improve basal melting parametrisations as implemented in most ice sheet models, and help reduce the observational knowledge gap that is affecting AIS future volume loss. However the lack of a continuous and widespread observational network on the continental shelf, hampers the interpretation of simulated water masses and basal melting, thus posing important limitations to numerical studies beneath the cavities. Basal melting characterisation proved to be difficult, because in order to disentangle the water masses mixing between themselves beneath the RIS, and mixing with meltwater, thresholds had to be defined in water masses properties, which introduced some subjectiveness in the choice. In fact any method based on water masses properties need to define ad-hoc thresholds, except for a freezing point criterion, which does discriminate only between "cold" and "warm" modes of basal melting. Even more difficult is to define paleo water masses based on their evolving properties, and in fact that was not attempted in this work. Finally, as it is, due to low vertical resolution at depth greater than 1000m on the slope, and the vertical discretization in z-levels, our model is not suitable for capturing outflows of DSW and RSBW formation: this poses limitations in its usefulness for interpretation of IODP cores near the Hillary Canyon, and more generally, to study the impact of the Ross Sea on the global Ocean. This limitation will be addressed in future applications, which may also take advantage of the optional MITgcm non-hydrostatic formulation, to better simulate RSBW cascading.

As for the paleo experiment, we find critical to the method employed the realistic implementation of boundary conditions, which proved to be not trivial and needed corrections for biases, and poses consistency issues when several models output are

employed. Care was needed to implement lateral ocean boundary conditions, and corrected for different mixed layer depth. A misrepresentation of the atmospheric variability in TraCE-21ka output, which was applied by necessity at monthly frequency, may impact consistently on the results, in particular on the simulated sea ice processes and currents strength.

Impact of uncertainties should have been analysed more thoroughly with sensitivity tests, applying different tuning of wind forcing, of ice shelf drag coefficient and the impact of the bias correction, separately for the ocean and the atmosphere. Another critical aspect of the methodology is the realistic implementation of grounding line migration during deglacial retreat, or ice shelves extension: both may create varying constraints and feedbacks for oceanic circulation and barriers for sea ice, affecting polynya opening locations. In this scenario, although we employed a reconstruction that best matched geological data, we are still missing part of these feedbacks, as the cavities and grounding line are fixed in space, at each snapshot. Moreover the parabolic ice shelf draft we imposed, for the snapshots before 13ka may poorly represent the real shape if the ice shelves draft, and the imposed draft depth at front, about 250m depth, and based on the present-day RIS thickness, may underestimate the real paleo ice shelves. Future applications would try to couple the MITgcm output with an ice sheet melting parametrisation, in order to also study the impact on the ice dynamics and the feedbacks on the ocean more realistically. Although these uncertainties affect all the work, in particular the paleo, we think that the overall methodology is quite robust, within the limits posed by uncertainty; as future work it is planned to compare the simulated results with observations.

Insight and future work

Implementation of tidal forcing is programmed for future work. However special care would be needed to apply tidal currents for paleo experiments. An oceanographic comparison with the large amount of sediment cores (box cores, gravity cores, scientific drilling) from the the Ross Sea continental shelf, continental slope and possibly the Hillary Canyon would provide information about past water masses, to validate the model at particular times. The model, inversely, can help interpretation of particular events or trends observed in the geological record. Model results for the present day can help ice sheet modellers to calibrate their parameterisations employing simulated turbulent coefficients and water masses, to include the impact of localised . It is planned to simulate the Middle Miocene with 6-hourly atmospheric forcing, provided by a companion institution; the bathymetry to be used is the backstripped one of Paxman et al. (2020). There are plans to apply the methodology

to smaller domains and bays of the Ross Sea, to help geological interpretation of proxies, and also to expand the field of study to the D'Urville Sea (Wilkes Land).

Certain uncertainties in the paleo experiments may be reduced by comparison with observations, whereas others are likely to remain unconstrained in the near future. For instance changes in the opening of seaice or polynyas may have been recorded in diatoms ecology changes. Polynyas may help identifying the ice shelf edge in a fully glacial state. Water masses properties (warm/cool, saline/fresh) may also be associated with the presence of particular foraminifera species, therefore constraining at least HSSW and CDW, although within ice shelf cavities, dark conditions may imply low or no productivity and scarcity of organisms. Bottom currents location may be checked against sedimentary deposits, whose morphology would indicate bottom current direction, and whose grain size would reveal the current intensity.

On the other hand, certain aspects are likely to remain fairly unconstrained in the near future. Pathways and timing of grounding line retreat are possible to reconstruct reliably only when the grounding line retreat alternates to periods of stability, which produce GZWs, that in turn can be dated. Where retreat is continuous such geological record is not produced, as in the Glomar Challenger Trough for instance. Water masses also show evolving characteristics in the simulations, inherited by the TraCE-21ka simulation. The thermohaline characteristics of the LGM ocean is still relatively unconstrained, as proxies for temperature and salinity are entangled between themselves and with global ice volume. Other important forcing such as winds are difficult to constrain for Antarctica, and would likely require an ensemble of models, to reduce uncertainty.

Appendix A

Nomenclature

General Acronyms

AACC Antarctic Coastal Current

ACC Antarctic Circumpolar Current

ADP Antarctic Dipole

ASF Antarctic Slope Front

ASL Amundsen Sea Low

ENSO El-Niño Southern Oscillation

GZW Grounding Zone Wedge

IOD Indian Ocean Dipole

MWP MeltWater Pulse

SAM Southern Annular Mode

SOI Southern Oscillation Index

XBT EXpendable Bathy-Thermograph

Geographical names

AAIW Antarctic Intermediate Water

AIS Antarctic Ice Sheet

AmIS Amery Ice Shelf

AP Antarctic Peninsula

ASC Along-Slope Current

BIIS British Islands Ice Sheet

CB Crary Bank

DT Drygalski Trough

EAIS East Antarctic Ice Sheet

FIS Fennoscandian Ice Sheet

FRIS Filchner-Ronne Ice Shelf

GCT Glomar Challenger Trough

GrIS Greenland Ice Sheet

HaB Hayes Bank

HoB Houtz Bank

IB Iselin Bank

JT Joides Trough

LIS Laurentide Ice Sheet

MB Mawson Bank

PB Pennel Bank

PT Pennel Trough

RB Ross Bank

RIS Ross Ice Shelf

SBKIS Svalbard-Barents-Kara Ice Sheet

TIS Totten Ice Shelf

TNB Terra Nova Bay

WAIS West Antarctic Ice Sheet

WD Whales Deep (basin)

Water masses

AABW Antarctic Bottom Water

AAIW Antarctic Intermediate Water

AASW Antarctic Surface Water

CDW Circumpolar Deep Water

DSW Dense Shelf Water

HSSW High Salinity Shelf Water

ISW Ice Shelf Water

LSSW Low Salinity Shelf Water

mCDW Modified Circumpolar Deep Water

mSW Modified Shelf Water

NADW North Atlantic Deep Water

RSBW Ross Sea Bottom Water

SW Shelf Water

Appendix B

Model parameters

Table B.1: Principal namelist variables of the MITgcm implementation used in this study.

Parameters	Value
rhoConst	1028
rhoConstFresh	1000
Tref	50 0
Sref	50 34.4
diffKzT	5.E-6
diffKzS	5.E-6
viscAhGridMax	1
viscAz	1.E-4
viscAhGrid	1.E-2
viscC2leith	1.
viscC2leithD	1.
viscC4Leith	0.1
viscC4Leithd	0.1
no_slip_sides	.FALSE.,
no_slip_bottom	.TRUE.,
selectBotDragQuadr	2
bottomDragQuadratic	1.5E3
eosType	'MDJWF'
rigidLid	.FALSE.
implicitFreeSurface	.TRUE.
useRealFreshWaterFlux	.TRUE.
nonlinFreeSurf	0
select_rStar	0,
exactConserv	.TRUE.

hFacInf	0.05
hFacMin	0.1,
hFacMinDz	20.,
nonHydrostatic	.FALSE.
readBinaryPrec	64
useCDScheme	.FALSE.
staggerTimeStep	.TRUE.
implicitViscosity	.TRUE.
implicitDiffusion	.TRUE.
tempAdvScheme	33
saltAdvScheme	33
selectCoriMap	3
f0	-1.45E-4
useFullLeith	.TRUE.
use3dCoriolis	.TRUE.
useSingleCpuIO	.TRUE.
writeBinaryPrec	32
debugLevel	0
highOrderVorticity	.TRUE.
cg2dMaxIters	500
cg2dTargetResidual	1.E-7
usingCartesianGrid	.TRUE.
xgOrigin	-747500
ygOrigin	-997500
dxSpacing	5000,
dySpacing	5000
SHELFICEtopoFile	'draft_paleo.data'
SHELFICEloadAnomalyFile	'pload_paleo_ice.data'
SHELFICEuseGammaFrict	.TRUE.
no_slip_shelfice	.FALSE.
SHELFICEwriteState	.TRUE.
SHELFICEboundaryLayer	.TRUE.
SHELFICEconserve	.TRUE.
SHELFICEadvDiffHeatFlux	.TRUE.
SHELFICEselectDragQuadr	2
SHELFICEthetaSurface	-20.0
SEAICEwriteState	.true.
LSR_ERROR	1.E-5

SEAICEnonLinIterMax	10
SEAICE_multDim	7
SEAICEadvScheme	33
SEAICEscaleSurfStress	.true.
SEAICE_useMultDimSnow	.true.
SEAICEetaZmethod	3
SEAICEaddSnowMass	.true.
SEAICEuseFlooding	.true.
SEAICE_frazilFrac	0.01
HO	0.25
SEAICE_dryIceAlb	0.69
SEAICE_wetIceAlb	0.61
SEAICE_drySnowAlb	0.78
SEAICE_wetSnowAlb	0.63
SEAICE_drag	0.00125
SEAICEpressReplFac	0

Appendix C

Backstripping

Ice sheet dynamics changes considerably, according to whether the bedrock lies above or below sea level, and in the latter case, according to the sloping of the bedrock (seaward = retrograde-sloping or landward = prograde-sloping). Some processes, such as the Marine Ice Sheet Instabilities can only occur on a bedrock lying below sea level and further amplified on a retrograde bed (See Chapter 1). Pinning points, such as ridges, seamount, or lateral mountain valleys, are critical to buttress ice flow, i.e. to provide back stress slowing the ice stream flow from the interior. Pinning points, however, evolve together with the morphology of the bed, shaped by ice sheet erosion, sediment transport and deposition. Currently, large sectors of the Antarctic margins have their bedrock below sea level, but this has not always been the case. For instance, the analysis of seismic profiles in the Ross Sea (De Santis et al., 1995, 1999) showed that in the past, large amounts of sediment, eroded by the waxing and waning of the AIS, were transported to the continental shelf margins. This contributed to the continental margin expansion (see Chapter 1.7). Recent works highlight the necessity of realistically incorporating past bathymetries as boundary conditions in numerical ice sheet and ocean modelling (e.g., Colleoni et al., 2018a; Paxman et al., 2020). This allows to better constrain tipping points in atmospheric CO_2 concentrations triggering the AIS advances and retreat and thus, past global mean sea level changes.

The reconstruction of paleobathymetries can be achieved, for example, by means of a technique called "backstripping" (Steckler and Watts, 1978). It consists of stripping-off sediment layers to restore the depth of underneath bedrock. But, it can also be used to restore the depth of an intermedaire sedimentary layer and thus reconstruct the bathymetric evolution of an area. The procedure consists in several steps: [1] decompaction of sediment layer, and [2] removal of sediment and water loading effect for a given time, [3] restoration of tectonic subsidence (due to the cooling of

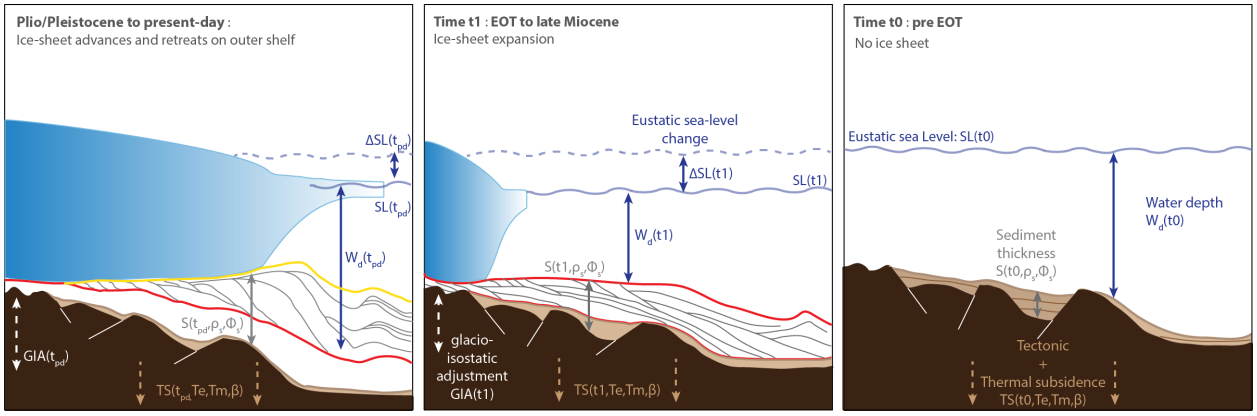

Figure C.1: Backstripping procedure applied to the Antarctic margin to restore the depth of the bed at the beginning of the post-rift period, i.e., at the Eocene-Oligocene Transition, when the AIS started to expand. Figure from Colleoni et al. (2018b), with the courtesy of Florence Colleoni.

the mantle and lithosphere over time). Several additional corrections can be applied the, as for example, local sea level variations. The backstripping procedure is applied sequentially starting from the most recent stratigraphic units to the oldest one. At each step, a decompaction correction is applied for all remaining underlying sediment layers, and applying glacio-isostatic adjustment. The calculation is done based on sedimentary units identified in the seismic profiles (red and yellow, Figure C.1). In the case of Antarctica, the expansion of the continental margin by sediment filling occurred after the rifting phase. The backstripping is thus applied to reconstruct the post-rift continental margin history (t0 in Figure C.1). The decompaction considers the lithological properties of sediments that affect the depth-dependent porosity and density, lithospheric and mantle rheological properties to calculate the deformation induced by sediment removal, and the thermal subsidence. Finally, cross comparisons between restored paleo-depths, seismic facies (e.g., grounding zone wedges) and lithofacies from drill sites can be used to validate the resulting paleo-bathymetry. In fact, the interpretation relies on a number of parameters and physical simplifications that approximate water, sediments, lithosphere, and mantle rheological properties and behavior.

The method was implemented as MATLAB program in the framework of the PNRA ANTIPODE project: PALEOSTRIPv1. 0 Colleoni et al. (2021), in annex to this chapter. It is included in this thesis since it was meant as a preliminary work in preparation for the Miocene paleo-oceanographic simulations, programmed for the project ANTIPODE, and planned as future work.

Reference:

Colleoni, F., De Santis, L., Pochini, E., Forlin, E., Geletti, R., Brancatelli, G., Tesauro M., Busetti M. & Braitenberg, C. (2021). PALEOSTRIPv1. 0–a user-friendly 3D backtracking software to reconstruct paleo-bathymetries. Geoscientific Model Development discussions, 1-33. https://doi.org/10.5194/gmd-14-5285-2021

Bibliography

Adcroft, A., Hill, C., and Marshall, J. Representation of topography by shaved cells in a height coordinate ocean model. *Monthly Weather Review*, 125(9):2293–2315, 1997.

Adkins, J. F., McIntyre, K., and Schrag, D. P. The salinity, temperature, and δ^{18}O of the glacial deep ocean. *Science*, 298(5599):1769–1773, 2002.

Adusumilli, S., Fricker, H. A., Medley, B., Padman, L., and Siegfried, M. R. Interannual variations in meltwater input to the Southern Ocean from Antarctic ice shelves. *Nature geoscience*, 13(9):616–620, 2020.

Anderson, J. B., Conway, H., Bart, P. J., Witus, A. E., Greenwood, S. L., McKay, R. M., Hall, B. L., Ackert, R. P., Licht, K., Jakobsson, M., et al. Ross Sea paleo-ice sheet drainage and deglacial history during and since the LGM. *Quaternary Science Reviews*, 100:31–54, 2014.

Anderson, J. B., Simkins, L. M., Bart, P. J., De Santis, L., Halberstadt, A. R. W., Olivo, E., and Greenwood, S. L. Seismic and geomorphic records of Antarctic Ice Sheet evolution in the Ross Sea and controlling factors in its behaviour. *Geological Society, London, Special Publications*, 475(1):223–240, 2019.

Anderson, J. T., Wilson, G. S., Fink, D., Lilly, K., Levy, R. H., and Townsend, D. Reconciling marine and terrestrial evidence for post LGM ice sheet retreat in southern McMurdo Sound, Antarctica. *Quaternary Science Reviews*, 157:1–13, 2017.

Anderson, R., Ali, S., Bradtmiller, L., Nielsen, S., Fleisher, M., Anderson, B., and Burckle, L. Wind-driven upwelling in the Southern Ocean and the deglacial rise in atmospheric CO2. *science*, 323(5920):1443–1448, 2009.

Arndt, J. E., Schenke, H. W., Jakobsson, M., Nitsche, F. O., Buys, G., Goleby, B., Rebesco, M., Bohoyo, F., Hong, J., Black, J., et al. The International Bathymetric Chart of the Southern Ocean (IBCSO) Version 1.0—A new bathymetric compilation

covering circum-Antarctic waters. *Geophysical Research Letters*, 40(12):3111–3117, 2013.

Arrigo, K. R., van Dijken, G. L., Ainley, D. G., Fahnestock, M. A., and Markus, T. Ecological impact of a large Antarctic iceberg. *Geophysical Research Letters*, 29 (7):8–1, 2002.

Arzeno, I. B., Beardsley, R. C., Limeburner, R., Owens, B., Padman, L., Springer, S. R., Stewart, C. L., and Williams, M. J. Ocean variability contributing to basal melt rate near the ice front of Ross Ice Shelf, Antarctica. *Journal of Geophysical Research: Oceans*, 119(7):4214–4233, 2014.

Asay-Davis, X. S., Jourdain, N. C., and Nakayama, Y. Developments in simulating and parameterizing interactions between the Southern Ocean and the Antarctic ice sheet. *Current Climate Change Reports*, 3(4):316–329, 2017.

Ashley, K. E., McKay, R., Etourneau, J., Jimenez-Espejo, F. J., Condron, A., Albot, A., Crosta, X., Riesselman, C., Seki, O., Massé, G., et al. Mid-Holocene Antarctic sea-ice increase driven by marine ice sheet retreat. *Climate of the Past*, 17(1):1–19, 2021.

Assmann, K., Hellmer, H., and Beckmann, A. Seasonal variation in circulation and water mass distribution on the Ross Sea continental shelf. *Antarctic Science*, 15 (1):3–11, 2003.

Bard, E., Hamelin, B., and Fairbanks, R. G. U-Th ages obtained by mass spectrometry in corals from Barbados: sea level during the past 130,000 years. *Nature*, 346 (6283):456–458, 1990.

Baroni, C. and Hall, B. L. A new Holocene relative sea-level curve for Terra Nova Bay, Victoria Land, Antarctica. *Journal of Quaternary Science*, 19(4):377–396, 2004.

Bart, P. J. Were West Antarctic ice sheet grounding events in the Ross Sea a consequence of East Antarctic ice sheet expansion during the middle Miocene? *Earth and Planetary Science Letters*, 216(1-2):93–107, 2003.

Bart, P. J. and DeSantis, L. Glacial intensification during the Neogene: A review of seismic stratigraphic evidence from the Ross Sea, Antarctica, continental shelf. *Oceanography*, 25(3):166–183, 2012.

Bart, P. J. and Tulaczyk, S. A significant acceleration of ice volume discharge preceded a major retreat of a West Antarctic paleo–ice stream. *Geology*, 48(4): 313–317, 2020.

Bart, P. J., DeCesare, M., Rosenheim, B. E., Majewski, W., and McGlannan, A. A centuries-long delay between a paleo-ice-shelf collapse and grounding-line retreat in the Whales Deep Basin, eastern Ross Sea, Antarctica. *Scientific reports*, 8(1): 1–9, 2018.

Begeman, C. B., Tulaczyk, S. M., Marsh, O. J., Mikucki, J. A., Stanton, T. P., Hodson, T. O., Siegfried, M. R., Powell, R. D., Christianson, K., and King, M. A. Ocean stratification and low melt rates at the Ross Ice Shelf grounding zone. *Journal of Geophysical Research: Oceans*, 123(10):7438–7452, 2018.

Bentley, M. J., Cofaigh, C. Ó., Anderson, J. B., Conway, H., Davies, B., Graham, A. G., Hillenbrand, C.-D., Hodgson, D. A., Jamieson, S. S., Larter, R. D., et al. A community-based geological reconstruction of Antarctic Ice Sheet deglaciation since the Last Glacial Maximum. *Quaternary Science Reviews*, 100:1–9, 2014a.

Bentley, M. J., Ó Cofaigh, C., Anderson, J. B., Conway, H., Davies, B., Graham, A. G., Hillenbrand, C.-D., Hodgson, D. A., Jamieson, S. S., Larter, R. D., Mackintosh, A., Smith, J. A., Verleyen, E., Ackert, R. P., Bart, P. J., Berg, S., Brunstein, D., Canals, M., Colhoun, E. A., Crosta, X., Dickens, W. A., Domack, E., Dowdeswell, J. A., Dunbar, R., Ehrmann, W., Evans, J., Favier, V., Fink, D., Fogwill, C. J., Glasser, N. F., Gohl, K., Golledge, N. R., Goodwin, I., Gore, D. B., Greenwood, S. L., Hall, B. L., Hall, K., Hedding, D. W., Hein, A. S., Hocking, E. P., Jakobsson, M., Johnson, J. S., Jomelli, V., Jones, R. S., Klages, J. P., Kristoffersen, Y., Kuhn, G., Leventer, A., Licht, K., Lilly, K., Lindow, J., Livingstone, S. J., Massé, G., McGlone, M. S., McKay, R. M., Melles, M., Miura, H., Mulvaney, R., Nel, W., Nitsche, F. O., O'Brien, P. E., Post, A. L., Roberts, S. J., Saunders, K. M., Selkirk, P. M., Simms, A. R., Spiegel, C., Stolldorf, T. D., Sugden, D. E., van der Putten, N., van Ommen, T., Verfaillie, D., Vyverman, W., Wagner, B., White, D. A., Witus, A. E., and Zwartz, D. A community-based geological reconstruction of Antarctic Ice Sheet deglaciation since the Last Glacial Maximum. *Quaternary Science Reviews*, 100:1–9, 2014b. ISSN 0277-3791. doi: https://doi.org/10.1016/j.quascirev.2014.06.025. URL https://www.sciencedirect.com/science/article/pii/S0277379114002546. Reconstruction of Antarctic Ice Sheet Deglaciation (RAISED).

Bergamasco, A., Defendi, V., Zambianchi, E., and Spezie, G. Evidence of dense water overflow on the Ross Sea shelf-break. *Antarctic Science*, 14(3):271–277, 2002.

Bergamasco, A., Defendi, V., Budillon, G., and Spezie, G. Downslope flow observations near Cape Adare shelf-break. *Antarctic Science*, 16(2):199–204, 2004.

Brendryen, J., Haflidason, H., Yokoyama, Y., Haaga, K. A., and Hannisdal, B. Eurasian Ice Sheet collapse was a major source of Meltwater Pulse 1A 14,600 years ago. *Nature Geoscience*, 13(5):363–368, 2020.

Broecker, W. S. Paleocean circulation during the last deglaciation: a bipolar seesaw? *Paleoceanography*, 13(2):119–121, 1998.

Bromwich, D. H. and Kurtz, D. D. Katabatic wind forcing of the Terra Nova Bay polynya. *Journal of Geophysical Research: Oceans*, 89(C3):3561–3572, 1984.

Bronselaer, B., Winton, M., Griffies, S. M., Hurlin, W. J., Rodgers, K. B., Sergienko, O. V., Stouffer, R. J., and Russell, J. L. Change in future climate due to Antarctic meltwater. *Nature*, 564(7734):53–58, 2018.

Budillon, G., Cordero, S. G., and Salusti, E. On the dense water spreading off the Ross Sea shelf (Southern Ocean). *Journal of Marine Systems*, 35(3-4):207–227, 2002.

Budillon, G., Pacciaroni, M., Cozzi, S., Rivaro, P., Catalano, G., Ianni, C., and Cantoni, C. An optimum multiparameter mixing analysis of the shelf waters in the Ross Sea. *Antarctic Science*, 15(1):105–118, 2003.

Budillon, G., Castagno, P., Aliani, S., Spezie, G., and Padman, L. Thermohaline variability and Antarctic bottom water formation at the Ross Sea shelf break. *Deep Sea Research Part I: Oceanographic Research Papers*, 58(10):1002–1018, 2011.

Carlson, A. E. and Clark, P. U. Ice sheet sources of sea level rise and freshwater discharge during the last deglaciation. *Reviews of Geophysics*, 50(4), 2012.

Castagno, P., Falco, P., Dinniman, M. S., Spezie, G., and Budillon, G. Temporal variability of the Circumpolar Deep Water inflow onto the Ross Sea continental shelf. *Journal of Marine Systems*, 166:37–49, 2017.

Castagno, P., Capozzi, V., DiTullio, G. R., Falco, P., Fusco, G., Rintoul, S. R., Spezie, G., and Budillon, G. Rebound of shelf water salinity in the Ross Sea. *Nature communications*, 10(1):1–6, 2019.

Chavaillaz, Y., Codron, F., and Kageyama, M. Southern westerlies in LGM and future (RCP4. 5) climates. *Climate of the Past*, 9(2):517–524, 2013.

Clark, P. U., Dyke, A. S., Shakun, J. D., Carlson, A. E., Clark, J., Wohlfarth, B., Mitrovica, J. X., Hostetler, S. W., and McCabe, A. M. The last glacial maximum. *science*, 325(5941):710–714, 2009.

Clough, J. W. and Hansen, B. L. The Ross ice shelf project. *Science*, 203(4379): 433–434, 1979.

Colleoni, F., De Santis, L., Montoli, E., Olivo, E., Sorlien, C. C., Bart, P. J., Gasson, E. G., Bergamasco, A., Sauli, C., Wardell, N., et al. Past continental shelf evolution increased Antarctic ice sheet sensitivity to climatic conditions. *Scientific reports*, 8(1):1–12, 2018a.

Colleoni, F., De Santis, L., Siddoway, C. S., Bergamasco, A., Golledge, N. R., Lohmann, G., Passchier, S., and Siegert, M. J. Spatio-temporal variability of processes across Antarctic ice-bed–ocean interfaces. *Nature Communications*, 9(1): 1–14, 2018b.

Colleoni, F., De Santis, L., Pochini, E., Forlin, E., Geletti, R., Brancatelli, G., Tesauro, M., Busetti, M., and Braitenberg, C. PALEOSTRIPv1.0–a user-friendly 3D backtracking software to reconstruct paleo-bathymetries. *Geoscientific Model Development*, 14(8):5285–5305, 2021.

Colleoni, F., De Santis, L., Naish, T. R., DeConto, R. M., Escutia, C., Stocchi, P., Uenzelmann-Neben, G., Hochmuth, K., Hillenbrand, C.-D., Van de Flierdt, T., et al. Past Antarctic ice sheet dynamics (PAIS) and implications for future sea-level change. In *Antarctic Climate Evolution*, pages 689–768. Elsevier, 2022.

Cramer, B., Toggweiler, J., Wright, J., Katz, M., and Miller, K. Ocean overturning since the Late Cretaceous: Inferences from a new benthic foraminiferal isotope compilation. *Paleoceanography*, 24(4), 2009.

Darelius, E., Fer, I., and Nicholls, K. W. Observed vulnerability of Filchner-Ronne Ice Shelf to wind-driven inflow of warm deep water. *Nature communications*, 7(1): 1–7, 2016.

Das, I., Padman, L., Bell, R. E., Fricker, H. A., Tinto, K. J., Hulbe, C. L., Siddoway, C. S., Dhakal, T., Frearson, N. P., Mosbeux, C., et al. Multidecadal basal melt rates and structure of the Ross Ice Shelf, Antarctica, using airborne ice penetrating radar. *Journal of Geophysical Research: Earth Surface*, 125(3):e2019JF005241, 2020.

De Santis, L., Anderson, J. B., Brancolini, G., and Zayatz, I. Seismic record of late Oligocene through Miocene glaciation on the central and eastern continental shelf of the Ross Sea. *Geology and Seismic Stratigraphy of the Antarctic Margin*, 68: 235–260, 1995.

De Santis, L., Prato, S., Brancolini, G., Lovo, M., and Torelli, L. The Eastern Ross Sea continental shelf during the Cenozoic: implications for the West Antarctic ice sheet development. *Global and Planetary Change*, 23(1-4):173–196, 1999.

De Santis, L., Mckay, R. M., and Kulhanek, D. K. Initial seismic stratigraphic results from IODP Exp. 374 in the Ross Sea. In *AGU Fall Meeting Abstracts*, volume 2018, pages PP22A–03, 2018.

DeConto, R. M. and Pollard, D. Contribution of Antarctica to past and future sea-level rise. *Nature*, 531(7596):591–597, 2016.

DeConto, R. M., Pollard, D., Alley, R. B., Velicogna, I., Gasson, E., Gomez, N., Sadai, S., Condron, A., Gilford, D. M., Ashe, E. L., et al. The Paris Climate Agreement and future sea-level rise from Antarctica. *Nature*, 593(7857):83–89, 2021.

Depoorter, M. A., Bamber, J., Griggs, J., Lenaerts, J. T., Ligtenberg, S. R., van den Broeke, M. R., and Moholdt, G. Calving fluxes and basal melt rates of Antarctic ice shelves. *Nature*, 502(7469):89–92, 2013.

Desbruyères, D. G., Purkey, S. G., McDonagh, E. L., Johnson, G. C., and King, B. A. Deep and abyssal ocean warming from 35 years of repeat hydrography. *Geophysical Research Letters*, 43(19):10–356, 2016.

Ding, Q., Steig, E. J., Battisti, D. S., and Küttel, M. Winter warming in West Antarctica caused by central tropical Pacific warming. *nature Geoscience*, 4(6): 398–403, 2011.

Dinniman, M. S. and Klinck, J. M. A model study of circulation and cross-shelf exchange on the west Antarctic Peninsula continental shelf. *Deep Sea Research Part II: Topical Studies in Oceanography*, 51(17-19):2003–2022, 2004.

Dinniman, M. S., Klinck, J. M., and Smith Jr, W. O. Influence of sea ice cover and icebergs on circulation and water mass formation in a numerical circulation model of the Ross Sea, Antarctica. *Journal of Geophysical Research: Oceans*, 112(C11), 2007.

Dinniman, M. S., Klinck, J. M., and Smith Jr, W. O. A model study of Circumpolar Deep Water on the West Antarctic Peninsula and Ross Sea continental shelves. *Deep Sea Research Part II: Topical Studies in Oceanography*, 58(13-16):1508–1523, 2011.

Dinniman, M. S., Klinck, J. M., and Hofmann, E. E. Sensitivity of circumpolar deep water transport and ice shelf basal melt along the West Antarctic Peninsula to changes in the winds. *Journal of Climate*, 25(14):4799–4816, 2012.

Dinniman, M. S., Klinck, J. M., Bai, L.-S., Bromwich, D. H., Hines, K. M., and Holland, D. M. The effect of atmospheric forcing resolution on delivery of ocean heat to the Antarctic floating ice shelves. *Journal of Climate*, 28(15):6067–6085, 2015.

Dinniman, M. S., Asay-Davis, X. S., Galton-Fenzi, B. K., Holland, P. R., Jenkins, A., and Timmermann, R. Modeling ice shelf/ocean interaction in Antarctica: A review. *Oceanography*, 29(4):144–153, 2016.

Dinniman, M. S., Klinck, J. M., Hofmann, E. E., and Smith, Walker O., J. Effects of Projected Changes in Wind, Atmospheric Temperature, and Freshwater Inflow on the Ross Sea. *Journal of Climate*, 31(4):1619–1635, 2018. ISSN 0894-8755. doi: 10.1175/JCLI-D-17-0351.1. URL https://doi.org/10.1175/JCLI-D-17-0351.1.

Dowdeswell, J., Ottesen, D., Evans, J., Cofaigh, C., and Anderson, J. Submarine glacial landforms and rates of ice-stream collapse. *Geology*, 36(10):819–822, 2008.

Dutrieux, P., De Rydt, J., Jenkins, A., Holland, P. R., Ha, H. K., Lee, S. H., Steig, E. J., Ding, Q., Abrahamsen, E. P., and Schröder, M. Strong sensitivity of Pine Island ice-shelf melting to climatic variability. *Science*, 343(6167):174–178, 2014.

Dyke, A. S. An outline of North American deglaciation with emphasis on central and northern Canada. *Developments in quaternary sciences*, 2:373–424, 2004.

Edwards, T. L., Nowicki, S., Marzeion, B., Hock, R., Goelzer, H., Seroussi, H., Jourdain, N. C., Slater, D. A., Turner, F. E., Smith, C. J., et al. Projected land ice contributions to twenty-first-century sea level rise. *Nature*, 593(7857):74–82, 2021.

Escutia, C., DeConto, R. M., Dunbar, R., Santis, L. D., Shevenell, A., and Naish, T. Keeping an eye on Antarctic Ice Sheet stability. *Oceanography*, 32(1):32–46, 2019.

Fairbanks, R. G. A 17, 000-year glacio-eustatic sea level record: influence of glacial melting rates on the Younger Dryas event and deep-ocean circulation. *Nature*, 342 (6250):637–642, 1989.

Favier, L., Durand, G., Cornford, S. L., Gudmundsson, G. H., Gagliardini, O., Gillet-Chaulet, F., Zwinger, T., Payne, A., and Le Brocq, A. M. Retreat of Pine Island Glacier controlled by marine ice-sheet instability. *Nature Climate Change*, 4(2):117–121, 2014.

Favier, L., Jourdain, N. C., Jenkins, A., Merino, N., Durand, G., Gagliardini, O., Gillet-Chaulet, F., and Mathiot, P. Assessment of sub-shelf melting parameterisations using the ocean–ice-sheet coupled model NEMO (v3. 6)–Elmer/Ice (v8. 3). *Geoscientific Model Development*, 12(6):2255–2283, 2019.

Foldvik, A., Gammelsrød, T., Nygaard, E., and Østerhus, S. Current measurements near Ronne Ice Shelf: Implications for circulation and melting. *Journal of Geophysical Research: Oceans*, 106(C3):4463–4477, 2001.

Foster, T. D. Temperature and salinity fields under the Ross Ice Shelf. *Antarct. J. US*, 13:81–82, 1978.

Foster, T. D. The temperature and salinity fine structure of the ocean under the Ross Ice Shelf. *Journal of Geophysical Research: Oceans*, 88(C4):2556–2564, 1983.

Fretwell, P., Pritchard, H. D., Vaughan, D. G., Bamber, J. L., Barrand, N. E., Bell, R., Bianchi, C., Bingham, R., Blankenship, D. D., Casassa, G., et al. Bedmap2: improved ice bed, surface and thickness datasets for Antarctica. *The Cryosphere*, 7(1):375–393, 2013.

Fürst, J. J., Durand, G., Gillet-Chaulet, F., Tavard, L., Rankl, M., Braun, M., and Gagliardini, O. The safety band of Antarctic ice shelves. *Nature Climate Change*, 6(5):479–482, 2016.

Galeotti, S., DeConto, R., Naish, T., Stocchi, P., Florindo, F., Pagani, M., Barrett, P., Bohaty, S. M., Lanci, L., Pollard, D., et al. Antarctic Ice Sheet variability across the Eocene-Oligocene boundary climate transition. *Science*, 352(6281): 76–80, 2016.

Gales, J., Rebesco, M., De Santis, L., Bergamasco, A., Colleoni, F., Kim, S., Accettella, D., Kovacevic, V., Liu, Y., Olivo, E., et al. Role of dense shelf water in the development of Antarctic submarine canyon morphology. *Geomorphology*, 372: 107453, 2021.

Galton-Fenzi, B., Hunter, J., Coleman, R., Marsland, S., and Warner, R. Modeling the basal melting and marine ice accretion of the Amery Ice Shelf. *Journal of Geophysical Research: Oceans*, 117(C9), 2012.

Garbe, J., Albrecht, T., Levermann, A., Donges, J. F., and Winkelmann, R. The hysteresis of the Antarctic ice sheet. *Nature*, 585(7826):538–544, 2020.

Gent, P. R. and Mcwilliams, J. C. Isopycnal mixing in ocean circulation models. *Journal of Physical Oceanography*, 20(1):150–155, 1990.

Gent, P. R., Willebrand, J., McDougall, T. J., and McWilliams, J. C. Parameterizing eddy-induced tracer transports in ocean circulation models. *Journal of Physical Oceanography*, 25(4):463–474, 1995.

Gersonde, R., Crosta, X., Abelmann, A., and Armand, L. Sea-surface temperature and sea ice distribution of the Southern Ocean at the EPILOG Last Glacial Maximum—a circum-Antarctic view based on siliceous microfossil records. *Quaternary science reviews*, 24(7-9):869–896, 2005.

Gill, A. Circulation and bottom water production in the Weddell Sea. In *Deep Sea Research and Oceanographic Abstracts*, volume 20, pages 111–140. Elsevier, 1973.

Gilmour, A. Ross ice shelf sea temperatures. *Science*, 203(4379):438–439, 1979.

Golledge, N. R., Menviel, L., Carter, L., Fogwill, C. J., England, M. H., Cortese, G., and Levy, R. H. Antarctic contribution to meltwater pulse 1A from reduced Southern Ocean overturning. *Nature communications*, 5(1):1–10, 2014.

Golledge, N. R., Kowalewski, D. E., Naish, T. R., Levy, R. H., Fogwill, C. J., and Gasson, E. G. The multi-millennial Antarctic commitment to future sea-level rise. *Nature*, 526(7573):421–425, 2015.

Golledge, N. R., Keller, E. D., Gomez, N., Naughten, K. A., Bernales, J., Trusel, L. D., and Edwards, T. L. Global environmental consequences of twenty-first-century ice-sheet melt. *Nature*, 566(7742):65–72, 2019.

Golledge, N. R., Clark, P. U., He, F., Dutton, A., Turney, C., Fogwill, C., Naish, T., Levy, R. H., McKay, R. M., Lowry, D. P., et al. Retreat of the Antarctic Ice Sheet during the Last Interglaciation and implications for future change. *Geophysical Research Letters*, 48(17):e2021GL094513, 2021.

Gordon, A. L., Orsi, A. H., Muench, R., Huber, B. A., Zambianchi, E., and Visbeck, M. Western Ross Sea continental slope gravity currents. *Deep Sea Research Part II: Topical Studies in Oceanography*, 56(13-14):796–817, 2009.

Gudmundsson, G. H., Paolo, F. S., Adusumilli, S., and Fricker, H. A. Instantaneous Antarctic ice sheet mass loss driven by thinning ice shelves. *Geophysical Research Letters*, 46(23):13903–13909, 2019.

Gwyther, D. E., O'Kane, T. J., Galton-Fenzi, B. K., Monselesan, D. P., and Greenbaum, J. S. Intrinsic processes drive variability in basal melting of the Totten Glacier Ice Shelf. *Nature communications*, 9(1):1–8, 2018.

Gwyther, D. E., Kusahara, K., Asay-Davis, X. S., Dinniman, M. S., and Galton-Fenzi, B. K. Vertical processes and resolution impact ice shelf basal melting: A multi-model study. *Ocean Modelling*, 147:101569, 2020a.

Gwyther, D. E., Spain, E. A., King, P., Guihen, D., Williams, G. D., Evans, E., Cook, S., Richter, O., Galton-Fenzi, B. K., and Coleman, R. Cold ocean cavity and weak basal melting of the sørsdal ice shelf revealed by surveys using autonomous platforms. *Journal of Geophysical Research: Oceans*, 125(6):e2019JC015882, 2020b.

Halberstadt, A. R. W., Simkins, L. M., Greenwood, S. L., and Anderson, J. B. Past ice-sheet behaviour: retreat scenarios and changing controls in the Ross Sea, Antarctica. *The Cryosphere*, 10(3):1003–1020, 2016.

Heimbach, P., Menemenlis, D., Losch, M., Campin, J.-M., and Hill, C. On the formulation of sea-ice models. Part 2: Lessons from multi-year adjoint sea-ice export sensitivities through the Canadian Arctic Archipelago. *Ocean Modelling*, 33(1-2):145–158, 2010.

Hellmer, H. H. and Olbers, D. J. A two-dimensional model for the thermohaline circulation under an ice shelf. *Antarctic Science*, 1(4):325–336, 1989.

Hellmer, H. H., Kauker, F., Timmermann, R., Determann, J., and Rae, J. Twenty-first-century warming of a large Antarctic ice-shelf cavity by a redirected coastal current. *Nature*, 485(7397):225–228, 2012.

Hellmer, H. H., Kauker, F., Timmermann, R., and Hattermann, T. The fate of the southern Weddell Sea continental shelf in a warming climate. *Journal of Climate*, 30(12):4337–4350, 2017.

Hersbach, H., Bell, B., Berrisford, P., Hirahara, S., Horányi, A., Muñoz-Sabater, J., Nicolas, J., Peubey, C., Radu, R., Schepers, D., et al. The ERA5 global reanalysis. *Quarterly Journal of the Royal Meteorological Society*, 146(730):1999–2049, 2020.

Holland, D., Hunter, J., Grosfeld, K., Hellmer, H., Jenkins, A., Morales Maqueda, M., Hemer, M., Williams, M., Klinck, J., and Dinniman, M. The ice shelf-ocean model intercomparison project (ISOMIP). In *AGU Fall Meeting Abstracts*, volume 2003, pages C41A–05, 2003.

Holland, D. M. and Jenkins, A. Modeling thermodynamic ice–ocean interactions at the base of an ice shelf. *Journal of Physical Oceanography*, 29(8):1787–1800, 1999.

Holland, P. R. and Feltham, D. L. The effects of rotation and ice shelf topography on frazil-laden ice shelf water plumes. *Journal of physical oceanography*, 36(12): 2312–2327, 2006.

Holland, P. R., Jenkins, A., and Holland, D. M. The response of ice shelf basal melting to variations in ocean temperature. *Journal of Climate*, 21(11):2558–2572, 2008.

Huang, H., Gutjahr, M., Eisenhauer, A., and Kuhn, G. No detectable Weddell Sea Antarctic bottom water export during the last and penultimate glacial maximum. *Nature communications*, 11(1):1–10, 2020.

Hughes, A. L., Gyllencreutz, R., Lohne, Ø. S., Mangerud, J., and Svendsen, J. I. The last Eurasian ice sheets–a chronological database and time-slice reconstruction, DATED-1. *Boreas*, 45(1):1–45, 2016.

Jacobs, S. and Giulivi, C. Thermohaline data and ocean circulation on the Ross Sea continental shelf. In *Oceanography of the Ross Sea Antarctica*, pages 3–16. Springer, 1999.

Jacobs, S., Helmer, H., Doake, C., Jenkins, A., and Frolich, R. Melting of ice shelves and the mass balance of Antarctica. *Journal of Glaciology*, 38(130):375–387, 1992.

Jacobs, S. S. On the nature and significance of the Antarctic Slope Front. *Marine Chemistry*, 35(1-4):9–24, 1991.

Jacobs, S. S. and Giulivi, C. F. Large multidecadal salinity trends near the Pacific–Antarctic continental margin. *Journal of Climate*, 23(17):4508–4524, 2010.

Jacobs, S. S., Amos, A. F., and Bruchhausen, P. M. Ross Sea oceanography and Antarctic bottom water formation. In *Deep Sea Research and Oceanographic Abstracts*, volume 17, pages 935–962. Elsevier, 1970.

Jacobs, S. S., Gordon, A. L., and Ardai Jr, J. Circulation and melting beneath the Ross Ice Shelf. *Science*, 203(4379):439–443, 1979.

Jacobs, S. S., Fairbanks, R. G., and Horibe, Y. Origin and evolution of water masses near the Antarctic continental margin: Evidence from $H_2^{18}O/H_2^{16}O$ ratios in seawater. *Oceanology of the Antarctic continental shelf*, 43:59–85, 1985.

Jacobs, S. S., Jenkins, A., Giulivi, C. F., and Dutrieux, P. Stronger ocean circulation and increased melting under Pine Island Glacier ice shelf. *Nature Geoscience*, 4 (8):519–523, 2011.

Jendersie, S., Williams, M. J., Langhorne, P. J., and Robertson, R. The density-driven winter intensification of the Ross Sea circulation. *Journal of Geophysical Research: Oceans*, 123(11):7702–7724, 2018.

Jenkins, A. and Jacobs, S. Circulation and melting beneath George VI ice shelf, Antarctica. *Journal of Geophysical Research: Oceans*, 113(C4), 2008.

Jenkins, A., Hellmer, H. H., and Holland, D. M. The role of meltwater advection in the formulation of conservative boundary conditions at an ice–ocean interface. *Journal of physical oceanography*, 31(1):285–296, 2001.

Jenkins, A., Dutrieux, P., Jacobs, S. S., McPhail, S. D., Perrett, J. R., Webb, A. T., and White, D. Observations beneath Pine Island Glacier in West Antarctica and implications for its retreat. *Nature Geoscience*, 3(7):468–472, 2010.

Jenkins, A., Dutrieux, P., Jacobs, S., Steig, E. J., Gudmundsson, G. H., Smith, J., and Heywood, K. J. Decadal ocean forcing and Antarctic ice sheet response: Lessons from the Amundsen Sea. *Oceanography*, 29(4):106–117, 2016.

Jenkins, A., Shoosmith, D., Dutrieux, P., Jacobs, S., Kim, T. W., Lee, S. H., Ha, H. K., and Stammerjohn, S. West Antarctic Ice Sheet retreat in the Amundsen Sea driven by decadal oceanic variability. *Nature Geoscience*, 11(10):733–738, 2018.

Jones, J. M., Gille, S. T., Goosse, H., Abram, N. J., Canziani, P. O., Charman, D. J., Clem, K. R., Crosta, X., de Lavergne, C., Eisenman, I., et al. Assessing recent trends in high-latitude Southern Hemisphere surface climate. *Nature Climate Change*, 6(10):917–926, 2016.

Joughin, I. and Alley, R. B. Stability of the West Antarctic ice sheet in a warming world. *Nature Geoscience*, 4(8):506–513, 2011.

Joughin, I., Smith, B. E., and Medley, B. Marine ice sheet collapse potentially under way for the Thwaites Glacier Basin, West Antarctica. *Science*, 344(6185):735–738, 2014.

Jourdain, N. C., Asay-Davis, X., Hattermann, T., Straneo, F., Seroussi, H., Little, C. M., and Nowicki, S. A protocol for calculating basal melt rates in the ISMIP6 Antarctic ice sheet projections. *The Cryosphere*, 14(9):3111–3134, 2020.

Kim, S., McKay, R. M., Santis, L. D., Kulhanek, D. K., Kim, S., et al. Deciphering Ross Sea West Antarctic Ice Sheet History: IODP Expedition 374. 2018.

Kimura, S., Nicholls, K. W., and Venables, E. Estimation of ice shelf melt rate in the presence of a thermohaline staircase. *Journal of Physical Oceanography*, 45(1): 133–148, 2015.

Kingslake, J., Scherer, R., Albrecht, T., Coenen, J., Powell, R., Reese, R., Stansell, N., Tulaczyk, S., Wearing, M., and Whitehouse, P. Extensive retreat and re-advance of the West Antarctic Ice Sheet during the Holocene. *Nature*, 558(7710):430–434, 2018.

Klinck, J. and Dinniman, M. Exchange across the shelf break at high southern latitudes. *Ocean Science*, 6(2), 2010.

Knorr, G. and Lohmann, G. Climate warming during Antarctic ice sheet expansion at the Middle Miocene transition. *Nature Geoscience*, 7(5):376–381, 2014.

Knorr, G., Barker, S., Zhang, X., Lohmann, G., Gong, X., Gierz, P., Stepanek, C., and Stap, L. B. A salty deep ocean as a prerequisite for glacial termination. *Nature Geoscience*, 14(12):930–936, 2021.

Knutti, R., Flückiger, J., Stocker, T., and Timmermann, A. Strong hemispheric coupling of glacial climate through freshwater discharge and ocean circulation. *Nature*, 430(7002):851–856, 2004.

Konrad, H., Shepherd, A., Gilbert, L., Hogg, A. E., McMillan, M., Muir, A., and Slater, T. Net retreat of Antarctic glacier grounding lines. *Nature Geoscience*, 11 (4):258–262, 2018.

Kulessa, B., Jansen, D., Luckman, A. J., King, E. C., and Sammonds, P. R. Marine ice regulates the future stability of a large Antarctic ice shelf. *Nature communications*, 5(1):1–7, 2014.

Kusahara, K. and Hasumi, H. Modeling Antarctic ice shelf responses to future climate changes and impacts on the ocean. *Journal of Geophysical Research: Oceans*, 118(5):2454–2475, 2013.

Ladant, J.-B., Donnadieu, Y., Lefebvre, V., and Dumas, C. The respective role of atmospheric carbon dioxide and orbital parameters on ice sheet evolution at the Eocene-Oligocene transition. *Paleoceanography*, 29(8):810–823, 2014.

Lamy, F., Chiang, J. C., Martínez-Méndez, G., Thierens, M., Arz, H. W., Bosmans, J., Hebbeln, D., Lambert, F., Lembke-Jene, L., and Stuut, J.-B. Precession modulation of the South Pacific westerly wind belt over the past million years. *Proceedings of the National Academy of Sciences*, 116(47):23455–23460, 2019.

Large, W. and Pond, S. Open ocean momentum flux measurements in moderate to strong winds. *Journal of physical oceanography*, 11(3):324–336, 1981.

Large, W. and Pond, S. Sensible and latent heat flux measurements over the ocean. *Journal of physical Oceanography*, 12(5):464–482, 1982.

Large, W. G., McWilliams, J. C., and Doney, S. C. Oceanic vertical mixing: A review and a model with a nonlocal boundary layer parameterization. *Reviews of Geophysics*, 32(4):363–403, 1994.

Laskar, J., Fienga, A., Gastineau, M., and Manche, H. La2010: a new orbital solution for the long-term motion of the Earth. *Astronomy & Astrophysics*, 532:A89, 2011.

Lellouche, J.-M., Greiner, E., Bourdallé-Badie, R., Garric, G., Melet, A., Drévillon, M., Bricaud, C., Hamon, M., Le Galloudec, O., Regnier, C., et al. The Copernicus global 1/12 oceanic and sea ice GLORYS12 reanalysis. *Frontiers in Earth Science*, 9:698876, 2021.

Levermann, A., Winkelmann, R., Albrecht, T., Goelzer, H., Golledge, N. R., Greve, R., Huybrechts, P., Jordan, J., Leguy, G., Martin, D., Morlighem, M., Pattyn, F., Pollard, D., Quiquet, A., Rodehacke, C., Seroussi, H., Sutter, J., Zhang, T., Van Breedam, J., Calov, R., DeConto, R., Dumas, C., Garbe, J., Gudmundsson, G. H., Hoffman, M. J., Humbert, A., Kleiner, T., Lipscomb, W. H., Meinshausen, M., Ng, E., Nowicki, S. M. J., Perego, M., Price, S. F., Saito, F., Schlegel, N.-J., Sun, S., and van de Wal, R. S. W. Projecting Antarctica's contribution to future sea level rise from basal ice shelf melt using linear response functions of 16 ice sheet models (LARMIP-2). *Earth System Dynamics*, 11(1):35–76, 2020. doi: 10.5194/esd-11-35-2020. URL https://esd.copernicus.org/articles/11/35/2020/.

Levy, R., Harwood, D., Florindo, F., Sangiorgi, F., Tripati, R., Von Eynatten, H., Gasson, E., Kuhn, G., Tripati, A., DeConto, R., et al. Antarctic ice sheet sensitivity to atmospheric CO2 variations in the early to mid-Miocene. *Proceedings of the National Academy of Sciences*, 113(13):3453–3458, 2016.

Levy, R. H., Meyers, S., Naish, T. R., Golledge, N. R., McKay, R. M., Crampton, J. S., DeConto, R., De Santis, L., Florindo, F., Gasson, E. G., et al. Antarctic ice-sheet sensitivity to obliquity forcing enhanced through ocean connections. *Nature Geoscience*, 12(2):132–137, 2019.

Lewis, E. and Perkin, R. Ice pumps and their rates. *Journal of Geophysical Research: Oceans*, 91(C10):11756–11762, 1986.

Li, X., Cai, W., Meehl, G. A., Chen, D., Yuan, X., Raphael, M., Holland, D. M., Ding, Q., Fogt, R. L., Markle, B. R., et al. Tropical teleconnection impacts on Antarctic climate changes. *Nature Reviews Earth & Environment*, 2(10):680–698, 2021.

Liakka, J., Colleoni, F., Ahrens, B., and Hickler, T. The impact of climate-vegetation interactions on the onset of the Antarctic ice sheet. *Geophysical Research Letters*, 41(4):1269–1276, 2014.

Licht, K. J. and Andrews, J. T. The 14C record of Late Pleistocene ice advance and retreat in the central Ross Sea, Antarctica. *Arctic, Antarctic, and Alpine Research*, 34(3):324–333, 2002.

Liu, Y., Moore, J. C., Cheng, X., Gladstone, R. M., Bassis, J. N., Liu, H., Wen, J., and Hui, F. Ocean-driven thinning enhances iceberg calving and retreat of Antarctic ice shelves. *Proceedings of the National Academy of Sciences*, 112(11): 3263–3268, 2015.

Liu, Z., Otto-Bliesner, B., He, F., Brady, E., Tomas, R., Clark, P., Carlson, A., Lynch-Stieglitz, J., Curry, W., Brook, E., et al. Transient simulation of last deglaciation with a new mechanism for Bølling-Allerød warming. *science*, 325 (5938):310–314, 2009.

Losch, M. Modeling ice shelf cavities in a z coordinate ocean general circulation model. *Journal of Geophysical Research: Oceans*, 113(C8), 2008.

Losch, M., Menemenlis, D., Campin, J.-M., Heimbach, P., and Hill, C. On the formulation of sea-ice models. Part 1: Effects of different solver implementations and parameterizations. *Ocean Modelling*, 33(1-2):129–144, 2010.

Lowry, D. P., Golledge, N. R., Bertler, N. A., Jones, R. S., and McKay, R. Deglacial grounding-line retreat in the Ross Embayment, Antarctica, controlled by ocean and atmosphere forcing. *Science Advances*, 5(8):eaav8754, 2019.

Lucchi, R. G., Sagnotti, L., Camerlenghi, A., Macrì, P., Rebesco, M., Pedrosa, M. T., and Giorgetti, G. Marine sedimentary record of Meltwater Pulse 1a along the NW Barents Sea continental margin. *arktos*, 1(1):1–14, 2015.

MacAyeal, D. R. Numerical simulations of the Ross Sea tides. *Journal of Geophysical Research: Oceans*, 89(C1):607–615, 1984a.

MacAyeal, D. R. Thermohaline circulation below the Ross Ice Shelf: A consequence of tidally induced vertical mixing and basal melting. *Journal of Geophysical Research: Oceans*, 89(C1):597–606, 1984b.

MacAyeal, D. R. Large-scale ice flow over a viscous basal sediment: Theory and application to ice stream B, Antarctica. *Journal of Geophysical Research: Solid Earth*, 94(B4):4071–4087, 1989.

Mack, S. L., Dinniman, M. S., Klinck, J. M., McGillicuddy Jr., D. J., and Padman, L. Modeling Ocean Eddies on Antarctica's Cold Water Continental Shelves and Their Effects on Ice Shelf Basal Melting. *Journal of Geophysical Research: Oceans*, 124(7):5067–5084, 2019. doi: 10.1029/2018JC014688. URL https://agupubs.onlinelibrary.wiley.com/doi/abs/10.1029/2018JC014688.

Majewski, W., Prothro, L. O., Simkins, L. M., Demianiuk, E. J., and Anderson, J. B. Foraminiferal patterns in deglacial sediment in the western Ross Sea, Antarctica: Life near grounding lines. *Paleoceanography and Paleoclimatology*, 35 (5):e2019PA003716, 2020.

Marshall, J. and Speer, K. Closure of the meridional overturning circulation through Southern Ocean upwelling. *Nature Geoscience*, 5(3):171–180, 2012.

Marshall, J., Adcroft, A., Hill, C., Perelman, L., and Heisey, C. A finite-volume, incompressible Navier Stokes model for studies of the ocean on parallel computers. *Journal of Geophysical Research: Oceans*, 102(C3):5753–5766, 1997a.

Marshall, J., Hill, C., Perelman, L., and Adcroft, A. Hydrostatic, quasi-hydrostatic, and nonhydrostatic ocean modeling. *Journal of Geophysical Research: Oceans*, 102(C3):5733–5752, 1997b.

Martin, M. A., Winkelmann, R., Haseloff, M., Albrecht, T., Bueler, E., Khroulev, C., and Levermann, A. The Potsdam Parallel Ice Sheet Model (PISM-PIK)–Part 2: Dynamic equilibrium simulation of the Antarctic ice sheet. *The Cryosphere*, 5 (3):727–740, 2011.

Masson-Delmotte, V., Zhai, P., Pirani, A., Connors, S. L., Péan, C., Berger, S., Caud, N., Chen, Y., Goldfarb, L., Gomis, M., et al. Climate change 2021: the physical science basis. *Contribution of working group I to the sixth assessment report of the intergovernmental panel on climate change*, page 2, 2021.

Mathiot, P., Jenkins, A., Harris, C., and Madec, G. Explicit representation and parametrised impacts of under ice shelf seas in the z* coordinate ocean model NEMO 3.6. *Geoscientific Model Development*, 10(7):2849–2874, 2017.

McDougall, T. J., Jackett, D. R., Wright, D. G., and Feistel, R. Accurate and computationally efficient algorithms for potential temperature and density of seawater. *Journal of Atmospheric and Oceanic Technology*, 20(5):730–741, 2003.

McGlannan, A. J., Bart, P. J., Chow, J. M., and DeCesare, M. On the influence of post-LGM ice shelf loss and grounding zone sedimentation on West Antarctic ice sheet stability. *Marine Geology*, 392:151–169, 2017.

McKay, R. M., De Santis, L., and Kulhanek, D. K. Ross Sea West Antarctic Ice Sheet History. *Proceedings of the International Ocean Discovery Program*, 374, 2019.

McPhail, S., Templeton, R., Pebody, M., Roper, D., and Morrison, R. Autosub long range AUV missions under the Filchner and Ronne ice shelves in the Weddell sea, Antarctica-an engineering perspective. In *OCEANS 2019-Marseille*, pages 1–8. IEEE, 2019.

McPhail, S. D., Furlong, M. E., Pebody, M., Perrett, J., Stevenson, P., Webb, A., and White, D. Exploring beneath the PIG Ice Shelf with the Autosub3 AUV. In *Oceans 2009-Europe*, pages 1–8. IEEE, 2009.

Members, M. P. Constraints on the magnitude and patterns of ocean cooling at the Last Glacial Maximum. *Nature Geoscience*, 2(2):127–132, 2009.

Members, M. P. Onset of deglacial warming in West Antarctica driven by local orbital forcing. *Nature*, 500(7463):440–444, 2013.

Members, M. P. Precise interpolar phasing of abrupt climate change during the last ice age. *Nature*, 520(7549):661–665, 2015.

Menviel, L., Timmermann, A., Timm, O. E., and Mouchet, A. Deconstructing the Last Glacial termination: the role of millennial and orbital-scale forcings. *Quaternary Science Reviews*, 30(9-10):1155–1172, 2011.

Michel, R., Linick, T., and Williams, P. Tritium and carbon-14 distributions in seawater from under the Ross Ice Shelf Project ice hole. *Science*, 203(4379): 445–446, 1979.

Miller, K. G., MouNtaiN, G. S., WriGht, J. D., and BroWNiNG, J. V. A 180-million-year record of sea level and ice volume variations from continental margin and deep-sea isotopic records. *Oceanography*, 24(2):40–53, 2011.

Moholdt, G., Padman, L., and Fricker, H. A. Basal mass budget of Ross and Filchner-Ronne ice shelves, Antarctica, derived from Lagrangian analysis of ICESat altimetry. *Journal of Geophysical Research: Earth Surface*, 119(11):2361–2380, 2014.

Monnin, E., Steig, E., Siegenthaler, U., Kawamura, K., Schwander, J., Stauffer, B., Stocker, T., Morse, D., Barnola, J., Bellier, B., et al. EPICA Dome C ice core high resolution Holocene and transition CO2 data. *IGBP PAGES/World Data Center for Paleoclimatology Data Contribution Series*, 55, 2004.

Morlighem, M., Rignot, E., Binder, T., Blankenship, D., Drews, R., Eagles, G., Eisen, O., Ferraccioli, F., Forsberg, R., Fretwell, P., et al. Deep glacial troughs and stabilizing ridges unveiled beneath the margins of the Antarctic ice sheet. *Nature Geoscience*, 13(2):132–137, 2020.

Mosola, A. B. and Anderson, J. B. Expansion and rapid retreat of the West Antarctic Ice Sheet in eastern Ross Sea: possible consequence of over-extended ice streams? *Quaternary Science Reviews*, 25(17-18):2177–2196, 2006.

Mouginot, J., Rignot, E., Scheuchl, B., and Millan, R. Comprehensive annual ice sheet velocity mapping using Landsat-8, Sentinel-1, and RADARSAT-2 data. *Remote Sensing*, 9(4):364, 2017.

Mouginot, J., Rignot, E., and Scheuchl, B. Continent-wide, interferometric SAR phase, mapping of Antarctic ice velocity. *Geophysical Research Letters*, 46(16): 9710–9718, 2019.

Naish, T., Powell, R., Levy, R., Wilson, G., Scherer, R., Talarico, F., Krissek, L., Niessen, F., Pompilio, M., Wilson, T., et al. Obliquity-paced Pliocene West Antarctic ice sheet oscillations. *Nature*, 458(7236):322–328, 2009.

Naish, T. R., Duncan, B., Levy, R., McKay, R. M., Escutia, C., De Santis, L., Colleoni, F., Gasson, E. G., DeConto, R. M., and Wilson, G. Antarctic Ice Sheet dynamics during the Late Oligocene and Early Miocene: climatic conundrums revisited. In *Antarctic Climate Evolution*, pages 363–387. Elsevier, 2022.

Nakayama, Y., Timmermann, R., Schrøder, M., and Hellmer, H. H. On the difficulty of modeling Circumpolar Deep Water intrusions onto the Amundsen Sea continental shelf. *Ocean Modelling*, 84:26–34, 2014.

Nakayama, Y., Menemenlis, D., Schodlok, M., and Rignot, E. Amundsen and B ellingshausen S eas simulation with optimized ocean, sea ice, and thermodynamic ice shelf model parameters. *Journal of Geophysical Research: Oceans*, 122(8): 6180–6195, 2017.

Nakayama, Y., Menemenlis, D., Zhang, H., Schodlok, M., and Rignot, E. Origin of Circumpolar Deep Water intruding onto the Amundsen and Bellingshausen Sea continental shelves. *Nature communications*, 9(1):1–9, 2018.

Nakayama, Y., Manucharyan, G., Zhang, H., Dutrieux, P., Torres, H. S., Klein, P., Seroussi, H., Schodlok, M., Rignot, E., and Menemenlis, D. Pathways of ocean heat towards Pine Island and Thwaites grounding lines. *Scientific reports*, 9(1): 1–9, 2019.

Nakayama, Y., Timmermann, R., and H Hellmer, H. Impact of West Antarctic ice shelf melting on Southern Ocean hydrography. *The Cryosphere*, 14(7):2205–2216, 2020.

Naughten, K. A., Meissner, K. J., Galton-Fenzi, B. K., England, M. H., Timmermann, R., Hellmer, H. H., Hattermann, T., and Debernard, J. B. Intercomparison of Antarctic ice-shelf, ocean, and sea-ice interactions simulated by MetROMS-iceshelf and FESOM 1.4. *Geoscientific Model Development*, 11(4):1257–1292, 2018.

Naughten, K. A., Jenkins, A., Holland, P. R., Mugford, R. I., Nicholls, K. W., and Munday, D. R. Modeling the Influence of the Weddell Polynya on the Filchner–Ronne Ice Shelf Cavity. *Journal of Climate*, 32(16):5289–5303, 2019.

Naughten, K. A., De Rydt, J., Rosier, S. H., Jenkins, A., Holland, P. R., and Ridley, J. K. Two-timescale response of a large Antarctic ice shelf to climate change. *Nature communications*, 12(1):1–10, 2021.

Neuhaus, S. U., Tulaczyk, S. M., Stansell, N. D., Coenen, J. J., Scherer, R. P., Mikucki, J. A., and Powell, R. D. Did Holocene climate changes drive West Antarctic grounding line retreat and readvance? *The Cryosphere*, 15(10):4655–4673, 2021.

Nicholls, K., Abrahamsen, E., Buck, J., Dodd, P., Goldblatt, C., Griffiths, G., Heywood, K., Hughes, N., Kaletzky, A., Lane-Serff, G., et al. Measurements beneath an Antarctic ice shelf using an autonomous underwater vehicle. *Geophysical Research Letters*, 33(8), 2006.

Nicholls, R. J., Tol, R. S., and Vafeidis, A. T. Global estimates of the impact of a collapse of the West Antarctic ice sheet: an application of FUND. *Climatic Change*, 91(1):171–191, 2008.

Obase, T., Abe-Ouchi, A., Kusahara, K., Hasumi, H., and Ohgaito, R. Responses of basal melting of Antarctic ice shelves to the climatic forcing of the Last Glacial Maximum and CO2 doubling. *Journal of Climate*, 30(10):3473–3497, 2017.

Orsi, A. H. and Whitworth, T. *Hydrographic Atlas of the World Ocean Circulation Experiment (WOCE): Volume 1: Southern Ocean*. WOCE International Project Office Southampton, UK, 2005.

Orsi, A. H. and Wiederwohl, C. L. A recount of Ross Sea waters. *Deep Sea Research Part II: Topical Studies in Oceanography*, 56(13-14):778–795, 2009.

Orsi, A. H., Johnson, G. C., and Bullister, J. L. Circulation, mixing, and production of Antarctic Bottom Water. *Progress in Oceanography*, 43(1):55–109, 1999.

Otto-Bliesner, B. L., Brady, E. C., Clauzet, G., Tomas, R., Levis, S., and Kothavala, Z. Last glacial maximum and Holocene climate in CCSM3. *Journal of Climate*, 19(11):2526–2544, 2006.

Padman, L., Erofeeva, S., and Joughin, I. Tides of the Ross sea and Ross ice shelf cavity. *Antarctic Science*, 15(1):31–40, 2003.

Padman, L., Howard, S. L., Orsi, A. H., and Muench, R. D. Tides of the northwestern Ross Sea and their impact on dense outflows of Antarctic Bottom Water. *Deep Sea Research Part II: Topical Studies in Oceanography*, 56(13-14):818–834, 2009.

Padman, L., Siegfried, M. R., and Fricker, H. A. Ocean tide influences on the Antarctic and Greenland ice sheets. *Reviews of Geophysics*, 56(1):142–184, 2018.

Paolo, F., Padman, L., Fricker, H., Adusumilli, S., Howard, S., and Siegfried, M. Response of Pacific-sector Antarctic ice shelves to the El Niño/Southern oscillation. *Nature geoscience*, 11(2):121–126, 2018.

Paolo, F. S., Fricker, H. A., and Padman, L. Volume loss from Antarctic ice shelves is accelerating. *Science*, 348(6232):327–331, 2015.

Pattyn, F. and Morlighem, M. The uncertain future of the Antarctic Ice Sheet. *Science*, 367(6484):1331–1335, 2020.

Paxman, G. J., Gasson, E. G., Jamieson, S. S., Bentley, M. J., and Ferraccioli, F. Long-term increase in Antarctic Ice Sheet vulnerability driven by bed topography evolution. *Geophysical Research Letters*, 47(20):e2020GL090003, 2020.

Pedro, J. B., Bostock, H. C., Bitz, C. M., He, F., Vandergoes, M. J., Steig, E. J., Chase, B. M., Krause, C. E., Rasmussen, S. O., Markle, B. R., et al. The spatial extent and dynamics of the Antarctic Cold Reversal. *Nature Geoscience*, 9(1): 51–55, 2016.

Peltier, W. Global glacial isostasy and the surface of the ice-age Earth: the ICE-5G (VM2) model and GRACE. *Annu. Rev. Earth Planet. Sci.*, 32:111–149, 2004.

Peltier, W. R., Argus, D., and Drummond, R. Space geodesy constrains ice age terminal deglaciation: The global ICE-6G_C (VM5a) model. *Journal of Geophysical Research: Solid Earth*, 120(1):450–487, 2015.

Petrelli, P., Bindoff, N., and Bergamasco, A. The sea ice dynamics of Terra Nova Bay and Ross Ice Shelf Polynyas during a spring and winter simulation. *Journal of Geophysical Research: Oceans*, 113(C9), 2008.

Pollard, D. and DeConto, R. Description of a hybrid ice sheet-shelf model, and application to Antarctica. *Geoscientific Model Development*, 5(5):1273–1295, 2012.

Pollard, D. and DeConto, R. M. Modelling West Antarctic ice sheet growth and collapse through the past five million years. *Nature*, 458(7236):329–332, 2009.

Pörtner, H.-O., Roberts, D. C., Masson-Delmotte, V., Zhai, P., Tignor, M., Poloczanska, E., and Weyer, N. The ocean and cryosphere in a changing climate. *IPCC Special Report on the Ocean and Cryosphere in a Changing Climate*, 2019.

Pritchard, H., Ligtenberg, S. R., Fricker, H. A., Vaughan, D. G., van den Broeke, M. R., and Padman, L. Antarctic ice-sheet loss driven by basal melting of ice shelves. *Nature*, 484(7395):502–505, 2012.

Prothro, L. O., Simkins, L. M., Majewski, W., and Anderson, J. B. Glacial retreat patterns and processes determined from integrated sedimentology and geomorphology records. *Marine Geology*, 395:104–119, 2018.

Prothro, L. O., Majewski, W., Yokoyama, Y., Simkins, L. M., Anderson, J. B., Yamane, M., Miyairi, Y., and Ohkouchi, N. Timing and pathways of east Antarctic ice sheet retreat. *Quaternary Science Reviews*, 230:106166, 2020.

Rabineau, M., Berné, S., Olivet, J.-L., Aslanian, D., Guillocheau, F., and Joseph, P. Paleo sea levels reconsidered from direct observation of paleoshoreline position during Glacial Maxima (for the last 500,000 yr). *Earth and Planetary Science Letters*, 252(1-2):119–137, 2006.

Redi, M. H. Oceanic isopycnal mixing by coordinate rotation. *Journal of Physical Oceanography*, 12(10):1154–1158, 1982.

Reerink, T. J., van de Berg, W. J., and van de Wal, R. S. W. OBLIMAP 2.0: a fast climate model–ice sheet model coupler including online embeddable mapping routines. *Geoscientific Model Development*, 9(11):4111–4132, 2016. doi: 10.5194/gmd-9-4111-2016. URL https://gmd.copernicus.org/articles/9/4111/2016/.

Reese, R., Gudmundsson, G. H., Levermann, A., and Winkelmann, R. The far reach of ice-shelf thinning in Antarctica. *Nature Climate Change*, 8(1):53–57, 2018.

Richter, O., Gwyther, D. E., King, M. A., and Galton-Fenzi, B. K. Tidal Modulation of Antarctic Ice Shelf Melting. *The Cryosphere Discussions*, pages 1–32, 2020.

Rignot, E., Jacobs, S., Mouginot, J., and Scheuchl, B. Ice-shelf melting around Antarctica. *Science*, 341(6143):266–270, 2013.

Rignot, E., Mouginot, J., Scheuchl, B., Van Den Broeke, M., Van Wessem, M. J., and Morlighem, M. Four decades of Antarctic Ice Sheet mass balance from 1979–2017. *Proceedings of the National Academy of Sciences*, 116(4):1095–1103, 2019.

Ringler, T., Petersen, M., Higdon, R. L., Jacobsen, D., Jones, P. W., and Maltrud, M. A multi-resolution approach to global ocean modeling. *Ocean Modelling*, 69: 211–232, 2013.

Rintoul, S. R., Hughes, C. W., and Olbers, D. The Antarctic circumpolar current system. In *International Geophysics*, volume 77, pages 271–XXXVI. Elsevier, 2001.

Rintoul, S. R., Silvano, A., Pena-Molino, B., van Wijk, E., Rosenberg, M., Greenbaum, J. S., and Blankenship, D. D. Ocean heat drives rapid basal melt of the Totten Ice Shelf. *Science Advances*, 2(12):e1601610, 2016.

Robin, G. d. Q. Formation, flow, and disintegration of ice shelves. *Journal of Glaciology*, 24(90):259–271, 1979.

Robinson, N., Stevens, C., and McPhee, M. Observations of amplified roughness from crystal accretion in the sub-ice ocean boundary layer. *Geophysical Research Letters*, 44(4):1814–1822, 2017.

Robinson, N. J., Williams, M. J., Stevens, C. L., Langhorne, P. J., and Haskell, T. G. Evolution of a supercooled Ice Shelf Water plume with an actively growing subice platelet matrix. *Journal of Geophysical Research: Oceans*, 119(6):3425–3446, 2014.

Roemmich, D., Church, J., Gilson, J., Monselesan, D., Sutton, P., and Wijffels, S. Unabated planetary warming and its ocean structure since 2006. *Nature climate change*, 5(3):240–245, 2015.

Russo, A., Bergamasco, A., Carniel, S., Grieco, L., Sclavo, M., and Spezie, G. Climatology and decadal variability of the Ross Sea shelf waters. *Advances in Oceanography and Limnology*, 2(1):55–77, 2011.

Ryan, S., Hellmer, H. H., Janout, M., Darelius, E., Vignes, L., and Schröder, M. Exceptionally warm and prolonged flow of Warm Deep Water toward the Filchner-Ronne Ice Shelf in 2017. *Geophysical Research Letters*, 47(13):e2020GL088119, 2020.

Sansiviero, M. and Maqueda, MÁ Morales and Fusco, G and Aulicino, G and Flocco, D and Budillon, G, j. v. p. y. p. Modelling sea ice formation in the Terra Nova Bay polynya.

Schaffer, J., Timmermann, R., Arndt, J. E., Steinhage, D., and Kanzow, T. RTopo-2: A global dataset of ice sheet topography, cavity geometry and ocean bathymetry to study ice-ocean interaction in Northeast Greenland. 2014.

Schmidtko, S., Heywood, K. J., Thompson, A. F., and Aoki, S. Multidecadal warming of Antarctic waters. *Science*, 346(6214):1227–1231, 2014.

Schoof, C. Ice sheet grounding line dynamics: Steady states, stability, and hysteresis. *Journal of Geophysical Research: Earth Surface*, 112(F3), 2007.

Shapiro, N. M. and Ritzwoller, M. H. Inferring surface heat flux distributions guided by a global seismic model: particular application to Antarctica. *Earth and Planetary Science Letters*, 223(1-2):213–224, 2004.

Shchepetkin, A. F. and McWilliams, J. C. The regional oceanic modeling system (ROMS): a split-explicit, free-surface, topography-following-coordinate oceanic model. *Ocean modelling*, 9(4):347–404, 2005.

Siegert, M., Alley, R. B., Rignot, E., Englander, J., and Corell, R. Twenty-first century sea-level rise could exceed IPCC projections for strong-warming futures. *One Earth*, 3(6):691–703, 2020.

Silvano, A., Rintoul, S. R., and Herraiz-Borreguero, L. Ocean-ice shelf interaction in East Antarctica. *Oceanography*, 29(4):130–143, 2016.

Silvano, A., Rintoul, S. R., Kusahara, K., Peña-Molino, B., van Wijk, E., Gwyther, D. E., and Williams, G. D. Seasonality of warm water intrusions onto the continental shelf near the Totten Glacier. *Journal of Geophysical Research: Oceans*, 124(6):4272–4289, 2019.

Silvano, A., Foppert, A., Rintoul, S. R., Holland, P. R., Tamura, T., Kimura, N., Castagno, P., Falco, P., Budillon, G., Haumann, F. A., et al. Recent recovery of Antarctic Bottom Water formation in the Ross Sea driven by climate anomalies. *Nature Geoscience*, 13(12):780–786, 2020.

Simkins, L. M., Anderson, J. B., Greenwood, S. L., Gonnermann, H. M., Prothro, L. O., Halberstadt, A. R. W., Stearns, L. A., Pollard, D., and DeConto, R. M. Anatomy of a meltwater drainage system beneath the ancestral East Antarctic ice sheet. *Nature Geoscience*, 10(9):691–697, 2017.

Spada, G., Melini, D., Galassi, G., and Colleoni, F. Modeling sea level changes and geodetic variations by glacial isostasy: the improved SELEN code. *arXiv preprint arXiv:1212.5061*, 2012.

Spence, P., Griffies, S. M., England, M. H., Hogg, A. M., Saenko, O. A., and Jourdain, N. C. Rapid subsurface warming and circulation changes of Antarctic coastal waters by poleward shifting winds. *Geophysical Research Letters*, 41(13):4601–4610, 2014.

St-Laurent, P., Klinck, J. M., and Dinniman, M. S. On the Role of Coastal Troughs in the Circulation of Warm Circumpolar Deep Water on Antarctic Shelves. *Journal of Physical Oceanography*, 43(1):51–64, 2013. ISSN 0022-3670. doi: 10.1175/JPO-D-11-0237.1. URL https://doi.org/10.1175/JPO-D-11-0237.1.

Steckler, M. and Watts, A. Subsidence of the Atlantic-type continental margin off New York. *Earth and planetary science letters*, 41(1):1–13, 1978.

Stevens, C., Hulbe, C., Brewer, M., Stewart, C., Robinson, N., Ohneiser, C., and Jendersie, S. Ocean mixing and heat transport processes observed under the Ross Ice Shelf control its basal melting. *Proceedings of the National Academy of Sciences*, 117(29):16799–16804, 2020.

Stewart, A. L. and Thompson, A. F. Connecting Antarctic cross-slope exchange with Southern Ocean overturning. *Journal of Physical Oceanography*, 43(7):1453–1471, 2013.

Stewart, A. L. and Thompson, A. F. Eddy-mediated transport of warm Circumpolar Deep Water across the Antarctic shelf break. *Geophysical Research Letters*, 42(2):432–440, 2015.

Stewart, A. L. and Thompson, A. F. Eddy generation and jet formation via dense water outflows across the Antarctic continental slope. *Journal of Physical Oceanography*, 46(12):3729–3750, 2016.

Stewart, A. L., Klocker, A., and Menemenlis, D. Circum-Antarctic shoreward heat transport derived from an eddy-and tide-resolving simulation. *Geophysical Research Letters*, 45(2):834–845, 2018.

Stewart, C. L., Christoffersen, P., Nicholls, K. W., Williams, M. J., and Dowdeswell, J. A. Basal melting of Ross Ice Shelf from solar heat absorption in an ice-front polynya. *Nature Geoscience*, 12(6):435–440, 2019.

Stocker, T. F. North-south connections. *Science*, 297(5588):1814–1815, 2002.

Sun, S., Pattyn, F., Simon, E. G., Albrecht, T., Cornford, S., Calov, R., Dumas, C., Gillet-Chaulet, F., Goelzer, H., Golledge, N. R., et al. Antarctic ice sheet response to sudden and sustained ice-shelf collapse (ABUMIP). *Journal of Glaciology*, 66 (260):891–904, 2020.

Tarasov, L. and Peltier, W. Arctic freshwater forcing of the Younger Dryas cold reversal. *Nature*, 435(7042):662–665, 2005.

Thompson, A. F., Stewart, A. L., Spence, P., and Heywood, K. J. The Antarctic Slope Current in a changing climate. *Reviews of Geophysics*, 56(4):741–770, 2018.

Thompson, D. W. and Wallace, J. M. Annular modes in the extratropical circulation. Part I: Month-to-month variability. *Journal of climate*, 13(5):1000–1016, 2000.

Thompson, D. W., Wallace, J. M., and Hegerl, G. C. Annular modes in the extratropical circulation. Part II: Trends. *Journal of climate*, 13(5):1018–1036, 2000.

Thompson, L., Smith, M., Thomson, J., Stammerjohn, S., Ackley, S., and Loose, B. Frazil ice growth and production during katabatic wind events in the Ross Sea, Antarctica. *The Cryosphere*, 14(10):3329–3347, 2020.

Timmermann, R., Wang, Q., and Hellmer, H. Ice-shelf basal melting in a global finite-element sea-ice/ice-shelf/ocean model. *Annals of Glaciology*, 53(60):303–314, 2012.

Tinto, K., Padman, L., Siddoway, C., Springer, S., Fricker, H., Das, I., Tontini, F. C., Porter, D., Frearson, N., Howard, S., et al. Ross Ice Shelf response to climate driven by the tectonic imprint on seafloor bathymetry. *Nature Geoscience*, 12(6): 441–449, 2019.

Turner, J. The el nino–southern oscillation and antarctica. *International Journal of Climatology: A Journal of the Royal Meteorological Society*, 24(1):1–31, 2004.

Turner, J., Orr, A., Gudmundsson, G. H., Jenkins, A., Bingham, R. G., Hillenbrand, C.-D., and Bracegirdle, T. J. Atmosphere-ocean-ice interactions in the Amundsen Sea embayment, West Antarctica. *Reviews of Geophysics*, 55(1):235–276, 2017.

Turner, J., Guarino, M. V., Arnatt, J., Jena, B., Marshall, G. J., Phillips, T., Bajish, C., Clem, K., Wang, Z., Andersson, T., et al. Recent decrease of summer sea ice in the Weddell Sea, Antarctica. *Geophysical Research Letters*, 47(11):e2020GL087127, 2020.

Turney, C. S., Fogwill, C. J., Golledge, N. R., McKay, N. P., van Sebille, E., Jones, R. T., Etheridge, D., Rubino, M., Thornton, D. P., Davies, S. M., et al. Early Last Interglacial ocean warming drove substantial ice mass loss from Antarctica. *Proceedings of the National Academy of Sciences*, 117(8):3996–4006, 2020.

Uotila, P., Goosse, H., Haines, K., Chevallier, M., Barthélemy, A., Bricaud, C., Carton, J., Fučkar, N., Garric, G., Iovino, D., et al. An assessment of ten ocean reanalyses in the polar regions. *Climate Dynamics*, 52(3-4):1613–1650, 2019.

Vieli, A. Retreat instability of tidewater glaciers and marine ice sheets. In *Snow and Ice-Related Hazards, Risks, and Disasters*, pages 671–706. Elsevier, 2021.

Wang, Q., Danilov, S., Hellmer, H., Sidorenko, D., Schroeter, J., and Jung, T. Enhanced cross-shelf exchange by tides in the western Ross Sea. *Geophysical Research Letters*, 40(21):5735–5739, 2013.

Weber, M. E., Clark, P. U., Ricken, W., Mitrovica, J. X., Hostetler, S. W., and Kuhn, G. Interhemispheric ice-sheet synchronicity during the Last Glacial Maximum. *Science*, 334(6060):1265–1269, 2011.

Wen, J., Wang, Y., Wang, W., Jezek, K., Liu, H., and Allison, I. Basal melting and freezing under the Amery Ice Shelf, East Antarctica. *Journal of Glaciology*, 56 (195):81–90, 2010. doi: 10.3189/002214310791190820.

Whitehouse, P. L., Gomez, N., King, M. A., and Wiens, D. A. Solid Earth change and the evolution of the Antarctic Ice Sheet. *Nature communications*, 10(1):1–14, 2019.

Whitworth, T. and Orsi, A. Antarctic Bottom Water production and export by tides in the Ross Sea. *Geophysical Research Letters*, 33(12), 2006.

Whitworth, T., Orsi, A., Kim, S., Nowlin, W., Locarnini, R., Jacobs, S., and Weiss, R. Ocean, Ice, and Atmosphere: Interac-tions at the Antarctic Continental Margin. *Antarctic Research Series, edited by: Jacobs, SS and Weiss, RF*, 75:1–28, 1998.

Wu, Y., Wang, Z., Liu, C., and Lin, X. Impacts of high-frequency atmospheric forcing on Southern Ocean circulation and Antarctic sea ice. *Advances in Atmospheric Sciences*, 37(5):515–531, 2020.

Wunsch, C. Pore fluids and the LGM ocean salinity—Reconsidered. *Quaternary Science Reviews*, 135:154–170, 2016.

Yeager, S. G., Shields, C. A., Large, W. G., and Hack, J. J. The low-resolution CCSM3. *Journal of Climate*, 19(11):2545–2566, 2006.

Yokoyama, Y., Anderson, J. B., Yamane, M., Simkins, L. M., Miyairi, Y., Yamazaki, T., Koizumi, M., Suga, H., Kusahara, K., Prothro, L., et al. Widespread collapse of the Ross Ice Shelf during the late Holocene. *Proceedings of the National Academy of Sciences*, 113(9):2354–2359, 2016.

Yokoyama, Y., Purcell, A., and Ishiwa, T. Gauging quaternary sea level changes through scientific ocean drilling. *Oceanography*, 32(1):64–71, 2019.

Yuan, X. ENSO-related impacts on Antarctic sea ice: a synthesis of phenomenon and mechanisms. *Antarctic Science*, 16(4):415–425, 2004.

Zhu, J., Xie, A., Qin, X., Wang, Y., Xu, B., and Wang, Y. An assessment of ERA5 reanalysis for Antarctic near-surface air temperature. *Atmosphere*, 12(2):217, 2021.

Zotikov, I. A. Antifreeze-Thermodrilling for Core through the Central Part of the Ross Ice Shelf (J-9 Camp), Antarctica. Technical report, Cold Rregions Research And Engineering Lab Hanover NH, 1979.